

Title	Electronic and optical properties of III-Nitride nanostructures
Authors	Patra, Saroj K.
Publication date	2019
Original Citation	Patra, S. K. 2019. Electronic and optical properties of III-Nitride nanostructures. PhD Thesis, University College Cork.
Type of publication	Doctoral thesis
Rights	© 2019, Saroj Kanta Patra. - <a href="http://creativecommons.org/licenses/by-nc-nd/3.0/">http://creativecommons.org/licenses/by-nc-nd/3.0/</a>
Download date	2024-04-18 05:39:51
Item downloaded from	<a href="https://hdl.handle.net/10468/8363">https://hdl.handle.net/10468/8363</a>

# Electronic and optical properties of III-Nitride nanostructures

Saroj Kanta Patra



Thesis submitted in partial fulfilment of the requirements  
of the degree of Doctor of Philosophy

at the  
Department of Electrical Engineering,  
University College Cork,  
National University of Ireland

Supervisor: Dr. Stefan Schulz  
Co-supervisor: Prof. Eoin P. O'Reilly  
Head of Department: Prof. Peter J. Parbrook

June 2019



# Contents

<b>Declaration of Authorship</b>	<b>vii</b>
<b>Dedication</b>	<b>viii</b>
<b>Acknowledgements</b>	<b>ix</b>
<b>List of Publications</b>	<b>x</b>
<b>0 Prologue</b>	<b>1</b>
<b>1 Introduction and Motivation</b>	<b>5</b>
1.1 Quantum dots . . . . .	6
1.2 Basic properties of III-N materials . . . . .	7
1.2.1 Crystal structure . . . . .	8
1.2.2 Polarization: Spontaneous and Piezoelectric . . . . .	10
<b>2 Theory of electronic and optical properties of wurtzite heterostructures</b>	<b>13</b>
2.1 Introduction to group theory and its application to the WZ band structure . .	14
2.1.1 Wurtzite band structure . . . . .	17
2.2 Electronic structure theory . . . . .	20
2.2.1 Electronic structure theory for bulk materials . . . . .	21
2.2.1.1 $\mathbf{k} \cdot \mathbf{p}$ theory . . . . .	21
2.2.1.2 Tight-binding model . . . . .	29
2.2.2 Electronic structure theory for QDs . . . . .	33
2.2.2.1 $\mathbf{k} \cdot \mathbf{p}$ theory for QDs . . . . .	33
2.2.2.2 Tight-binding model for QDs . . . . .	34
2.3 Strain effects . . . . .	35
2.3.1 Incorporation of strain effects in $\mathbf{k} \cdot \mathbf{p}$ model . . . . .	35
2.3.2 Incorporation of strain in Tight-binding model . . . . .	36
2.4 Calculation of strain fields . . . . .	37
2.4.1 Surface integral method . . . . .	37
2.4.2 Continuum elasticity approach . . . . .	38
2.4.3 Atomistic valence force field method . . . . .	39
2.5 Piezoelectricity . . . . .	41
2.6 Many-body states . . . . .	44
2.6.1 Hartree Approximation . . . . .	45

2.6.2	Configuration Interaction Method . . . . .	48
2.6.3	Example of a CI calculation . . . . .	50
2.6.4	Excitonic structure and Fine structure splitting . . . . .	53
<b>3</b>	<b>Excitonic and biexcitonic properties of nonpolar InGaN/GaN QDs</b>	<b>63</b>
3.1	Theoretical Framework . . . . .	64
3.2	Nonpolar InGaN/GaN quantum dot geometries . . . . .	67
3.3	Results . . . . .	68
3.3.1	Built-in potential . . . . .	68
3.3.2	Excitonic and biexcitonic properties . . . . .	72
3.3.3	Radiative lifetime . . . . .	78
3.4	Conclusion . . . . .	83
<b>4</b>	<b>Engineering the polarization properties of nonpolar InGaN QDs at elevated temperatures</b>	<b>85</b>
4.1	Theoretical framework and QD geometry . . . . .	86
4.2	Results and discussion . . . . .	88
4.2.1	Theoretical calculations of DOLP at cryogenic conditions . . . . .	89
4.2.2	Theoretical study on the impact of temperature and QD geometry on DOLP . . . . .	92
4.3	Comparison with experiment . . . . .	94
4.3.1	QD emission at cryogenic temperatures: Theory experiment comparison . . . . .	94
4.3.2	Statistical study of DOLP as a function of temperature: Theory experiment comparison . . . . .	95
4.4	Conclusion . . . . .	97
<b>5</b>	<b>Impact of second-order piezoelectricity on built-in fields, electronic and optical properties of <i>c</i>- and non-<i>c</i>-plane heterostructures</b>	<b>99</b>
5.1	Theory . . . . .	100
5.1.1	Polarization vector fields in WZ III-N semiconductor nanostructures . . . . .	100
5.1.2	Theoretical Framework and Material input parameters . . . . .	102
5.2	Results . . . . .	103
5.2.1	Built-in potential in III-N heterostructures grown along different crystallographic directions . . . . .	103
5.2.1.1	Impact of second-order piezoelectricity on built-in fields in III-N QWs . . . . .	103
5.2.1.2	Impact of second-order piezoelectricity on built-in potential in wurtzite III-N QDs . . . . .	107
5.2.2	Electronic and optical properties of InGaN/GaN QDs grown along different crystallographic directions . . . . .	113
5.2.2.1	Impact of first-order piezoelectricity and spontaneous polarization on electronic and optical properties . . . . .	113
5.2.2.2	Impact of second-order piezoelectric effects on the electronic and optical properties . . . . .	117
5.2.3	Impact of second-order piezoelectricity on emission wavelength and radiative lifetime as a function of In content . . . . .	120
5.3	Conclusion . . . . .	122
<b>6</b>	<b>Atomistic analysis of electronic and optical properties of wurtzite QDs</b>	<b>125</b>

6.1	Dot geometry . . . . .	126
6.2	Single-particle states and energies by VCA . . . . .	127
6.2.1	Effect of strain and built-in field . . . . .	128
6.2.2	Influence of spin-orbit coupling . . . . .	131
6.3	Impact of Random alloy fluctuations on electronic properties . . . . .	134
6.4	Fine structure splitting . . . . .	138
6.5	Conclusion . . . . .	142
<b>A</b>	<b>Classes and Irreducible representations of <math>C_{6v}</math> point group</b>	<b>145</b>
<b>B</b>	<b>Material parameter sets used for k·p and tight-binding calculations</b>	<b>151</b>
<b>C</b>	<b>Expressions for first- and second-order piezoelectric, spontaneous polarization vector fields as a function of <math>\theta</math></b>	<b>155</b>
	<b>Bibliography</b>	<b>159</b>




# Declaration

I, Saroj Kanta Patra, declare that this thesis entitled ‘Electronic and optical properties of III-Nitride nanostructures’ and the work presented in it are my own. I confirm that:

- This work was done wholly or mainly while in candidature for a research degree at this University.
- Where any part of this thesis has previously been submitted for a degree or any other qualification at this University or any other institution, this has been clearly stated.
- Where I have consulted the published work of others, this is always clearly attributed.
- Where I have quoted from the work of others, the source is always given. With the exception of such quotations, this thesis is entirely my own work.
- I have acknowledged all main sources of help.
- Where the thesis is based on work done by myself jointly with others, I have made clear exactly what was done by others and what I have contributed myself.

Signed:



Saroj Kanta Patra

---

Date:

---



To my parents



# Acknowledgements

I am grateful to my supervisor, Dr. Stefan Schulz for giving me the opportunity to work with him. I still remember our first meeting when Stefan ‘Sir’ asked me to drop ‘Sir’ while addressing him. He was always available to guide and support me when I got stuck (*even in weekends*). I have learnt/am still learning a lot of things from him (not only physics but also things like how to plan a work well in advance,...). His constant encouragement and friendly behavior created a nice atmosphere and I thoroughly enjoyed my Ph.D. tenure.

Thanks are also due to my co-supervisor, Prof. Eoin O’ Reilly, who had helped me a lot during my initial days in my journey from an Electronics engineer to a Ph.D. student in Photonics theory group.

I would also like to thank Prof. Robert A. Taylor’s team at the University of Oxford, UK for the excellent experimental results which supported our theoretical studies. I would like in particular thank Tong Wang for his patient hearing of my stupid questions. I would also like to thank Prof. Rachel A. Oliver, University of Cambridge, UK for her excellent expertise in growth and structural characterization of nitride quantum dots which made our modelling easier.

I thank the members of my progress review committee at Tyndall, Prof. Eoin O’ Reilly and Mr. Brian Corbett for their time and valuable inputs during my yearly reviews. I also thank my thesis examiners, Prof. Peter J. Parbrook from Tyndall National Institute and Dr. Alessandro Pecchia from CNR- Institute Studio Materiali Nanostrutturai for their time to examine this thesis.

I thank the Science Foundation of Ireland for providing the funding that supported my research (13/SIRG/2210).

I want to thank my friends (Daniel, Siviu, Chris, Amy, Reza and Edmond) at photonics theory group for helping me whenever needed. Also, many thanks to Tuhin, Dhiman, Swatchith, Kankana, Aman who made me feel in Ireland like home.

The thesis is dedicated to my parents, who had gone through a lot of hardship and it is they for whom I have reached where I am today. Finally, I would like to thank my wife Sarita for being always there for me.

# Publications

Parts of this work has been published in the following:

## 1. Refereed journal articles

- “Polar, semi- and non-polar nitride-based quantum dots: influence of substrate orientation and material parameter sets on electronic and optical properties”, Saroj K. Patra, Oliver Marquardt and Stefan Schulz, *Opt. Quant. Electron* **48**, 151 (2016).
- “Non-polar  $\text{In}_x\text{Ga}_{1-x}\text{N}/\text{GaN}$  quantum dots: impact of dot size and shape anisotropies on excitonic and biexcitonic properties”, Saroj K. Patra and Stefan Schulz, *J. Phys. D. Appl. Phys.* **50**, 025108 (2017).
- “Theoretical and experimental analysis of radiative recombination lifetimes in nonpolar  $\text{InGaN}/\text{GaN}$  quantum dots”, Saroj K. Patra, Tong Wang, Tim J. Puchtler, Tongtong Zhu, Rachel A. Oliver, Robert A. Taylor and Stefan Schulz, *Phys. Stat. Solidi. B* **254**, 8 (2017).
- “Direct generation of linearly polarized single photons with a deterministic axis in quantum dots”, Tong Wang, Tim J. Puchtler, Saroj K. Patra, Tongtong Zhu, Muhammad Ali, Tom Badcock, Tao Ding, Rachel A. Oliver, Stefan Schulz, and Robert A. Taylor, *Nanophotonics* **6**, 5 (2017).
- “Deterministic optical polarisation in nitride quantum dots at thermoelectrically cooled temperatures”, Tong Wang, Saroj K. Patra, Tim J. Puchtler, Tongtong Zhu, John. C. Jarman, Rachel A. Oliver, Stefan Schulz, and Robert A. Taylor, *Sci. Rep.* **7**, 12067 (2017).
- “Electrostatic built-in fields in wurtzite III-N nanostructures: Impact of growth plane on second-order piezoelectricity”, Saroj K. Patra and Stefan Schulz, *Phys. Rev. B* **96**, 155307 (2017).
- “Impact of second-order piezoelectricity on electronic and optical properties of  $c$ -plane  $\text{In}_x\text{Ga}_{1-x}\text{N}$  quantum dots: Consequences for long wavelength emitters”, Saroj K. Patra and Stefan Schulz, *Appl. Phys. Lett.* **111**, 103103 (2017).
- “Electronic and optical properties of polar, semi- and non-polar  $\text{InGaN}$  QDs: The role of second-order piezoelectric effects”, Saroj K. Patra and Stefan Schulz, *Jpn. J. Appl. Phys.* **58**, SCCB38 (2019).

## 2. Conferences

- “Electronic and optical properties of non-polar InGa<sub>N</sub>/Ga<sub>N</sub> quantum dots: Impact of shape anisotropies and Coulomb effects”, Saroj K. Patra and Stefan Schulz, in *UK semiconductors*, Sheffield (2016).
- “Efficient single and entangled photon sources using nonpolar InGa<sub>N</sub> dots”, Saroj K. Patra, Eoin O’ Reilly, and Stefan Schulz, at *Tyndall National Institute*, Cork (2016).
- “Electronic and optical properties of non-polar InGa<sub>N</sub>/Ga<sub>N</sub> quantum dots: Insights from experiment and Theory”, Saroj K. Patra, Tong Wang, Tim J. Puchtler, Tongtong Zhu, Muhammad Ali, Tom Badcock, Tao Ding, Rachel A. Oliver, Robert A. Taylor and Stefan Schulz, in *International Workshop for Nitrides (IWN)*, Orlando (2016).
- “Theoretical study of the optical properties of a-plane InGa<sub>N</sub>/Ga<sub>N</sub> quantum dots”, Saroj K. Patra and Stefan Schulz, in *Euro-TMCS II*, at Tyndall National Institute, Cork (2016).
- “Non-classical light generation beyond the 200 K thermoelectric barrier with a-plane InGa<sub>N</sub> quantum dots”, Saroj K. Patra and Stefan Schulz, in *UKNC*, University of Oxford, Oxford (2017).
- “Linearly polarized single photon sources using non-polar InGa<sub>N</sub> QDs : The way forward to room temperature on-chip polarization encoding in quantum cryptography and quantum computing”, Saroj K. Patra, Tong Wang, Tim J. Puchtler, Tongtong Zhu, John C. Jarman, Rachel A. Oliver, Robert A. Taylor and Stefan Schulz, in *Tyndall National Institute*, Cork (2017).
- “Built-in fields, electronic and optical properties of III-Nitride nanostructures: The role of nonlinear piezoelectric effects”, Saroj K. Patra and Stefan Schulz, in *UKNC 2018*, University of Manchester, Manchester (2018).
- “Carrier localization in Ga<sub>N</sub>/AlGa<sub>N</sub> MQWs: Insights from theory and experiment”, A. Roble, Saroj K. Patra S. Church, M. A. Leontiadou, P. Dawson, M. J. Kappers, R. A. Oliver, S. Schulz, and D. M. Graham, in *UK semiconductors*, Sheffield (2018).
- “Electronic and Optical properties of Ga<sub>N</sub>/AlGa<sub>N</sub> quantum wells: Role of random alloy fluctuations in the barrier”, Saroj K. Patra and Stefan Schulz, in *IEEE Photonics Conference*, Virginia (2018).
- “Theoretical and experimental analysis of carrier localization effects in Ga<sub>N</sub>/AlGa<sub>N</sub> QWs”, Saroj K. Patra, A. Roble, S. Church, M. A. Leontiadou, P. Dawson, M. J. Kappers, R. A. Oliver, D. M. Graham and Stefan Schulz, in *Photonics Ireland-2018*, Cork (2018).

- “Theory of second-order piezoelectric fields in III-N nanostructures”, Saroj K. Patra and Stefan Schulz, in *18<sup>th</sup> International Conference on Numerical Simulation of Optoelectronic Devices (NUSOD)*, Hongkong (2018).
- “Impact of second-order piezoelectricity on built-in fields, electronic and optical properties of *c*- and non *c*-plane heterostructures”, Saroj K. Patra and Stefan Schulz, in *International Workshop on Nitride Semiconductors*, Kanazawa, Japan (2018).
- “Electronic and optical properties of InGaN/GaN quantum dots: Insights from full atomistic many body calculations”, Saroj K. Patra and Stefan Schulz, in *UKNC*, Strathclyde (2019).

## Contributions to Invited Talk

- “Non-polar InGaN Quantum Dots: Polarised Single-Photon Sources with Temperature-dependent Fine Structure Splitting, Reduced Lifetime and Spectral Diffusion”, T. Wang, T. J. Puchtler, T. Zhu, Saroj K. Patra, H. P. Springbett, J. C. Jarman, C. C. Kocher, L. P. Nuttall, R. A. Oliver, S. Schulz, R. A. Taylor *International Workshop on Nitride Semiconductors*, Kanazawa, Japan (2018).
- “Nitride Single Photon Sources ”, Tongtong Zhu, John C. Jarman, Christopher X. Ren, Fengzai Tang, Claudius C. Kocher, Tim J. Puchtler, Benjamin P. L. Reid, Tong Wang, Saroj K. Patra, Stefan Schulz, Robert A. Taylor and Rachel A. Oliver *IEEE Photonics Conference*, Reston, VA, USA (2018).
- “Single photon sources based on non-polar InGaN quantum dots”, Tongtong Zhu, John C. Jarman, Christopher X. Ren, Fengzai Tang, Claudius C. Kocher, Stephen A. Lennon, Luke Nuttall, Benjamin P. L. Reid, Saroj K. Patra, Stefan Schulz, Robert A. Taylor and Rachel A. Oliver *19<sup>th</sup> International Conference on Metal organic Vapour phase Epitaxy*, Japan (2018).

# Chapter 0

## Prologue

Quantum dot (QD) technology is no longer novel and according to Ref [1], global QDs market is estimated to be valued at  $\approx$  \$27.5 billion by 2030. A vast majority of this figure is attributed to the optoelectronic industries where QD displays are potentially outpacing organic light emitting diode (OLED) displays with a compound annual growth rate of  $\approx$  37% [2]. This trend is also visible from a report by IHS markit [2] which mentions that over 6.5 million QD TVs have been ordered to be shipped in 2020 which is 0.5 million more than the units of OLED TVs ordered. Given this technological revolution, more and more research has been focused on QDs lately [3, 4].

In addition to the above-mentioned display technologies, QDs have been used in a wide variety of applications [5–7] such as producing images of cancer tumours [5], humidity and pressure sensors [6], to treat antibiotic resistant infections [8], non-toxic low cost solar cells [9], catalysts [10] and so on. Over recent years, QDs have also attracted considerable interest due to their potential for non-classical light emitters such as single- and entangled-photon sources [7, 11, 12]. These non-classical light emitters are the cornerstone for quantum cryptography and quantum computing applications [11].

In this thesis, we target QD structures based on a semiconductor material known as “indium gallium nitride” (InGaN) with an aim to achieve efficient single and entangled photon emitters. Here, we investigate the electronic and optical properties of InGaN QDs as a function of crystallographic growth angle. Especially, we focus on InGaN QD structures grown along a so-called nonpolar direction of the underlying crystal structure. As we will show later, this novel approach not only allows us to keep the benefits of the nitride system (large band offsets) but at the same time allows for distinct new features such as circumventing basically the strong electrostatic built-in fields. The common problem of growing these structures is an increased probability of defect generation due to the lack of high quality nonpolar GaN buffer layers [13]. Additionally, the much-lower In incorporation efficiency in nonpolar planes present difficulties

for strain-driven Stranski-Krastanov growth of these dots [13]. Despite the challenges, there has been recent progress in the growth of nonpolar InGaN QDs [13–15]. Yang *et al* [13] successfully grew nonpolar InGaN QDs by introducing aluminium gallium nitride (AlGaN)/aluminium nitride (AlN) interlayers prior to the GaN buffer layer. In another report, Zhu *et al* [14] used a modified droplet epitaxy method for the growth of high quality nonpolar InGaN QDs. Given these recent advances in the growth of nonpolar QDs, a detailed theoretical understanding of the electronic and optical properties is of essential importance. This thesis aims to provide a comprehensive understanding of these systems and is structured as follows.

## Overview of the thesis

After a general introduction of nitride systems and semiconductor QDs in Chapter 1, we present an overview of the theoretical models utilized in this thesis to calculate the electronic and optical properties of these QDs in Chapter 2. In this chapter, we describe the well established  $\mathbf{k} \cdot \mathbf{p}$  and tight-binding model followed by a brief introduction to group theory which is very useful in predicting different electronic properties. The influence of spin-orbit interaction, strain effects arising from the lattice mismatch of constituent materials, and piezoelectricity on the electronic structure theories are presented. Finally, we describe many-body theories which are crucial for the analysis of optical properties in these systems. Here, the excitonic structure and fine structure splitting of different QD systems are also explained.

In Chapter 3, we focus on the excitonic, biexcitonic properties and radiative lifetime of the nonpolar QDs with an aim to achieve high speed single-photon emission. In addition to the single-photon emission, we also target entangled photon emission by tuning the exciton and biexciton transitions. Furthermore, quantum cryptography applications also require single photon sources to be highly polarized in nature and at the same time realistic scalable on-chip applications require operation of dots at elevated temperatures. Therefore, in Chapter 4, we study the polarization properties of these systems as a function of temperature. In these analyses, we study the influence of various parameters e.g. QD geometry and composition on the single-particle properties. The results obtained from our theoretical analysis has been validated by comparison with experiments.

Additionally, the theoretical studies in nitride-based QDs have been mainly restricted to first-order piezoelectric effects till now. In contrast, for other III-V QD systems, e.g. InGaAs, it has been demonstrated that second-order effects are crucial for a complete and realistic description of built-in fields and the connected electronic and optical properties [16]. Such an analysis is missing in nitride-based QDs especially when grown on non-*c*-plane substrates. Therefore in Chapter 5, we discuss the impact of second order piezoelectric effects on the electronic and optical properties of QDs as a function of crystallographic growth angle.

Turning back to non-classical light emitters, in Chapter 6, our calculations are directed towards understanding the impact of random alloy fluctuations on electronic and optical properties of  $c$ -plane InGaN/GaN QDs. Here we address this question by means of a fully atomistic many-body theoretical framework. The related excitonic structure and fine structure splitting values are also calculated. This study is essential to explore the potential benefit of nitride-based QDs for entangled photon emitters.

Finally, summary of the thesis and an outlook are given in Chapter 7.



# Chapter 1

## Introduction and Motivation

As pointed out in the prologue, semiconductor QDs have attracted considerable interest within past few decades due to their broad spectrum of applications ranging from high-efficiency optoelectronic devices, such as light emitting diodes [17, 18], laser diodes [19–22] to non-classical light emitters such as single- and entangled-photon sources for quantum computing applications [11, 12, 23–26]. Traditionally, ultra-pure non-classical light sources have been realized by using standard III-V materials such as indium arsenide (InAs) and gallium arsenide (GaAs) material systems [7, 27, 28]. Due to low cost and less toxicity, arsenide based QDs are popular among the research community [29]. However, due to narrow band gap of both GaAs ( $E_{g,\text{GaAs}} \approx 1.518$  eV) and InAs ( $E_{g,\text{InAs}} \approx 0.413$  eV) [30], the typical emission wavelengths of these devices are in the range of few  $\mu\text{m}$  [30]. On the other hand, QDs based on III-Nitride compounds (GaN, AlN, InN) and their connected alloys (InGaN and AlGaN) can span almost the entire spectrum e.g. infrared (IR) [31] to ultraviolet (UV) [32] due to their band gap tunability ranging from 0.69 eV (InN) [31], 3.51 eV (GaN) [31] to 6.0 eV (AlN) [33]. Apart from light emission, due to these wide band gap and high breakdown field ( $E_{br,\text{GaN}} \approx 4$  MV/cm,  $E_{br,\text{AlN}} \geq 10$  MV/cm) [33], GaN and AlN are also suitable for high power and high frequency applications such as military communication satellites and high frequency transistors [33]. When compared to a GaAs based system, the output power density of GaN based devices are  $\approx 5$ -10 times larger [34].

Due to these enormous advantages, nitride systems have generated much interest over the last few decades [35]. However, there remain still several open questions. For instance, realization of high-quality light emitting devices at longer wavelengths requires growth of InGaN alloys with high indium content. One of the main roadblocks in achieving this is the large lattice mismatch between InN and GaN ( $\approx 10\%$ ) [36] which incorporates huge strain while growing high In content structures and results in misfit dislocations degrading optical properties [37]. As we will show later, another important issue which affects device efficiencies when nitride heterostructures grown along  $c$ -axis is the presence of electrostatic built-in fields. This arises

from spontaneous and piezoelectric polarization fields present in nitride heterostructures [38]. Even though other III-V materials exhibit piezoelectric properties, nitride systems incorporate both polarization fields [39].

Given the unique features of nitride material systems, the aim of this chapter is to analyze these fundamental properties and highlight the differences to other material systems. That will include discussions of the underlying crystal structure, different growth planes as well as the electrostatic built-in field leading to the so-called quantum confined stark effects (QCSE). We will also outline the challenges in the modeling of nitride QD systems. To achieve this we proceed in the following way. In Sec. 1.1 we start with a brief overview of the fundamental aspects of QDs including growth mechanisms in different material systems. We then turn to nitride systems in Sec. 1.2, and discuss differences in terms of crystal structure for instance to the standard arsenide systems in Sec. 1.2.1. Finally, in Sec. 1.2.2, we will turn to the polarization effects and discuss its consequences for the electronic structure.

## 1.1 Quantum dots

Quantum dots are formed when carriers are confined along all three directions with physical dimensions in the order of de-Broglie wavelength. This quantum confinement can be achieved by several means, for instance, in a solution [40] or by growing epitaxial layers on other semiconductor materials [41, 42], called as nanocrystallites and self-assembled QDs respectively. In this thesis, we will only focus on self-assembled QDs which are formed when a semiconductor structure with a given band gap is embedded in a matrix of semiconductor with a large band gap [41, 42]. Due to quantization of energy along all three directions, QDs exhibit discrete energy spectrum like atoms. Therefore, QDs are often referred to as “artificial atoms”. Due to this loss of translational symmetry along all three directions, QDs exhibit delta-like density of states. However, they possess several different characteristics as compared to atoms and bulk semiconductor structures [43]. Especially, their tunable optical characteristics where emission wavelength in principle can be changed easily by varying material composition and/or dot geometry.

Several techniques for the preparation of semiconductor QD structures have been reported [43] in the literature. They can be realized for instance by using lithography [7, 43], metal organic chemical vapour deposition (MOCVD) [14, 44] or molecular beam epitaxy (MBE) [17, 21, 45]. Using lithographic methods, fragments of well defined size and shapes can be etched from bulk semiconductors to realize QDs. The other possibility that has recently gained interest is the formation of QDs by self-assembled clustering through Stranski-Krastanow (S-K) growth [45, 46] or droplet epitaxy method [14, 47]. S-K growth is driven by the strain originating from the lattice mismatch between the dot and the barrier material. When a semiconductor

material A is grown epitaxially on top of another semiconductor material B, the initial growth happens to be a quasi-two-dimensional layer-by-layer growth of material A on top of the B surface. When the growth exceeds a certain critical thickness [46], the strain energy stored in the system due to lattice mismatch between the material A and material B is reduced through the formation of three-dimensional objects called QDs. A self-assembled QD grown through S-K method is shown schematically in Fig. 1.1. The shape of the QD structures grown through this method usually depends on several parameters such as the underlying crystal lattice, growth temperature, and growth rate.

On the other hand, in droplet epitaxy method, formation of QDs do not require elastic strain between the dot and the barrier material [48, 49]. Here the growth takes place through vapour-liquid-solid mechanism [48] where the supersaturation of the liquid droplets occur via interaction with the species carried by the beams in the vapour phase [49]. For instance, in droplet epitaxy of III-V systems, first nano-meter sized metallic droplets (Group-III) are formed on the growth surface through sudden annealing [14] which then react with group-V beams to form QDs. As pointed out earlier, we will only deal with QDs formed through the above mentioned self-assembled processes in this thesis. Typical dimension of QDs in a quantum dot ensemble

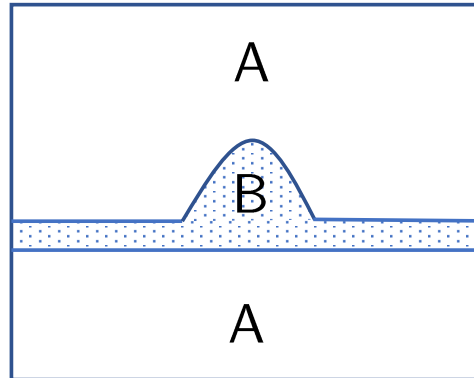


FIGURE 1.1: Schematic diagram of a self-assembled QD where a semiconductor material B is embedded inside a semiconductor material A

scatter in the range of 3 nm and 30 nm which contains around  $10^4$ – $10^6$  atoms. Using the above described methods, high quality QDs have been produced in both arsenide and nitride material systems. Since in this thesis we are mainly interested in the nitride systems, we turn to the discussion of basic features in these materials in the next section.

## 1.2 Basic properties of III-N materials

One of the several particularities of III-N system is the underlying crystal structure which has far reaching consequences in the electronic band structure [50]. For instance, as pointed out earlier, this unique crystal structure gives rise to polarization fields which in turn leads to

the so-called QCSE affecting the device performance [51]. Therefore, we start this section by discussing the underlying crystal structure where we outline how III-N structures are grown along different crystallographic directions in current state-of-the-art devices and subsequently turn to the polarization properties.

### 1.2.1 Crystal structure

III-Nitrides (GaN, InN, AlN) and their connected alloys (InGaN and AlGaN) crystallize preferentially in the wurtzite (WZ) crystal phase whereas other typical arsenide-based materials crystallize in the zincblende (ZB) phase [30]. Fig. 1.2 illustrates a WZ crystal structure where  $a$  and  $c$  corresponds to the lattice constants along the basal plane and height of the unit cell, respectively. An ideal WZ crystal can be thought of as two interpenetrating hexagonal close-packed (hcp) lattices offset along the  $c$ -axis by  $5/8$  of the  $c$  lattice constant. The layers in a WZ structure show an ABABAB- type stacking sequence and alternate between anions and cations. The atoms indicated in red represent cations (Ga,In,Al) whereas blue denotes anions

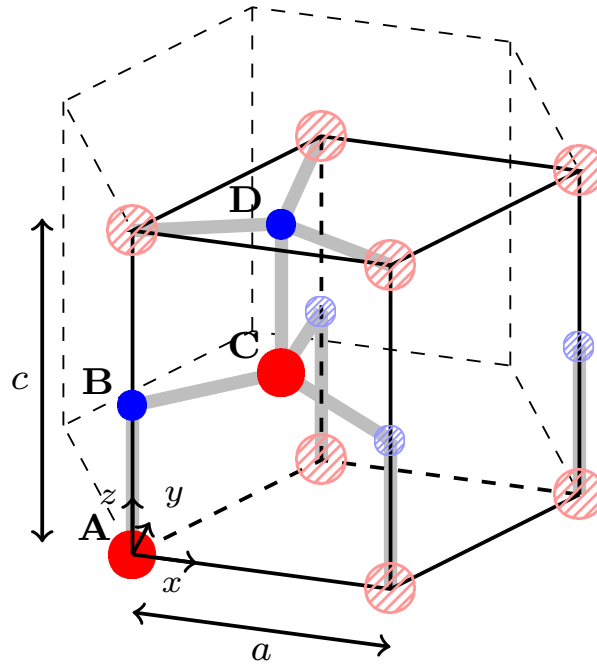


FIGURE 1.2: Wurtzite unit cell [52]

(N). The primitive unit cell of a WZ structure contains four atoms, two anions and two cations. In Fig. 1.2 the atoms inside the primitive unit cell are given by filled symbols. The atomic

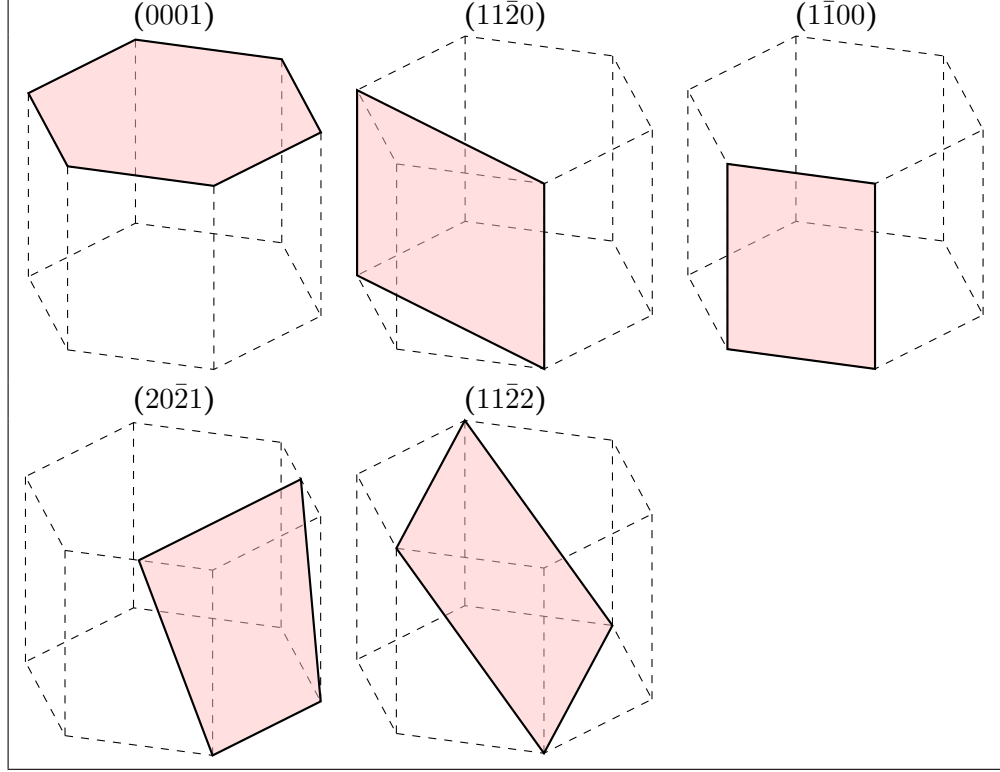


FIGURE 1.3: Different planes of a wurtzite crystal structure

positions inside the primitive unit cell are given by,

$$\begin{aligned}
 \mathbf{r}_A &= (0, 0, 0), \\
 \mathbf{r}_B &= (0, 0, u_0 c), \\
 \mathbf{r}_C &= \left( a/2, \sqrt{3}a/6, c/2 \right), \\
 \mathbf{r}_D &= \left( a/2, \sqrt{3}a/6, (1/2 + u_0)c \right),
 \end{aligned} \tag{1.1}$$

where  $u_0$  is an internal parameter of the WZ structure; for an ideal WZ structure,  $u_0=3/8$  [50]. The Cartesian coordinates are also indicated in the figure.

III-Nitride WZ heterostructures as we will discuss in later chapters are grown along different crystallographic planes and the following notations are used to denote them. In general, lattice planes and directions in a crystal are defined by Miller indices [53], which are denoted by  $(hkl)$  and  $[hkl]$ , respectively. Here  $h, k, l$  are the reciprocal values of the intersection of a plane with the Cartesian axis in a direct lattice. However, to denote planes and directions in hexagonal lattices like WZ, Miller-Bravais indices [50] are used, which contain an extra index  $i$  such that  $i = -(h + k)$ . In other words, the crystal planes in a WZ structure are denoted as  $(hkil)$ . Using this notation, schematic illustrations of different planes of a WZ structure are shown in Fig. 1.3. Here, we have used the same orientation of the Cartesian coordinates as in Fig. 1.2.

In standard convention, the plane normal to the  $z$ -direction of the WZ structure is regarded as the  $c$  (0001)-plane and the axis parallel to  $z$ -direction is labelled as  $c$  ([0001])-axis.

It is to note that  $c$ -direction is the most widely used growth direction [38]. The planes for which the  $c$ -axis lies within the growth plane are defined as  $a$  (11 $\bar{2}$ 0)- and  $m$  (1 $\bar{1}$ 00)-planes. Additionally, we also show two other experimentally relevant planes [54], (11 $\bar{2}$ 2) and (20 $\bar{2}$ 1) in Fig. 1.3 which are at an angle  $\theta = 58^\circ$  and  $\theta = 75^\circ$  to the  $c$ -axis.

These planes are often classified as polar, semi- and nonpolar planes. The  $c$ -plane is polar whereas  $a$ - and  $m$ - planes are nonpolar planes. All other planes are called semipolar planes. This originates from the unique features of WZ materials which are spontaneous and piezoelectric polarization and is discussed in detail in the following section.

### 1.2.2 Polarization: Spontaneous and Piezoelectric

Semiconductor materials with a lack of inversion symmetry exhibit an electric polarization under applied stress [38, 55–57]. This strain mediated electric polarization is the so-called piezoelectric polarization. The piezoelectric polarization ( $\mathbf{P}_{\text{pz}}$ ) vector field in a semiconductor material can be written, up to second-order, using Voigt notation as [57]:

$$P_{\text{pz},\mu} = P_{\text{pz},\mu}^{\text{FO}} + P_{\text{pz},\mu}^{\text{SO}} = \sum_{j=1}^6 e_{\mu j} \varepsilon_j + \frac{1}{2} \sum_{j,k=1}^6 B_{\mu jk} \varepsilon_j \varepsilon_k. \quad (1.2)$$

Here  $P_{\text{pz},\mu}^{\text{FO}} = \sum_{j=1}^6 e_{\mu j} \varepsilon_j$  is the first-order contribution and  $P_{\text{pz},\mu}^{\text{SO}} = \frac{1}{2} \sum_{j,k=1}^6 B_{\mu jk} \varepsilon_j \varepsilon_k$  is the second-order part. The first-order piezoelectric coefficients are denoted by  $e_{\mu j}$  and  $B_{\mu jk}$  are second-order ones. The strain tensor components (in Voigt notation) are given by  $\varepsilon_j$ . In III-N heterostructures, most widely only first-order contributions to the polarization field are used [39]. For WZ semiconductors the well known first-order contribution  $\mathbf{P}_{\text{pz}}^{\text{FO}}$  has only three independent piezoelectric coefficients, namely  $e_{33}$ ,  $e_{15}$  and  $e_{31}$  [58]. Turning to second-order terms, initial studies on second-order piezoelectricity have been performed by several groups [55, 57, 59] for III-N WZ systems. We will present a detailed study and explicit expressions for the first and second-order piezoelectric polarization vectors for a WZ structure in later chapters.

In both ZB and WZ structures, each atom has four nearest neighbours which are arranged in a tetrahedral manner. Due to difference in electronegativity between atoms, each bond has a certain dipole moment. In ZB structures, these dipole moments cancel each other and the net dipole moment is zero due to the crystal symmetry [60]. However, in III-N WZ structures, due to the underlying symmetry and electronic distributions, certain directions (0001) present net dipoles even without application of strain [38, 58]. We call this as spontaneous polarization ( $\mathbf{P}_{\text{sp}}$ ) where polarization is defined as net dipole moment per unit volume. Thus in a standard

$c$ -plane description, where the  $c$ -axis is usually parallel to the  $z$ -axis of the coordinate system, the spontaneous polarization vector field  $\mathbf{P}_{\text{sp}}$  reads: [58]

$$\mathbf{P}_{\text{sp}} = \begin{pmatrix} 0 \\ 0 \\ P_{\text{sp}} \end{pmatrix}. \quad (1.3)$$

As stated earlier,  $\mathbf{P}_{\text{sp}}$  is a unique feature of WZ structures and is not present in materials having a ZB crystal structure. Typical spontaneous polarization values of GaN, InN and AlN wurtzite structures are -0.040, -0.049 and -0.091 C/m<sup>2</sup> [61], respectively. However, it should be noted that a variety of different values has been reported in the literature [62]. The sign of the spontaneous polarization is negative assuming that the polarization is defined by the direction from the anion (N) to the cation (Ga/In/Al) along the [0001] direction. The magnitude of  $P_{\text{sp}}$  depends on  $\frac{c}{a}$  ratio and the difference of electronegativity between the constituent atoms [63]. The direction of  $P_{\text{sp}}$  is illustrated in Fig. 1.4 where similar to Fig. 1.2 red denotes cations (Ga, Al, In) and blue denotes the anions (N).

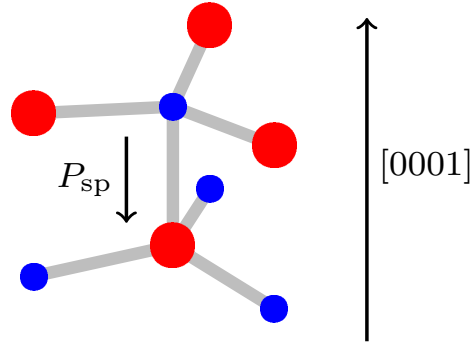


FIGURE 1.4: A stick and ball diagram representing the direction of spontaneous polarization. Red denotes cations (Ga, Al, In) and blue denotes anions (N).

Overall, the total polarization vector field  $\mathbf{P}_{\text{Tot}}$  in a WZ system is the sum of piezoelectric and spontaneous polarization vector fields,  $\mathbf{P}_{\text{Tot}} = \mathbf{P}_{\text{sp}} + \mathbf{P}_{\text{pz}}^{\text{FO}} + \mathbf{P}_{\text{pz}}^{\text{SO}}$ .

From electrodynamics, we know already that when we have a discontinuity in the polarization vector field, these give rise to an electrostatic built-in field [64]. Accordingly, when WZ heterostructures are grown along  $c$ -axis, the polarization differences in the dot and matrix materials give rise to a built-in electric field. This field results in the QCSE which tilts the energy band structure and leads to the localisation of electron and hole wave functions on the opposite sides of the structure. QCSE is much stronger in case of III-N WZ systems as compared to ZB systems due to the presence of both spontaneous and piezoelectric contributions. In Fig. 1.5, we outline a schematic band structure depicting the electron and hole wave functions with and without built-in field for a semiconductor material B embedded inside a semiconductor material A. As discussed above, the electrostatic built-in field has a detrimental effect on the

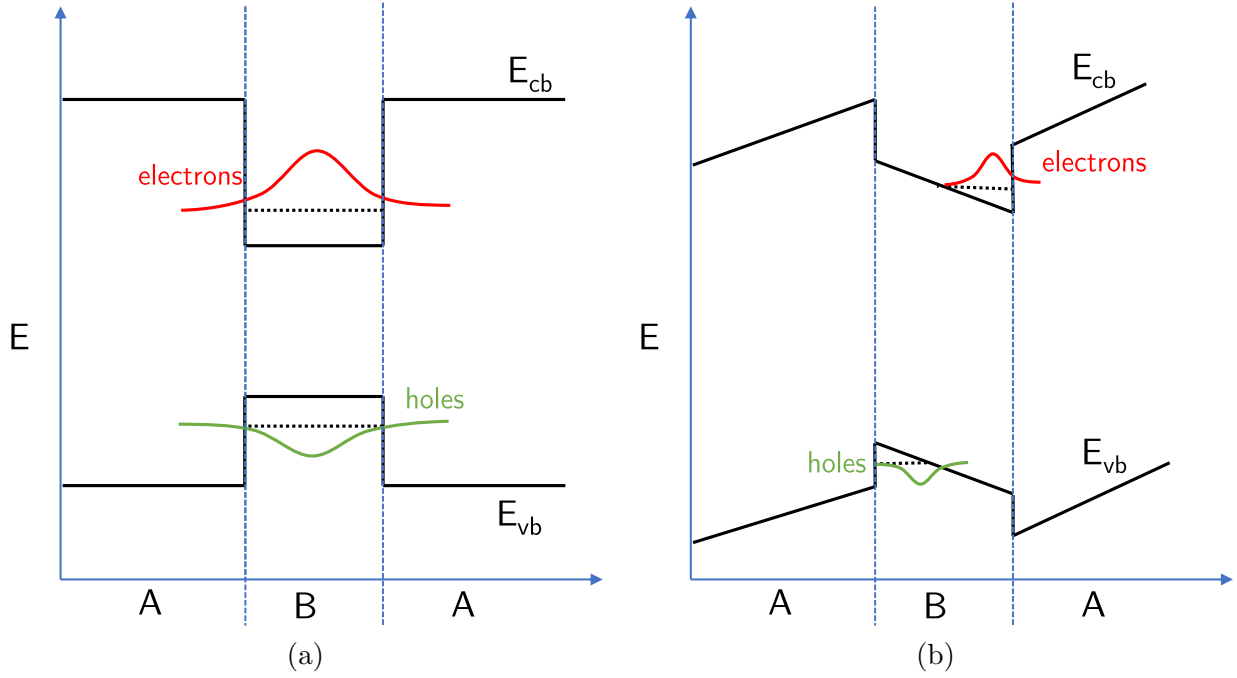


FIGURE 1.5: One dimensional band diagram (a) excluding (b) including the internal electrostatic built-in field created by piezoelectric and spontaneous polarizations for a semiconductor material B (e.g. InGaN) embedded inside a semiconductor material A (e.g. GaN) [65]. Electron and hole wave functions are denoted by red and green respectively.

optical properties of the system. Therefore focus shifted to growth on the non- and semipolar planes [54, 66, 67], which have been introduced in the previous section. If we now look back at the semi- and nonpolar planes, we have a situation in the nonpolar system, where the  $c$ -axis lies in the growth plane which can ideally circumvent discontinuities in the polarization vector field. We will discuss this in more detail in the next chapter.

Having discussed the fundamental aspects of both QDs and nitride systems, we now move to the question how to theoretically model these systems. A key requirement here is the calculation of electronic band structure for a QD system of an arbitrary shape. From our previous discussions, it is immediately clear that modeling nitride QD systems is challenging as we are dealing here with very large ( $10^4$ – $10^6$  atoms) systems. At the same time, due to loss of translational invariance, QDs lack fundamental symmetry properties of bulk systems which makes the calculations considerably more difficult. Finally, we also have to take into account the inherent properties of nitride systems, such as polarization fields. Therefore, to account for all the ingredients, we need a theoretical model that allows us to calculate electronic structure, not only for the bulk system as well as for the QDs, which is the topic of the next chapter.

## Chapter 2

# Theory of electronic and optical properties of wurtzite heterostructures

Having discussed the fundamental properties of III-N bulk as well as QDs in Chapter 1, we now turn our attention to the calculation of electronic and optical properties of these systems. In Fig. 2.1, we present a schematic workflow outlining different steps to achieve this task. The electronic properties of a material system is usually specified in terms of its electronic band structure. Therefore, in the first step, we need an underlying electronic structure theory (cf. Fig. 2.1) which will be used to calculate single-particle states and energies. As discussed in the last chapter, one also needs to account for strain and built-in potential effects in the electronic structure theory. The type of strain and built-in field calculations to use is usually determined by the underlying electronic structure theory. Together with strain, built-in potential and an appropriate electronic structure theory, one can solve one-particle Schrödinger equation and obtain single-particle energies and eigenstates of the system. Additionally, if we are interested in optical properties such as entangled photon emission, this is inherently a many-body problem. Therefore, as we will show later, one needs to consider many-body effects to accurately describe optical properties of these systems [29]. Accordingly, we discuss different electronic structure theories in Sec. 2.2. In the next step, in Sec. 2.3, we describe how to incorporate strain in different models and subsequently, outline various methods to calculate strain, namely continuum elasticity method, surface integral method and valence force field method in Sec. 2.4. Equipped with the underlying strain theories, we then describe the procedure to calculate piezoelectric potential in Sec. 2.5. Finally, we introduce different many-body theories in Sec. 2.6. All these approaches are fully numerical in nature. But group theory has been used over the years to predict fundamental properties such as optical selection rules, degeneracy of eigenvalues, phase

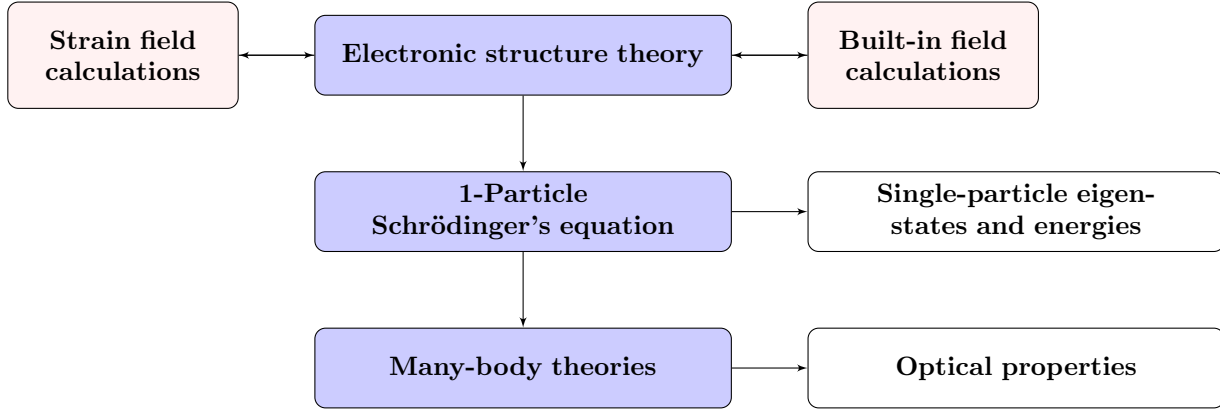


FIGURE 2.1: General workflow for the calculation of electronic and optical properties

transitions [53] without doing explicit calculations and is also a powerful tool to check our numerical results. Given these advantages, before we start with the numerical aspects, we present a brief introduction to group theory, which will later help us to benchmark our results.

## 2.1 Introduction to group theory and its application to the WZ band structure

In this section, we will deal with the practical use of group theory and illustrate the power of using group theory and tensor algebra in explaining and to draw conclusions for electronic properties of a semiconductor with a WZ crystal structure. We will not cover derivations of the fundamental postulates or advanced aspects of this topic. Detailed discussions on this topic can be found elsewhere [68, 69].

In a first step, we introduce few group theoretical concepts required for our analysis. Group theory [53] transforms many complex symmetry operations of a crystal into simple linear algebra. This begs the question what exactly is the symmetry? The *symmetry group* of a crystal consists of all operations that transforms the crystal structure into itself. In a crystal lattice, these include *translation group*, *point group*, and *space group* symmetries. The translation group corresponds to a set of translations which keeps the system unchanged. The point group involve symmetry operations/elements ( $g$ ) such as rotations, reflections, inversion or combinations of these operations around one point in the lattice. On the other hand, the space group involves a combination of a point group symmetry operation and a translation. The commonly used symmetry operations in this thesis are:

- E: Identity. This operation corresponds to doing nothing to the structure and every group has at least this element.

- $C_n$ : N-fold axis of rotation. Here, a rotation by  $\frac{360^\circ}{n}$  leaves the system unchanged. Here,  $n$  is an integer. Rotations are counter-clockwise by convention.
- $\sigma$ : Mirror planes of symmetry.  $\sigma_v$  denotes vertical mirror planes passing through faces and  $\sigma_d$  denotes mirror planes passing through vertices.
- $i$ : Inversion of the structure through a single point called as the inversion center.

To denote point and space groups, Schoenflies notation has been used in this thesis [70]. In this notation, the point groups are denoted by a letter symbol and a subscript. For instance, the symbol  $C_{nv}$  denotes a point group with  $n$ -fold rotation axis.  $v$  indicates that this group has additional  $n$  mirror planes parallel to the axis of rotation. The Schoenflies notation has several advantages. First, the general features of the group, e.g. the symmetry elements are contained in the notation itself. Secondly, this notation is the widely used in spectroscopy [70]. In this notation, within each point group, space groups are simply numbered in the order in which they appear in the International Tables for Crystallography (IUCR). This number is written as a superscript to the point group notation. For instance, a space group corresponding to the  $C_{6v}$  point group is  $C_{6v}^4$ . Usually, the symmetry elements ( $g$ ) contained in the point and space groups are grouped into *classes*. As an example, we have listed all the symmetry elements and classes belonging to the  $C_{6v}$  point group in Appendix A. As we will show later, this is the point group with which we will be dealing later in this chapter. Therefore, we are focussing on the  $C_{6v}$  point group. For each of the symmetry elements  $g$  in a group, one can construct a transformation matrix,  $\Gamma(g)$  which is called a *representative* of the corresponding symmetry operation. The complete set of transformation matrices form the matrix *representation* of the group. These transformation matrices act on basis functions of our choice and as a result, the representation depends on the chosen basis. However, several important aspects of a symmetry group can already be obtained from the traces of the matrix representation. The trace ( $Tr$ ) of a matrix is the sum of the matrix elements on the diagonal, and is also called the *character* of the representation. The character gives a short hand version of the matrix representation. Often, the matrix representation of a group is simplified into smaller matrices. For instance, if the representation matrix  $R$  can be expressed in a block diagonal form such that

$$R = \begin{bmatrix} R_1 & & 0 \\ & R_2 & \\ 0 & & R_3 \end{bmatrix},$$

then,  $R_1$ ,  $R_2$  and  $R_3$  are said to be *irreducible representations* (IRR) of the group. In the Appendix A, as an example, we have summarized irreducible representations for the  $C_{6v}$  point group in a  $x$ ,  $y$ ,  $z$  coordinate basis. If all of the possible IRRs of a group are summarized in a table, we call this a *character table*. As an illustrative example, the character table of a  $C_{6v}$  point group is shown in Table 2.1. In the character table, the first entry in the first row

TABLE 2.1: Character table of  $C_{6v}$  point group

$C_{6v}$	$E$	$2C_6$	$2C_3$	$C_2$	$3\sigma_d$	$3\sigma_v$	Basis functions
$A_1$	1	1	1	1	1	1	$1, z$
$A_2$	1	1	1	1	-1	-1	$R_z$
$B_1$	1	-1	1	-1	-1	1	
$B_2$	1	-1	1	-1	1	-1	
$E_1$	2	1	-1	-2	0	0	$(x, y), (R_x, R_y)$
$E_2$	2	-1	-1	2	0	0	$(xy), (x^2 - y^2)$
<b><math>E_{1/2}</math></b>	2	$\sqrt{3}$	1	0	0	0	
<b><math>E_{3/2}</math></b>	2	0	-2	0	0	0	
<b><math>E_{5/2}</math></b>	2	$-\sqrt{3}$	1	0	0	0	

is the name of the point group, here  $C_{6v}$ . The first row (except last element) corresponds to the symmetry operations assembled into different classes. Thus for instance,  $C_{6v}$  point group contains six different classes. On the other hand, the first column excluding the first entry gives different IRRs of the group. We can see here that some of the IRRs are marked in bold. These IRRs are the so-called *double group* representations. When an extra degree of freedom (e.g. spin) is introduced in the system, this introduces extra symmetries and subsequently additional IRRs have to be considered accounting for symmetry operations in spin space. More discussions on this will follow in later sections. The final column lists a number of functions that transform as the IRR of the group after applying a symmetry operation. These can be coordinate axes  $(x, y, z)$ , rotations  $(R_x)$  etc. The rest of the table denotes how the characters of the IRR transform under each of the symmetry operations. The column corresponding to the identity element ( $E$ ) gives the *dimensionality* of the IRR [53, 70]. This is because  $E$  denotes identity matrix of the IRR and leaves it unchanged. As seen from Table 2.1, there are only 1- and 2-dimensional IRR in the  $C_{6v}$  point group.

These group theoretical aspects can not only be applied to spatial properties but also to quantum mechanics. The eigenfunctions and eigenstates of a particle originating from the solution of time-independent Schrödinger's equation is usually governed by symmetry considerations and since group theory can transform many complex symmetry operations to simple mathematical concepts, it has direct applications in quantum mechanics. As pointed out in detail by Dresselhaus [68], some of such applications include using IRRs of a group to classify different wave functions and predicting degeneracy of a system. The dimensionality of a group can be directly related to possible degeneracies in the system (neglecting the rare accidental degeneracies) due to the fact that this is the number of times a state belonging to that particular IRR appears in the system [53, 68]. Additionally, as we will show later, for an accurate description of semiconductors, relativistic effects like “spin-orbit” coupling (SOC) should be included in the analysis which can affect these degeneracies. From a group theoretical point of view, SOC can be included in the description by representing spin-dependent wave functions by double

group IRRs. Equipped with these group theoretical concepts, we now move to the discussion of the band structure of a WZ crystal.

### 2.1.1 Wurtzite band structure

In the following, we are mainly interested in the electronic structure of III-N WZ structures, such as InN and GaN, which have a direct band gap. In these materials, the top of the valence band (VB) and the bottom of the conduction band (CB) are situated at the same  $\mathbf{k}$ -point in the first Brillouin Zone. This is one of the high symmetry points of the first Brillouin zone, commonly referred to as the  $\Gamma$  point which corresponds to  $\mathbf{k}=0$ . The region around this point is of major importance for the optical properties of these systems [53]. Therefore, we will analyze symmetry properties of the electronic bands of a WZ system in the vicinity of the  $\Gamma$  point. The space group for a WZ structure is  $C_{6v}^4$  [53]. Since we are mainly interested in the  $\Gamma$  point, we have to find the operations of the point group associated with the space group  $C_{6v}^4$ , which transforms this point to itself plus a reciprocal lattice vector. In case of the WZ structures, the corresponding point group is the  $C_{6v}$  group. The character table for this point group has already been presented in Table 2.1 [71].

We now utilize the group theoretical concepts developed in the last section to study the electronic band structure of a WZ crystal. Through this, we can classify electronic wave function according to different IRRs of  $C_{6v}$ . In principle, the electronic wave function ( $\psi$ ) is made up of a spatial ( $\phi$ ) and a spin part ( $\xi$ ).  $\psi$  behaves differently depending on the presence of spin. Without taking spin into account in the description,  $\psi$  is a scalar function where as with spin, the  $\psi$  is a spinor [72]. Furthermore, as stated earlier, with the inclusion of spin we have to deal with double group and its corresponding IRRs. Therefore, we will separately discuss the electronic band structure of a WZ crystal in the absence and in the presence of SOC.

#### Without spin-orbit coupling ( $\Delta_{so} = 0$ )

The time-independent Schrödinger equation does not include terms that act on the spin [73]. Therefore, in the absence of SOC ( $\Delta_{so} = 0$ ), we can decouple the spatial ( $\phi$ ) and spin ( $\xi$ ) components of the wave function. We first study the spatial part  $\phi$  of the electronic states and will move to the spin discussions later. To label different electronic bands according to the IRR of the point group  $C_{6v}$ , the symmetry properties of the bands is required. In other words, the underlying basis functions need to be known. Since crystals are made up of atoms, our starting point is to look at the atomic orbitals of the constituent atoms. When we look at the atomic orbitals of the individual atoms that constitute a III-N structure, we know that cations (Ga, In, Al) belong to group-III elements of the periodic table and anions are group-V (N) elements. Therefore, typically the valence electrons occupy  $s$  and  $p$  orbitals [63]. For instance,

the electronic configuration of Ga:  $[\text{Ar}] 3d^{10} 4s^2 4p^1$  and N:  $[\text{He}] 2s^2 2p^1$ . When individual atoms belonging to group-III and group-V are brought together, these partially filled  $s$  and  $p$  orbitals combine to form tetrahedral bonds through  $sp^3$  hybridization [74]. In this process, they form filled *bonding* and unfilled *antibonding* molecular orbitals. Once these atoms merge to form a crystal, the corresponding molecular orbitals coalesce to form energy band structure of the material. The bonding molecular orbitals primarily form filled VBs and antibonding states form the unfilled CBs. Typically, one finds that for WZ semiconductors, at the  $\Gamma$  point, the CB is predominantly  $s$ -like (antibonding) while the VB states are predominantly  $p$ -like (bonding) in character [75]. Having discussed the orbital characters of different bands, we can now label

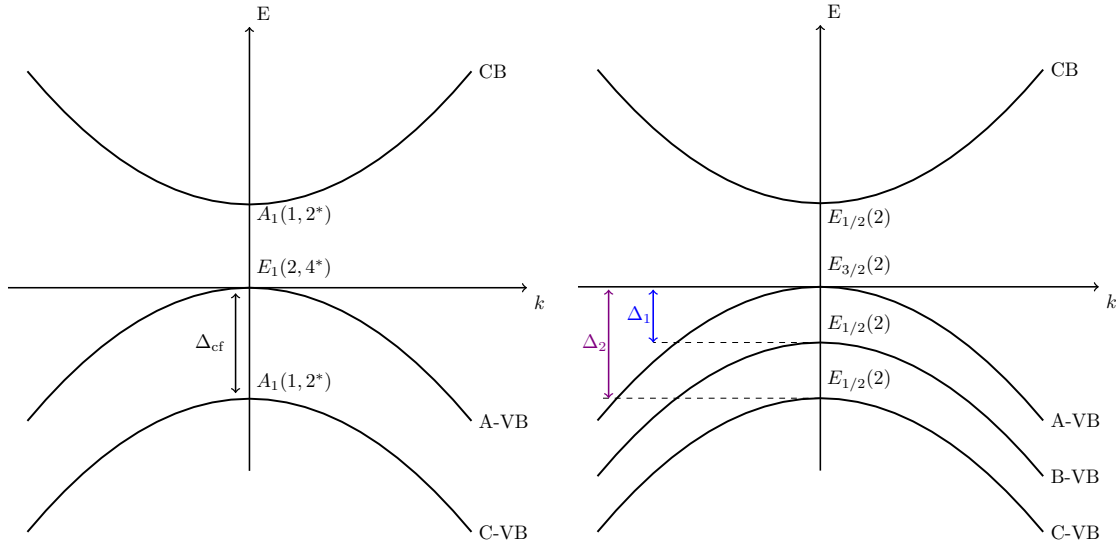


FIGURE 2.2: Schematic band structure of a WZ crystal with one CB and three VBs (a) in the absence and (b) in the presence of SOC. The different bands are labelled according to group representation notations as discussed in the main text. The degeneracies of the bands are given in brackets. “\*” denotes spin degeneracies.

them according to the IRR of  $C_{6v}$ . As described earlier, in the absence of SOC e.g. where spin is a good quantum number, one has to deal with IRRs belonging to the single groups  $C_{6v}$ . Looking at the basis functions in the different IRR of the point group  $C_{6v}$  given in Table 2.1, we find that the  $s$ -like CB transforms according to the  $A_1$  representation. On the other hand, one finds that  $p_x$ - and  $p_y$ -like functions belong to the  $E_1$  IRR while a  $p_z$ -like function transforms as  $A_1$ . Therefore, for the VB states, one should expect a doubly degenerate band belonging to  $E_1$  and a non-degenerate band corresponding to  $A_1$  since  $E_1$  is a 2-D IRR while  $A_1$  is an 1-D IRR. For our analysis, we denote the doubly degenerate band and the non-degenerate band by A- and C-VB, respectively.

However, it is to note that group theory can not provide insights into the energetic ordering of these states. In WZ structures, the energetic ordering between A- and C-VB arises from the crystal field splitting ( $\Delta_{cf}$ ) which is due to the anisotropy between  $a$ - and  $c$ -axis [50] of the WZ structure. This is reflected in group theory by the fact that  $p_x$  and  $p_y$  orbitals belong to

$\Gamma$	$A_1$	$A_2$	$B_1$	$B_2$	$E_1$	$E_2$
$\Gamma \otimes D_{1/2}$	$E_{1/2}$	$E_{1/2}$	$E_{5/2}$	$E_{5/2}$	$E_{1/2} \oplus E_{3/2}$	$E_{3/2} \oplus E_{5/2}$

TABLE 2.2: Direct product of single group IRRs  $\Gamma$  with spin IRR  $D_{1/2}$ 

different IRR than the  $p_z$  orbital in the  $C_{6v}$  point group. This is different to ZB semiconductors for instance, where all of the  $p$  orbitals ( $p_x$ ,  $p_y$  and  $p_z$ ) belong to same IRR [76]. A schematic illustration of the band structure of a bulk WZ crystal with  $\Delta_{cf} \geq 0$  is illustrated in Fig. 2.2. The degeneracies are given in brackets. In our discussions above, we have only treated the spatial part through its IRR. We can now include the spin separately in this description. It is known that a spin wave function in a WZ crystal transforms as the IRR  $D_{1/2}$  [68] which is two-dimensional in nature [68].<sup>1</sup> This introduces an additional double degeneracies in the structure. Correspondingly, A-VB will be four-fold (originating from  $E_1$  and  $D_{1/2}$ ) and the CB, C-VB will be two-fold degenerate (originating from  $A_1$  and  $D_{1/2}$ ). The extra degeneracies due to spin states are denoted by the symbol “\*” symbols in the Fig. 2.2 (a). Having discussed the electronic band structure without SOC, in the following, we discuss how group theory can be applied to study the electronic band structure in the presence of SOC for a WZ structure.

### With spin-orbit coupling ( $\Delta_{so} \neq 0$ )

With the inclusion of SOC, as stated earlier, one has to consider **double groups** [68, 76] to classify different states where the wave function  $\psi$  can no longer be written as a simple product of  $\phi$  and  $\chi$ . If we denote the single group IRRs by  $\Gamma$ , the IRRs of the double group are obtained from the direct product of the single group representations  $\Gamma$  with spin representation  $D_{1/2}$ . The result is given in Table 2.2 for the  $C_{6v}$  point group. Here “ $\otimes$ ” denotes direct product between two IRRs.

From this table, we see that the CB and C-VB belong to the  $E_{1/2}$  representation. Each of these states are doubly degenerate since  $E_{1/2}$  is a 2-D representation (cf. Table 2.1). On the other hand, the direct product  $E_1 \otimes D_{1/2} = E_{1/2} \oplus E_{3/2}$ . Therefore, the A-VB splits into two doubly degenerate states due to SOC which we denote as A- and B-VBs. A schematic illustration of lower most CB and three topmost VBs with SOC near the  $\Gamma$  point is now given in Fig. 2.2 (b) where the degeneracy of the bands is given in brackets. In summary, we have described the bulk band structure of WZ structures in the presence and absence of SOC by using group theory. The combined effect of crystal field splitting and SOC leads to a three-edge VB structure for WZ bulk systems. It has been found that the crystal field splitting energy for

<sup>1</sup> $D_{1/2}$  is deduced from the full rotational symmetry of a free atom. For a rotation around an angle  $\alpha$ , the elements of the representation matrix  $D_j$  are  $\exp(-im\alpha)$  where  $-j \leq m \leq j$ . Correspondingly, the character of this group are found as

$$Tr(D_j) = \exp(-ij\alpha) + \dots + \exp(ij\alpha) = \frac{\sin(j\alpha)}{\sin(j\alpha/2)} \quad (2.1)$$

The dimension of a  $D_j$  state is  $(2j)+1$  and therefore,  $D_{1/2}$  is two dimensional in our case.

AlN is negative ( $\approx -169$  meV [62]) while for InN and GaN they are positive and of the order of 10-40 meV [62]. However, it is found that the spin-orbit splitting energies in III-N structures are very small (5-20 meV) when compared to As based materials such as GaAs and InAs where spin-orbit splitting energies are found to be 294 meV and 310 meV respectively [77].

In conclusion, group theory is a powerful tool for predicting the character of different bands or degeneracies present in the electronic band structure without an explicit numerical calculation. Therefore, it is extremely useful to benchmark numerical calculations with respect to for instance, predicted degeneracy of states. However, group theory is unable to provide any insight into the energetic ordering or energetic separation of different band states ( $\Delta_1, \Delta_2$  etc). Thus, it can not replace explicit numerical calculations which can be used not only to calculate energetic separation of different bands but also optical spectra and emission wavelength [68]. Therefore, we need a suitable electronic structure theory to determine these features which is the topic of the next section.

## 2.2 Electronic structure theory

In this section, we outline various theoretical approaches to calculate the electronic band structure for WZ semiconductor bulk system and how it can be applied to study QDs. Electronic band structure methods are usually grouped into ab-initio [78, 79] and semi-empirical [80–82] methods. Ab-initio methods like density functional theory (DFT) are in principle free from empirical fitting parameters and present an atomistic approach to determine electronic band structure [79]. DFT is suitable for the calculation of bulk band structures, however, fail for large structures like QDs due to its computational expense [83] since it involves calculation of  $\approx 10^4 - 10^6$  atoms as discussed in the introduction. As a result, the focus shifted to semi-empirical methods such as  $\mathbf{k} \cdot \mathbf{p}$  theory [84, 85], empirical pseudopotential methods [86, 87] and tight-binding (TB) methods [81, 82].  $\mathbf{k} \cdot \mathbf{p}$  theory is a relatively simple method for calculating the electronic structure of both bulk as well as QDs which operates on a continuum level. This model works very well if the atomistic details of the underlying structures are negligible [56, 88]. On the other hand, empirical pseudopotential methods and TB models can describe the microscopic details of the underlying crystal structures while at the same time being scalable to large systems [89]. In this chapter, we will only discuss  $\mathbf{k} \cdot \mathbf{p}$  and TB methods which have been employed in this work to investigate the electronic structure of III-N QDs. Here, we start with a discussion of  $\mathbf{k} \cdot \mathbf{p}$  methods and TB approaches for bulk systems followed by procedures to extend these methods to QDs. It is to note that in both these methods, we work in the Born-Oppenheimer [53] and single-electron approximations [53] where, respectively (i) the ionic motions are neglected so that atomic nuclei can be assumed to be fixed at their equilibrium positions and (ii) interactions with other electrons are combined into a effective potential so

that a given electron can be treated independently of all other electrons. As a result, we use one electron Schrödinger equation to evaluate electronic eigenstates of the crystal.

### 2.2.1 Electronic structure theory for bulk materials

In the following, we start with a discussion of  $\mathbf{k} \cdot \mathbf{p}$  theory where we present the bulk Hamiltonian for a WZ crystal structure. Subsequently, we introduce general aspects of the TB method and outline procedures to obtain a TB Hamiltonian for a bulk WZ crystal.

#### 2.2.1.1 $\mathbf{k} \cdot \mathbf{p}$ theory

$\mathbf{k} \cdot \mathbf{p}$  theory is a perturbative approach to solve the time-independent Schrödinger equation [84]. Within this method, the band structure is calculated in the vicinity of a chosen  $k$  point [53, 85]. The bulk  $\mathbf{k} \cdot \mathbf{p}$  Hamiltonian for WZ structures was first introduced by Chuang and Chang [90] back in 1996 to calculate their band structures. The Hamiltonian used in this thesis is based on the above work. The Chuang and Chang WZ  $\mathbf{k} \cdot \mathbf{p}$  Hamiltonian is a modification of the Luttinger-Kohn model [91] which is a popular method for studying electronic and optical properties of bulk and QW structures [91, 92]. Here, the general concept is that the bands of primary interest are considered exactly, usually denoted as class-A bands, and energetically remote bands are treated as a perturbation, usually denoted as class-B bands using Löwdin's perturbation theory [93]. In the following, we briefly describe this procedure for a bulk WZ system.

The time-independent Schrödinger equation in a periodic crystal at a particular wave vector  $\mathbf{k}$  is expressed as [53]:

$$\hat{H}_0 \psi_{n\mathbf{k}}(\mathbf{r}) = E_n(\mathbf{k}) \psi_{n\mathbf{k}}(\mathbf{r}), \quad (2.2)$$

where  $\hat{H}_0$  is given by

$$\hat{H}_0 = -\frac{\hbar^2}{2m_0} \nabla^2 + V(\mathbf{r}). \quad (2.3)$$

Here,  $n$  is the band index,  $E_n(\mathbf{k})$  is the energy of  $n$ th band at wave vector  $\mathbf{k}$  and  $\psi_{n\mathbf{k}}(\mathbf{r})$  is the corresponding electronic wave function. The first and second term of the Hamiltonian  $\hat{H}_0$  corresponds to kinetic and potential energy respectively. Since electron moves in a periodic potential, we have  $V(\mathbf{r}) = V(\mathbf{r} + \mathbf{R})$  where  $\mathbf{R} = n_1 \mathbf{a}_1 + n_2 \mathbf{a}_2 + n_3 \mathbf{a}_3$  is a lattice vector;  $\mathbf{a}_1, \mathbf{a}_2, \mathbf{a}_3$  are the basis vectors, and  $n_1, n_2$  and  $n_3$  are integers. Due to this periodic nature of the crystal potential, the electron wave function  $\psi_{n\mathbf{k}}(\mathbf{r})$  can be expressed as Bloch functions [53]:

$$\psi_{n\mathbf{k}}(\mathbf{r}) = e^{i\mathbf{k} \cdot \mathbf{r}} u_{n\mathbf{k}}(\mathbf{r}), \quad (2.4)$$

where  $u_{n\mathbf{k}}(\mathbf{r})$  is the periodic part of the Bloch function. Here, the band index  $n$  includes spin components. Depending on the material system under investigation, relativistic corrections such as the SOC may have to be included in the description [94] which originates from the interaction between spin angular momentum and orbital angular momentum of an electron [53]. Here, SOC is included in the analysis by adding a spin-orbit operator  $\hat{H}_{\text{so}}$  to the bulk Hamiltonian  $\hat{H}_0$ . More details on how to derive this correction can be found in Ref. [76]. When including SOC, the bulk Hamiltonian is now given by,

$$\hat{H} = \underbrace{-\frac{\hbar^2}{2m_0}\nabla^2 + V(\mathbf{r})}_{\hat{H}_0} + \underbrace{\frac{\hbar}{4m_0^2c^2}(\nabla V \times \mathbf{p}) \cdot \boldsymbol{\sigma}}_{\hat{H}_{\text{so}}}, \quad (2.5)$$

where,  $\boldsymbol{\sigma}$  is the tensor of the Pauli spin matrices [53]. Now, using the Hamiltonian  $\hat{H}$  and plugging the Bloch wave function, Eq. (2.4), into the Schrödinger Eq. (2.2) one is left with

$$\left[ \underbrace{-\frac{\hbar^2}{2m_0}\nabla^2 + V(\mathbf{r})}_{\hat{H}_0} + \underbrace{\frac{\hbar}{4m_0^2c^2}(\nabla V \times \mathbf{p}) \cdot \boldsymbol{\sigma}}_{\hat{H}_{\text{so}}} + \underbrace{\frac{\hbar}{m_0}\mathbf{k} \cdot \mathbf{p}}_{\hat{H}'} + \frac{\hbar^2 k^2}{2m_0} + \frac{\hbar^2}{4m_0^2c^2}(\nabla V \times \mathbf{k}) \cdot \boldsymbol{\sigma} \right] u_{n\mathbf{k}}(\mathbf{r}) = E_n(k)u_{n\mathbf{k}}(\mathbf{r}). \quad (2.6)$$

The last term on the left hand side of the Eq. (2.6) is a  $\mathbf{k}$ -dependent spin-orbit perturbation term (crystal momentum) and is much smaller compared to  $\mathbf{p}$ -dependent spin-orbit terms (electron-momentum) [92]. For this reason, the last term on the left hand side is usually neglected and we follow this approach here. The occurrence of  $\mathbf{k} \cdot \mathbf{p}$  term is the reason why this model is called  $\mathbf{k} \cdot \mathbf{p}$  perturbation theory. Since in this work our aim is to calculate the electronic and optical properties of a semiconductor material with a direct gap, we focus here on the  $\Gamma$  point ( $\mathbf{k} = \mathbf{0}$ ) where both CB-edge and VB-edges coincide. At  $\Gamma$  point, the above functions satisfy

$$\hat{H}(\mathbf{k} = \mathbf{0})u_{n\mathbf{0}}(\mathbf{r}) = E_n(\mathbf{0})u_{n\mathbf{0}}(\mathbf{r}). \quad (2.7)$$

Once the terms  $E_n(\mathbf{0})$  and  $u_{n\mathbf{0}}(\mathbf{r})$  are known, one can solve Eq. (2.6) by treating the  $\mathbf{k}$ -dependent terms perturbatively. Thus assuming that we know a system of band-edge functions  $u_{n'\mathbf{0}}(\mathbf{r})$  ( $n' = 1, 2, \dots, N$ ) one can expand the eigenfunctions of the system  $u_{n\mathbf{k}}(\mathbf{r})$  by:

$$u_{n\mathbf{k}}(\mathbf{r}) = \sum_{n'}^N a_{n'}(\mathbf{k})u_{n'\mathbf{0}}(\mathbf{r}). \quad (2.8)$$

Now, the coefficients  $a_{n'}(\mathbf{k})$  can be obtained by putting the expansion defined in Eq. (2.8) in Eq. (2.6) and multiplying from the left by a complex conjugate of an arbitrary Bloch state

$u_{n\mathbf{0}}(\mathbf{r})$  [92]. In this process, we have to solve a system of linear equations as

$$\sum_{n'}^N \left( \hat{H}_{nn'} - E_n(k) \delta_{nn'} \right) a_{n'}(\mathbf{k}) = 0. \quad (2.9)$$

To solve Eq. (2.9), we will use Löwdin's perturbation method [93] where the index  $n'$  is divided into two sets, namely  $j$  and  $\gamma$  such that  $j$  belongs to states of interest (class-A) and  $\gamma$  belongs to energetically higher lying states (class-B) which introduce perturbation to class-A states. In our case, states of interest are the states which are energetically closer to the CB- and VB-edge. With this framework, we rewrite Eq. (2.8) as

$$u_{n\mathbf{k}}(\mathbf{r}) = \sum_j^A a_j(k) u_{j\mathbf{0}}(\mathbf{r}) + \sum_\gamma^B a_\gamma(k) u_{\gamma\mathbf{0}}(\mathbf{r}). \quad (2.10)$$

Löwdin [93] showed that within this ansatz, one can express Eq. (2.9) as follows:

$$\sum_{j'}^A \left( \hat{H}_{jj'}^{LK} - E_n(\mathbf{k}) \delta_{jj'} \right) a_{j'}(\mathbf{k}) = 0, \quad (2.11)$$

where  $\left( \hat{H}_{jj'}^{LK} \right)$  is the so-called Luttinger-Kohn Hamiltonian, which is given by

$$\hat{H}_{jj'}^{LK} = \hat{H}_{jj'}^A + \sum_\gamma^B \frac{\hat{H}_{j\gamma}' \hat{H}_{\gamma j'}'}{E_0 - E_\gamma}. \quad (2.12)$$

Here  $j, j' \in A$  and  $\gamma \neq j, j'$ . The first term describes coupling between class-A states and second term is the effect of class-B states on class-A states. Now, we need to evaluate the Hamiltonian  $\hat{H}_{jj'}^{LK}$  in terms of available basis states,  $u_{j'\mathbf{0}}$ . For this reason, we now switch to bra and ket notations. The term  $\hat{H}_{jj'}^A$  is evaluated as:

$$\hat{H}_{jj'}^A = \underbrace{\langle u_{j\mathbf{0}} | \hat{H}_0 + \hat{H}_{so} | u_{j'\mathbf{0}} \rangle}_{H_{jj'}(\mathbf{k}=0)} + \frac{\hbar^2 k^2}{2m_0} \delta_{jj'} + \left\langle u_{j\mathbf{0}} \left| \frac{\hbar}{m_0} \mathbf{k} \cdot \mathbf{p} \right| u_{j'\mathbf{0}} \right\rangle. \quad (2.13)$$

The term  $\left\langle u_{j\mathbf{0}} \left| \frac{\hbar}{m_0} \mathbf{k} \cdot \mathbf{p} \right| u_{j'\mathbf{0}} \right\rangle$  is neglected since  $j, j' \in A$  and this perturbation has no effect on class-A states [93]. To evaluate second term of  $\hat{H}_{jj'}^{LK}$  in Eq. (2.12) we now introduce the following notation:

$$\hat{H}_{j\gamma}' \cong \left\langle u_{j\mathbf{0}} \left| \frac{\hbar}{m_0} \mathbf{k} \cdot \mathbf{p} \right| u_{\gamma\mathbf{0}} \right\rangle = \sum_\alpha \frac{\hbar k_\alpha}{m_0} p_{j\gamma}^\alpha, \quad (2.14)$$

where  $\alpha = x, y, z$ ,  $\gamma \in B$  and  $p_{j\gamma}^\alpha = \langle u_{j0} | p_\alpha | u_{\gamma 0} \rangle$ . Therefore, the second term can be written as:

$$\begin{aligned} \sum_{\gamma} \frac{\hat{H}'_{j\gamma} \hat{H}'_{\gamma j'}}{E_0 - E_{\gamma}} &= \frac{\hbar^2}{m_0} \sum_{\gamma} \sum_{\alpha, \beta} \frac{k_{\alpha} k_{\beta} p_{j\gamma}^{\alpha} p_{\gamma j'}^{\beta}}{m_0 (E_0 - E_{\gamma})} \\ &= \frac{\hbar^2}{2m_0} \sum_{\gamma} \sum_{\alpha, \beta} k_{\alpha} k_{\beta} \frac{p_{j\gamma}^{\alpha} p_{\gamma j'}^{\beta} + p_{j\gamma}^{\beta} p_{\gamma j'}^{\alpha}}{m_0 (E_0 - E_{\gamma})}. \end{aligned} \quad (2.15)$$

Here, we have used the relation:

$$\begin{aligned} \sum_{\alpha, \beta} (p_{j\gamma}^{\alpha} p_{\gamma j'}^{\beta} + p_{j\gamma}^{\beta} p_{\gamma j'}^{\alpha}) &= \sum_{\alpha, \beta} \langle u_{j0} | p_{\alpha} | u_{\gamma 0} \rangle \langle u_{\gamma 0} | p_{\beta} | u_{j'0} \rangle + \sum_{\alpha, \beta} \langle u_{j0} | p_{\beta} | u_{\gamma 0} \rangle \langle u_{\gamma 0} | p_{\alpha} | u_{j'0} \rangle \\ &= \sum_{\alpha, \beta} 2p_{j\gamma}^{\alpha} p_{\gamma j'}^{\beta}. \end{aligned} \quad (2.16)$$

Combining Eq. (2.13) and Eq. (2.15) we get the full Hamiltonian:

$$\hat{H}_{jj'}^{LK} = \hat{H}_{jj'}(\mathbf{k} = 0) + \frac{\hbar^2 k^2}{2m_0} \delta_{jj'} + \frac{\hbar^2}{2m_0} \sum_{\gamma} \sum_{\alpha, \beta} k_{\alpha} k_{\beta} \frac{p_{j\gamma}^{\alpha} p_{\gamma j'}^{\beta} + p_{j\gamma}^{\beta} p_{\gamma j'}^{\alpha}}{m_0 (E_0 - E_{\gamma})}. \quad (2.17)$$

We can rework Eq. (2.17) in a way that all  $\mathbf{k}$ -dependent terms are accumulated into a single term so that  $\hat{H}_{jj'}^{LK}$  can be expressed as:

$$\hat{H}_{jj'}^{LK} = \hat{H}_{jj'}(\mathbf{k} = 0) + \sum_{\alpha, \beta} D_{jj'}^{\alpha\beta} k_{\alpha} k_{\beta}, \quad (2.18)$$

with

$$D_{jj'}^{\alpha\beta} = \frac{\hbar^2}{2m_0} \left\{ \delta_{jj'} \delta_{\alpha\beta} + \sum_{\gamma} \frac{p_{j\gamma}^{\alpha} p_{\gamma j'}^{\beta} + p_{j\gamma}^{\beta} p_{\gamma j'}^{\alpha}}{m_0 (E_0 - E_{\gamma})} \right\}. \quad (2.19)$$

Here,  $j, j' \in A$ ,  $\gamma \in B$  and  $\alpha, \beta = x, y, z$ . Equipped with these equations, one can evaluate Hamiltonian matrix elements for both CB and VBs. Depending on the number of bands taken into account, different Hamiltonians are found in the literature [95]. Standard approaches for III-V materials utilize for example, 8-band Hamiltonian which includes three VBs and one CB per spin [88]. However, there exists more sophisticated models which utilize even higher number of bands [95]. A widely used model for wide band gap systems is the 6+2 band Hamiltonian where the VB- and CB-Hamiltonians are considered separately. Since we are dealing with  $\text{In}_x\text{Ga}_{1-x}\text{N}$  materials for low  $x$  values (0.20–0.30), the band gaps of these materials are large. Therefore, we follow this approach and neglect the coupling between CB and VBs. In the following, we present a 1-band Hamiltonian for the CB and a 6-band Hamiltonian to describe VBs. The following Hamiltonian is derived under the assumption that in the coordinate system,  $z$ -axis is parallel to the  $c$ -axis of the WZ structure.

- 1-band model for conduction band

Here, we use band-edge wave function of  $S$  symmetry as the bases for class-A states such that  $|u_{j\mathbf{0}}\rangle = |u_{1\mathbf{0}}\rangle = |S; \uparrow\rangle$ . Now, we can derive the CB Hamiltonian in the  $|S; \uparrow\rangle$  basis using Eq. (2.18) and Eq. (2.19) as:

$$\widehat{H}_{\text{CB}} = E_c + \frac{1}{m_{e,\parallel}^*} (k_x^2 + k_y^2) + \frac{1}{m_{e,\perp}^*} k_z^2, \quad (2.20)$$

where  $m_{e,\parallel}^*$  and  $m_{e,\perp}^*$  are the in- and out of-  $c$ -plane effective mass of the CB and is expressed as

$$\begin{aligned} \frac{1}{m_{e,\parallel}^*} &= \frac{\hbar^2}{2m_0} + \frac{\hbar^2}{m_0^2} \sum_{\gamma}^B \frac{|p_{S\gamma}^x|^2}{E_c - E_{\gamma}} \\ \frac{1}{m_{e,\perp}^*} &= \frac{\hbar^2}{2m_0} + \frac{\hbar^2}{m_0^2} \sum_{\gamma}^B \frac{|p_{S\gamma}^z|^2}{E_c - E_{\gamma}}. \end{aligned} \quad (2.21)$$

All other terms vanish due to parity considerations [92]. While evaluating the CB Hamiltonian we have neglected SOC and have used following relations.  $\langle S | \widehat{H}_0 | S \rangle = E_c$  and  $|p_{S\gamma}^x|^2 = |p_{S\gamma}^y|^2$  due to in-plane symmetry of the WZ structure [50, 90]. However, due to an asymmetry between  $a$  and  $c$  axis of the WZ structure,  $|p_{S\gamma}^x|^2 = |p_{S\gamma}^y|^2 \neq |p_{S\gamma}^z|^2$ . In the following, we have made an isotropic effective mass approximation [96] for the CB and assumed that  $m_{e,\perp}^* = m_{e,\parallel}^*$ . This is a widely used approximation made in the literature [62, 96]. The CB effective mass parameters used in thesis for different materials are summarized in Table B.2 of Appendix B.

- 6-band Model for valence band

Turning to the VB, we use band-edge wave functions of  $X$ ,  $Y$ ,  $Z$  symmetry as the bases for class-A states. Thus we are left with six basis states so that  $|u_{j\mathbf{0}}\rangle$  is given by,

$$\begin{pmatrix} |u_{10}\rangle \\ |u_{20}\rangle \\ |u_{30}\rangle \\ |u_{40}\rangle \\ |u_{50}\rangle \\ |u_{60}\rangle \end{pmatrix} = \begin{pmatrix} |X; \uparrow\rangle \\ |Y; \uparrow\rangle \\ |Z; \uparrow\rangle \\ |X; \downarrow\rangle \\ |Y; \downarrow\rangle \\ |Z; \downarrow\rangle \end{pmatrix}. \quad (2.22)$$

The  $\mathbf{k}$ -independent VB-edge Hamiltonian in this basis can be written as [96]

$$\hat{H}_{jj'}(\mathbf{k} = \mathbf{0}) = \begin{bmatrix} E_v + \Delta_{\text{cf}} & -i\frac{\Delta_{\text{so}}}{3} & 0 & 0 & 0 & \frac{\Delta_{\text{so}}}{3} \\ i\frac{\Delta_{\text{so}}}{3} & E_v + \Delta_{\text{cf}} & 0 & 0 & 0 & -i\frac{\Delta_{\text{so}}}{3} \\ 0 & 0 & E_v & -\frac{\Delta_{\text{so}}}{3} & i\frac{\Delta_{\text{so}}}{3} & 0 \\ 0 & 0 & -\frac{\Delta_{\text{so}}}{3} & E_v + \Delta_{\text{cf}} & i\Delta & 0 \\ 0 & 0 & -i\frac{\Delta_{\text{so}}}{3} & -i\frac{\Delta_{\text{so}}}{3} & E_v + \Delta_{\text{cf}} & 0 \\ \frac{\Delta_{\text{so}}}{3} & i\frac{\Delta_{\text{so}}}{3} & 0 & 0 & 0 & E_v \end{bmatrix}, \quad (2.23)$$

where  $\Delta_{\text{so}}$  and  $\Delta_{\text{cf}}$  are the SOC and crystal-field splitting energies respectively. Diagonalizing the Hamiltonian matrix Eq. (2.23), we find the following doubly degenerate VB-edge energies as [90]:

$$\begin{aligned} E_1 &= E_v + \Delta_{\text{cf}} + \frac{\Delta_{\text{so}}}{3}, \\ E_2 &= E_v + \frac{\Delta_{\text{cf}}}{2} - \frac{\Delta_{\text{so}}}{6} + \sqrt{(\Delta_{\text{cf}} + \Delta_{\text{so}})^2 - \frac{8}{3}\Delta_{\text{cf}}\Delta_{\text{so}}}, \\ E_3 &= E_v + \frac{\Delta_{\text{cf}}}{2} - \frac{\Delta_{\text{so}}}{6} - \sqrt{(\Delta_{\text{cf}} + \Delta_{\text{so}})^2 - \frac{8}{3}\Delta_{\text{cf}}\Delta_{\text{so}}}. \end{aligned} \quad (2.24)$$

As expected from our group theoretical analysis presented in Sec. 2.1, we find here a three-edge VB structure. However, from Eq. (2.24), we can now also calculate the splitting of the different bands. Once the values for the spin-orbit coupling and crystal field splitting energies are known, we obtain [76, 90]:

$$\Delta_{1,2} = \frac{1}{2}(\Delta_{\text{cf}} + \Delta_{\text{so}} \mp \sqrt{(\Delta_{\text{cf}} + \Delta_{\text{so}})^2 - \frac{8}{3}\Delta_{\text{cf}}\Delta_{\text{so}}}),$$

where  $\Delta_1 = E_1 - E_2$  and  $\Delta_2 = E_1 - E_3$ .

We will now evaluate the  $D$  matrix which is a  $3 \times 3$  matrix per spin state. Before doing this, we use notation from Ref. [90] below which reflects the asymmetry between the  $x$ - and the  $z$ -axis of the WZ structure [50]:

$$\begin{aligned} L_1 &= D_{XX}^{xx} = D_{YY}^{yy}, \\ L_2 &= D_{ZZ}^{zz}, \\ M_1 &= D_{XX}^{yy} = D_{YY}^{xx}, \\ M_2 &= D_{XX}^{zz} = D_{YY}^{zz}, \\ M_3 &= D_{XX}^{xz} = D_{ZZ}^{yy}, \\ N_1 &= 2D_{XY}^{xy}, \\ N_2 &= 2D_{XZ}^{xz} = 2D_{YZ}^{yz}. \end{aligned} \quad (2.25)$$

In the above, we have assumed that due to Hermiticity  $(D_{jj'}^{\alpha\beta})^* = D_{j'j}^{\beta\alpha}$ . Equipped with the above, we now calculate as an example two different terms of the  $D$  matrix.

(1) Case 1:  $j = j'$

As an illustrative example, we derive the matrix element  $j = j' = |X\rangle$ .

$$\begin{aligned}
\sum_{\alpha\beta} D_{XX}^{\alpha\beta} k_\alpha k_\beta &= D_{XX}^{xx} k_x^2 + 2D_{XX}^{xy} k_x k_y + D_{XX}^{yy} k_y^2 + 2D_{XX}^{xz} k_x k_z + D_{XX}^{zz} k_z^2 + 2D_{XX}^{yz} k_y k_z \\
&= D_{XX}^{xx} k_x^2 + D_{XX}^{yy} k_y^2 + D_{XX}^{zz} k_z^2 \\
&= L_1 k_x^2 + M_1 k_y^2 + M_2 k_z^2.
\end{aligned} \tag{2.26}$$

In the above evaluation, several terms vanish due to the parity considerations [92].

(2) Case 2:  $j \neq j'$

Here, as an example, we derive the matrix element for  $j = |X\rangle$  and  $j' = |Y\rangle$ .

$$\begin{aligned}
\sum_{\alpha\beta} D_{XY}^{\alpha\beta} k_\alpha k_\beta &= D_{XY}^{xx} k_x^2 + D_{XY}^{xy} k_x k_y + D_{XY}^{yx} k_y k_x + D_{XY}^{yy} k_y^2 + 2D_{XY}^{xz} k_x k_z + D_{XY}^{zz} k_z^2 + 2D_{XY}^{yz} k_y k_z \\
&= D_{XY}^{xy} k_x k_y + D_{XY}^{yx} k_y k_x \\
&= N_1 k_x k_y.
\end{aligned} \tag{2.27}$$

Using the above rules, we can evaluate all other terms and consequently, the  $D_{3 \times 3}$  matrix becomes [90, 96]:

$$D_{3 \times 3} = \begin{bmatrix} L_1 k_x^2 + M_1 k_y^2 + M_2 k_z^2 & N_1 k_x k_y & N_2 k_x k_z \\ N_1 k_x k_y & M_1 k_x^2 + L_1 k_y^2 + M_2 k_z^2 & N_2 k_y k_z \\ N_2 k_x k_z & N_2 k_y k_z & M_3 (k_x^2 + k_y^2) + L_2 k_z^2 \end{bmatrix}. \tag{2.28}$$

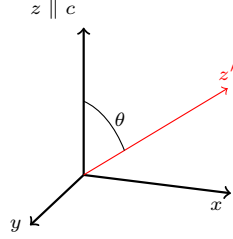
The full  $D_{6 \times 6}$  matrix taking into account spin (cf. Eq. (2.22)) therefore reads [90]:

$$D_{6 \times 6} = \begin{pmatrix} D_{3 \times 3} & 0 \\ 0 & \overline{D_{3 \times 3}} \end{pmatrix}. \tag{2.29}$$

Here  $\overline{D_{3 \times 3}}$  is the complex conjugate of  $D_{3 \times 3}$ . Finally, the Hamiltonian  $\hat{H}_{\text{VB}}$  describing three energetically highest lying VB states is obtained by adding Eq. (2.23) and (2.29), following Eq. (2.17) as:

$$\hat{H}_{\text{VB}} = \hat{H}_{jj'}(\mathbf{k} = 0) + \hat{D}. \tag{2.30}$$

This is the full 6-band  $\mathbf{k} \cdot \mathbf{p}$  bulk Hamiltonian for VB states. To evaluate this Hamiltonian for a particular material, one needs to know the values of  $L_1$ ,  $L_2$ ,  $M_1$ ,  $M_2$ ,  $M_3$ ,  $N_1$  and  $N_2$ . In literature, these parameters are usually expressed in terms of Luttinger-like effective mass parameters,  $A_i$ . The relation between the above parameters  $L_j$  and Luttinger-like parameters  $A_i$  [96] is given by:  $L_1 = (A_2 + A_4 + A_5)$ ,  $L_2 = A_1$ ,  $M_1 = (A_2 + A_4 - A_5)$ ,  $M_2 = (A_1 + A_3)$ ,  $M_3 = A_2$ ,  $N_3 = 2A_5$ ,  $N_2 = \sqrt{2}A_6$ . In this thesis, the VB effective mass parameters of different materials are given in terms of  $A_i$  and is summarized in Table B.2 of Appendix B.

FIGURE 2.3: Crystallographic growth angle  $\theta$  for a rotation around  $y$ -axis

As stated earlier, the model discussed till now is only applicable when the growth direction ( $z$ -axis) of the structures is parallel to the  $c$ -axis of the WZ structure. However, as described in the previous sections, there is a strong interest in structures grown along different crystallographic directions. Therefore, we will briefly demonstrate how to modify the Hamiltonian as a function of the crystallographic growth angle  $\theta$  around the  $y$ -axis (cf. Fig. 2.3). To achieve this, we have to rotate and express the  $\mathbf{k} \cdot \mathbf{p}$  Hamiltonian as a function of growth angle  $\theta$ . This is performed in three steps.

- Step 1: Rotate the basis functions: This involves transformation of the basis functions to a new coordinate system. In general, one has to simultaneously transform spatial and spin parts of the basis states. However, we have neglected the rotations of spin part of the basis functions here given that SOC effects are small in III-N systems as compared to other III-V materials [97]. For instance, the basis functions in a new coordinate (primed) is related to the old basis functions (unprimed) by

$$\begin{aligned} & [|X'; \uparrow\rangle, |Y'; \uparrow\rangle, |Z'; \uparrow\rangle, |X'; \downarrow\rangle, |Y'; \downarrow\rangle, |Z'; \downarrow\rangle]^T = \\ & \begin{bmatrix} U & 0 \\ 0 & U \end{bmatrix} \times [|X; \uparrow\rangle, |Y; \uparrow\rangle, |Z; \uparrow\rangle, |X; \downarrow\rangle, |Y; \downarrow\rangle, |Z; \downarrow\rangle]^T, \end{aligned} \quad (2.31)$$

where  $U$  is a unitary rotation matrix around the  $y$ -axis of the original coordinate system for the spatial coordinates and is defined as

$$U = \begin{bmatrix} \cos \theta & 0 & \sin \theta \\ 0 & 1 & 0 \\ -\sin \theta & 0 & \cos \theta \end{bmatrix}. \quad (2.32)$$

- Step 2: Replace the wave vector  $\mathbf{k}$  of the un-rotated system by the rotated ones. This is performed by following transformations:

$$k'_i = \sum_{\alpha} U_{i\alpha} k_{\alpha}. \quad (2.33)$$

- Step 3: Re-express the matrix in terms of modified basis states.

Since the basis vectors are related by  $U|\psi\rangle = |\psi'\rangle$ , the Hamiltonian can be written in the new basis as,  $\hat{H}' = U\hat{H}U^{-1}$ .

Using these three steps we can define the Hamiltonian as a function of  $\theta$ . It is to note that this approach can be generalized by considering a second rotation described by the angle  $\varphi$  around the  $z$ -axis. In this more general case, relevant for instance in nanowire systems [98] or basal plane stacking faults where WZ and zincblende phase (oriented along the [111]-direction) are mixed [99], a rotation matrix  $\tilde{U}$  reads [100]:

$$\tilde{U} = \begin{pmatrix} \cos \theta \cos \varphi & \cos \theta \sin \varphi & -\sin \theta \\ -\sin \varphi & \cos \varphi & 0 \\ \sin \theta \cos \varphi & \sin \theta \sin \varphi & \cos \theta \end{pmatrix}. \quad (2.34)$$

Further generalization can be achieved by considering a third angle (Euler angles). Rotation matrices for that case are given for example in Ref. [101]. However, for all our studies here we are using  $\varphi = 0$  where  $\tilde{U}$  reduces to  $U$  defined in Eq. (2.32).

In summary, we have presented and discussed the derivation of a  $\mathbf{k} \cdot \mathbf{p}$  Hamiltonian for a bulk WZ structure. Additionally, we have outlined the procedure to modify the Hamiltonian as a function of growth angle  $\theta$ . Overall,  $\mathbf{k} \cdot \mathbf{p}$  perturbation theory is a continuum-based method which gives insight into the bound electron and hole states. However, this model can not describe the atomistic details of the underlying crystal structure. Therefore, when we are interested in the microscopic description of the low-dimensional systems, an atomistic approach such as TB is suitable which is the topic of the next section.

### 2.2.1.2 Tight-binding model

In this section, the general aspects of TB theory are explained in detail, including a discussion of the widely used two-center approximation. The procedure how to include SOC in the TB is also outlined.

#### General aspects

As the name suggests, this electronic band structure theory is based on the principle that electrons are tightly bound to their respective atoms. The starting point for this method is an isolated atom. Subsequently, the analysis is extended to a crystal. The time-independent Schrödinger equation for an isolated atom located at  $\mathbf{R}_n$  is given by

$$\hat{H}_{\text{at}}|n, b, \mathbf{R}_n\rangle = E_{\text{at}}|n, b, \mathbf{R}_n\rangle,$$

with

$$\hat{H}_{\text{at}} = -\frac{\hbar^2}{2m_0}\nabla^2 + V_{\text{at}}(\mathbf{R}_n, b),$$

where  $|n, b, \mathbf{R}_n\rangle$  denotes a localized atomic-like basis state centered at an atom of type  $b$  with a orbital type  $n$  at a position  $\mathbf{R}_n$ ;  $E_{\text{at}}$  denotes atomic orbital energies and  $V_{\text{at}}$  denotes the atomic potential of the corresponding atom. When we consider a crystal, we have thousands of atoms arranged in a periodic manner determined by the crystal structure. Due to interactions between the orbitals on different atoms, the electronic wave functions are modified and the new Hamiltonian can be expressed as:

$$\hat{H}_{\text{bulk}} = \hat{H}_{\text{at}} + \sum_{\substack{i \neq n \\ b'}} V_{\text{at}}(\mathbf{R}_i, b').$$

Here,  $\hat{H}_{\text{at}}$  is the Hamiltonian of an isolated atom and  $\sum_{\substack{i \neq n \\ b'}} V_{\text{at}}(\mathbf{R}_i, b')$  is the potential generated by all other atoms in the lattice. As described in the previous sections, crystal wave vector  $\mathbf{k}$  is a good quantum number in the bulk system due to the periodicity of the crystal. Thus, we can classify the basis states according to  $\mathbf{k}$  and accordingly, the equation we have to solve is

$$\hat{H}_{\text{bulk}}|\mathbf{k}\rangle = E(\mathbf{k}). \quad (2.35)$$

The above equation can be solved through the following steps.

### 1. Construction of Bloch-type basis states

The first step is to construct basis states by the superposition of the atomic orbitals of isolated atoms. Due to the periodicity of the crystal, a wave function that fulfils Bloch's theorem can be constructed via:

$$|n, b, \mathbf{k}\rangle = \frac{1}{\sqrt{N}} \sum_i e^{i\mathbf{k} \cdot (\mathbf{R}_i + \mathbf{t}_b)} |n, b, \mathbf{R}_i\rangle, \quad (2.36)$$

where the atoms are located at vector positions  $\mathbf{R}_i + \mathbf{t}_b$  in the unit cell  $\mathbf{R}_i$ . We can have more than one atoms per unit cell. The basis vector  $\mathbf{t}_b$  denotes the positions of atoms inside the unit cell. Similar to before,  $n, b$  denotes the orbital type and atom type respectively.  $N$  is the total number of unit cells included in the system, and the summation is performed over all unit cells of the crystal.

### 2. Writing crystal eigenstates as a linear combination of constructed basis states

Now, in a crystal, one can construct such ansatz for each atomic orbital of an atom and each atom in the unit cell of the crystal. This introduces  $\sum_n$  and  $\sum_b$  respectively. Therefore, we get

$$|\mathbf{k}\rangle = \sum_{n,b} |n, b, \mathbf{k}\rangle. \quad (2.37)$$

### 3. Expanding Hamiltonian in terms of the ansatz

The Schrödinger equation can now be expressed in terms of Bloch type basis states by substituting Eq. (2.37) into Eq. (2.35) and multiplying from the left by the complex conjugate of an arbitrary atomic orbital  $|m, b', \mathbf{k}\rangle$ . This leads us to

$$\sum_{n,b} [\langle m, b', \mathbf{k} | \hat{H}_{\text{bulk}} | n, b, \mathbf{k} \rangle - E(\langle m, b', \mathbf{k} | n, b, \mathbf{k} \rangle)] = 0. \quad (2.38)$$

Now the task is to evaluate overlap matrix elements  $(\langle m, b', \mathbf{k} | n, b, \mathbf{k} \rangle)$  and Hamiltonian matrix elements  $\langle m, b', \mathbf{k} | \hat{H}_{\text{bulk}} | n, b, \mathbf{k} \rangle$ . Keeping in mind the basic assumptions of a TB model [80] that electrons are tightly bound to the nucleus, a widely used assumption is overlap matrix element between second nearest neighbors, third nearest neighbors and so on, are small. Nonetheless, the basis states with respect to their nearest neighbors might not fully orthogonal to each other. However, one can use localized basis states that can be orthogonalized with Löwdin-transformation [93] with respect to all the sites. These Löwdin orbitals preserve the symmetry of the atomic orbitals (e.g.  $s$ ,  $p_x$ ) from which they are derived. Accordingly, one obtains  $\langle m, b', \mathbf{k} | n, b, \mathbf{k} \rangle = \delta_{n,m} \delta_{b,b'}$ .

Turning to the Hamiltonian, by using Eq. 2.36,  $\langle m, b', \mathbf{k} | \hat{H}_{\text{bulk}} | n, b, \mathbf{k} \rangle$  can be written as

$$\langle m, b', \mathbf{k} | \hat{H}_{\text{bulk}} | n, b, \mathbf{k} \rangle = \frac{1}{N} \sum_{j,i} e^{i\mathbf{k} \cdot (\mathbf{R}_j + \mathbf{t}'_b - \mathbf{R}_i - \mathbf{t}_b)} \langle m, b', \mathbf{R}_j | \hat{H}_{\text{bulk}} | n, b, \mathbf{R}_i \rangle. \quad (2.39)$$

The above summation is performed over  $N$  unit cells. Here,  $\mathbf{R}_i$  and  $\mathbf{R}_j$  ranges over the unit cells. The matrix elements in the Hamiltonian  $\langle m, b', \mathbf{R}_j | \hat{H}_{\text{bulk}} | n, b, \mathbf{R}_i \rangle$  can be divided into two contributions. If real space lattice vectors  $\mathbf{R}_i = \mathbf{R}_j$  and  $\mathbf{t}_b = \mathbf{t}'_b$ , the matrix elements are “on-site” and represent atomic orbital energies. On the other hand, if  $\mathbf{R}_i$  and  $\mathbf{R}_j$  are not equal (orbitals are situated at different sites), we obtain hopping matrix elements. They describe the probability for an electron to hop from a site  $\mathbf{R}_j$  with orbital  $m$  and atom type  $b'$  to a site  $\mathbf{R}_i$  having orbital  $n$  and atom type  $b$ . If  $(\mathbf{R}_j + \mathbf{t}'_b) - (\mathbf{R}_i + \mathbf{t}_b)$  is the distance between atoms, these matrix elements are called first nearest neighbor elements, second next neighbor elements and so on. These integrals decay rapidly with the distance between the atoms [29, 76, 102]. Therefore, typically one restricts the interactions to nearest neighbor matrix elements and occasionally to second nearest neighbors [81, 102, 103] even though these matrix elements are expected to be smaller than the nearest neighbors. The number of hopping matrix elements can be further reduced by assuming a two-center approximation of Slater and Koster [104]. In general, off-site matrix elements are three-center integrals, which involves orbital  $m$  at site  $\mathbf{R}_j$ , orbital  $n$  at site  $\mathbf{R}_i$  and potential energy as part of the Hamiltonian on a third site, let's say,  $\mathbf{R}_k$ . However, according to Slater and Koster's approach [104], one can neglect in a first approximation these three-center integrals and consider two-center integrals where the potentials are only considered for the atoms at which orbitals are located. Using

these approximations, hopping matrix elements between different orbitals can be derived in terms of the directional cosines which is described in detail elsewhere [76].

So far, we have not discussed how these TB matrix elements can be calculated. There are different approaches [76, 103] to deal with this problem. Using DFT based TB methods [103, 105, 106], one could directly calculate the overlap and Hamiltonian matrix elements. The other widely used approach is the empirical TB model where the matrix elements are treated as parameters and fitted to the known bulk band structure values [81, 89, 102, 103]. In this thesis, empirical TB models are employed [76, 102].

The size of the TB Hamiltonian is the number of atomic orbitals considered as basis states multiplied by the number of atoms in the system. If atomic orbitals are labelled as  $s$ ,  $p$ ,  $d$  etc. according to their symmetry properties, different TB models can be specified as  $scp_a^3$  (one  $s$ -like orbital on the cation and three  $p$ -like orbitals on the anion) [107],  $sp^3$  (one  $s$ -like and three  $p$ -like orbitals on each atom) [102, 103],  $sp^3s^*$  ( $s^*$  accounts for energetically higher lying orbitals) [108] and so on. Depending on the characteristics of the underlying band structure, different TB models can be employed [103]. More details on the TB model used in this thesis is presented in Chapter 6.

### Inclusion of spin-orbit coupling

As described in previous sections, the inclusion of SOC effects is very often necessary for an accurate description of the electronic structure of semiconductors. Usually, SOC is included in the TB model by following the approach proposed by Chadi [109], which has the benefit of not increasing the basis states numbers. Similar to the  $\mathbf{k} \cdot \mathbf{p}$  approach, the spin-orbit Hamiltonian  $\hat{H}_{\text{so}}$  is added to the bulk Hamiltonian  $\hat{H}_{\text{bulk}}$  as:

$$\hat{H} = \hat{H}_{\text{bulk}} + \hat{H}_{\text{so}}, \quad (2.40)$$

where the atomic spin-orbit operator  $\hat{H}_{\text{so}} = \frac{1}{2m^2c^2} \frac{1}{r} \frac{\partial V_{\text{atom}}}{\partial r} \hat{\mathbf{L}} \cdot \hat{\mathbf{s}}$ . Here,  $V_{\text{atom}}$  is the atomic potential,  $\hat{\mathbf{L}}$  is the angular momentum operator and  $\hat{\mathbf{s}}$  is the spin operator. In this work, the SOC is assumed to couple only  $p$  orbitals at the same atom. In general, SOC interactions for nearest neighbors can also be included in a TB model [110], however it has been found that for III-nitrides [111], interaction among on-site  $p$ -like orbitals are sufficient to reproduce the splitting in the VB structure at the  $\Gamma$  point. It is to note that  $s$ -like state (angular momentum number  $l = 0$ ) is not affected by SOC since it has constant angular part. Following discussions

presented in Ref. [111], the only non-zero matrix elements of the spin-orbit Hamiltonian are,

$$\begin{aligned}\langle p_x; \pm | \hat{H}_{\text{so}} | p_z; \mp \rangle &= \pm \lambda, \\ \langle p_x; \pm | \hat{H}_{\text{so}} | p_y; \pm \rangle &= \mp i \lambda, \\ \langle p_y; \pm | \hat{H}_{\text{so}} | p_z; \mp \rangle &= -i \lambda.\end{aligned}\tag{2.41}$$

For convenience, we have denoted the states  $|\uparrow\rangle$  and  $|\downarrow\rangle$  by  $|+\rangle$  and  $|-\rangle$  respectively.  $\lambda$  is a free adjustable parameter that can be used to reproduce splittings in the VB near the  $\Gamma$  point and is tabulated in Table B.3 of Appendix B.

### 2.2.2 Electronic structure theory for QDs

Having described  $\mathbf{k} \cdot \mathbf{p}$  model and TB model for bulk systems in general and in particular for WZ structures, we now move towards extending the model to heterostructures. Since we are mainly interested in QDs, we will outline the changes required to adopt the models to calculate the electronic structure of QDs.

#### 2.2.2.1 $\mathbf{k} \cdot \mathbf{p}$ theory for QDs

The  $\mathbf{k} \cdot \mathbf{p}$  model described in the last section to describe the electronic structure of WZ bulk semiconductors makes use of Bloch's theorem which originates from crystal periodicity. Due to this periodicity,  $\mathbf{k}$  is a good quantum number in bulk binary systems. However, this periodicity no longer exists since quantum confinement breaks the translational symmetry in the heterostructure. Therefore, we have to make changes to the developed formalism to be able to use it for describing the electronic structure of a heterostructure. For a QD, the confinement occurs along all three spatial directions. The standard approach is now to use the following substitutions [112, 113]:

$$\begin{aligned}k_x &\rightarrow \hat{k}_x = -i \frac{\partial}{\partial x}, \\ k_y &\rightarrow \hat{k}_y = -i \frac{\partial}{\partial y}, \\ k_z &\rightarrow \hat{k}_z = -i \frac{\partial}{\partial z}.\end{aligned}\tag{2.42}$$

Additionally, in QDs, the material parameters become spatially dependent and vary through out the structure. Hence, care must be taken when introducing the substitution (cf. Eq. (2.42)) that operators are still Hermitian [112, 113]. Therefore, to retain Hermiticity, symmetrization of individual element of the Hamiltonian matrix [112, 113] is performed as:

$$\begin{aligned}T k_x &\rightarrow \frac{1}{2} (T \hat{k}_x + \hat{k}_x T), \\ T k_x k_y &\rightarrow \frac{1}{2} (\hat{k}_x T \hat{k}_y + \hat{k}_y T \hat{k}_x),\end{aligned}\tag{2.43}$$

where  $T$  represents any material parameter of the bulk  $\mathbf{k} \cdot \mathbf{p}$  model. For instance, the term  $L_1 k_x^2$  in the  $D_{3 \times 3}$  matrix is replaced by  $(-\frac{\partial}{\partial x} L_1 \frac{\partial}{\partial x})$ .

### 2.2.2.2 Tight-binding model for QDs

Similar to  $\mathbf{k} \cdot \mathbf{p}$  models, bulk TB models can also be extended and modified to calculate the electronic structure of heterostructures and of interests for us here are QDs. As stated in the last section, since Bloch's theorem is no longer applicable due to the loss of translational symmetry, matrix elements at each lattice site are set according to the occupying atom. The TB wave function  $|\phi\rangle$  for a QD can be expressed in terms of localized orbitals  $|n, b, \mathbf{R}_i\rangle$  as,

$$|\phi\rangle = \sum_{n,b,i} c_{n,b,\mathbf{R}_i} |n, b, \mathbf{R}_i\rangle. \quad (2.44)$$

The time-independent Schrödinger equation can therefore be written as,

$$\sum_{n,b,i} \langle m, b', \mathbf{R}_j | \hat{H} | n, b, \mathbf{R}_i \rangle c_{n,b,\mathbf{R}_i} - E c_{m,b',\mathbf{R}_j} = 0, \quad (2.45)$$

where  $E$  is the corresponding energy eigenvalue and usually for the different matrix elements  $\langle m, b', \mathbf{R}_j | \hat{H} | n, b, \mathbf{R}_i \rangle$  TB parameters of the bulk materials are used.

In this thesis, we mainly deal with InGaN QDs embedded within a GaN matrix, where the nearest neighbor environment of the nitrogen atom will be Ga and/or In atoms. Determining on-site matrix elements for cations is not problematic since each cation (Ga/In) is surrounded by four nearest neighbor N atoms. Therefore, one can directly extend bulk TB parameters for cations to nanostructures [114]. However, due to the (potential) variations in the nearest neighbor environment, the nitrogen on-site energy values can not unambiguously be determined [114]. Additionally, due to differences in the band gap of InGaN and GaN, the relative position of the CB- and VB-edges need to be taken into account. This is incorporated in the model by shifting the diagonal matrix elements by the VB offset between dot and matrix material which we denote by  $\Delta E_v$ . Accordingly, the matrix elements of the Hamiltonian in the QD region is modified as:

$$\langle m, b', \mathbf{R}_j | \hat{H} | n, b, \mathbf{R}_i \rangle = \langle m, b', \mathbf{R}_j | \hat{H}_{\text{bulk}} | n, b, \mathbf{R}_i \rangle + \Delta E_v \delta_{\mathbf{R}_i, \mathbf{R}_j} \delta_{b,b'} \delta_{m,n}. \quad (2.46)$$

From the above discussion, we see that TB matrix elements in principle depends on the distance between the atoms. Therefore, in a heterostructure of two materials having different lattice constants (e.g. InN and GaN), the distance between two lattice sites will be different from the corresponding values in the bulk system. Therefore, for an accurate description of the electronic structure, one needs to include strain effects in the analysis which is the topic of the next section.

## 2.3 Strain effects

In this section, we first outline procedures to incorporate strain effects into  $\mathbf{k} \cdot \mathbf{p}$  theory and TB model. Subsequently we discuss three different approaches to calculate the strain field which is present in the nanostructure.

### 2.3.1 Incorporation of strain effects in $\mathbf{k} \cdot \mathbf{p}$ model

To introduce strain effects into a  $\mathbf{k} \cdot \mathbf{p}$  model, we follow the approach developed by Pikus and Bir [115]. This is achieved by adding an extra term to the unstrained Hamiltonian  $\hat{H}_{jj'}^{LK}$  (cf. Eq. (2.17)) as

$$\hat{H}_{\mathbf{k} \cdot \mathbf{p}} = \hat{H}_{jj'}^{LK} + \hat{H}_\varepsilon. \quad (2.47)$$

It has been shown that [90, 92]  $\hat{H}_\varepsilon$  can be obtained from  $\hat{H}_{jj'}^{LK}$  by replacing  $k_\alpha k_\beta$  by  $\varepsilon_{\alpha\beta}$ . Accordingly, the matrix elements of the Hamiltonian  $\hat{H}_\varepsilon$  can be written as:

$$\left(\hat{H}_\varepsilon\right)_{jj'} = \sum_{\alpha,\beta} \left(\hat{D}_\varepsilon\right)_{jj'}^{\alpha\beta} \varepsilon_{\alpha\beta}. \quad (2.48)$$

Here,  $\hat{D}_\varepsilon$  is the deformation potential operator. According to the type of  $\mathbf{k} \cdot \mathbf{p}$  Hamiltonian employed in the electronic structure theory, strain Hamiltonian  $\hat{H}_\varepsilon$  can be  $6 \times 6$ ,  $8 \times 8$ , and so on. As described in the last section, in this thesis, we have used a 6-band model for VBs and a 1-band model for the CB in electronic structure calculations. Therefore, we present now  $1 \times 1$  and  $6 \times 6$  strain Hamiltonians to incorporate strain effects in CB and VBs respectively.

- Strain Hamiltonian for the conduction band:

The strain contributions to the CB is obtained using here again  $|S\rangle$ -like basis states as:

$$\hat{H}_{\varepsilon, \text{CB}} = a_{c,\parallel} (\varepsilon_{xx} + \varepsilon_{yy}) + a_{c,\perp} \varepsilon_{zz}. \quad (2.49)$$

Here,  $a_{c,\parallel} = \langle S | \hat{D}_\varepsilon^{xx} | S \rangle = \langle S | \hat{D}_\varepsilon^{yy} | S \rangle$  and  $a_{c,\perp} = \langle S | \hat{D}_\varepsilon^{zz} | S \rangle$  are the CB deformation potentials parallel and perpendicular to the  $c$ -axis respectively. Different deformation potentials stems from the previously described asymmetry between  $a$  and  $c$  axis. All other terms vanish due to parity considerations [92].

- Strain Hamiltonian for the valence band

The strain Hamiltonian  $\hat{H}_\varepsilon$  for the VB states can be derived in the  $(|X\rangle, |Y\rangle, |Z\rangle)$  basis introduced above. Following Ref [90, 96], the strain Hamiltonian for the VBs can be written

as:

$$\left(\hat{H}_\varepsilon\right)_{3 \times 3} = \begin{pmatrix} l_1 \varepsilon_{xx} + m_1 \varepsilon_{yy} + m_2 \varepsilon_{zz} & n_1 \varepsilon_{xy} & n_2 \varepsilon_{xz} \\ n_1 \varepsilon_{xy} & m_1 \varepsilon_{xx} + l_1 \varepsilon_{yy} + m_2 \varepsilon_{zz} & n_2 \varepsilon_{yz} \\ n_2 \varepsilon_{xz} & n_2 \varepsilon_{yz} & m_3 (\varepsilon_{xx} + \varepsilon_{yy}) + l_2 \varepsilon_{zz} \end{pmatrix}. \quad (2.50)$$

The coefficients  $l_1, l_2, m_1, m_2, m_3, n_1, n_2$  can be obtained in the same manner as the previously described  $L_1, L_2, M_1, M_2, M_3, N_1, N_2$  parameters by replacing  $\hat{D}$  by  $\hat{D}_\varepsilon$ . Similar to Luttinger-like effective mass parameters  $A_i$ , these coefficients is related to measurable VB deformation potentials  $D_i$  [90, 96] by,  $l_1 = (D_2 + D_4 + D_5), l_2 = D_1, m_1 = (D_2 + D_4 - D_5), m_2 = (D_1 + D_3), m_3 = D_2, n_3 = 2D_5, n_2 = \sqrt{2}D_6$ . The full  $\left(\hat{H}_{\varepsilon, \text{VB}}\right)_{6 \times 6}$  strain Hamiltonian taking into account spin (cf. Eq. (2.22)) therefore reads [96]:

$$\left(\hat{H}_{\varepsilon, \text{VB}}\right)_{6 \times 6} = \begin{pmatrix} \left(\hat{H}_\varepsilon\right)_{3 \times 3} & 0 \\ 0 & \overline{\left(\hat{H}_\varepsilon\right)_{3 \times 3}} \end{pmatrix}. \quad (2.51)$$

Here  $\overline{\left(\hat{H}_\varepsilon\right)_{3 \times 3}}$  is the complex conjugate of  $\left(\hat{H}_\varepsilon\right)_{3 \times 3}$ .

### 2.3.2 Incorporation of strain in Tight-binding model

The TB Hamiltonian should also include corrections from strain effects for a realistic description of electronic and optical properties. In a microscopic picture, the strain field is induced in a heterostructure due to different bond lengths of the constituting atoms. Therefore, atoms in the nanostructure are displaced from their original positions in an unstrained bulk lattice. In general, strain effects can be included in the TB description as bond angle and bond length corrections to the inter-site matrix elements of the TB Hamiltonian [116, 117]. Even more sophisticated models account for strain corrections to the on-site energies [118]. In these methods, the different deformation potentials are evaluated through a fitting procedure [118] which might not be able to produce all deformation potentials correctly. Furthermore, in this approach especially when introducing on-site corrections in addition to bond length and bond angle corrections, a large number of free adjustable parameters have to be determined [118]. In this work, we use a different approach which is entirely based on the on-site-corrections [119]. As we will discuss in more detail, we use a  $sp^3$  basis where on-site corrections can be included via Pikus-Bir Hamiltonian [115]. With this approach,  $\Gamma$  point deformation potentials can be inputted directly without the need of any fitting procedure [119] and correspondingly, the energetic splitting of different bands are correctly described [119]. It should be noted that this model is only fitted to the  $\Gamma$  point and therefore, different band parameters can not be reproduced at the boundary of the first Brillouin zone. However, as described before, we are mainly interested in the properties of a material system near  $\Gamma$  point. Additionally, for instance in

InN, energies of  $M$  and  $A$   $k$ -points are energetically far away from the CB edge [61]. Therefore, this approach should be sufficient for our purpose. The deformation potential required for the calculations of different matrix elements can either be extracted from the experimental data or can be calculated by DFT [61, 120].

Having outlined the procedure to incorporate strain effects in a  $\mathbf{k} \cdot \mathbf{p}$  and TB model, we have to calculate the strain tensor components  $\varepsilon_{ij}$  that go into the strain corrections for the total Hamiltonian. Therefore, we present different methods to calculate strain fields in the next section.

## 2.4 Calculation of strain fields

As already indicated above, there are different approaches to calculate strain fields in a system [103, 121, 122]. Since QDs involve million of atoms, calculation of strain using ab-initio methods fail due to this huge problem size [123]. We outline three different methods used in this thesis to calculate strain fields in a QD system namely, (a) a surface integral method (b) a continuum elasticity based approach and (c) an atomistic valence force field approach (VFF). In general, the model for calculating the strain field should match the underlying electronic structure theory. In other words, if we are using a continuum-based  $\mathbf{k} \cdot \mathbf{p}$  theory the corresponding strain field should also be calculated in a continuum frame. Therefore, depending on the electronic structure theory, we can choose the appropriate strain field calculations.

### 2.4.1 Surface integral method

The surface integral method presented here is a simple real space model that for certain dot geometries (e.g. cuboid) can give analytic results for strain fields in and around a dot. This method uses surface integrals to evaluate strain values. The shortcoming of this method is the use of same elastic constant inside and outside of the dot. However, there are several advantages associated with this approach. In this method it is assumed that the QD is buried in an infinite system; therefore, boundary condition will not play a role. Furthermore, we can utilize this method with any arbitrary underlying grid which makes it attractive for use in both continuum and atomistic electronic structure theory. Overall, this method is a good starting point for calculating strain field of a QD for an arbitrary shape.

Here, we only provide expressions for calculating the strain field around a QD structure. Detailed derivation of this method is given by Williams *et al* [124]. In this method, the strain is calculated via [124]:

$$\varepsilon_{ij}(\mathbf{r}) = \delta_{ij}\varepsilon_0\chi_{QD} + \frac{\varepsilon_0 A}{4\pi} \int_{QD} \frac{(x_i - x'_i)}{|\mathbf{r} - \mathbf{r}'|^3} \hat{\mathbf{n}}_j \cdot d\mathbf{S}', \quad (2.52)$$

where  $(x_1, x_2, x_3) = (x, y, z)$  and points on the surface of the dot are denoted by primed symbols. The integral is taken over the surface of the dot.  $\hat{\mathbf{n}}_j$  is the unit vector in the  $j$  direction, and  $A = (1 + \nu)/(1 - \nu)$  where  $\nu$  is Poisson's ratio. For a WZ system,  $\nu = C_{13}/(C_{11} + C_{12})$  where  $C_{ij}$  are the elastic constants of the dot material.  $\chi_{QD}$  is the characteristic function of the dot such that  $\chi_{QD} = 1$  inside the dot and zero outside.  $d\mathbf{S}'$  is the elemental surface area vector normal to the dot surface. Finally, the isotropic misfit strain  $\varepsilon_0$  is defined by,

$$\varepsilon_0 = \frac{1}{3} (2\varepsilon_{0a} + \varepsilon_{0c}), \text{ with}$$

$$\varepsilon_{0a} = \frac{a_M - a_{QD}}{a_{QD}}, \varepsilon_{0c} = \frac{c_M - c_{QD}}{c_{QD}}.$$

where  $a_{QD/M}$  and  $c_{QD/M}$  are lattice constants of QD/matrix material along  $x$  and  $z$ -axis ( $c$ -axis), respectively.

### 2.4.2 Continuum elasticity approach

To circumvent the problem of using the same elastic constants between the dot and barrier material, we move to another continuum-based strain approach. This model is based on the assumptions that two crystals have a similar crystal structure and match perfectly at the interface forming a coherent interface. In other words, the lattice mismatch of the active region and its surrounding material is sufficiently small and can be accommodated by an elastic strain. This is consistent with previously assumed infinitesimal strain theory in the Pikus-Bir model and therefore, is a widely used approach to evaluate strain fields for use in continuum-based  $\mathbf{k} \cdot \mathbf{p}$  models [90, 96]. Without such interface, misfit dislocations and defects are generated in the system, and the continuum elasticity model cannot be applied directly. We have used formalism developed by Povolotskyi *et al* [125] and Marquardt *et al* [126] to calculate strain fields in this study.

In this method, first, it is assumed that the bulk crystal structures of the materials forming the heterostructure are similar to a particular “reference” lattice structure and they can be transformed into the reference lattice structure by applying a small strain. Due to coherent nature of interfaces, this transformation is a diagonal tensor and is described by [125, 126],

$$\varepsilon_{ij}^0 = \begin{pmatrix} \frac{a_x^r - a_x^0}{a_x^0} & 0 & 0 \\ 0 & \frac{a_y^r - a_y^0}{a_y^0} & 0 \\ 0 & 0 & \frac{a_z^r - a_z^0}{a_z^0} \end{pmatrix}, \quad (2.53)$$

where  $a_x^r, a_y^r, a_z^r$  are the lattice constants of the reference structure with the condition that we have coherent interfaces and  $a_x^0, a_y^0, a_z^0$  are the lattice constants of unstrained bulk material that is strained here to a reference lattice constant. In our case of hexagonal WZ crystals, this

strain tensor is defined by  $\varepsilon_{xx}^0 = \varepsilon_{yy}^0 = \frac{a^r - a^0}{a^0}$  and  $\varepsilon_{zz}^0 = \frac{c^r - c^0}{c^0}$ . This is since the lattice constant along the  $c$ -direction is different from in-plane lattice constants, as discussed already above.

If we define a displacement vector field  $\mathbf{u}$  with respect to the reference lattice such that  $\mathbf{u} = \mathbf{r} - \mathbf{r}'$ , where  $\mathbf{r}'$  and  $\mathbf{r}$  are coordinates of a point before and after deformation, the complete strain tensor now can be defined in terms of this displacement fields as [125, 126]:

$$\varepsilon_{ij} = \frac{1}{2} \left( \frac{\partial u_i}{\partial x_j} + \frac{\partial u_j}{\partial x_i} \right) + \varepsilon_{ij}^0. \quad (2.54)$$

Therefore, in order to find the strain tensor components  $\varepsilon_{ij}$  that go into the Hamiltonian  $\hat{H}_\varepsilon$  (cf. Eq. (2.48)), we have to determine the displacement field. The displacement field can be obtained by minimizing the elastic energy  $F$  which is in general given by:

$$F = \frac{1}{2} \int_{\Omega_0} C_{ijkl}(\mathbf{r}) \varepsilon_{ij}(\mathbf{r}) \varepsilon_{kl}(\mathbf{r}) d^3\mathbf{r}, \quad (2.55)$$

where  $C_{ijkl}$  is the elastic stiffness tensor and  $\Omega_0$  is volume of the cell. The above minimization with respect to the displacement field  $\mathbf{u}$  leads us to a set of partial differential equation as [125, 126]:

$$\frac{\delta F[u_x, u_y, u_z]}{\delta u_j} = \frac{\partial}{\partial r_i} \left( C_{ijkl} \left( \frac{\partial u_k}{\partial r_l} + \varepsilon_{kl}^0 \right) \right) = 0, \quad j = x, y, z. \quad (2.56)$$

From Eq. (2.56), we can now determine the displacement field, and subsequently, strain tensor components can be evaluated by using Eq. (2.54).

### 2.4.3 Atomistic valence force field method

Continuum-based strain approaches such as the surface integral method or the continuum elasticity method are extremely fast and give first quantitative insights into the strain effects in large sized systems, such as QDs. However, these approaches might not be able to capture the symmetry properties of the underlying lattice. This is well known for instance in InAs/GaAs QD systems where the predicted symmetry from a continuum-based model is  $C_{4v}$  while the real symmetry of the QD system is  $C_{2v}$ . These microscopic effects can be accurately captured in an atomistic model and also complements underlying atomistic electronic structure theory such as the TB model. Therefore, in structures where atomistic details are necessary, we need alternate atomistic approaches for evaluation of strain.

For this purpose, we briefly describe here an atomistic valence force field (VFF) approach which gives a basic description of crystal elasticity on the basis of forces acting among the individual atoms in the nearest neighbor environment. This method uses an interaction potential to calculate the relaxed atomic coordinates. There are quite a number of VFFs used in literature for different compounds [127–129]. In this study, we have used Martin's VFF method [129]

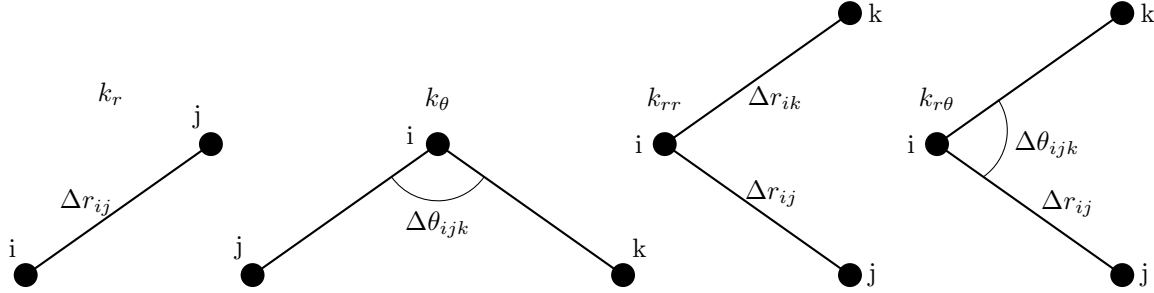


FIGURE 2.4: Valence force field interaction terms contributing to Eq. (2.57). From left to right: bond stretch,  $k_r$ ; bond bending,  $k_\theta$ ; bond-bond,  $k_{rr}$ ; bond-angle,  $k_{r\theta}$ . Taken with permission from D. Tanner [130]

which includes electrostatic interactions in the system explicitly and reproduces attributes of a real WZ system such as  $c/a$  ratios and internal parameters  $u$ . In the here used model, the total energy of an atom  $i$  [119] is given by,

$$\begin{aligned}
 U_i = & \frac{1}{2} \sum_{j \neq i} \frac{1}{2} k_r (r_{ij} - r_{ij}^0)^2 + \sum_{j \neq i} \sum_{k \neq i, k > j} \left\{ \frac{1}{2} k_\theta^i r_{ij}^0 r_{ik}^0 (\theta_{ijk} - \theta_{ijk}^0)^2 \right. \\
 & + k_{r\theta}^i [r_{ij}^0 (r_{ij} - r_{ij}^0) + r_{ik}^0 (r_{ik} - r_{ik}^0)] (\theta_{ijk} - \theta_{ijk}^0) \\
 & \left. + k_{rr}^i (r_{ij} - r_{ij}^0) (r_{ik} - r_{ik}^0) \right\} + \sum'_{j \neq i} \frac{Z_i^* Z_j^* e^2}{4\pi\epsilon_r \epsilon_0 r_{ij}} \\
 & - \frac{1}{2} \sum_{j \neq i} \frac{1}{4} \alpha_M \frac{Z_i^* Z_j^* e^2}{4\pi\epsilon_r \epsilon_0 r_{ij}^0{}^2} (r_{ij} - r_{ij}^0) .
 \end{aligned} \tag{2.57}$$

Here  $i$  refers to the atom under consideration while  $j$  and  $k$  run over all the possible nearest neighbors for each  $i$  except the term marked with a prime symbol. The term containing primed symbol corresponds to long-range Coulomb interaction and runs over the whole crystal. In the case of our WZ system, each primitive cell contains four atoms. Therefore, for the unit cell our evaluation includes 16 bond lengths and 24 bond angles. The different force constants are denoted by  $k_r$ ,  $k_\theta^i$ ,  $k_{r\theta}^i$ , and  $k_{rr}^i$  and the interactions they are describing are shown schematically in Fig. 2.4. The term  $k_r$  and  $k_\theta$  describes the resistance to changes in bond length and bond angle when the atom moves away from its equilibrium position. Similarly, the term  $k_{rr}^i$  measures the response in a particular bond to changes occurring in its neighboring bond ;  $k_{r\theta}^i$  refers to the interaction between the angle between two bonds, and the bonds themselves. For instance, bond lengths will increase with a decrease in the bond angle. The term  $r_{ij}$  denotes the bond length between atom  $i$  and  $j$  and  $\theta_{ijk}$  gives the angle between the bonds  $r_{ij}$  and  $r_{ik}$  and can be defined by  $\cos^{-1} \left( \frac{\mathbf{r}_{ij} \cdot \mathbf{r}_{ik}}{|\mathbf{r}_{ij}| |\mathbf{r}_{ik}|} \right)$ . The equilibrium bond lengths and bond angles are denoted by  $r_{ij}^0$  and  $\theta_{ijk}^0$ , respectively.  $Z_i^*$  denotes the effective charge of atom  $i$  in a point charge model [119]. The elementary charge, permittivity of the vacuum, dielectric constants of the materials are given by  $e$ ,  $\epsilon_0$  and  $\epsilon_r$  respectively.  $\alpha_M$  is the Madelung constant. Finally, a factor  $1/2$  is

introduced to the bond-stretching terms to avoid double counting in the same unit cell. Here described force constants are adjustable parameters and they are obtained by fitting to the elastic constants and lattice constants [119] of the material under investigation. It is to note that the model used in this work is different for instance to the model proposed by Camacho and Niquet [131] which does not include electrostatic interaction explicitly and accounts for the deviation of the  $c/a$  ratio of real WZ structures by considering different force constants along the  $c$ -axis and in-plane directions. The VFF model described above has been implemented in the software package LAMMPS [114, 132].

After relaxation of atomic positions through the VFF method, the local strain tensor  $\epsilon_{ij}$  can be found out as [61]:

$$\begin{pmatrix} \epsilon_{xx} & \epsilon_{xy} & \epsilon_{xz} \\ \epsilon_{yx} & \epsilon_{yy} & \epsilon_{yz} \\ \epsilon_{zx} & \epsilon_{zy} & \epsilon_{zz} \end{pmatrix} = \begin{pmatrix} R_{12,x}^0 & R_{23,x}^0 & R_{34,x}^0 \\ R_{12,y}^0 & R_{23,y}^0 & R_{34,y}^0 \\ R_{12,z}^0 & R_{23,z}^0 & R_{34,z}^0 \end{pmatrix}^{-1} \times \begin{pmatrix} R_{12,x} & R_{23,x} & R_{34,x} \\ R_{12,y} & R_{23,y} & R_{34,y} \\ R_{12,z} & R_{23,z} & R_{34,z} \end{pmatrix} - I. \quad (2.58)$$

Here,  $R_{12}^0$ ,  $R_{23}^0$ , and  $R_{34}^0$  are the tetrahedron edges before strain and  $R_{12}$ ,  $R_{23}$ , and  $R_{34}$  are the distorted tetrahedron edges.  $I$  corresponds to the  $3 \times 3$  identity matrix.

Additionally, the strain present in the structures can induce piezoelectricity in the system as discussed already in Sec. 1.2.2. Therefore, piezoelectric effects need to be considered when calculating the electronic structure of III-N heterostructure and correspondingly discussed in the next section.

## 2.5 Piezoelectricity

In this section, we discuss how to include piezoelectric effects in  $\mathbf{k} \cdot \mathbf{p}$  and TB theory followed by outlining different methods to calculate the same. In the introduction, we have already outlined that III-V nitrides experience a polarization vector field which is the sum of spontaneous and piezoelectric polarization. As we will show later, this polarization vector field can induce an electrostatic potential energy  $V_p(\mathbf{r})$  in a heterostructure. Similar to the strain Hamiltonian  $\hat{H}_\epsilon$ ,  $V_p(\mathbf{r})$  can be added as an additional contribution to the  $\mathbf{k} \cdot \mathbf{p}$  Hamiltonian [96]. On the other hand,  $V_p(\mathbf{r})$  can be added as an on-site correction to the TB Hamiltonian [76] to incorporate effects of piezoelectricity in a TB model.

Here, we will restrict this general discussion to the widely used first-order piezoelectricity. The second-order piezoelectricity will be discussed in later chapters. To first-order, the magnitude of piezoelectric response is connected to strain  $\epsilon_j$  (Voigt notation) via the first-order piezoelectric tensor  $e_{\mu j}$ . This first-order ansatz is linear in strain. For systems with a WZ crystal structure one is left with 18 first-order coefficients  $e_{\mu j}$  of which only three are independent quantities,

namely  $e_{33}$ ,  $e_{15}$  and  $e_{31}$  [58, 133]. Taking this into account and considering only first-order contributions in Eq. (1.2) one is left with the widely used and well-known  $c$ -plane piezoelectric polarization vector field  $\mathbf{P}_{\text{pz}}^{\text{FO}}$  [58]:

$$\mathbf{P}_{\text{pz}}^{\text{FO}} = \begin{pmatrix} 2e_{15}\varepsilon_{xz} \\ 2e_{15}\varepsilon_{yz} \\ e_{31}(\varepsilon_{xx} + \varepsilon_{yy}) + e_{33}\varepsilon_{zz} \end{pmatrix}. \quad (2.59)$$

Please note, in Eq. (2.59) we have used the Cartesian notation for the strain tensor  $\varepsilon_{ij}$ ; in Eq. (1.2) Voigt notation  $\varepsilon_j$  has been applied. The connection between these notations is given by  $\varepsilon_1 = \varepsilon_{xx}$ ,  $\varepsilon_2 = \varepsilon_{yy}$ ,  $\varepsilon_3 = \varepsilon_{zz}$ ,  $\varepsilon_4 = (\varepsilon_{yz} + \varepsilon_{zy}) = 2\varepsilon_{yz}$ ,  $\varepsilon_5 = (\varepsilon_{xz} + \varepsilon_{zx}) = 2\varepsilon_{xz}$ ,  $\varepsilon_6 = (\varepsilon_{xy} + \varepsilon_{yx}) = 2\varepsilon_{xy}$  [133]. More details on the connection between Voigt and Cartesian notation can be found in Ref. [133]. From Eq. (2.59) it is clear that  $x$ - and  $y$ -components are determined by shear strain  $\varepsilon_{ij}$  (Cartesian notation), with  $i \neq j$ , and the first-order piezoelectric coefficient  $e_{15}$ . The  $z$ -component is determined by the diagonal parts of the strain tensor  $\varepsilon_{ii}$  and the two piezoelectric coefficients  $e_{31}$  and  $e_{33}$ .

Depending on the underlying strain theory, one can calculate  $V_p(\mathbf{r})$  in different ways. We present in the following three different methods to calculate piezoelectric potential.

#### *Built-in potential from surface-integral methods*

Since total polarization vector field in a WZ structure consists of spontaneous and piezoelectric polarization, we evaluate these different contributions to the total electrostatic built-in field separately. Similar to the strain field calculations, the surface integral method can also be applied to the electrostatic built-in potential due to spontaneous polarization. For the spontaneous polarization induced potential in a heterostructure, one is left with:

$$\varphi_{\text{sp}}(\mathbf{r}) = \frac{P_{\text{sp, QD}} - P_{\text{sp, M}}}{4\pi\epsilon_r\epsilon_0} \int_{\text{QD}} \frac{\hat{\mathbf{n}}_3 \cdot d\mathbf{S}'}{|\mathbf{r} - \mathbf{r}'|}, \quad (2.60)$$

where  $\epsilon_r$  is the dielectric constant of the QD region,  $\hat{\mathbf{n}}_3$  is the unit vector along the growth direction.  $d\mathbf{S}$  is the elemental area with the vector normal to the QD surface.  $P_{\text{sp, QD/M}}$  are the spontaneous polarization components for QD/matrix. The built-in potential due to piezoelectric polarization can be obtained by:

$$\varphi_{\text{pz}}(\mathbf{r}) = J \int_{\text{QD}} \frac{(x_3 - x'_3)^2}{|\mathbf{r} - \mathbf{r}'|^3} \hat{\mathbf{n}}_3 \cdot d\mathbf{S}' + K \int_{\text{QD}} \frac{1}{|\mathbf{r} - \mathbf{r}'|} \hat{\mathbf{n}}_3 \cdot d\mathbf{S}', \quad (2.61)$$

where

$$J = \frac{-\varepsilon_0 A (2e_{15} - e_{33} + e_{31})}{8\pi\epsilon_0\epsilon_r} \quad (2.62)$$

$$K = \frac{\varepsilon_0}{8\pi\epsilon_0\epsilon_r} [4e_{31} + 2e_{33} - A(2e_{15} + e_{31} + e_{33})]. \quad (2.63)$$

Here,  $e_{15}$ ,  $e_{31}$  and  $e_{33}$  are the first-order piezoelectric polarization coefficients as discussed already above.  $x_3$  is the component of  $\mathbf{r}$  along growth direction. The derivation of these equations can be found somewhere else [134]. Finally, the total electrostatic potential energy is given by,

$$V_p(\mathbf{r}) = -e(\varphi_{\text{sp}}(\mathbf{r}) + \varphi_{\text{pz}}(\mathbf{r})) . \quad (2.64)$$

#### *Built-in potential from continuum elasticity theory*

With the knowledge of total polarization vector  $\mathbf{P}_{\text{Tot}}(\mathbf{r})$  in a heterostructure, the electrostatic potential  $\varphi_{\text{Tot}}(\mathbf{r})$  can be obtained by solving the Poisson's equation

$$4\pi\epsilon_0\nabla(\epsilon_r(\mathbf{r})\nabla\varphi_{\text{Tot}}(\mathbf{r})) = \rho_p(\mathbf{r}) , \quad (2.65)$$

where  $\epsilon_0$  and  $\epsilon_r$  are the vacuum dielectric constant and relative permittivity of the material.  $\rho_p(\mathbf{r})$  is the polarization charge density and is equal to  $-\nabla\mathbf{P}_{\text{Tot}}(\mathbf{r})$ . Correspondingly, the electrostatic built-in potential energy is given by,

$$V_p(\mathbf{r}) = -e(\varphi_{\text{Tot}}(\mathbf{r})) . \quad (2.66)$$

#### *Built-in potential from VFF model*

The macroscopic polarization theories described in the above cannot account for the microscopic features of the underlying atoms under strain, for instance the change in bond lengths and bond angles around the atoms [52]. Therefore, to consider the effect of local strain on electric polarization, a local polarization theory is required [61]. In this theory, the total polarization vector is divided into macroscopic and microscopic contributions. Correspondingly, the local polarization vector field at an atomic site 0 is written as :

$$P_i = \sum_{j=1}^6 e_{ij}^{(0)} \varepsilon_j + P_i^{\text{sp}} - \frac{e}{V_0} \frac{\mathcal{Z}_i^0}{N_{\text{coor}}^0} \left( \sum_{\alpha=1}^{N_{\text{coor}}^0} \ell_i^\alpha - \sum_{j=1}^3 (\delta_{ij} + \varepsilon_{ij}) \sum_{\alpha=1}^{N_{\text{coor}}^0} \ell_{j,0}^\alpha \right) , \quad (2.67)$$

where the first term is the macroscopic piezoelectric contribution and is called as the “clamped-ion” term where the ionic coordinates are not allowed to relax.  $\varepsilon_j$  is the macroscopic strain components in Voigt notation and  $e_{ij}^{(0)}$  are the clamped-ion piezoelectric coefficients. The local contribution, on the other hand, is evaluated at each atomic site and involves the deformation of the nearest neighbor environment around the atom under consideration which is denoted as “0”.  $P_i^{\text{sp}}$  is the contribution arising from spontaneous polarization. Through local contributions, we can define a dipole moment for each tetrahedron of the entire cell.  $\delta_{ij}$  is the Kronecker delta and  $V_0$  is the volume of the tetrahedra comprising an atomic site and all of its nearest neighbors.  $e$  is the elementary electronic charge,  $\mathcal{Z}_i^0$  is the Born effective charge tensor of the atom for which the local polarization is being computed and  $N_{\text{coor}}^0$  is the number of nearest neighbors. The

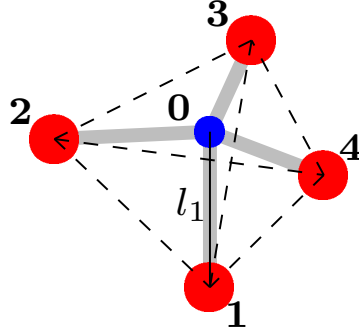


FIGURE 2.5: Different tetrahedron edges in a first nearest-neighbor environment. The bond vector pointing from atom 0 towards atom  $\alpha$  is denoted  $l_\alpha$

parameter  $\ell_i^\alpha, \ell_{j,0}^\alpha$  is the bond vector pointing from the central atom towards atom  $\alpha$  before and after strain respectively. One of such bond vectors is presented in Fig. 2.5. It is to note that all parameters except the strain ( $\varepsilon_j$ ) and bond vectors ( $\ell^\alpha$ ) are system independent and can be obtained from DFT calculations [61, 119].

Utilizing the polarization vector field  $\mathbf{P}$ , the built-in potential can be calculated by solving Poisson's equation. In an atomistic framework, a straight forward implementation of Poisson's equation is difficult due to abrupt changes in the polarization vectors and that the lattice after relaxation is highly asymmetric. Therefore, we make use of a point dipole method as described in [61] where the electrostatic potential is calculated at a desired position  $\mathbf{r}$  due to the presence of a point dipole at another point, let's say  $\mathbf{r}_0$ . This method is described in detail in Ref [52].

Equipped with the here presented electronic structure theories and how to calculate and include strain and piezoelectricity effects, one can solve one-particle Schrödinger equation and obtain single-particle properties such as energies and wave functions for a QD system for instance. These results are often used to describe physical behavior of the QD systems since they capture all structural properties such as size and shape of the dot, strain profile and piezoelectricity. However, it is only applicable for a single charge carrier occupying the dot. In reality, QDs contain more than one charge carrier and therefore, in experiments many-particle interactions determine the electronic and optical properties [29] which is the topic of discussion of the following section.

## 2.6 Many-body states

To calculate many-particle properties, it is necessary to account for Coulomb interaction between the charge carriers [135, 136]. In this section, we introduce two different approaches, namely Hartree approximation [88, 137] and Configuration Interaction method [135, 138] to include Coulomb interactions between the carriers. Finally, we will close this chapter with a

discussion on excitonic fine structure splitting (FSS) which is of great interests for quantum entanglement [139].

The many-body Hamiltonian in a crystal for an interacting electron system usually takes the form

$$\hat{H} = \sum_i \hat{H}(\mathbf{r}_i) + \frac{1}{2} \sum_i \sum_{\substack{j \\ i \neq j}} \hat{V}(\mathbf{r}_i - \mathbf{r}_j) , \quad (2.68)$$

where the first term is a summation of the single-particle Hamiltonians  $\hat{H}$  and  $\hat{V}$  is the interaction operator between the particles. The position of a particle is denoted by  $\mathbf{r}_\alpha$  where  $\alpha$  denotes the particle and takes the values  $1, 2, \dots, N$ . The interaction operator is multiplied by  $\frac{1}{2}$  since the double summation over  $i$  and  $j$  counts each pair twice. Now, to obtain the eigenstates of such system we have to solve many-particle Schrödinger equation:

$$\hat{H}\Psi(\mathbf{r}_1, \mathbf{r}_2, \dots, \mathbf{r}_N) = E\Psi(\mathbf{r}_1, \mathbf{r}_2, \dots, \mathbf{r}_N) , \quad (2.69)$$

where  $\Psi(\mathbf{r}_1, \mathbf{r}_2, \dots, \mathbf{r}_N)$  is the many-particle wave function. Due to the presence of  $\approx 10^{28}$  electrons in a solid, it is not possible to find exact solutions to the Schrödinger equation for many electron atoms. Therefore, one must look for approximations that render the Schrödinger equation tractable to a numerical solution.

### 2.6.1 Hartree Approximation

We start with a simple approximation, namely the Hartree approximation to solve the many-body problem. In this approach, fundamentally we make the assumption that many-body wave function is a simple product of single-particle states such that,

$$\Psi(\mathbf{r}_1, \dots, \mathbf{r}_n) = \psi_1(\mathbf{r}_1) \psi_2(\mathbf{r}_2) \dots \psi_n(\mathbf{r}_n) . \quad (2.70)$$

In spite of the numerical tractability of Hartree approach, this crude approximation fails to capture essential physics [140, 141]. For instance, due to fermionic nature of electrons, the many-body electron wave function should be antisymmetric with respect to interchange in electronic coordinates. This condition cannot be satisfied with the approach presented in Eq. (2.70). However, for the cases where we are only interested in the energetic corrections in the energy spectrum and charge density redistributions due to Coulomb effects, this approach is sufficient. We will come back to the discussion of other sophisticated approaches in the next section.

In this thesis, we are mainly interested in excitonic and biexcitonic properties of the system. Therefore, we present here the implementation of Hartree's approximation for the specific case of an exciton (1 electron, 1 hole) and a biexciton (2 electrons, 2 holes). According

to Eq. (2.70), the initial ansatz is that the excitonic wave function  $\Psi_X(\mathbf{r}_1 = \mathbf{r}_e, \mathbf{r}_2 = \mathbf{r}_h)$  is described as a direct product of electron  $\psi_e$  and hole  $\psi_h$  single-particle ground states. ( $\Psi_X(\mathbf{r}_e, \mathbf{r}_h) = \psi_e(\mathbf{r}_e)\psi_h(\mathbf{r}_h)$ ) [88]. The idea is now that of a mean field approximation so that the electron and holes are separately treated and their energies and wave functions are modified due to the presence of the other particles. Therefore, within this ansatz the Hamiltonian can be written as [88]:

$$\begin{aligned} [\hat{H} + V_e]\psi_h &= E_h^X \psi_h , \\ [\hat{H} + V_h]\psi_e &= E_e^X \psi_e , \end{aligned} \quad (2.71)$$

where  $\hat{H}$  is the single-particle (empty-dot) Hamiltonian while  $V_e$  and  $V_h$  are the potentials generated by the presence of the electron and hole in the dot, respectively. Here, in the first step, we neglect the presence of other particles. The resulting wave functions now serve as initial guess to the excitonic wave function, and their effect on the potential is calculated by solving

$$-e|\psi_e|^2 = \epsilon_0\epsilon_r\Delta V_e , \quad e|\psi_h|^2 = \epsilon_0\epsilon_r\Delta V_h , \quad (2.72)$$

where  $\epsilon_r$  is the dielectric constant and  $\epsilon_0$  the vacuum permittivity. In general,  $\epsilon_r$  is position dependent, however in our calculations, since we are dealing with QDs having low In content (15%-30%) and that the wave functions are mainly localized in the dot region, we have taken the  $\epsilon_r$  value to be position independent and have assumed,  $\epsilon_r = \epsilon_{r,dot}$ . Using this potential, we then calculate new wave functions for the carriers and the process is repeated until the desired level of self-consistency is achieved. The convergence criteria of the self-consistency loop is set to 0.1 meV, meaning that convergence is reached once energies of successive iterations differ by no more than 0.1 meV. In doing so we account for the attractive Coulomb interaction between the carriers in the dot and the related deformation of the wave functions. The exciton recombination energy  $E^X$  and binding energy  $E_X^b$  are calculated via [113]

$$E^X = E_e^X - E_h^X + J_{eh} , \quad (2.73)$$

$$E_X^b = E_e - E_h - E^X , \quad (2.74)$$

where  $E_e$  and  $E_h$  are single-particle electron and hole energies of the empty dot.  $E_e^X$  and  $E_h^X$  are obtained from Eq. (2.71). The Coulomb matrix element  $J_{eh}$  is calculated via:

$$J_{eh} = (\langle \psi_h | V_e | \psi_h \rangle - \langle \psi_e | V_h | \psi_e \rangle) / 2 . \quad (2.75)$$

Note that  $J_{eh}$  is included in Eq. (2.73) to avoid double counting of the Coulomb interaction. Similarly to the exciton, the biexciton (2 electron, 2 hole) ground state is obtained from [88]

$$[\hat{H} + 2V_e + V_h]\psi_h = E_h^{XX}\psi_h , \quad (2.76)$$

$$[\hat{H} + 2V_h + V_e]\psi_e = E_e^{XX}\psi_e , \quad (2.77)$$

with the biexciton recombination energy  $E^{XX}$  and the biexciton binding energy  $E_{XX}^b$  defined as [88]

$$E^{XX} = (2E_e^{XX} - 2E_h^{XX} + 4J_{eh} - J_{ee} - J_{hh}) - (E_e^X - E_h^X + J_{eh}) , \quad (2.78)$$

$$E_{XX}^b = 2E^X - (2E_e^{XX} - 2E_h^{XX} + 4J_{eh} - J_{ee} - J_{hh}) . \quad (2.79)$$

Here, the biexciton recombination energy  $E^{XX}$  is defined as the energetic difference between the biexciton ground state energy  $(2E_e^{XX} - 2E_h^{XX} + 4J_{eh} - J_{ee} - J_{hh})$  and the exciton ground state energy  $(E_e^X - E_h^X + J_{eh})$ . The repulsive electron-electron  $J_{ee}$  and hole-hole interaction  $J_{hh}$  is calculated via:

$$J_{ee} = \langle \psi_e | V_e | \psi_e \rangle , \quad (2.80)$$

$$J_{hh} = -\langle \psi_h | V_h | \psi_h \rangle . \quad (2.81)$$

The here presented Hartree approximation is sufficient to establish trends in excitonic and biexcitonic properties of a QD system. However, as stated earlier, this approach fails to preserve the antisymmetric nature of the fermion wave functions under exchange of particles. The simplest assumption for reflecting the fermionic character of an electrons/hole wave function is a Slater determinant which leads to Hartree-Fock equations [113] as:

$$\Psi(\mathbf{r}_1, \mathbf{r}_2, \dots, \mathbf{r}_N) = \frac{1}{\sqrt{N!}} \det(\psi(\mathbf{r}_1) \psi(\mathbf{r}_2) \dots \psi(\mathbf{r}_N)) . \quad (2.82)$$

In this approach, the Fock terms deal with the exchange requirement of the fermions exactly [113]. However, in an interacting electron system, the full many-body ground state cannot be described by a single Slater determinant. In other words, these equations neglect correlation effects arising due to many-body interactions. Therefore, to successfully incorporate the effects of both exchange and correlation in the many-body problem, we discuss in the next section a sophisticated approach, the so-called ‘‘Configuration Interaction’’ (CI) scheme.

### 2.6.2 Configuration Interaction Method

In full CI method, the many-body Hamiltonian is expanded in the basis of uncorrelated many-particle states. In a QD picture, these uncorrelated basis states are constructed by using for instance bound single-particle states. In the CI approach, the Coulomb interaction is treated exactly among the states taken into account. However, if all of the bound states are considered, it becomes computationally expensive. Previous studies [142] have reported that it is not always necessary to include all of the bound states for the properties we are interested in. The contribution of the higher lying states to the CI depends on the energetic separation between the different states. Usually, the calculation of excitonic effects are restricted to a smaller number of bound states where these configurations are treated exactly in a restricted Hilbert space [142]. We follow this approximation here.

Now, we turn to the many-particle CI Hamiltonian. In the last section, we discussed many-body problem in the language of “first quantization”. As discussed above, when working in this formalism, we work with Slater determinants. However, it is more convenient to deal with the many-particle interactions in the formalism of “second quantization” or the occupation-number representation [143]. Since identical particles are indistinguishable, instead of focusing on individual state of particles  $(\psi_1 \otimes \psi_2 \otimes \dots \otimes \psi_N)$ , we can use a basis that describes number of particles occupying each state in a set of single-particle states. In this basis, instead of a wave function  $\psi_n$ , we use Dirac state  $|n\rangle$ . For instance, in a  $N$ -particle system, the state vectors are then represented as  $|n_1, n_2, n_3, \dots\rangle$  where  $\sum_j n_j = N$ . Here,  $n_1$  particles occupy state 1,  $n_2$  particles occupy state 2 and so on. It is to note that  $n_i$  can only take values 0 or 1 for fermions.

This formalism involves the use of so-called creation and annihilation operators [143]. The creation operator  $\lambda_i^\dagger$  creates a particle in state  $i$  and acts on the state vectors as,

$$\lambda_i^\dagger |n_1, n_2, \dots, n_i, \dots\rangle = (-1)^{\sum_{\mu < i} n_\mu} (1 - n_i) |n_1, n_2, \dots, 1_i, \dots\rangle, \quad (2.83)$$

where  $(-1)^{\sum_{\mu < i} n_\mu}$  is a phase factor. On the other hand, the annihilation operator  $\lambda_i$  removes a particle from state  $i$  and acts on the state vectors as:

$$\lambda_i |n_1, n_2, \dots, n_i, \dots\rangle = (-1)^{\sum_{\mu < i} n_\mu} n_i |n_1, n_2, \dots, 0_i, \dots\rangle. \quad (2.84)$$

In this method, the antisymmetry properties of fermions is automatically ensured by the characteristics anti-commutation relation of these operators [143]. For instance,

$$\begin{aligned} \lambda_i \lambda_j |n_1, n_2, \dots, n_i, \dots, n_j, \dots\rangle &= (-1)^{\sum_{\mu < i} n_\mu} (-1)^{\sum_{\mu < j} n_\mu} n_i n_j |n_1, n_2, \dots, 0_i, \dots, 0_j, \dots\rangle, \\ \lambda_j \lambda_i |n_1, n_2, \dots, n_i, \dots, n_j, \dots\rangle &= (-1)^{\sum_{\mu < i} n_\mu} (-1)^{\sum_{\mu < j} n_\mu - 1} n_i n_j |n_1, n_2, \dots, 0_i, \dots, 0_j, \dots\rangle \\ &= -\lambda_i \lambda_j |n_1, n_2, \dots, n_i, \dots, n_j, \dots\rangle. \end{aligned}$$

In other words, the Slater determinants of single-particle states in first quantization turns into products of creation operators acting on a vacuum state in second quantization [143]. Here, vacuum state  $|0\rangle$  corresponds to a state containing no fermions. In general, the many-particle Hamiltonian of a system of interacting electrons and holes in the above presented second quantization formalism is given by [136],

$$\begin{aligned} \hat{H} = & \sum_i \left( E_i^e e_i^\dagger e_i + E_i^h h_i^\dagger h_i \right) \\ & + \underbrace{\frac{1}{2} \sum_{ijkl} V_{ijkl}^{ee} e_i^\dagger e_j^\dagger e_k e_l + \frac{1}{2} \sum_{ijkl} V_{ijkl}^{hh} h_i^\dagger h_j^\dagger h_k h_l - \sum_{ijkl} V_{ijkl}^{eh,dir} e_i^\dagger h_j^\dagger h_k e_l + \sum_{ijkl} V_{ijkl}^{eh,ex} e_i^\dagger h_j^\dagger h_l e_k}_{\hat{H}_c} . \end{aligned} \quad (2.85)$$

Here,  $E_i^e$  and  $E_i^h$  are single-particle electron and hole energies of state  $i$ , respectively. The creation operator  $\lambda_i^\dagger$  creates an electron ( $\lambda_i^\dagger = e_i^\dagger$ ) or hole ( $\lambda_i^\dagger = h_i^\dagger$ ) in the single-particle state  $i$  while the annihilation operators  $\lambda_i$  removes an electron ( $\lambda_i = e_i$ ) or hole ( $\lambda_i = h_i$ ) from state  $i$ . The Coulomb interaction between the particles in the states  $i, j, k, l$  is described by the terms  $V_{ijkl}^{\lambda\lambda'}$ . These terms can be divided into four categories such as electron-electron, hole-hole, electron-hole direct interaction and electron-hole exchange interaction, respectively. The first two terms of  $\hat{H}_c$  correspond to repulsion between two carriers of same charge. Here, electrons and holes are annihilated in states  $k, l$  and correspondingly created in states  $i$  and  $j$ . The third term corresponds to the direct Coulomb attraction between electron and hole where an electron and hole is annihilated in the states  $k$  and  $l$  and then created in states  $i$  and  $j$ , respectively. The last term corresponds to the electron-hole exchange interaction which is a pure quantum mechanical effect and has no classical analogue. The factor  $\frac{1}{2}$  is included in the  $e - e$  and  $h - h$  interaction to avoid double counting arising due to indistinguishability of particles.

Now, we will turn to the calculation of the Coulomb matrix elements  $V_{ijkl}$ . In this work, we are only interested in excitonic (1-electron and 1-hole) properties of the system, therefore, we will not discuss terms corresponding to  $e - e$  interaction ( $V_{ijkl}^{ee}$ ) and  $h - h$  interactions ( $V_{ijkl}^{hh}$ ). The remaining direct and exchange Coulomb matrix elements can be calculated by

$$\begin{aligned} V_{ijkl}^{eh,dir} &= \int d\mathbf{r} \int d\mathbf{r}' \psi_{e,i}^*(\mathbf{r}) \psi_{h,j}^*(\mathbf{r}') V(\mathbf{r} - \mathbf{r}') \psi_{h,k}(\mathbf{r}') \psi_{e,l}(\mathbf{r}) , \\ V_{ijkl}^{eh,ex} &= \int d\mathbf{r} \int d\mathbf{r}' \psi_{e,i}^*(\mathbf{r}) \psi_{h,j}^*(\mathbf{r}') V(\mathbf{r} - \mathbf{r}') \psi_{e,k}(\mathbf{r}') \psi_{h,l}(\mathbf{r}) , \end{aligned} \quad (2.86)$$

where  $\psi_{e,\alpha}(\mathbf{r})$  and  $\psi_{h,\beta}(\mathbf{r})$  are the single-particle electron and hole wave functions for state  $\alpha$  and  $\beta$  respectively. The screened Coulomb potential is given by,

$$V(\mathbf{r} - \mathbf{r}') = \frac{e_0^2}{4\pi\epsilon_0\epsilon_r |\mathbf{r} - \mathbf{r}'|} . \quad (2.87)$$

In the above,  $e_0$  denotes the electron charge,  $\epsilon_0$  is the vacuum dielectric constant, and  $\epsilon_r$  is the dielectric constant of the dot region. In general,  $\epsilon_r$  is position dependent. However, as discussed earlier, since we are dealing with low In content QDs plus that the wave functions are mainly localized in the dot, we have assumed  $\epsilon_r = \epsilon_{\text{dot}}$  for the whole structure. When discussing TB theory in Sec 2.2.2.2, we had pointed out that the wave function  $\psi_i(\mathbf{r})$  can be expressed in terms of localized orbitals as:

$$\psi_i(\mathbf{r}) = \sum_{\mathbf{R}\alpha} c_{\mathbf{R}\alpha}^i \phi_{\mathbf{R}\alpha}(\mathbf{r}). \quad (2.88)$$

Putting the expansion defined in Eq. (2.88) into Eq. (2.86),  $V_{ijkl}$  can be reformulated as:

$$V_{ijkl} = \sum_{\mathbf{R}_1 \mathbf{R}_2 \mathbf{R}_3 \mathbf{R}_4} \sum_{\alpha \beta \gamma \delta} c_{\mathbf{R}_1 \alpha}^{i*} c_{\mathbf{R}_2 \beta}^{j*} c_{\mathbf{R}_3 \gamma}^k c_{\mathbf{R}_4 \delta}^l \cdot \int d^3 r d^3 r' V(\mathbf{r} - \mathbf{r}') \phi_{\alpha \mathbf{R}_1}^*(\mathbf{r}) \phi_{\beta \mathbf{R}_2}^*(\mathbf{r}') \phi_{\gamma \mathbf{R}_3}(\mathbf{r}') \phi_{\delta \mathbf{R}_4}(\mathbf{r}). \quad (2.89)$$

However, it has been shown previously that [76], due to the long range nature of the direct Coulomb interaction, instead of using full wave functions  $\psi_i(\mathbf{r})$ , one can approximately calculate the Coulomb matrix elements from the TB coefficients  $c_{\mathbf{R}\alpha}^i$  as [76]:

$$V_{ijkl} = \sum_{\mathbf{R} \mathbf{R}'} \sum_{\alpha \beta} c_{\mathbf{R}\alpha}^{i*} c_{\mathbf{R}'\beta}^{j*} c_{\mathbf{R}\beta}^k c_{\mathbf{R}'\alpha}^l V(\mathbf{R} - \mathbf{R}'),$$

$$\text{with } V(\mathbf{R} - \mathbf{R}') = \frac{e_0^2}{4\pi\epsilon_0\epsilon_r|\mathbf{R} - \mathbf{R}'|} \quad \text{for } \mathbf{R} \neq \mathbf{R}' \quad (2.90)$$

$$\text{and } V(0) = \frac{1}{V_{uc}^2} \int_{uc} d^3 r d^3 r' \frac{e_0^2}{4\pi\epsilon_0|\mathbf{r} - \mathbf{r}'|} \approx V_c.$$

Here,  $V_{uc}$  is the unit cell volume and we have neglected screening for the on-site term. The validity of the above approximations can be found elsewhere [76]. After calculating these Coulomb matrix elements, the CI Hamiltonian can be constructed in terms of the uncorrelated basis states by diagonalizing the many-body Hamiltonian,  $\hat{H}$ , Eq. (2.85). Subsequently, we obtain the interacting many-particle states. A detailed description of this method can be found in Refs [135, 138, 142]. However, we can have a qualitative understanding of the problem by analysing it for a simple exciton system, which is presented in the next section.

### 2.6.3 Example of a CI calculation

In this section, we present a simple example for calculating the exciton problem (1 electron and 1 hole) using the CI method. Here, we are mainly interested in how the excitonic spectra can be evaluated using the CI method. Therefore, we have to only focus on the last two terms of the many-body Hamiltonian  $\hat{H}_c$  (cf. Eq. (2.85)). In other words, for an exciton,

$$\hat{H}_c = - \underbrace{\sum_{ijkl} V_{ijkl}^{eh,dir} e_i^\dagger h_j^\dagger h_k e_l}_{\hat{H}_{c,dir}} + \underbrace{\sum_{ijkl} V_{ijkl}^{eh,ex} e_i^\dagger h_j^\dagger h_l e_k}_{\hat{H}_{c,ex}}. \quad (2.91)$$

In our simple case, we take only electron and hole ground states into account. One can now include spin in each of these states. The ground state of electron and holes is two fold degenerate due to spin degeneracy. If we include SOC in the description, the spin is no longer a good quantum number. Also, in a QD system, due to band mixing effects, even the total angular momentum is not a good quantum number. However, these states are still doubly degenerate due to time reversal symmetry [76]<sup>2</sup>. Therefore, to include spin and taking into account SOC in the description, we assume two possible basis states for both electrons and holes such that  $|n_{e1}, n_{e2}, n_{h1}, n_{h2}\rangle$  are the occupation numbers for the electrons occupying states  $n_{e1}$  or  $n_{e2}$  and the holes occupying states  $n_{h1}$  or  $n_{h2}$ . In such a scenario, we can have four possible states,  $|1, 0, 1, 0\rangle$ ,  $|1, 0, 0, 1\rangle$ ,  $|0, 1, 1, 0\rangle$ , and  $|0, 1, 0, 1\rangle$ , thus giving a  $4 \times 4$  CI problem. For convenience, we denote the above four state vectors as  $|c_1v_1\rangle$ ,  $|c_1v_2\rangle$ ,  $|c_2v_1\rangle$  and  $|c_2v_2\rangle$ , respectively where the excitonic state  $|c_iv_j\rangle$  indicates which state is occupied by the electrons/holes.

As an example, we will evaluate one matrix element, i.e.  $\langle c_1v_2 | \hat{H}_c | c_1v_2 \rangle$  in this basis. The matrix element for the direct term  $\hat{H}_{c,dir}$  is given by,

$$\begin{aligned}
 \langle c_1v_2 | \hat{H}_{c,dir} | c_1v_2 \rangle &= \langle c_1v_2 | \sum_{ij} V_{ij21}^{eh,dir} e_i^\dagger h_j^\dagger h_2 e_1 | c_1v_2 \rangle \\
 &= \langle c_1v_2 | V_{1121}^{eh,dir} e_1^\dagger h_1^\dagger h_2 e_1 | c_1v_2 \rangle + \langle c_1v_2 | V_{1221}^{eh,dir} e_1^\dagger h_2^\dagger h_2 e_1 | c_1v_2 \rangle \\
 &\quad + \langle c_1v_2 | V_{2121}^{eh,dir} e_2^\dagger h_1^\dagger h_2 e_1 | c_1v_2 \rangle + \langle c_1v_2 | V_{2221}^{eh,dir} e_2^\dagger h_2^\dagger h_2 e_1 | c_1v_2 \rangle \\
 &= \langle c_1v_2 | V_{1121}^{eh,dir} | c_1v_1 \rangle + \langle c_1v_2 | V_{1221}^{eh,dir} | c_1v_2 \rangle + \langle c_1v_2 | V_{2121}^{eh,dir} | c_2v_1 \rangle + \langle c_1v_2 | V_{2221}^{eh,dir} | c_2v_2 \rangle \\
 &= V_{1221}^{eh,dir}
 \end{aligned} \tag{2.92}$$

Similarly, the matrix element for the exchange term  $\hat{H}_{c,ex}$  is give by,

$$\begin{aligned}
 \langle c_1v_2 | \hat{H}_{c,ex} | c_1v_2 \rangle &= \langle c_1v_2 | \sum_{ij} V_{ij12}^{eh,ex} e_i^\dagger h_j^\dagger h_2 e_1 | c_1v_2 \rangle \\
 &= \langle c_1v_2 | V_{1112}^{eh,ex} e_1^\dagger h_1^\dagger h_2 e_1 | c_1v_2 \rangle + \langle c_1v_2 | V_{1212}^{eh,ex} e_1^\dagger h_2^\dagger h_2 e_1 | c_1v_2 \rangle \\
 &\quad + \langle c_1v_2 | V_{2112}^{eh,ex} e_2^\dagger h_1^\dagger h_2 e_1 | c_1v_2 \rangle + \langle c_1v_2 | V_{2212}^{eh,ex} e_2^\dagger h_2^\dagger h_2 e_1 | c_1v_2 \rangle \\
 &= \langle c_1v_2 | V_{1112}^{eh,ex} | c_1v_1 \rangle + \langle c_1v_2 | V_{1212}^{eh,ex} | c_1v_2 \rangle + \langle c_1v_2 | V_{2112}^{eh,ex} | c_2v_1 \rangle + \langle c_1v_2 | V_{2212}^{eh,ex} | c_2v_2 \rangle \\
 &= V_{1212}^{eh,ex}
 \end{aligned} \tag{2.93}$$

---

<sup>2</sup> The time reversal symmetry is a non-geometrical symmetry which introduces additional degeneracies in the system. In general, when the time reversal operator acts on a state, we obtain another state that is degenerate to it and is the complex conjugate of the original state accompanied by a spin flip. This degeneracy is the so-called Kramer's degeneracy in quantum mechanics.

When evaluating the above, we have used the relation that the terms  $\langle c_i v_j | c_k v_l \rangle$  are only non-zero if  $i = k$  and  $j = l$ . Similarly other matrix elements of the  $\hat{H}_c$  can be found as

$$\begin{aligned} \left[ \hat{H}_c \right]_{4 \times 4} &= \left[ \hat{H}_{c,dir} \right]_{4 \times 4} + \left[ \hat{H}_{c,ex} \right]_{4 \times 4} \\ &= \begin{bmatrix} V_{1111}^{eh,dir} & V_{1121}^{eh,dir} & V_{1112}^{eh,dir} & V_{1122}^{eh,dir} \\ V_{1211}^{eh,dir} & V_{1221}^{eh,dir} & V_{1212}^{eh,dir} & V_{1222}^{eh,dir} \\ V_{2111}^{eh,dir} & V_{2121}^{eh,dir} & V_{2112}^{eh,dir} & V_{2122}^{eh,dir} \\ V_{2211}^{eh,dir} & V_{2221}^{eh,dir} & V_{2212}^{eh,dir} & V_{2222}^{eh,dir} \end{bmatrix} + \begin{bmatrix} V_{1111}^{eh,ex} & V_{1112}^{eh,ex} & V_{1121}^{eh,ex} & V_{1122}^{eh,ex} \\ V_{1211}^{eh,ex} & V_{1212}^{eh,ex} & V_{1221}^{eh,ex} & V_{1222}^{eh,ex} \\ V_{2111}^{eh,ex} & V_{2112}^{eh,ex} & V_{2121}^{eh,ex} & V_{2122}^{eh,ex} \\ V_{2211}^{eh,ex} & V_{2212}^{eh,ex} & V_{2221}^{eh,ex} & V_{2222}^{eh,ex} \end{bmatrix}, \end{aligned} \quad (2.94)$$

Using time reversal symmetry [76] properties, the only non-zero terms for the direct-Coulomb matrix elements are,  $V_{1111}^{eh,dir} = V_{1221}^{eh,dir} = V_{2112}^{eh,dir} = V_{2222}^{eh,dir} = C \in \mathbb{R}$ . Using similar arguments, the number of independent elements for exchange matrix elements can be reduced to:

$$\begin{aligned} V_{1111}^{eh,ex} &= V_{2222}^{eh,ex} = C_1 \in \mathbb{R}, \\ V_{1112}^{eh,ex} &= (V_{1211}^{eh,ex})^* = (-V_{2221}^{eh,ex})^* = -V_{2122}^{eh,ex} = C_2 \in \mathbb{C}, \\ V_{1121}^{eh,ex} &= (V_{2111}^{eh,ex})^* = (-V_{2212}^{eh,ex})^* = -V_{1222}^{eh,ex} = C_3 \in \mathbb{C}, \\ V_{1122}^{eh,ex} &= (V_{2211}^{eh,ex})^* = C_4 \in \mathbb{C}, \\ V_{1212}^{eh,ex} &= V_{2121}^{eh,ex} = C_5 \in \mathbb{R}, \\ V_{1221}^{eh,ex} &= (V_{2112}^{eh,ex})^* = C_6 \in \mathbb{C}. \end{aligned}$$

Therefore, the matrix representation of the CI Hamiltonian for the lowest four exciton states in the presence of SOC in the CI basis  $\{|c_1 v_1\rangle, |c_1 v_2\rangle, |c_2 v_1\rangle, |c_2 v_2\rangle\}$  is given by,

$$\left[ \hat{H}_c \right]_{4 \times 4} = \begin{bmatrix} C & 0 & 0 & 0 \\ 0 & C & 0 & 0 \\ 0 & 0 & C & 0 \\ 0 & 0 & 0 & C \end{bmatrix} + \begin{bmatrix} -C_1 & -C_2 & -C_3 & -C_4 \\ -C_2^* & -C_5 & -C_6 & C_3 \\ -C_3^* & -C_6^* & -C_5 & C_2 \\ -C_4^* & C_3^* & C_2^* & -C_1 \end{bmatrix}, \quad (2.95)$$

where the first matrix corresponds to the electron-hole direct Coulomb interaction and the second matrix represents electron-hole exchange interaction.

Once we know the Coulomb matrix elements, we can diagonalize the Hamiltonian and get the interacting many-particle states and the excitonic energy spectrum. These matrix elements crucially depends on the model we use to calculate them (e.g. atomistic or continuum) and also on the symmetry of the underlying system. To get a first insight into the exciton energy levels, we investigate a special case where we have no SOC in the system.

Special case: As stated earlier, in the absence of SOC we can decouple the spatial and spin parts. Therefore, the single-particle basis states can be classified as  $|n_{e1}, n_{e2}, n_{h1}, n_{h2}\rangle \equiv$

$|n_{e\uparrow}, n_{e\downarrow}, n_{h\uparrow}, n_{h\downarrow}\rangle$  where  $|n_{e\uparrow}\rangle(|n_{h\uparrow}\rangle)$  corresponds to an electron (hole) ground state with spin-up whereas state  $|n_{e\downarrow}\rangle(|n_{h\downarrow}\rangle)$  corresponds to an electron (hole) ground state with spin-down.

Since spin is now a good quantum number, this causes certain terms namely,  $C_2, C_3, C_4$  and  $C_5$  to vanish due to the orthogonality of the spin states. Additionally, we get  $C_1=C_6$ , due to identical orbital parts of the electron (hole) ground state wave functions. Therefore, the Hamiltonian  $\hat{H}_c$  further restricts to,

$$\hat{H}_c = \begin{bmatrix} C & 0 & 0 & 0 \\ 0 & C & 0 & 0 \\ 0 & 0 & C & 0 \\ 0 & 0 & 0 & C \end{bmatrix} + \begin{bmatrix} -C_1 & 0 & 0 & 0 \\ 0 & 0 & -C_1 & 0 \\ 0 & -C_1 & 0 & 0 \\ 0 & 0 & 0 & -C_1 \end{bmatrix}. \quad (2.96)$$

If we diagonalize the Hamiltonian analytically, we obtain triply degenerate triplet state ( $E = C - C_1$ ) and a non-degenerate singlet state ( $E = C + C_1$ ). Therefore, from this simple model, we conclude that electron-hole exchange effects split the energy of singlet and triplet states by  $2C_1$ . If there is no exchange effects in the system, the second term of  $\hat{H}_c$  vanishes and we get a four-fold degenerate exciton state. This situation is illustrated schematically in Fig. 2.6 and the level splitting due to electron-hole exchange is usually referred to as the excitonic fine structure. In general, an exciton state can now be labelled as *bright* or *dark* according to its optical activity. Therefore, the energetic splitting between two exciton states can be bright-bright, dark-dark or bright-dark splittings [144]. These splittings are usually referred to as fine structure splitting (FSS). In the said case, due to spin conservation, the singlet state and one of the triplet states is dark while the two other triplet states are bright. Accordingly, we obtain a bright-dark FSS between the singlet and triplet state in this simple example.

It is to note that FSS is an important characteristics of many-body states and has crucial impact for instance on the generation of entangled photon emission [12]. In the next section, we will therefore discuss in more detail the FSS and its connection to entangled photon emission. Since the FSS depends on the symmetry of the underlying system, we will also provide a group theoretical analysis of the expected FSS in different systems.

#### 2.6.4 Excitonic structure and Fine structure splitting

As already pointed out, the excitonic FSS has recently drawn a lot of attention for quantum entanglement [139]. QDs in principle can generate polarization entangled photon pairs when they exhibit zero bright-bright FSS in the energy spectrum of the excitonic structure. One way of achieving this is to use the biexciton-exciton cascade. One of such scheme is outlined in Fig. 2.7 (a) where the biexciton first decays into the exciton by creation of a either left ( $\sigma^+$ ) or right ( $\sigma^-$ ) circularly polarized photon. In the subsequent step, the exciton decays to ground state

Without Exchange	With Exchange
	$C + C_1 (1x)$
	-----
	Dark
$C(4x)$	
-----	
Dark (1x)	
Dark (1x)	
Bright (2x)	
	$C - C_1 (3x)$
	-----
	Dark (1x)
	Bright (2x)

FIGURE 2.6: Schematic illustration of energy structure without spin orbit coupling in the absence (left) and in the presence (right) of the electron-hole exchange interaction for the exciton ground state.

by emission of a photon with opposite polarization to the first branch. Correspondingly, the emission spectra of photons from different cascades overlap due to degeneracies of intermediate excitonic states and removes the “which-path” information creating polarization entanglement of the emitted photons [145]. When the intermediate bright exciton ground states differ by

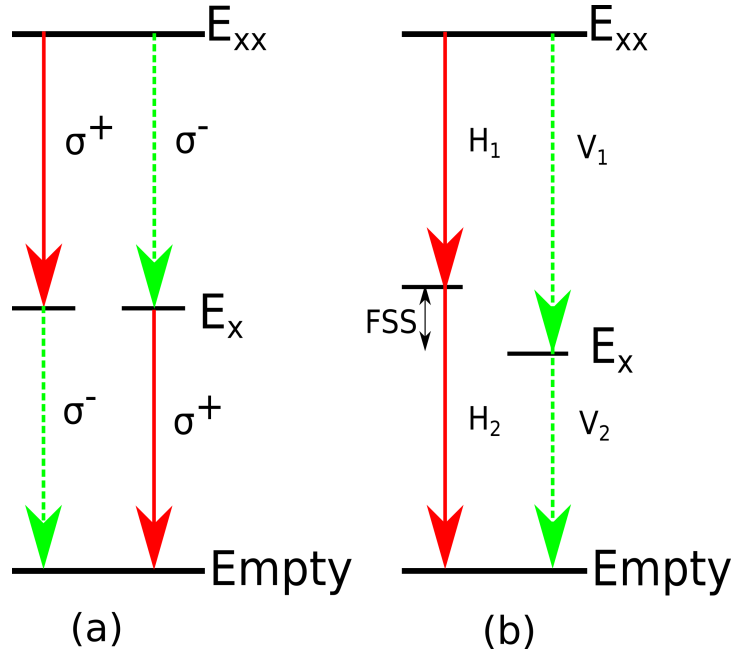


FIGURE 2.7: Transition Scheme for biexciton-exciton decay for (a) Zero FSS, entanglement is achieved and the transitions emit circularly ( $\sigma$ ) polarized light (b) Non zero FSS, all four possible transitions correspond to different energies.

a small amount of energy, typically greater than their respective linewidth [29], we obtain a non-zero FSS. Such a case is illustrated in Fig. 2.7 (b) where the emitted photons are linearly polarized and different transitions labelled with  $H_i$  ( $V_i$ ) with  $i=1,2$  emit horizontally (vertically) polarized light with respect to a given axis. Here, the different energies of the possible

transitions allow to distinguish between photons originating from the left and right cascade which destroys the polarization entanglement of photons.

As pointed out in the last section, the excitonic fine structure and as a result, the FSS in a QD depends on the underlying crystal symmetry and the magnitude of electron-hole exchange interaction between the carriers. Therefore, in the first step we analyze the effect of the underlying crystal symmetries on the FSS with the help of group theoretical concepts presented in Sec. 2.1. Special attention will be paid to the effect of exchange interaction on the energetic structure. Through this analysis, we can easily show the application of group theory to get first insights into the FSS. We start with the well studied InAs/GaAs system such that we can use this analysis to compare and highlight differences to the III-N system which has a different underlying crystal symmetry. Equipped with the insights from As systems, we will move to the discussion of III-N systems in the next step. Overall, the outcome of this analysis will help us to benchmark our numerical results which will be presented in later chapters.

### InAs/GaAs QDs

In (001) InAs/GaAs QDs, for ideal QD geometries (lens shaped, rectangular truncated structures) the  $T_d$  symmetry of the ZB crystal reduces to a  $C_{2v}$  symmetry [100] since inversion is no longer a symmetry operation of the system. We will discuss here how this reduction in symmetry leads to a non-vanishing FSS in ZB (001) QDs [144]. For a simplified discussion, we take into account only the ground state electron ( $e_0$ ) and hole ( $h_0$ ) states in the CI expansion defined in Sec. 2.6.2. The lowest four excitonic states without and with SOC is presented in Fig. 2.8 and 2.9 respectively. We start our analysis without SOC, where the orbital and spin parts can be decoupled and treated independently. It has been observed that in this case, electron ground state ( $e_0$ ) has a dominant  $s$ -like character and the hole ground state ( $h_0$ ) has either a  $p_x$ - or  $p_y$ -like character [146]. As stated in the group theory section, in the absence of SOC, the electronic states of the orbital part can be described by single group representations of  $C_{2v}$ . The character table and direct product of different IRRs for a  $C_{2v}$  point group is presented in Table 2.3 and Table 2.4 respectively. Here, the double group IRRs are denoted in bold. Following Table 2.3, we find that  $e_0$  state transforms according to  $A_1$  while  $h_0$  state transforms as either  $B_1$  or  $B_2$  [146]. Since excitonic states in our case can be obtained by pairing single-particle electron ( $e_i$ ) and hole ground states ( $h_j$ ), their symmetry can be expressed as

$$\Gamma_X = \Gamma_e \otimes \Gamma_h, \quad (2.97)$$

where  $\Gamma_e$  and  $\Gamma_h$  are IRR of electron ( $e_i$ ) and hole ( $h_j$ ) states and “ $\otimes$ ” corresponds to direct product. Accordingly, here following Table 2.4, the orbital part of the ground state exciton transforms according to  $A_1 \otimes B_1(B_2) = B_1(B_2)$ , which is a 1-D representation.

TABLE 2.3: Character table of  $C_{2v}$  point group.

$C_{2v}$	$E$	$C_2$	$\sigma_x$	$\sigma_y$	Basis functions
$A_1$	1	1	1	1	$1, z$
$A_2$	1	1	-1	-1	$R_z$
$B_1$	1	-1	-1	1	$x, R_y$
$B_2$	1	-1	1	-1	$y, R_x$
$E_{1/2}$	2	0	0	0	

TABLE 2.4: Direct products of representation for a  $C_{2v}$  point group.

$C_{2v}$	$A_1$	$A_2$	$B_1$	$B_2$	$E_{1/2}$
$A_1$	$A_1$	$A_2$	$B_1$	$B_2$	$E_{1/2}$
$A_2$		$A_1$	$B_2$	$B_1$	$E_{1/2}$
$B_1$			$A_1$	$A_2$	$E_{1/2}$
$B_2$				$A_1$	$E_{1/2}$
$E_{1/2}$				$A_1 \oplus A_2 \oplus B_1 \oplus B_2$	

Now turning to the spin part, similar to the orbital case, the spin components of an exciton state ( $D_X$ ) can be represented by a direct product of spin wave function representations of electron ( $D_e$ ) and holes ( $D_h$ ) as  $D_X = D_e \otimes D_h$ . As discussed earlier, the spin wave function transforms according to the  $D_{1/2}$  IRR which is doubly degenerate. Correspondingly, we get  $D_X = D_{1/2} \otimes D_{1/2} = D_0 \oplus D_1$  [147]. Since the degeneracies of a  $D_j$ -symmetric state is  $(2j+1)$  [147], the addition of spin can form a one-dimensional singlet state and a three dimensional triplet state. It is important to note that group theory gives only insight into the general aspects of the symmetry of the different exciton states, but not on the energy ordering or energy separations (e.g. magnitude of singlet-triplet splitting). To gain insights into this for instance, CI calculations are required [135, 138]. As described in our example of the CI model, in the absence of exchange interaction, the exciton ground state is four-fold degenerate. Here, by combining orbital ( $B_1/B_2$ ) and spin ( $D_0 \oplus D_1$ ) parts we get the same conclusion. With exchange effects, the four-fold degenerate state splits into singlet ( $B_1/B_2 \otimes D_0$ ) and triplet ( $B_1/B_2 \otimes D_1$ ) states. Turning to selection rules, one can find the singlet state is dark and in the triplet, one state is dark and two states are bright [140]. The polarization of the bright states can be predicted following Table 2.3 where a  $B_1/B_2$  exciton is allowed to emit  $x/y$ -polarized radiation. In summary, for this case, the singlet exciton state is dark whereas two of the triplet exciton state can emit  $x/y$ -polarized light and one is dark. This finding is schematically illustrated in Fig. 2.8. In the presence of SOC effects, spin is no longer a good quantum number. Therefore, the single-particle states transform according to double groups of  $C_{2v}$  [148]. As described before, the representations in this group is obtained from the direct product of single  $C_{2v}$  group and spin  $D_{1/2}$  group. Accordingly, the IRR labelling of the ground electron ( $A_1 \otimes D_{1/2}$ ) and hole states ( $B_1 \otimes D_{1/2}$ ) will be  $E_{1/2}$  since the  $C_{2v}$  double group has only one IRR. As a consequence, we can determine the symmetry labels of the ground state exciton between  $e_0$  and  $h_0$  using the direct product Table 2.4 as  $E_{1/2} \otimes E_{1/2} = A_1 \oplus B_1 \oplus B_2 \oplus A_2$ . When

FIGURE 2.8: Schematic evolution of excitonic structure for a  $C_{2v}$  exciton without spin orbit coupling in the absence (left) and in the presence (right) of the electron-hole exchange interaction.

Without Exchange	With Exchange
	1x
	-----
	B <sub>1</sub> /B <sub>2</sub> (D <sub>0</sub> ) [Dark]
4x	
-----	
B <sub>1</sub> /B <sub>2</sub> (D <sub>0</sub> ) [Dark] (1x)	
B <sub>1</sub> /B <sub>2</sub> (D <sub>1</sub> ) [Dark] (1x)	
B <sub>1</sub> /B <sub>2</sub> (D <sub>1</sub> ) [Bright,X/Y] (2x)	
	3x
	-----
	B <sub>1</sub> /B <sub>2</sub> (D <sub>1</sub> ) [Dark] (1x)
	B <sub>1</sub> /B <sub>2</sub> (D <sub>1</sub> ) [Bright, X/Y] (2x)

exchange effects are included, all of these states are non-degenerate and therefore, the four exciton ground state could be expected. However, it is to note that the splitting will depend on the system under consideration. Moving to the selection rules, following Table 2.3 we find that  $A_2$  state is dark, and  $B_1$ ,  $B_2$ ,  $A_1$  are polarized along  $x$ ,  $y$  and  $z$  direction respectively. This condition is schematically illustrated in Fig. 2.9. Since two linearly polarized photons ( $x$  and  $y$ ) have unequal energies, we have non-zero bright-bright FSS in a  $C_{2v}$  symmetric ZB QD and this leads to the above discussed effect that polarization entanglement is lost.

FIGURE 2.9: Schematic evolution of excitonic structure for a  $C_{2v}$  exciton with spin orbit coupling in the absence (left) and in the presence (right) of the electron-hole exchange interaction.

Without Exchange	With Exchange
	1x
	-----
	A <sub>1</sub> [Bright,Z]
	1x
4x	
-----	
A <sub>1</sub> [Bright,Z] (1x)	B <sub>1</sub> [Bright,X]
B <sub>1</sub> [Bright,X] (1x)	
B <sub>2</sub> [Bright,Y] (1x)	
A <sub>2</sub> [Dark] (1x)	
	1x
	-----
	B <sub>2</sub> [Bright,Y]
	1x
	-----
	A <sub>2</sub> [Dark]

### III-Nitride QDs

In the next step, we move to the discussion of (0001) WZ QDs. In this case, for an idealized system, the  $C_{6v}$  point group symmetry of a bulk WZ system is reduced to a  $C_{3v}$  symmetry [100, 136]. Similar to the previous case, we start our analysis with the case of neglecting SOC effects. Thus, we can treat the orbital and spin parts separately. Here, electronic states of the orbital part can be described by the  $C_{3v}$  single group representations. For a WZ QD with  $C_{3v}$  symmetry, the symmetry of the electron ground state  $e_0$  is usually of dominant  $s$ -like character [136, 148] and correspondingly transforms as  $A_1$  (cf. Table 2.5). On the other hand, the hole ground state  $h_0$  can be formed by any linear combination of  $p_x$ - and  $p_y$ -like states [136, 148]. Therefore,  $h_0$  state transforms according to  $E$  representation of  $C_{3v}$  single group (cf. Table 2.5). Since  $E$  is a 2-D representation, this state will be a doubly degenerate state. More details on the character of single-particle states for a  $C_{3v}$  QD are presented in the result section. Following Table 2.6, which shows the direct product of different IRRs, the

TABLE 2.5: Character table of  $C_{3v}$  point group.

$C_{3v}$	$E$	$2C_3$	$3\sigma_v$	Basis functions
$A_1$	1	1	1	1, z
$A_2$	1	1	-1	$R_z$
$E$	2	-1	0	(x, y)
$E_{1/2}$	2	1	0	
$^1E_{3/2}$	2	-1	i	
$^2E_{3/2}$	2	-1	-i	

TABLE 2.6: Direct products of representation for a  $C_{3v}$  point group.

$C_{3v}$	$A_1$	$A_2$	$E$	$E_{1/2}$	$^1E_{3/2}$	$^2E_{3/2}$
$A_1$	$A_1$	$A_2$	$E$	$E_{1/2}$	$^1E_{3/2}$	$^2E_{3/2}$
$A_2$		$A_1$	$E$	$E_{1/2}$	$^2E_{3/2}$	$^1E_{3/2}$
$E$			$A_1 \oplus \{A_2\} \oplus E$	$E_{1/2} \oplus ^1E_{3/2} \oplus ^2E_{3/2}$	$E_{1/2}$	$E_{1/2}$
$E_{1/2}$				$A_1 \oplus \{A_2\} \oplus E$	$E$	$E$
$^1E_{3/2}$					$A_2$	$A_1$
$^2E_{3/2}$						$A_2$

orbital part of the exciton states obtained through  $e_0$ - $h_0$  transition transforms as  $A_1 \otimes E = E$ . Here, the corresponding exciton state is doubly degenerate since  $E$  is a 2-D IRR. Coming to the spin components, similar to the  $C_{2v}$  case, the spins of an electron and hole can form a singlet or triplet states. Now, combining orbitals and spin parts together, each of these states will be doubly degenerate due to the  $E$  symmetry arising from the orbital part. In the absence of exchange interaction, the exciton ground state is eight-fold degenerate. When exchange interaction is included in the analysis, we get a two-fold degenerate state stemming from  $E$  symmetry of the orbital part and the 1-D  $D_0$  IRR of the spin part and a six-fold degenerate state stemming from  $E$  symmetry of the orbital part and the 3-D  $D_1$  IRR of the spin part.

Since  $E$  is allowed to emit  $(x, y)$ -polarized light, we find that the two-fold degenerate exciton state is dark while the six-fold degenerate exciton state consists of four bright  $((x, y)$ -polarized) and two dark states. The excitonic structure for a  $C_{3v}$  exciton without SOC is presented in Fig. 2.10. In the next step, we include SOC in the analysis. As stated before, we now have to

FIGURE 2.10: Schematic evolution of excitonic structure for a  $C_{3v}$  exciton without spin orbit coupling in the absence (left) and in the presence (right) of the electron-hole exchange interaction.

Without Exchange	With Exchange
	2x
	-----
	E (D <sub>0</sub> ) [Dark]
8x	
-----	
E (D <sub>0</sub> ) [Dark] (2x)	
E (D <sub>1</sub> ) [Dark] (2x)	
E (D <sub>1</sub> ) [Bright,XY] (4x)	
	6x
	-----
	E (D <sub>1</sub> ) [Dark] (2x)
	E (D <sub>1</sub> ) [Bright, XY] (4x)

deal with the  $C_{3v}$  double group. Following the discussion of the  $C_{2v}$  case, the electron ground state transforms according to  $(A_1 \otimes D_{1/2} = E_{1/2})$  [148]. On the other hand, the hole ground state transforms according to  $E \otimes D_{1/2} = E_{1/2} \oplus E_{3/2}$  [148]. This immediately gives us the result that the doubly degenerate state represented by  $E$  splits into states of  $E_{1/2}$  and  $E_{3/2}$  symmetry in the presence of SOC. Following Table 2.5, we find these states are also doubly degenerate.

FIGURE 2.11: Schematic evolution of excitonic structure for a Type-I  $C_{3v}$  exciton with spin orbit coupling in the absence (left) and in the presence (right) of the electron-hole exchange interaction.

Without Exchange	With Exchange
	2x
	-----
	E [Bright, XY]
4x	
-----	
E [Bright,XY] (2x)	
E [Bright,XY] (2x)	
	2x
	-----
	E [Bright, XY]

Therefore, one can possibly find two types of excitons in the system, namely type-I and type-II depending on the IRR that describes the hole state (e.g.  $E_{1/2}$  and  $E_{3/2}$ ). The excitonic levels

FIGURE 2.12: Schematic evolution of excitonic structure for a Type-II  $C_{3v}$  exciton with spin orbit coupling in the absence (left) and in the presence (right) of the electron-hole exchange interaction.

Without Exchange	With Exchange
	2x
	-----
	E [Bright, XY]
4x	1x
-----	-----
E [Bright,XY] (2x)	A <sub>1</sub> [Bright, Z]
A <sub>1</sub> [Bright,Z] (2x)	
A <sub>2</sub> [Dark] (1x)	
	1x
	-----
	A <sub>2</sub> [Dark]

for a type-I and type-II exciton with SOC are presented in Fig. 2.11 and Fig. 2.12, respectively. As described previously, the symmetry labels of the exciton states are determined by using the direct product representation Table 2.6. For type-I excitons,  $E_{1/2} \otimes E_{3/2} = E \oplus E$ , where  $E$  is a 2-D IRR. Following Table 2.5, we find two doublets of bright exciton states which are polarized along  $(x, y)$  direction, thus perpendicular to  $c(z)$ -axis. If there is no exchange interaction between electron and hole states, this excitonic state is four-fold degenerate. However, when exchange interaction is included, splitting is introduced between the two  $E$ -symmetric states. Going back to the biexciton-exciton cascade, we now have a non-zero bright-bright FSS between two pairs of  $E$  states. However, more importantly, we have also zero bright-bright FSS for each pair of doubly degenerate  $E$  states. Therefore, for each of these pairs, we get back the situation of Fig. 2.7 (a) where due to the degeneracies of the bright  $E$  states both left and right cascades emit circularly polarized light and polarization entanglement is achieved. In this case, each of the doubly degenerate bright states can produce polarization entangled photon pairs.

Moving to type-II excitons, we obtain  $E_{1/2} \otimes E_{1/2} = A_1 \oplus A_2 \oplus E$ . Following Table 2.5, we find an excitonic state transforming according to  $A_1$  can emit a  $z$ -polarized light,  $E$  related exciton states (doubly degenerate) emit  $(x, y)$ -polarized light and the state transforming according to  $A_2$  is dark. Without electron-hole exchange interactions, all of these states are degenerate. When exchange effects are included, we obtain non-zero bright-bright ( $A_1$ - $E$ ) and bright-dark( $A_1$ - $A_2$ ,  $A_2$ - $E$ ) FSSs. However, like the previous case, the doubly degenerate  $(x, y)$  polarized  $E$  states results in zero FSS (bright-bright) and we should find the situation of Fig. 2.7 (a) where polarization entanglement is achieved for a light incident perpendicular to the QD sample.

In summary, we find that through the group theoretical analysis presented above, one can predict the behavior of excitonic fine structure for III-N QD systems. This is extremely useful in the sense that we can benchmark our numerical results against the predicted optical spectra. Symmetry of the underlying crystal structure plays an important role in determining the FSS

in a material system. We conclude that due to differences in the crystal structure of As (ZB) and III-N (WZ) systems, the excitonic fine structure of these systems are entirely different. Therefore, one can not simply carry over the analysis in one material system to the other. We find that in principle, zero bright-bright FSS is possible in case of ideal (0001) WZ QDs having  $C_{3v}$  symmetry whereas such feature is not present in  $C_{2v}$  symmetric (001) ZB QDs. It is also to note that when growing InAs/GaAs QDs on (111) substrates, one is also left with a  $C_{3v}$  symmetry [100]. Recent measurements on (111) grown InGaAs<sub>1- $\delta$</sub> N <sub>$\delta$</sub> /GaAs( $\delta \ll 1$ ) QDs have also revealed vanishing FSS in these systems [149]. Therefore, it is highly attractive to grow dots of  $C_{3v}$  symmetry ((0001) WZ or (111) ZB) for entangled photon emission in contrast to  $C_{2v}$  symmetric (001) ZB systems.

Overall, in this chapter we presented different electronic structure theories such as  $\mathbf{k} \cdot \mathbf{p}$  theory and TB model for the calculation of single-particle energies and wave functions. We then outlined the procedure to incorporate strain and piezoelectricity effects in the models and the ways to evaluate them. Subsequently, we introduced theory for calculation of many-particle properties within the Hartree and CI approach. Special attention was paid to the excitonic fine structure for III-V WZ structures. Having equipped with the theoretical framework, we will now apply all these models to calculate electronic and optical properties of QD systems and that will be the topic of the next section.



## Chapter 3

# Excitonic and biexcitonic properties of nonpolar InGaN/GaN QDs

As stated in the introduction, due to large band offsets, QDs based on group III-N have been demonstrated as single-photon emitters near room temperature [24, 150]. For instance, Holmes and co-workers [24] have demonstrated single-photon emission from GaN/AlGaIn QDs, grown along the crystallographic  $c$ -axis, up to 350 K. However, when discussing the basic properties of III-N WZ systems in Sec. 1.2, we had stressed that when growing nitride-based heterostructures along  $c$ -direction, the optical properties of these systems are significantly affected by the presence of very strong electrostatic built-in fields (order of MV/cm) [51]. The presence of these fields leads to large radiative recombination lifetimes  $\tau$  of the order of several ns [151, 152] and consequently results in single-photon emission with a low repetition rate. Furthermore, using pure GaN QDs produces single-photon emission in the UV spectral regime, while commercial single-photon detectors operate in the blue spectral range [153]. Thus to circumvent these problems, InGaIn/GaN dots grown on nonpolar planes offer in principle the advantage that (i) built-in fields should be strongly reduced compared to  $c$ -plane systems [154], (ii) their electronic and optical properties should be far less affected by extended defects when compared to nonpolar InGaIn/GaN QWs and (iii) by changing the In content in the dot, the emission wavelength can be tuned into the blue spectral region. In terms of entangled photon emission, even though the combined symmetry of QD system and underlying crystal lattice in a nonpolar system prevents using the biexciton-exciton cascade for such an application [155, 156], the time reordering scheme [157] could be applied. In this scheme excitonic and biexcitonic transitions are brought in resonance (“color coincidence”) [158]. Such a situation can potentially be achieved in a nonpolar InGaIn/GaN QD by changes in dot size and shape.

Thus for all these applications, a detailed understanding of the inter-relationship between the QD geometrical features and the electronic and optical properties is required. However, in

comparison to QW systems, far less theoretical studies have focused on the properties of nonpolar InGaN/GaN dots [159–162]. Hong *et al.* [159] focused mainly on the impact of the material parameter choice and the growth plane on the electronic properties of these systems. Initial calculations on excitonic properties have also been performed. Schuh, Barthel and co-workers [161, 162] accounted for excitonic effects in the framework of sophisticated CI calculations, further confirming that Coulomb effects are important for an accurate description of the optical properties of nonpolar systems. However, these calculations [161, 162] have been performed for pure InN/GaN dots, thus the impact of changes in the In content are not investigated. Additionally, both Ref. [159] and Refs. [161, 162] do not study in detail how dot size affect quantities such as radiative lifetime when compared with *c*-plane dots, given its importance for the repetition rate of single-photon emission from these structures. Furthermore, biexcitonic effects are not addressed in Refs. [159, 161, 162], which present an essential ingredient to understand the optical properties of nonpolar InGaN/GaN QDs. Especially with respect to the time reordering scheme [157], it is of central importance to gain initial insights into the combined effect of how changes in In content, dot size and shape impact excitonic and biexcitonic properties of nonpolar InGaN/GaN QDs.

Here, we address these questions by means of a symmetry adapted  $\mathbf{k} \cdot \mathbf{p}$  model (cf. Sec. 2.2.1.1) connected with self-consistent Hartree calculations (cf. Sec. 2.6). The chapter is organized as follows. In the following section, the ingredients of our theoretical framework are described. In Sec. 3.2 available experimental data for nonpolar InGaN/GaN QDs are reviewed and the here assumed model geometries are introduced. Our results are presented in Sec. 3.3. In a first step, in Sec. 3.3.1, we analyze the impact of dot size and shape anisotropies on the built-in potential. This analysis is followed by a study of excitonic and biexcitonic properties, in Sec. 3.3.2. After that, we turn to the calculations of oscillator strength  $f$  and radiative lifetime  $\tau$  in Sec. 3.3.3 where we compare our theoretical data with experiments performed in the group of Prof. R. A. Taylor (University of Oxford, UK) and available literature results. Finally we summarize our results in Sec. 3.4.

## 3.1 Theoretical Framework

In this chapter, the electronic and optical properties of *a*-plane InGaN/GaN QDs have been addressed by means of a continuum based 6+2 band  $\mathbf{k} \cdot \mathbf{p}$  model discussed in detail in Sec. 2.2.1.1. The model has been implemented in the plane wave-based software library S/Phi/nX [126, 163] and a schematic illustration of the numerical implementation is given in Fig. 3.1. The model uses analytic expressions for the stiffness tensor, the piezoelectric and spontaneous polarization vector fields, as a function of the incline angle  $\theta$  to the WZ *c*-axis, which can be derived using the procedure presented in Sec. 2.2.1.1. Here, the strain field is modeled in the framework of continuum elasticity by minimizing the total elastic energy of the whole system with respect to

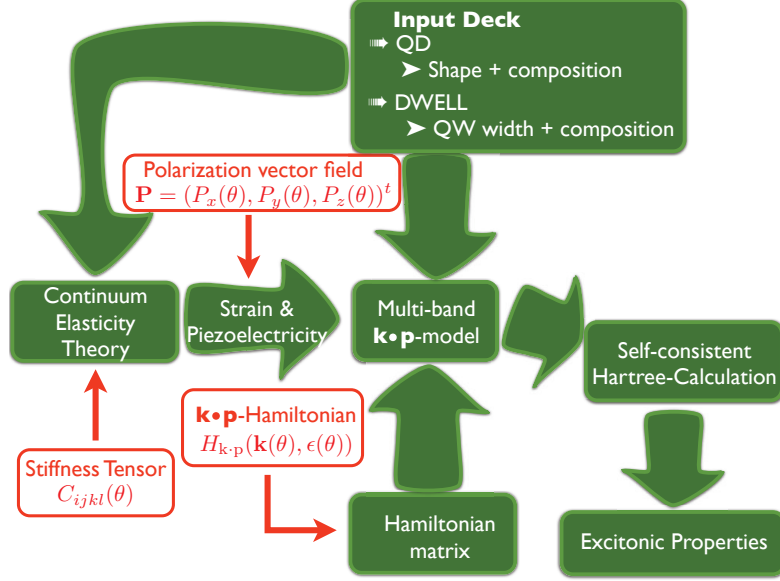


FIGURE 3.1: Schematic illustration of the work-flow in S/Phi/nX [160].

the displacement field as described in Sec. 2.4.2. Moving to the input parameters, it is important to note that there is still a large degree of uncertainty in several key material parameters such as piezoelectric coefficients, band offsets, deformation potentials and especially how these parameters change with composition [36, 160, 164–166]. Even though most material parameter sets predict similar trends for polar and nonpolar growth planes, absolute numbers might depend on the accurate knowledge of the material parameters and could therefore vary between different sets [167]. The material parameters used in this study are summarized in Table B.2 of Appendix B.

The  $\mathbf{k} \cdot \mathbf{p}$  model allows us to evaluate the QD single-particle states. To account for excitonic effects, the  $\mathbf{k} \cdot \mathbf{p}$  model is connected to self-consistent Hartree calculations as detailed in Sec. 2.6. We use here equations outlined in the said section (cf. Eq. (2.73), (2.74), (2.78), (2.79)) to calculate exciton (biexciton) recombination energies,  $E^X$  ( $E^{XX}$ ) and exciton (biexciton) binding energies,  $E_X^b$  ( $E_{XX}^b$ ). Furthermore, we are also interested in the analysis of the radiative lifetime  $\tau$  of nonpolar InGaN/GaN QDs and how this quantity compares to  $c$ -plane systems. In general  $\tau$  can be calculated from [168]

$$\tau = \frac{2\pi\epsilon_0 m_0 c^3 \hbar^2}{n e^2 (E^X)^2 f}, \quad (3.1)$$

where  $\epsilon_0, m_0, c, \hbar$  denote the vacuum permittivity, the free electron mass, the vacuum speed of light and Planck's constant (divided by  $2\pi$ ). Furthermore, to evaluate Eq. (3.1), information about the excitonic recombination energy  $E^X$ , the oscillator strength  $f$  and the refractive index  $n$  of the matrix material is required. To determine  $n$  we apply a Sellmeier type law [169, 170], allowing us to calculate  $n$  as a function of the wavelength  $\lambda$  via  $n(\lambda) = \sqrt{a_n + b_n \lambda^2 / (\lambda^2 - c_n^2)}$

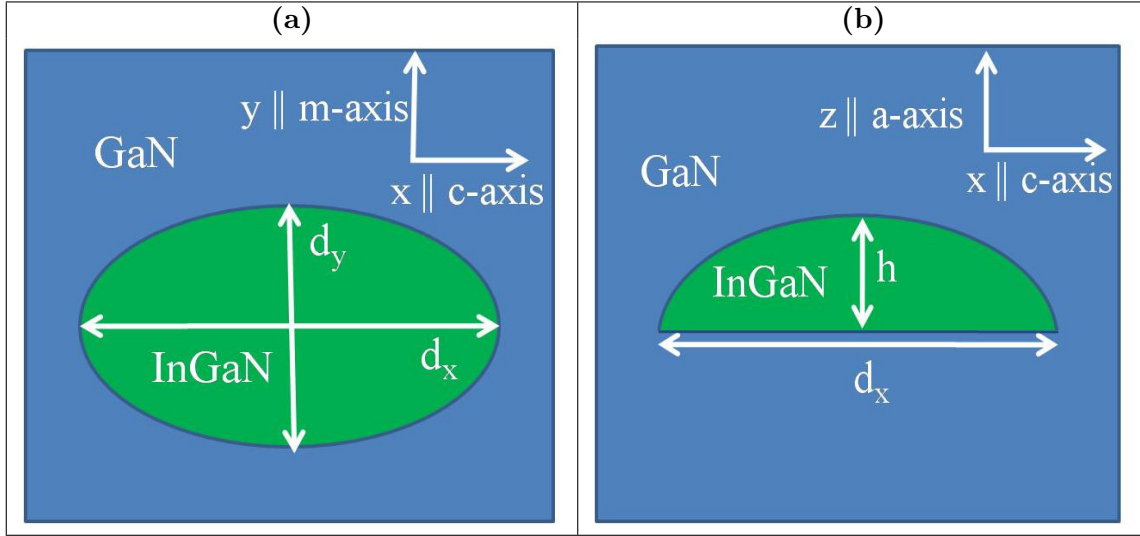


FIGURE 3.2: (a) top-view (b) side-view of the here used lens shaped InGaN/GaN  $a$ -plane dot with the respective co-ordinate system.

with  $a_n = 5.15$  nm,  $b_n = 0.35$  nm and  $c_n = 339.8$  nm. Here,  $\lambda$  is calculated from  $E^X$  using the relation  $\lambda = hc/E^X$ , where  $h$  is Planck's constant. The procedure to calculate  $E^X$  has already been described earlier (cf. Eq. (2.73)). Equipped with the knowledge about  $E^X$  and the ground state electron  $\psi_e$  and hole  $\psi_h$  wave functions, the oscillator strength  $f$  is calculated via [168]

$$f = \frac{2\hbar^2}{m_0 E^X} \sum_{\alpha} \left| \int \psi_e^*(\mathbf{r}) (\mathbf{a} \cdot \mathbf{k}) \psi_h^{\alpha}(\mathbf{r}) d^3\mathbf{r} \right|^2. \quad (3.2)$$

Here,  $\mathbf{a}$  is the light polarization vector of the incident light and  $\mathbf{k} = -i\nabla$ .  $\alpha$  denotes hole wave functions representing the same degenerate hole energy level  $E_h^X$ . Making use of the fact that electron and hole wave functions can be casted as linear combinations of the product of Bloch functions  $|u_i\rangle$  and envelope functions  $|\phi_i\rangle$ ,  $\psi = \sum_i |u_i\rangle |\phi_i\rangle$ , the integral can be expressed in terms of the Kane matrix element  $E_P$  and is proportional to  $\langle s|k_i|p_j\rangle = \delta_{i,j} \sqrt{\frac{m_0 E_P}{2\hbar^2}}$ . In the following we have used  $E_P = (2E_{P\parallel} + E_{P\perp})/3$  [151], and the values for  $E_{P\parallel}$  and  $E_{P\perp}$  have been taken from Refs. [36, 171]. The light polarization vector  $\mathbf{a}$  is always chosen to be perpendicular to the sample surface ( $\mathbf{a} = \frac{1}{2}(1, 1, 0)^T$ ).

Having briefly summarized the theoretical framework, the QD geometry and size is required as further input to the model. Thus we review in the following section the available literature data for nonpolar InGaN/GaN QDs and discuss the model geometry assumed in our theoretical study.

### 3.2 Nonpolar InGaN/GaN quantum dot geometries

The electronic and optical properties of a QD system crucially depend on the geometrical features of the dot [172]. Experimentally it presents an extremely challenging task to obtain detailed information on these quantities, especially after the dots are capped [173, 174]. An additional complication for the here studied nonpolar *a*-plane InGaN/GaN QDs is the growth of these systems in general. Only recently, these structures have successfully been grown [175]. Atomic force microscopy (AFM) studies of uncapped *a*-plane InGaN dots have revealed structures with a height of  $7 \pm 3$  nm [14]. Typical base diameters in the case of nonpolar GaN/AlGaIn QDs are of the order 20 nm-30 nm [176]. Previous theoretical works on nonpolar InGaN/GaN QDs have assumed lens-shaped geometries [161, 162]. It should be noted that usually after capping of these structures the dot dimensions are reduced [173], and consequently in-plane (base length/base diameter) and out-of growth plane (height of the dot) features are not well known. To account for this we proceed in the following way.

In our calculations, we have two different scenarios. For both of these steps, our starting point is a lens-shaped dot. In the first set of calculations presented in Sec. 3.3.1 and Sec. 3.3.2, we are mainly interested in how changes in In content, different dot parameters (shape, size) affect built-in potential, exciton and biexciton properties of nonpolar dots and how these properties can be tuned in an aim to achieve entangled photon emission via the time-reordering scheme. Therefore, here we assume that both the height as well as the in-plane dimensions of this dot structure can vary. As a result, the height is varied between 2 and 5 nm and the base diameter between 30 and 5 nm. To be sensitive to changes in the in-plane symmetry, we keep one axis,  $d_x$ , fixed at 30 nm and the perpendicular direction,  $d_y$ , is varied between 30 nm and 5 nm. Thus the base of the QD can either be circular symmetric ( $d_x = d_y = 30$  nm) or highly elliptic ( $d_x = 30$  nm;  $d_y = 5$  nm). To measure this asymmetry by one parameter, we introduce the *in-plane aspect ratio*  $\alpha$ , defined as  $\alpha = d_x/d_y$ . Thus,  $\alpha$  varies between 1 and 6. Furthermore, as we will show later, our calculations show that such a deformation of the dot gives trends in the biexciton binding energies  $E_{XX}^b$  that are in good agreement with experimental data [177]. To account for changes in In content, the In content is varied between 15% to 25%.

However, in the next set of calculations presented in Sec. 3.3.3 we are mainly interested in the general trends of the oscillator strength  $f$  and as a result the radiative lifetime  $\tau$  in these nonpolar dots and how these quantities compare with *c*-plane dots. To study the impact of dot size on the results, we assume here two different cases. First, the diameter ( $d_x = d_y$ ) of the nanostructure is varied between 6 nm and 24 nm, while keeping the dot height  $h$  constant at 2.5 nm. Second, the diameter ( $d_x = d_y$ ) is kept fixed at 24 nm and  $h$  is now allowed to vary between 2 nm and 5 nm. It is to note that in this set of calculations, we assume only symmetric dots having  $\alpha = 1$  and denote the diameter as  $d$  ( $d_x = d_y$ ). The change in the in-plane aspect ratio  $\alpha$  might affect the result as well, but we are mostly interested in how changes

in the dot volume affect the general trends in  $\tau$  values, which is effectively captured by the above discussed assumptions. In this case, to investigate how the growth plane affects  $\tau$ , all geometric QD features are carried over to calculations for  $c$ -plane dots. Thus when we compare  $c$ - and  $a$ -plane InGaN/GaN QDs in our theoretical studies, changes in the calculated quantities arise entirely from the difference in the growth plane and not due to variations in QD geometry. It should be noted that even though we carry over geometries and sizes based on assumptions for nonpolar InGaN dots to describe  $c$ -plane systems, these assumptions, especially for the dot size, should give a good first approximation of realistic  $c$ -plane QDs [178]. With respect to the In content, we have chosen a value of 15% in this set of calculations. We will discuss the impact of the In content on the results in more detail when we compare our results with experiment in Sec. 3.3.3.

In our coordinate system the  $z$ -axis has been chosen to be parallel to the  $a$ -axis (growth direction), while the  $x$ -axis is parallel to the  $c$ -axis. The  $y$ -axis is aligned along the  $m$ -axis. A schematic illustration of top and side-view of the assumed geometry is given in Fig. 3.2. Regarding the numerical aspects of the study, all calculations have been performed on a supercell with dimension  $50 \times 50 \times 30 \text{ nm}^3$ , using periodic boundary conditions. For efficient calculations, a step size of 0.25 nm and 0.5 nm are employed along growth and in-plane direction, respectively. This accounts for the fact that the minimum dot height is only 2 nm while the base diameter is at least 5 nm.

### 3.3 Results

Having introduced the theoretical framework and the QD model geometry, we here present the results of our calculations. We start in Sec. 3.3.1 with a detailed analysis of the electrostatic built-in potential of nonpolar InGaN/GaN QDs. Excitonic and biexcitonic properties are discussed in Sec. 3.3.2. Finally, in Sec. 3.3.3 we evaluate radiative lifetime values and compare our theoretical results with experimental data from Prof. R. A. Taylor's group (University of Oxford, UK) on nonpolar InGaN/GaN QDs and also the literature.

#### 3.3.1 Built-in potential

The aim of this section is to provide a detailed analysis of the built-in potential in lens-shaped nonpolar InGaN/GaN dots. Special attention is paid to the impact of the dot shape and size on the results.

In a first step we focus our attention on a lens-shaped dot with a circular base ( $d_x = d_y = 30 \text{ nm}$ ) and a height of  $h = 2.5 \text{ nm}$ . The In content is 25%. To gain insight into the benefit of using nonpolar InGaN/GaN dots in terms of the built-in potential, we compare the total (spontaneous

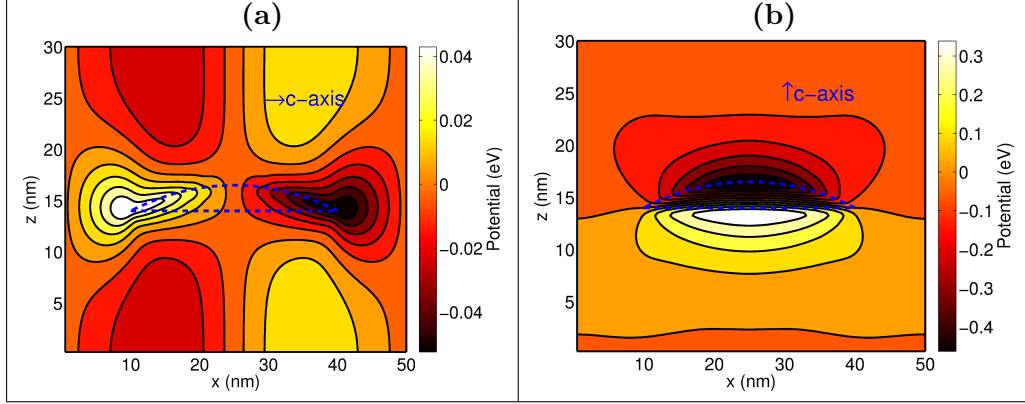


FIGURE 3.3: Contour plot of total (spontaneous + piezoelectric) built-in potential for a cut through the centre of a lens shaped  $\text{In}_{0.25}\text{Ga}_{0.75}\text{N}/\text{GaN}$  QD grown along the (a)  $a$ -axis and (b)  $c$ -axis.

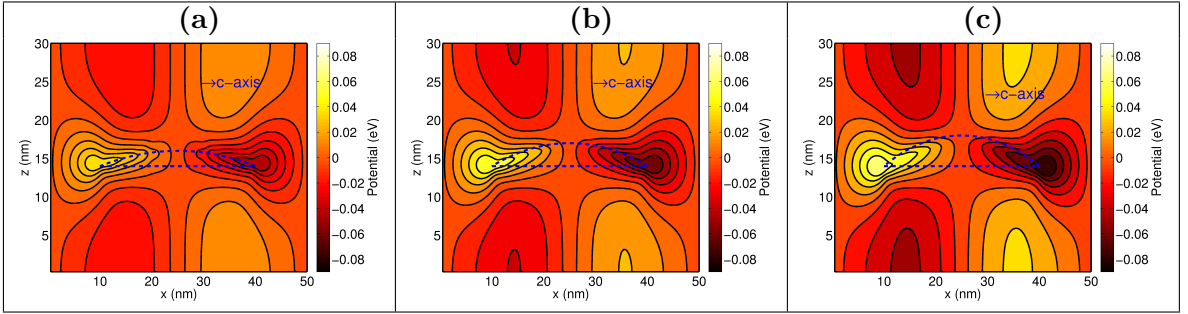


FIGURE 3.4: Contour plot of the total (spontaneous + piezoelectric) built-in potential for a slice through the centre of the lens shaped  $\text{In}_{0.25}\text{Ga}_{0.75}\text{N}/\text{GaN}$   $a$ -plane dot with  $d_x = 30$  nm and  $d_y = 30$  nm in the  $x$ - $z$  plane. The results are shown for (a) height  $h = 2$  nm, (b) height  $h = 3$  nm and (c) height  $h = 4$  nm.

+ piezoelectric) built-in potential of the nonpolar dot with the built-in potential of an identical  $c$ -plane dot. Using the same QD geometry allows us to flesh out effects originating entirely from the change in the growth plane. The results are displayed in Fig. 3.3 for a slice through the centre of the dot in the  $x - z$  plane. Note that in the  $c$ -plane system the  $c$ -axis is parallel to the  $z$ -axis, while in the nonpolar case the  $c$ -axis is parallel to the  $x$ -axis. One can infer from Fig. 3.3 that the built-in potential of the here studied  $a$ -plane  $\text{InGaN}$  dot is significantly reduced compared to its  $c$ -plane counterpart (note the different potential scales). However, it should be noted that the nonpolar system is *not* field free. This originates from the fact that the nonpolar QD is a three-dimensional object and thus still exhibits  $c$ -axis oriented facets. This finding is consistent with the results obtained by different groups [154, 161, 162]. Given that we are still left with facets oriented along the  $c$ -axis, the magnitude and the profile of the built-in potential will change with changes in the QD geometrical features. Depending how strongly the built-in potential varies with changes in the dot geometry, electronic and optical properties might or might not be strongly affected by the built-in field. Thus, before turning to the analysis of the excitonic and biexcitonic properties, we establish here how the built-in potential changes with changes in the dot geometry.

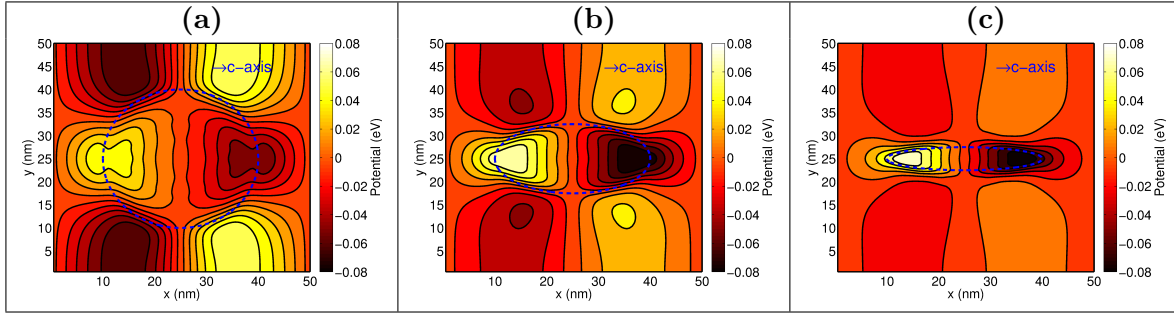


FIGURE 3.5: Contour plot of the total (spontaneous + piezoelectric) built-in potential for a slice through the lens shaped  $\text{In}_{0.25}\text{Ga}_{0.75}\text{N}/\text{GaN}$   $a$ -plane QD at  $z = 1.25$  nm. The height of the dot is  $h = 2.5$  nm and the in-plane aspect ratio  $\alpha$  is (a)  $\alpha = 1$ , (b)  $\alpha = 2$  and (c)  $\alpha = 6$ .

In a first step we study the impact of the QD height on the built-in potential. For this investigation we use a circular symmetric base ( $d_x = d_y = 30$  nm). Figure 3.4 shows a slice through the centre of the nonpolar  $\text{In}_{0.25}\text{Ga}_{0.75}\text{N}/\text{GaN}$  dot in the  $x - z$  plane for a QD height of (a)  $h = 2$  nm, (b)  $h = 3$  nm and (c)  $h = 4$  nm. As one can see, with increasing QD height the magnitude of the built-in potential increases since the surface area oriented along the  $c$ -axis increases. Consequently, the spatial separation between the electron and hole wave functions should be affected by this effect. We will come back to consequences of the QD height on the electronic and excitonic properties in the following sections.

In a second step we analyze the impact of the in-plane aspect ratio  $\alpha$  on the built-in potential profile and magnitude. In Fig. 3.5 the built-potential profile in the  $x - y$  plane for a dot with height of  $h = 2.5$  nm is presented for different values of  $\alpha$ , namely (a)  $\alpha = 1$ , (b)  $\alpha = 2$  and (c)  $\alpha = 6$ . The slice shown here is at 1.25 nm above the base of the QD. Several interesting features can be inferred from Fig. 3.5. When comparing the  $\alpha = 1$  case, Fig. 3.5 (a), with the situation where  $\alpha = 2$ , Fig. 3.5 (b), we observe that the magnitude of the built-in potential increases with increasing  $\alpha$ . However, when increasing  $\alpha$  further, see Fig. 3.5 (b) and (c), this increase is less pronounced. Additionally, when comparing Fig. 3.5 (a) and (b), we find that not only the magnitude of the built-in potential is affected but also the positions of the maxima and minima values. While in the  $\alpha = 1$  case the extrema of the potential are located mainly *outside* the dot, the maxima and minima are located *inside* the QD for  $\alpha = 2$ . Thus, not only does the built-in potential increase when changing from  $\alpha = 1$  to  $\alpha = 2$ , the wave functions will also be even more strongly exposed to the deeper potential energy pockets introduced by the built-in potential. To shed more light on the behavior of the potential magnitude and the profile when changing  $\alpha$  from 1 to 2, we have decomposed the total built-in potential into its different components. Figure 3.6 shows line-scans through the QD along the  $x$ -axis ( $c$ -axis) at  $z = 1.25$  nm and  $y = 25$  nm. The QD interfaces are indicated by vertical lines. Figure 3.6(a) depicts the total built-in potential for the chosen line-scan and reflects the data shown in Fig. 3.5. The red circles correspond to  $\alpha = 1$  while the black squares depict the data for  $\alpha = 2$ . As discussed above, with increasing  $\alpha$  the magnitude of the built-in potential is increased and as

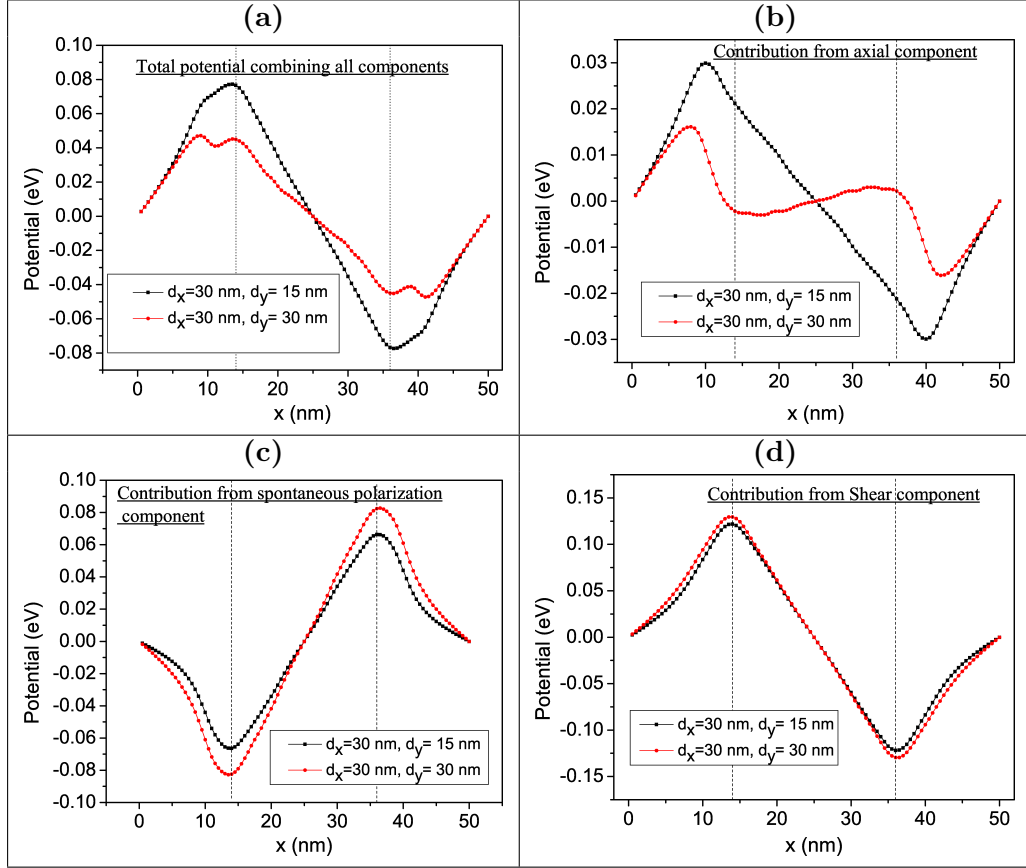


FIGURE 3.6: Built-in potential of a lens shaped  $\text{In}_{0.25}\text{Ga}_{0.75}\text{N}/\text{GaN}$  dot for a line scan at  $y = 25$  nm and  $z = 1.25$  nm above the dot base along  $x$ -axis for  $\alpha = 1$  (red circles) and  $\alpha = 2$  (black squares). The total (spontaneous + piezoelectric) potential  $\phi^{total}$  is displayed in (a) while (b) shows the axial contribution  $\phi_{ax}$  ( $e_{15} = P_{sp} = 0$ ,  $e_{31} \neq 0$ ,  $e_{33} \neq 0$ ). The contribution  $\phi_{sp}$  arising entirely from the spontaneous polarization ( $e_{15} = 0$ ,  $P_{sp} \neq 0$ ,  $e_{31} = 0$ ,  $e_{33} = 0$ ) is shown in (c) and (d) depicts the shear strain related part  $\phi_{e_{15}}$  ( $e_{15} \neq 0$ ,  $P_{sp} = 0$ ,  $e_{31} = 0$ ,  $e_{33} = 0$ ).

well as the potential extrema are shifted. To decompose the total built-in potential into its different components, we start with the axial contribution  $\phi_{ax}$ . In this case we have set the shear strain related piezoelectric coefficient  $e_{15}$  and the spontaneous polarization  $P_{sp}$  to zero so that only  $e_{31}$  and  $e_{33}$  contribute to the built-in potential. The axial contribution  $\phi_{ax}$  is shown in Fig. 3.6 (b), revealing that there is a significant difference in  $\phi_{ax}$  when changing  $\alpha$ . Compared to  $\alpha = 1$ ,  $\phi_{ax}$  is strongly increased in the  $\alpha = 2$  case. Additionally,  $\phi_{ax}$  for  $\alpha = 1$  is significantly reduced *inside* the QD when compared to  $\alpha = 2$  case. We attribute this to changes in the strain tensor components  $\varepsilon_{xx}$  and  $\varepsilon_{yy}$ . In a second step we turn to contributions arising from the spontaneous polarization only ( $e_{33} = e_{31} = e_{15} = 0$ ), which we denote by  $\phi_{sp}$ . The data are shown in Fig. 3.6 (c). In the case of  $\phi_{sp}$ , the absolute numbers are smaller for  $\alpha = 2$  when contrasted with the data for  $\alpha = 1$ . However, it should be noted that  $\phi_{sp}$  is opposite in sign to  $\phi_{ax}$ . Finally we look at the shear strain related contribution  $\phi_{e_{15}}$  ( $P_{sp} = e_{33} = e_{31} = 0$ ), which is shown in Fig. 3.6 (d) for the two  $\alpha$  values. In comparison with the spontaneous part  $\phi_{sp}$ ,  $\phi_{e_{15}}$  is again opposite in sign but comparable in magnitude. Thus large parts of  $\phi_{e_{15}}$  and

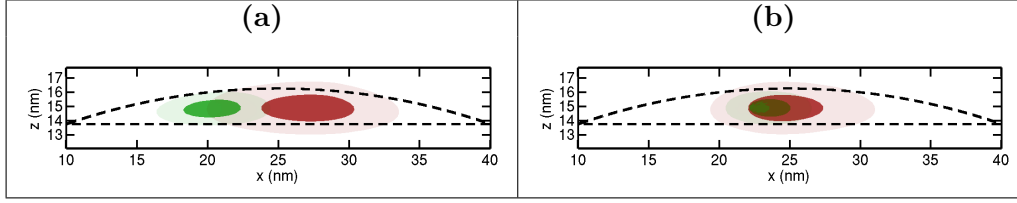


FIGURE 3.7: Isosurface plots of the electron (red) and hole (green) ground state charge densities (a) without and (b) with Coulomb effects included in the calculations. The light (dark) isosurface corresponds to 5% (50%) of the maximum value.

$\phi_{sp}$  might cancel each other.

Overall this analysis shows that the built-in potential in a nonpolar InGa<sub>N</sub>/Ga<sub>N</sub> dot is very sensitive to the actual geometry and one is left with a complicated interplay of different components as indicated above. Having discussed that the residual built-in field depends strongly on the QD geometry, we now turn to study its impact on the excitonic properties of the system.

### 3.3.2 Excitonic and biexcitonic properties

Equipped with the knowledge about the changes in the built-in potential when the structural properties of the lens-shaped nonpolar InGa<sub>N</sub>/Ga<sub>N</sub> QD change, we focus our attention in a first step on the excitonic properties of these structures. Before looking at the excitonic recombination and binding energies, we start with the analysis of the combined effect of attractive Coulomb interaction and built-in potential. In Fig. 3.7 (a) isosurface plots of the single-particle (no Coulomb effect included) electron  $\psi_e^0$  (red) and hole  $\psi_h^0$  (green) ground state charge densities are displayed. The light (dark) isosurfaces correspond to 5% (50%) of the maximum values. The results are shown for the nonpolar In<sub>0.25</sub>Ga<sub>0.75</sub>N/GaN dot with  $d_x = d_y = 30$  nm and  $h = 2.5$  nm. When looking at Fig. 3.7 (a), one observes that the charge densities are slightly spatially separated along the  $x$ -direction ( $c$ -axis). This behavior can be attributed to the presence of the residual built-in potential discussed in the previous section and shown in Fig. 3.3 (a). When including the attractive Coulomb interaction in the calculation, we find that this effect overcomes the spatial separation of the charge carriers due to the residual built-in field, as shown in Fig. 3.7 (b). It should be noted that this compensation of the built-in field due to the Coulomb effect is in strong contrast to  $c$ -plane systems, where the electronic and optical properties are dominated by the built-in field. Coulomb effects, in terms of the wave function overlap, are therefore of secondary importance in  $c$ -plane dots [141, 179]. Consequently, our calculations predict much smaller radiative lifetimes in  $a$ -plane QDs when compared to  $c$ -plane counterparts, due to the larger wave function overlap in the  $a$ -plane systems. More details on the comparison of radiative lifetimes in  $c$ - and  $a$ -plane QDs is presented in Sec. 3.3.3.

Having discussed the impact of the Coulomb interaction on the wave function overlap, we study now its effect on the emission energy. Here we compare the single-particle ground state

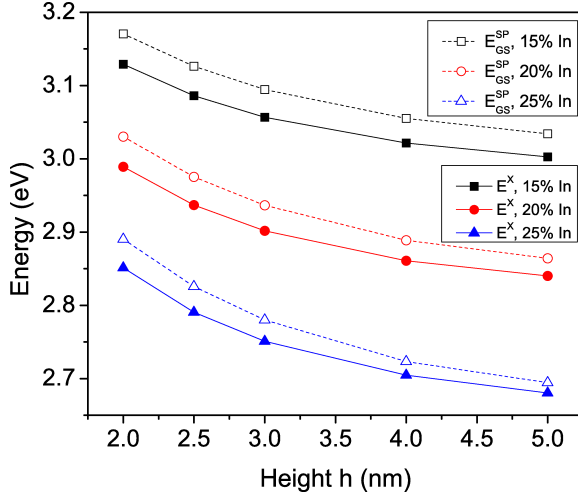


FIGURE 3.8: Single-particle ground state transition energy  $E_{GS}^{SP}$  and the exciton recombination energy  $E^X$  as a function of the QD height  $h$  and for different In concentrations.

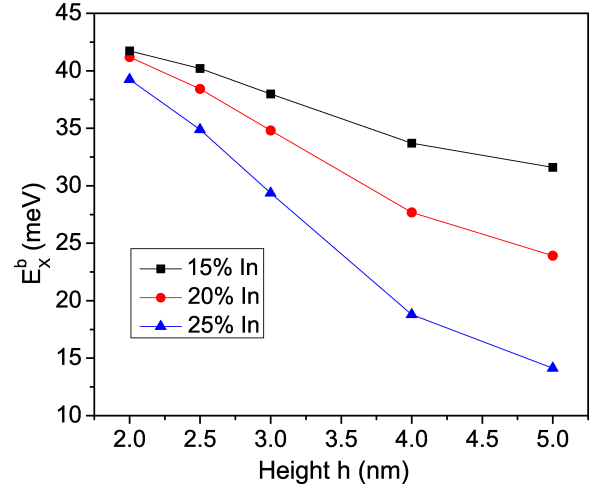


FIGURE 3.9: Exciton binding energy  $E_X^b$  as a function of the QD height  $h$  and for different In concentrations.

transition energy,  $E_{GS}^{SP} = E_e - E_h$  (no Coulomb effects) with the excitonic recombination energy  $E^X$ , given by Eq. (2.73). The results are depicted in Fig. 3.8 as a function of the dot height  $h$ . In general we find that  $E^X$  is shifted to lower energies when compared to  $E_{GS}^{SP}$ . This effect arises from the attractive Coulomb interaction between electron and hole. Looking at the impact of the dot height  $h$  on the recombination energies in more detail, we find that the impact of the Coulomb interaction between the carriers is more pronounced for smaller dot heights ( $h = 2$  nm) when compared to the taller dots ( $h = 4 - 5$  nm). This behavior is also reflected in the exciton binding energies  $E_X^b$ , which is displayed in Fig. 3.9 as a function of the dot height  $h$  and can be attributed to changes in the built-in potential. As discussed in Sec. 3.3.1, with increasing dot height the magnitude of the built-in potential increases and consequently the spatial separation of the electron and hole ground state wave functions. This leads then to a reduction of the Coulomb matrix element  $|J_{eh}|$  and thus to reduced excitonic binding energies. With increasing In content the effect becomes more pronounced since the strain dependent piezoelectric contribution is increased. Consequently, even though the built-in potential is strongly reduced in a nonpolar InGaN/GaN QD when compared to the polar system, changes in built-in potential due to changes in the structural properties can affect the optical properties significantly. For instance, in the 25% In case (blue triangles), the exciton binding energy  $E_X^b$  drops by approximately a factor of two when going from  $h = 2$  nm to  $h = 4$  nm (cf. Fig. 3.9).

We now turn to study in a second step the impact of the in-plane aspect ratio  $\alpha$  on the emission energy. Figure 3.10 displays  $E_{GS}^{SP}$  and  $E^X$  as a function of  $\alpha$ . The results are shown for In contents of 15%, 20% and 25%, respectively. Here all calculations have been performed for a dot height of  $h = 2.5$  nm. When increasing  $\alpha$ , we find an increase in both  $E_{GS}^{SP}$  and  $E^X$ . This

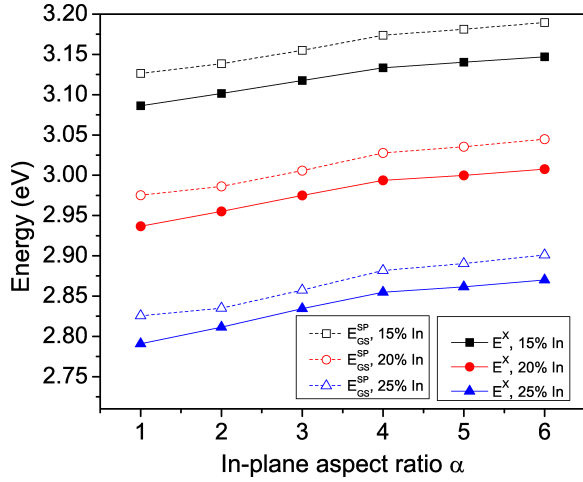


FIGURE 3.10: Ground state single-particle transition energy  $E_{GS}^{SP}$  and exciton recombination energy  $E_X^b$  as a function of the in-plane aspect ratio  $\alpha$  and for different In concentrations.

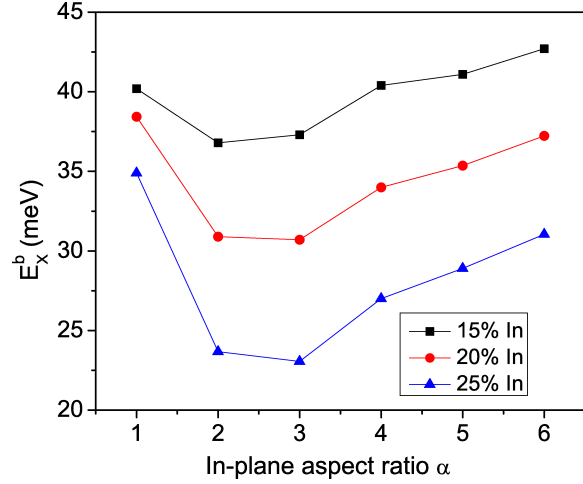


FIGURE 3.11: Excitonic binding energy  $E_X^b$  as a function of the in-plane aspect ratio  $\alpha$  and for different In concentrations.

results from the fact that with increasing  $\alpha$  the volume of the QD is reduced and therefore the band gap is increased. To shed more light on the impact of  $\alpha$  on the excitonic properties, we investigated also the excitonic binding energy  $E_X^b$  as a function of  $\alpha$ . The results are displayed in Fig. 3.11. When looking at  $E_X^b$  as a function of  $\alpha$ , we observe here an unusual behavior, with  $E_X^b$  decreasing first before it increases. From a naive QW picture one could have expected that with decreasing dot volume, the electron and hole wave function overlap should initially increase before it starts to decrease since wave functions leak into the barrier material. With increasing (decreasing) wave function overlap the  $E_X^b$  should increase (decrease). Thus one could have expected that  $E_X^b$  increases first with increasing  $\alpha$  before it starts to decrease when  $\alpha$  is further increased. This trend is also normally observed in QW structures [180–182]. However, here we observe the opposite. For instance, in the 25% In case (blue triangles)  $E_X^b$  drops by more than 10 meV when changing  $\alpha$  from 1 to 2. Additionally, when looking at the results in more detail, the initial drop in  $E_X^b$  is more pronounced for higher In contents, suggesting that the built-in field is responsible for this unusual trend. We have already discussed in Sec. 3.3.1 that the built-in potential of the dot changes with changes in  $\alpha$ . To shed more light onto the behavior of a first decreasing and then increasing  $E_X^b$  with increasing  $\alpha$ , we have performed an additional calculation for 25% In in which we neglect the built-in potential. The results of this analysis are depicted in Fig. 3.12 and reveals that indeed the residual built-in field significantly modifies  $E_X^b$ . In absence of the field (red circles),  $E_X^b$  increases with increasing  $\alpha$  as one would have expected from the nonpolar QW analysis discussed above.

So far we have discussed only excitonic properties of nonpolar InGa<sub>N</sub>/Ga<sub>N</sub> QDs. For a detailed understanding of the optical properties of these systems, biexcitonic features are also of interest. Especially with respect to applications targeting entangled photon emission via the

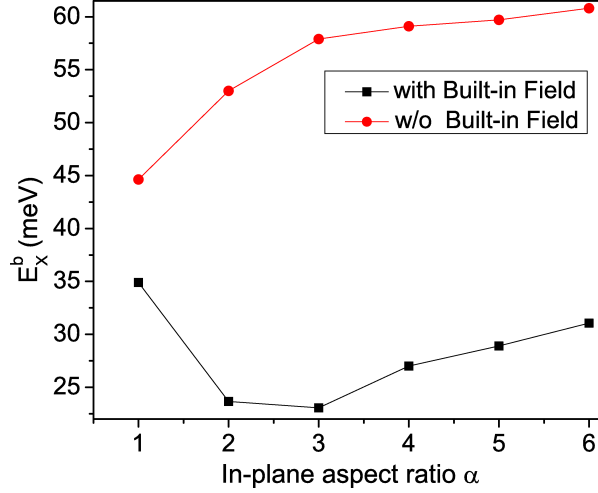


FIGURE 3.12: Excitonic binding energy  $E_X^b$  as a function of in-plane aspect ratio  $\alpha$ . The calculations have been performed in the presence (black squares) and the the absence (red circles) of the built-in field. An In content of 25% has been assumed.

time reordering scheme [157] this question is of interest. Therefore we study in the following sections the impact of the QD geometry on the biexcitonic recombination  $E^{XX}$  and binding energy  $E_{XX}^b$ . We start with  $E^{XX}$  and turn to  $E_{XX}^b$  in Sec. 3.3.2 where we compare this quantity with available experimental data.

To understand the impact of the QD shape on the biexcitonic properties we have analyzed  $E^{XX}$  both as a function of the dot height  $h$  (cf. Fig. 3.13) and the in-plane aspect ratio  $\alpha$  (cf. Fig. 3.14). In general we find similar trends as in the excitonic recombination energy  $E^X$  shown in Figs. 3.8 and 3.10, respectively. For instance, similarly to Fig. 3.8 for the excitonic recombination energy  $E^X$ ,  $E^{XX}$  decreases with increasing height  $h$ . Also,  $E^{XX}$  increases with increasing  $\alpha$ , again similar to  $E^X$  (cf. Fig. 3.10).

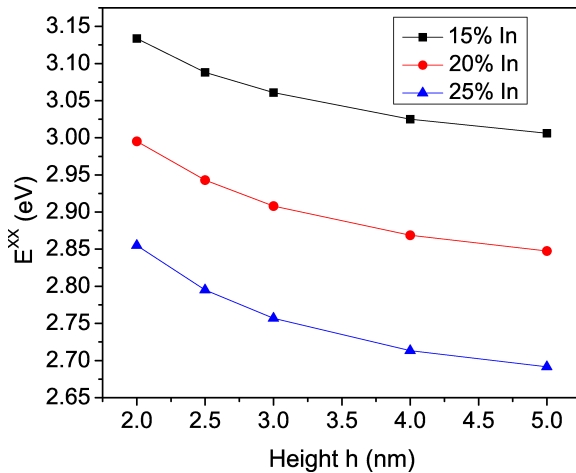


FIGURE 3.13: Variation of biexcitonic recombination energy  $E^{XX}$  as a function of dot height  $h$ . The results are displayed for different In concentrations.

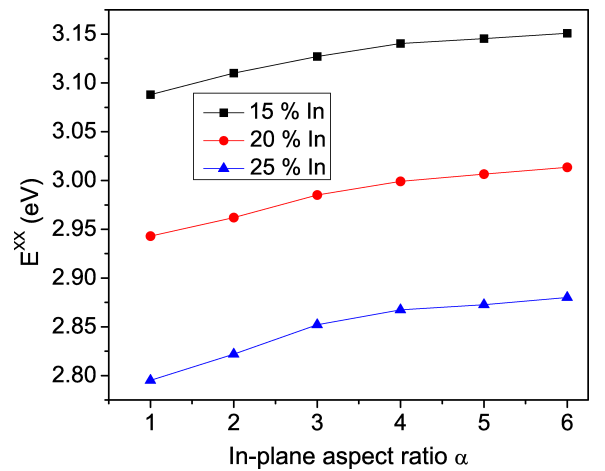


FIGURE 3.14: Biexcitonic recombination energy  $E^{XX}$  as a function of in-plane aspect ratio  $\alpha$  and for different In concentrations.

The analysis of the biexciton binding energy  $E_{XX}^b$  and how it changes with QD geometry is presented in the following section. Here we also compare our theoretical results with available experimental data.

### Comparison with experimental data

In this section, we relate our theoretical results to available experimental literature data. J.T. Griffiths *et al.* [67] presented an experimental study of photoluminescence and cathodoluminescence characteristics of *a*-plane InGaN/GaN QDs. The experimentally reported recombination energies for these structures range from 2.63 to 2.72 eV. For 25% In, our theoretically predicted  $E^X$  values are close to 2.7 eV, cf. Fig. 3.8. This indicates that the here chosen dot geometries and higher In contents give a reasonable first approximation of these structures, given that almost no detailed experimental information on their shape and size is available.

Furthermore, B. P. L. Reid and co-authors [177] have measured the biexcitonic binding energies  $E_{XX}^b$  of these dots. Their experimental studies showed an anti-binding biexciton with  $E_{XX}^b \approx -36$  meV. As discussed above, to calculate  $E_{XX}^b$  very accurately, one would have to go beyond the here used self-consistent Hartree calculations, since this approach neglects exchange and correlation effects [183]. However, since we are interested in general trends and effects caused by changes in the QD geometry, the applied approach should be sufficient to address these questions. Moreover, it is important to note that the experimentally obtained  $E_{XX}^b$  is quite large, indicating that the direct Coulomb interaction between the carriers should dominate over exchange and correlations effects [140].

In general we find that for the chosen dot geometries and the higher the In content, the better the agreement with the experimentally reported exciton recombination energies. Thus, to compare our data with experimental data, we have focused in the following on dots with 25% In. We study here again how geometrical dot features affect  $E_{XX}^b$ . In the first step, we analyze the impact of the dot height  $h$  on  $E_{XX}^b$ . The results are shown in Fig. 3.15. One can infer that  $E_{XX}^b$  decreases with increasing height  $h$ . We attribute this behavior to the fact that with increasing height  $h$  the built-in field inside the dot increases (cf. Sec. 3.3.1) leading to a stronger confinement of the charge carriers at the QD interfaces and thus the electron and hole wave function overlap will be decreased. Overall this will give rise to a reduction in the magnitude of the attractive Coulomb interaction  $J_{eh}$  while the repulsive contributions  $J_{ee}$  and  $J_{hh}$  both increase. This effect is consistent with previous theoretical studies of *c*-plane InGaN/GaN QDs [141]. The combination of these factors leads to the observed decrease in  $E_{XX}^b$ .

So far we have assumed a circular base, and thus  $\alpha = 1$ . We turn now to study the impact of the in-plane aspect ratio  $\alpha$  on  $E_{XX}^b$ . Figure 3.16 presents the results of this analysis. In

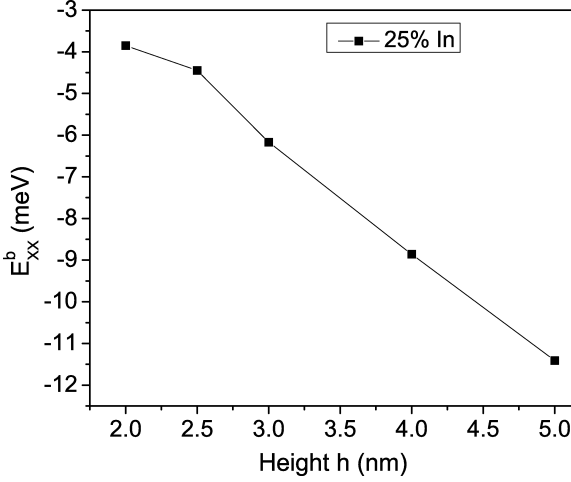


FIGURE 3.15: Biexcitonic binding energy  $E_{XX}^b$  as a function of the dot height  $h$ . The In content is 25%.

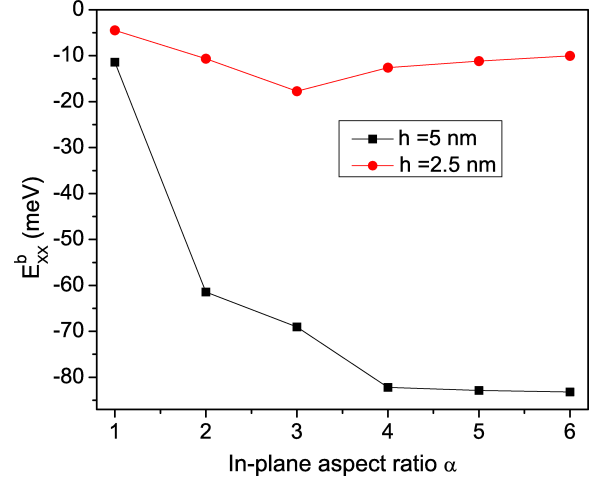


FIGURE 3.16: Biexcitonic binding energy  $E_{XX}^b$  as a function of the in-plane aspect ratio  $\alpha$  for an In content of 25%.

the first step we focus on the results for  $h = 2.5$  nm (red circles). The data shows that  $\alpha$  can slightly modify the value of  $E_{XX}^b$ . For instance when  $\alpha$  changes from 1 to 3,  $E_{XX}^b$  drops by approximately 10 meV. It should be noted that this probably is the upper limit for the drop in  $E_{XX}^b$  since exchange and correlation effects will increase  $E_{XX}^b$  and one might be left with the situation of a binding ( $E_{XX}^b > 0$ ) biexciton, especially for  $\alpha = 1$ . Similarly to  $E_X^b$ , we observe here that with increasing  $\alpha$ ,  $E_{XX}^b$  decreases first and then starts to increase before attaining a constant value. We attribute this behavior to the changes in built-in field discussed in Sec. 3.3.1 and 3.3.2. Even though we cannot predict the transition between binding and anti-binding biexciton, our calculations show that small nonpolar InGaN/GaN QDs are promising candidates to achieve a degeneracy of excitonic and biexcitonic transitions (“color coincidence”). As discussed above, this is a prerequisite for entangled photon emission from these structures via the time reordering scheme.

On the other hand, the theoretically predicted minimum biexciton binding energy  $E_{XX}^b$  for  $h = 2.5$  nm and an In content of 25% is -18 meV for  $\alpha = 3$ , which is much smaller in magnitude than the experimentally reported value in Ref. [177] (-36 meV). Thus, to analyze trends in  $E_{XX}^b$  that would result in values close to the experimentally measured value, we have increased the QD height  $h$  to  $h = 5$  nm. The results are shown in Fig. 3.16 (black squares) and it is found that  $E_{XX}^b$  decreases from -12 meV to -62 meV when  $\alpha$  changes from 1 to 2. Again we attribute this behavior to the increase in the built-in potential for  $h = 5$  nm when compared to  $h = 2.5$  nm.  $E_{XX}^b$  continues to decrease till  $\alpha = 4$  before attaining a constant value (For  $\alpha = 6$ ,  $E_{XX}^b \approx -82$  meV). This analysis reveals that the QD geometry, as expected, has significant impact on  $E_{XX}^b$ , indicating that further combined experimental and theoretical studies are required to shed more light on the geometrical dot features. Nevertheless, the here presented study gives already first insights into the dependence of  $E_{XX}^b$  on dot size and shape.

Having investigated the built-in potential, the excitonic and biexcitonic properties of  $a$ -plane InGaN/GaN QDs, in the next step, we move to the calculation of radiative lifetime in  $a$  plane InGaN QDs and how they compare with  $c$ -plane dots.

### 3.3.3 Radiative lifetime

Here, we start with an analysis of the oscillator strength  $f$  in  $a$ - and  $c$ -plane dots and how this quantity is affected by changes in dot size. Having established these general trends in  $f$ , we study in a second step how  $\tau$  changes with QD size. The theoretical results presented in this section are also complemented by experimental data from our collaborators.

#### Analysis of oscillator strength $f$

Here, we study the oscillator strength  $f$  as a function of the dot diameter  $d$  and the dot height  $h$ . It is to remind the reader that we have performed our calculations on symmetric dots here where  $d_x = d_y = d$ . We start with  $d$  and vary this quantity between 6 nm and 24 nm, while  $h$  is kept constant at 2.5 nm. To compare the increase or reduction in  $f$  when changing the dot geometry more easily, we work in the following with the *relative* oscillator strength  $\tilde{f}^\beta(d)$  for  $c$ - ( $\beta = c$ ) and  $a$ -plane ( $\beta = a$ ) InGaN/GaN QDs. We define this quantity as:

$$\tilde{f}^\beta(d) = \frac{f^\beta(d)}{f^\beta(6)} . \quad (3.3)$$

Here,  $f^\beta(6)$  denotes the oscillator strength calculated from Eq. (3.2) for a dot with height  $h = 2.5$  nm and a base diameter of  $d = 6$  nm.  $f^\beta(d)$  is the oscillator strength calculated as a function of  $d$ . Thus  $\tilde{f}^\beta(6) = 1$ . The results of this analysis are depicted in Fig. 3.17 with and without Coulomb interaction for both polar and nonpolar dots. Looking at  $\tilde{f}^\beta(d)$  without Coulomb effects, we find that in the nonpolar case (open circles),  $\tilde{f}^a(d)$  decreases by a factor of 2 to a value of  $\tilde{f}^a(24) = 0.46$  when  $d$  changes from 6 nm to 24 nm. A similar behavior is observed for the polar case (open squares), however, here the effect is more pronounced, showing that for  $d = 24$  nm  $\tilde{f}^c(24) \approx 0.30$ . This behavior can be explained by the following factors. For both  $c$ - and  $a$ -plane systems, the increase in  $d$  leads to an increase in the QD volume and consequently to an increase in the magnitude of the built-in field [160], which results in a stronger localization of the charge carriers at the interfaces. Therefore, the spatial separation between the carriers is increased, leading to a reduction in  $\tilde{f}^\beta$ . This brings us to another factor that affects  $f$  in the nonpolar case. Even though the built-in field is reduced in the  $a$ -plane QD, when compared with the  $c$ -plane structures, we are left with an increased distance between the two QD interfaces oriented along the  $c$ -axis. Consequently, the charge carriers can spatially be separated over a larger distance in the  $a$ -plane structure. However, the

stronger reduction in  $\tilde{f}^\beta(d)$  for the  $c$ -plane QDs, when compared to the nonpolar structures, is attributed to the fact that the built-in fields are much stronger in the  $c$ -plane case. This dominates over the larger spatial extension of the dot along the  $c$ -axis in the nonpolar case. Thus, to a first approximation, when neglecting the Coulomb interaction in the system, both  $a$ - and  $c$ -plane dots show similar trends in terms  $\tilde{f}^\beta(d)$ .

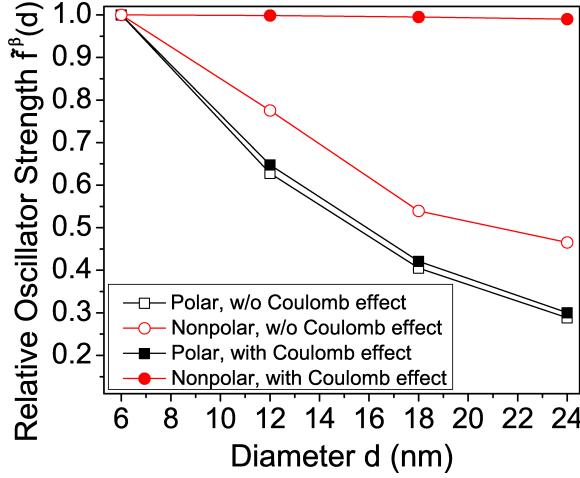


FIGURE 3.17: Relative oscillator strength  $\tilde{f}^\beta(d)$  of polar and nonpolar  $\text{In}_{0.15}\text{Ga}_{0.85}\text{N}/\text{GaN}$  QDs as a function of the base diameter  $d$  with and without Coulomb effect. The height  $h$  of the dots is kept fixed at 2.5 nm.

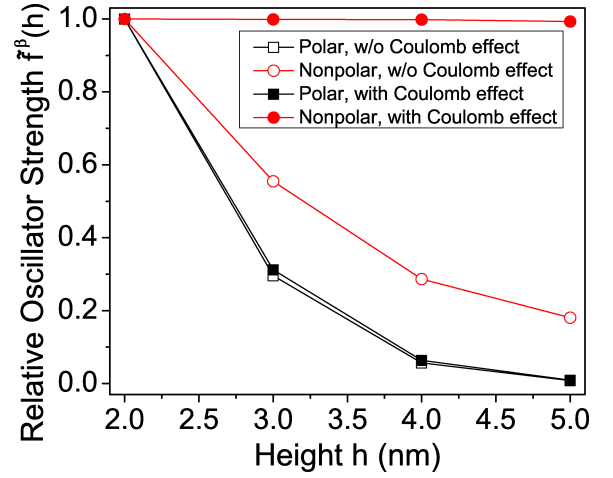


FIGURE 3.18: Relative oscillator strength  $\tilde{f}^\beta(h)$  of polar and nonpolar  $\text{In}_{0.15}\text{Ga}_{0.85}\text{N}/\text{GaN}$  QDs as a function of the dot height  $h$  with and without Coulomb effect. The base diameter  $d$  of the dots is kept fixed at 24 nm.

This situation is completely changed when including Coulomb effects in the calculations, as depicted in Fig. 3.17. Here we find that the attractive Coulomb interaction between electrons and holes overcomes the residual built-in field in the nonpolar case (filled circles), resulting in an almost constant value of  $\tilde{f}^a(d)$ . It is also evident that the Coulomb effect has very little impact on  $\tilde{f}^c(d)$ . Thus the oscillator strength  $f$  in the polar case (filled squares) is mainly dominated by the electrostatic built-in field, while the Coulomb effects dominate the wave function overlap in the nonpolar case.

To further analyze the impact of the QD size on the results, we have also performed calculations with varying dot heights  $h$ . Similar to the above discussions, we define here the relative oscillator  $\tilde{f}^\beta(h)$ , where  $\tilde{f}^\beta(h)$  is normalized to the oscillator strength of a dot with height  $h = 2$  nm. The dot diameter  $d$  is kept constant at  $d = 24$  nm. Figure 3.18 shows the variation of  $\tilde{f}^\beta(h)$  with and without Coulomb effect for both polar and nonpolar  $\text{InGaN}/\text{GaN}$  dots. In comparison to Fig. 3.17 where we have varied the dot diameter  $d$ , we observe here similar trends in  $\tilde{f}^a(h)$ . Again, due to the reduced built-in fields in the  $a$ -plane dot when compared to the  $c$ -plane structures in the absence of Coulomb effects,  $\tilde{f}^a(h)$  (open circles) is always larger than  $\tilde{f}^c(h)$  (open squares). For the largest system studied here,  $d = 24$  nm and  $h = 5$  nm,  $\tilde{f}^c \approx 0$  while  $\tilde{f}^a \approx 0.18$ .

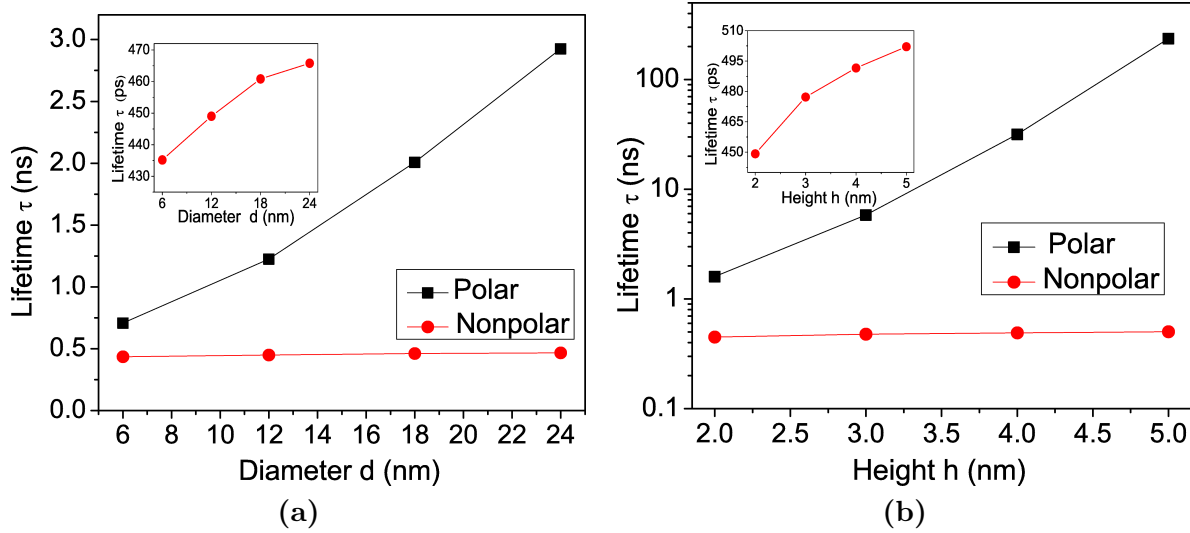


FIGURE 3.19: (a) Recombination lifetime  $\tau$  as a function of QD base diameter  $d$ . The dot height is kept fixed at  $h = 2.5$  nm (b) Recombination lifetime  $\tau$  as a function of QD height  $h$ . The base diameter of the dot is 24 nm. The inset shows nonpolar data (red circles) separately from the polar data (black squares) to visualize trends more clearly.

When taking Coulomb effects into account, we find again that the oscillator strength  $\tilde{f}^c$  in the polar structures (filled squares) is dominated by the built-in field, while in the nonpolar system (filled circles) Coulomb effects become important. In the nonpolar case, this results in the situation that  $\tilde{f}^a$  is almost independent of  $h$ .

Overall, our analysis reveals that for nonpolar InGa<sub>N</sub>/Ga<sub>N</sub> QDs variations in the dot size are of secondary importance for the (relative) oscillator strength since the attractive Coulomb effect is dominant. Thus for an accurate theoretical description of the optical properties of these systems, Coulomb effects have to be included. So far we have only studied the relative oscillator strength without directly comparing to experimental measurements of the exciton lifetime. We therefore study the radiative recombination lifetime  $\tau$  and how this quantity changes with variations in the dot geometric features in the next section. The comparison between theory and experiment is addressed in Sec. 3.3.3.

### Calculation of radiative lifetime $\tau$

Equipped with the knowledge about changes in the oscillator strength  $f$  with QD size, the variation of the radiative lifetime  $\tau$ , Eq. (3.1), in polar and nonpolar InGa<sub>N</sub>/Ga<sub>N</sub> dots is studied here. We start our analysis by looking at the impact of the dot diameter  $d$  on  $\tau$ . For this study the height of the dot is chosen to be  $h = 2.5$  nm, while the base diameter varies between 6 nm and 24 nm. The calculated lifetimes are displayed in Fig. 3.19 (a) for the polar (black square) and nonpolar (red circle) InGa<sub>N</sub>/Ga<sub>N</sub> dots. For the polar QDs we observe that  $\tau$  increases with increasing dot diameter  $d$ . In contrast to this,  $\tau$  stays approximately constant

for the nonpolar system, at least when compared with the polar case. This observation is consistent with the behavior of the oscillator strength discussed in the previous section and displayed in Fig. 3.17, since  $\tau$  is inversely proportional to  $f$ , cf. Eq. (3.1). Thus larger values of  $f$  lead to smaller values of  $\tau$ . Looking at the absolute values of  $\tau$  for both the polar and the nonpolar dots, we find here that for the  $c$ -plane dots, values in the range of several nanoseconds are obtained, consistent with literature experimental data [184, 185]. For the nonpolar dots, also displayed in the inset of Fig. 3.19 (a), our calculated  $\tau$  values are in the range of 435 ps to 465 ps. It should be noted that this variation, even though  $\tilde{f}^a(d)$  is approximately constant, arises from the fact that  $E^X$  varies when the dot volume increases. In this case,  $E^X$  is shifted to smaller energies resulting in an increase of  $\tau$ , given that  $\tau$  is inversely proportional to  $E^X$ , cf. Eq. (3.1).

In the second step, we investigate the impact of the QD height  $h$  on  $\tau$ . In these calculations the dot height ranges from 2 nm to 5 nm. The base diameter for these studies is kept constant at  $d = 24$  nm. In the case of the nonpolar dots, the  $\tau$  values change only slightly from around 450 ps to approximately 500 ps when  $h$  changes from 2 nm to 5 nm (see inset of Fig. 3.19 (b)). This finding is consistent with the observation that the oscillator strength  $f$  stays approximately constant when changing  $h$  (cf. Fig. 3.18). Again the variation in  $E^X$  leads to the slight increase in  $\tau$ , as displayed in Fig. 3.19 (b) for the nonpolar dot. For the polar dots,  $\tau$  increases exponentially with increasing height  $h$ , stemming from the fact that  $f$  decreases dramatically with increasing dot height  $h$  (cf. Fig. 3.18). This results from both the increase in the built-in potential and the accompanied shift in  $E^X$  to lower energies, and thus contributing to the increase in  $\tau$ .

Overall our theoretical calculations show that the radiative recombination lifetimes in  $c$ -plane systems strongly depend on the nanostructure size. However, this is not the case, at least when compared to the  $c$ -plane systems, for nonpolar InGaN/GaN dots. In the next section we will summarize the theoretical results and compare them to the experimental data obtained by our partners in Oxford and literature values.

## Experimental results and comparison with experiment

Growth and optical characterization of self-assembled nonpolar  $a$ -plane (11 $\bar{2}$ 0) InGaN/GaN QDs were carried out by our collaborators at the University of Cambridge and Oxford, respectively. The samples were grown by modified droplet epitaxy (MDE), a metal-organic vapour phase epitaxy (MOVPE) method originally developed for the fabrication of  $c$ -plane QDs [44], but adapted to the growth of  $a$ -plane QDs by Zhu *et al.* [14]. The micro-photoluminescence ( $\mu$ PL) experiments of the samples were carried out under two-photon excitation which suppresses the relative strength of emission from the underlying QWs (formed due to growth routine) making the investigation and analysis of the QD emission more efficient and accurate.

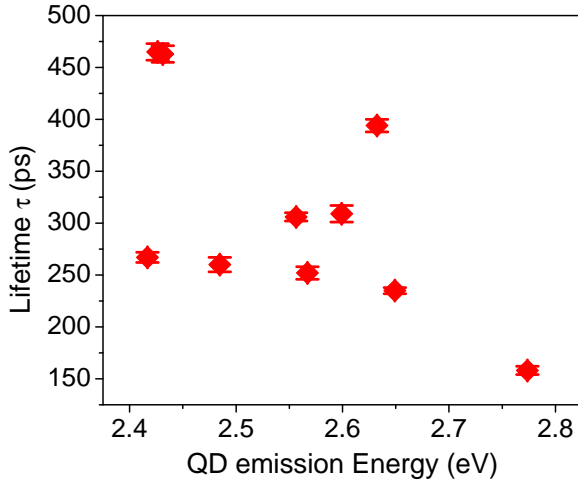


FIGURE 3.20: Recombination lifetime  $\tau$  obtained experimentally as a function of the QD emission energy. The error bars are also indicated in the figure.

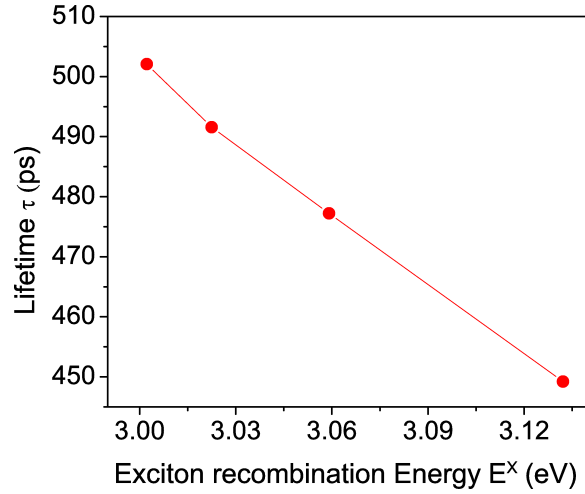


FIGURE 3.21: Recombination lifetime  $\tau$  as a function of exciton recombination energy  $E^X$ .

The QD PL can then be directed to a photomultiplier tube (PMT) for time-correlated single-photon counting (TCSPC) from which the radiative lifetime of the QD nanostructures can be measured. More details on the growth and optical characterization can be found elsewhere [186].

The radiative lifetime data of 10 typical *a*-plane InGa<sub>N</sub> QDs are shown in Fig. 3.20 as a function of QD emission energy. In general, lifetimes obtained from TRPL measurements range from 150 to 500 ps with the majority around 250-300 ps. These values are indeed an order of magnitude smaller than values found in *c*-plane systems [184, 185]. Other studies of nonpolar QDs grown by both MDE and an alternative method show radiative lifetimes [14, 67] around 500 ps to 600 ps. Furthermore, these studies observe a vague trend that with decreasing QD emission energy the radiative lifetime  $\tau$  increases. To achieve a better statistical average, this analysis has to be extended to a much large number of dots. However, this is beyond the scope of the present study. Overall, the experimental data demonstrates that the use of the nonpolar *a*-plane reduces the undesired QCSE, increasing the exciton oscillator strength and producing much shorter lifetimes, when compared to *c*-plane systems.

As discussed in the previous section, for the here chosen geometries and In content of 15% we find  $\tau$  values in the range of 435 ps to 500 ps. So far we have presented our theoretical data for  $\tau$  as a function of the dot height or diameter. To compare theory with experiment more easily, we have re-plotted the theoretical data shown in Fig. 3.19 (b) for  $\tau$  as a function of the exciton recombination energy  $E^X$ . The re-plotted data is displayed in Fig. 3.21. Comparing these results with the experimental values given in Fig. 3.20, several features are of interest. Firstly, we observe that for the geometry and In content assumed here, the  $\tau$  values obtained from theory are similar in magnitude to the experimental ones, but higher. It should also be noted that the exciton recombination energies are larger than the experimentally measured

QD emission energies. Thus with increasing the In content above 15%, the excitonic transition energies would be shifted to values closer to the experimentally observed values. However, in doing so, since  $\tau$  is inversely proportional to  $E^X$  as discussed before,  $\tau$  should increase further, resulting in a larger disagreement between theory and experiment on  $\tau$ . Conversely, when reducing the In content below 15%, the agreement in  $\tau$  between theory and experiment is improved, but the theoretical exciton recombination energies would be shifted to higher values. Therefore, further theoretical and experimental studies are required to extend this analysis. For instance, experimental insight into the In content and the QD geometry is of central importance, since it is a crucial ingredient for our modeling. From a theoretical perspective, as discussed already in Sec. 5.1, uncertainties in the material parameters and their alloy dependence affect the calculated values. Moreover, as shown in nonpolar InGaN/GaN QWs [187], random alloy fluctuations lead to strong carrier localization effects which also affect radiative lifetimes. These alloy fluctuations inside a nonpolar InGaN/GaN QD could therefore also be important for a detailed understanding of the electronic and optical properties of *a*-plane QDs.

However, whilst the dots analyzed for this paper present shorter lifetimes than those predicted by theory, our former analysis of other, similar structures, suggests somewhat longer lifetimes [14, 67]. Values between 500-600 ps have for example been quoted in Refs. [14] and [67], which are in good agreement with the here presented theoretical data. Furthermore, the trend observed in the calculations that with decreasing  $E^X$  the radiative lifetime  $\tau$  increases (cf. Fig. 3.21), is also vaguely visible in the experimental data (cf. Fig. 3.20). However, it should be noted that in the experiment the variations in lifetimes might also be affected by a combination of variations in In content and dot size. Furthermore, in-plane shape asymmetries in *a*-plane QDs can also give rise to a spread in exciton energies due to changes in the QD volume and connected modifications in the built-in potential. The in-plane anisotropies have not been considered in the theoretical modeling of the oscillator strength and the radiative lifetime. Nevertheless, the theoretical description presented gives radiative lifetimes which are comparable in magnitude to the experimental data obtained here and in previous studies, and forms now a good starting point for future combined experimental and theoretical investigations.

### 3.4 Conclusion

In summary, we have investigated the built-in potential, the excitonic, biexcitonic properties and the radiative lifetime of *a*-plane InGaN/GaN QDs. Our analysis reveals that the built-in fields in nonpolar InGaN/GaN QDs are strongly reduced when compared to their *c*-plane counterparts. However, it should be noted that these systems are not field free and changes in the dot geometry significantly affect these fields. We find here also a complicated interplay between axial, shear strain and spontaneous polarization contributions when the dot geometry changes.

In contrast to *c*-plane systems, we find that the attractive Coulomb interaction between electron and hole compensates the spatial separation of the carriers due to the residual built-in field. However, the analysis also reveals, even though the built-in field is strongly reduced, it significantly affects the excitonic properties. For instance, when changing the in-plane dot geometry, the exciton binding energy changes in an unusual way in comparison to nonpolar QWs. We have shown that these changes are related to changes in the built-in field, highlighting that built-in fields in nonpolar InGa<sub>N</sub>/Ga<sub>N</sub> dots are important for a detailed understanding of the optical properties. In the next step, our theoretical data is compared with available experimental literature results. The analysis of the biexciton binding energies indicated for instance that the experimentally realized dots are relatively large with high In content ( $\geq 25\%$ ). Furthermore, the investigation of the biexciton binding energy  $E_{XX}^b$  allowed us also to establish trends in  $E_{XX}^b$  when QD geometrical features change. This gave initial insight into potential use of nonpolar InGa<sub>N</sub>/Ga<sub>N</sub> QDs for entangled photon emission via the time reordering scheme.

Finally, we presented a combined theoretical and experimental study of the radiative recombination lifetimes in *a*-plane (11 $\bar{2}$ 0) InGa<sub>N</sub>/Ga<sub>N</sub> QDs. Our calculations show that for an accurate description of the optical properties of the here studied nonpolar InGa<sub>N</sub> QD systems, Coulomb effects play a central role. For instance, we find here that the oscillator strength in a nonpolar system is almost unaffected by changes in the QD size, which is in contrast to its *c*-plane counterpart. While in the *c*-plane system the wave function overlap is dominated by the electrostatic built-in field, in the nonpolar case the attractive Coulomb interaction compensates the spatial separation of the charge carriers due to the residual built-in field. This leads to the situation that the radiative lifetime in the nonpolar system is one order of magnitude smaller when compared to the *c*-plane system. The calculated radiative lifetimes are in good agreement with literature data and comparable in magnitude to the here measured ones.

Overall our results indicate that nonpolar QDs are promising candidates for next generation visible wavelength single-photon emitters where the repetition rate compared to *c*-plane systems can be improved dramatically.

## Chapter 4

# Engineering the polarization properties of nonpolar InGaN QDs at elevated temperatures

In last chapter, we discussed the excitonic and biexcitonic properties as well as the radiative lifetime of the nonpolar InGaN dots with the aim to target entangled photon emission and high speed single photon emission. Here, we explore another important characteristics of QD systems namely light polarization properties which is essential for a number of optoelectronic and quantum information applications, such as QD liquid crystal displays [188], optical quantum computing [189], and quantum key distribution [190–192]. As described earlier, these 0D nanostructures possess a delta function-like density of states similar to atoms, whilst being thousands of times larger. Since their size and shape can be manipulated in the solid-state, QDs offer an easier path towards integration and development on semiconductor platforms than other comparable systems, such as atoms [193], molecules [194] and 2D nanostructures [195, 196]. However, in most QD systems, polarized light output can only be achieved using an external polarization filter to define a desired polarization state. Such configurations can be cumbersome and will incur a loss of at least 50%. To mitigate these undesired losses, direct polarization control from the light source would be desirable. More importantly, for realistic scalable on-chip applications, one challenge that a QD system will inevitably face is the operation at temperatures high enough to reach the regime of on-chip electronic temperature regulation by thermoelectric cooling. Commercial Peltier coolers can maintain a stable temperature difference of  $\sim 100$  K, allowing devices to work at  $\sim 190$  K. As such, it is important not only to demonstrate QD properties, such as polarization control, under cryogenic conditions, but also to investigate their performance and behaviour at thermoelectrically cooled temperatures. In this respect, as discussed earlier, nitride-based heterostructures are suitable for operation at such high temperatures due to their large band offsets and exciton binding energies [197]. As such, there have

been several reports of polarized QD emission in conventional *c*-plane nitrides [198–204] at cryogenic temperatures. However, due to the stochastic process of QD formation, the resultant extent and direction of anisotropy are completely random, giving rise to uncertain degrees of optical linear polarization (DOLP) along arbitrary directions that are less than desirable in polarization-based applications. A few attempts have been made to control the strain state of the QDs, including dots in nanowires [205–207], elliptical nanowires [25], and asymmetric pyramidal QDs [208]. Although the direction has been defined, the geometries of the structures make electrical contacting challenging. As such, a simpler and more practical method is needed to achieve polarization control, for the realization of on-chip polarized single-photon generation and related applications.

To this end, in this chapter, we investigate the robustness and temperature sensitivity of the optical polarization properties of nonpolar InGa<sub>N</sub> QDs and compare our results with experimental studies performed by our collaborators at the University of Oxford in the group of Prof. R. A. Taylor. The chapter is organised as follows. We start in Sec 4.1 with the theoretical framework used for the calculations, followed by the discussion of the here assumed QD geometry. Subsequently, we move to the results and discussions in Sec. 4.2. Here, we first present the results of the DOLP at cryogenic conditions in Sec. 4.2.1. Thereafter, the analysis is extended to peltier cooled temperatures in Sec. 4.2.2. Furthermore, it is well known that for InGaAs/GaAs QDs shape anisotropies have a significant effect upon the optical polarization properties of QDs [172]. Therefore, this raises the question of how strongly shape anisotropies affect the optical properties of self-assembled *a*-plane InGa<sub>N</sub>/Ga<sub>N</sub> QDs, and thus how robust these QDs might be in generating highly polarized photons against shape deformations. Hence, we also provide an investigation of the effect of dot geometry on the DOLP of *a*-plane InGa<sub>N</sub> QDs. Finally, in Sec. 4.3 we compare our findings to insights from statistically significant experimental data.

## 4.1 Theoretical framework and QD geometry

In general, the DOLP of a light is the ratio of the intensity of the polarized part of the light to its total intensity [209, 210]. The DOLP [209, 210] is usually defined as:

$$\rho = (I_{\perp} - I_{\parallel}) / (I_{\perp} + I_{\parallel}) \quad (4.1)$$

where  $I_{\perp}$  and  $I_{\parallel}$  denotes the averaged intensities measured perpendicular and parallel to the WZ *c*-axis in our case. Theoretically, the intensity of a light can be related to the spontaneous emission rate  $R_{\text{sp}}$  and therefore, the temperature dependence of the  $\rho$  has been addressed in

this thesis on the basis of  $R_{\text{sp}}$  [18] as:

$$R_{\text{sp}}(T) = \int d(\hbar\omega) \frac{2e^2 n \hbar \omega}{m_0^2 \epsilon_0 c^3 \hbar^2} \sum_{i,j} |\mathbf{a} \cdot \mathbf{p}_{i,j}|^2 \frac{1}{\sqrt{2\pi}\sigma} \exp \left[ -\frac{(\Delta E_{i,j} - \hbar\omega)^2}{2\sigma^2} \right] f^e(E_i^e) f^h(E_j^h) . \quad (4.2)$$

Here  $e$ ,  $\epsilon_0$ ,  $m_0$ ,  $c$ ,  $\hbar$ ,  $n$  denote elementary charge, vacuum permittivity, free electron mass, vacuum speed of light, Planck's constant (divided by  $2\pi$ ) and the refractive index, respectively. The energetic separation between the electron state  $i$  and the hole state  $j$  is given by  $\Delta E_{i,j}$ . The inhomogeneous broadening parameter is denoted by  $\sigma$ . Experimentally, the values of full width at half maximum for the here studied nonpolar InGaN/GaN QDs are of the order of 0.5-3 meV [211]. Given these extremely small numbers compared to nonpolar InGaN/GaN QWs [187], inhomogeneous broadening is neglected here. The momentum matrix element between electron state  $i$  and hole state  $j$  is given by  $|\mathbf{a} \cdot \mathbf{p}_{i,j}|^2$ , and can be calculated via

$$|\mathbf{a} \cdot \mathbf{p}_{i,j}|^2 = \sum_{c,v} |\langle u_c | \mathbf{a} \cdot \mathbf{p} | u_v \rangle|^2 |\langle \phi_c^i | \phi_v^j \rangle|^2, \quad (4.3)$$

where  $\mathbf{a}$  is the polarization of the incident light,  $u_\alpha$  denote the Bloch functions;  $\phi_\alpha$  are the envelope functions. The subscripts  $\alpha = c$  and  $\alpha = v$  denote conduction (electron) and valence (hole) states, respectively. Details on the calculation of these quantities are given in Ref. [88]. The Fermi-functions for electrons and holes are denoted by  $f^e$  and  $f^h$ , respectively and are given by,

$$\begin{aligned} f^e(E_i^e) &= \frac{1}{1 + \exp[(E_i - E_{fn})/k_B T]} , \\ f^h(E_j^h) &= \frac{1}{1 + \exp[(E_{fp} - E_j)/k_B T]} . \end{aligned}$$

Here  $E_{fp}$  and  $E_{fn}$  are quasi-Fermi levels obtained from the injected carrier density [18]. The electron and hole energies for state  $i$  and  $j$  are denoted by  $E_i^e$  and  $E_j^h$ , respectively. To obtain the quasi-Fermi levels for electrons and holes up to 300 K, we include 10 electron and 30 hole states (neglecting the Kramers degeneracy of each state) in the calculations. These Fermi functions account for the effect that with increasing temperature  $T$  excited electron and hole states are populated.

Given that  $R_{\text{sp}}$  depends on the light polarization vector  $\mathbf{a}$  and the temperature  $T$  via the Fermi-functions, we can now define the temperature dependence of the DOLP  $\rho$  via

$$\rho(T) = \frac{R_{\text{sp}}^\perp(T) - R_{\text{sp}}^\parallel(T)}{R_{\text{sp}}^\perp(T) + R_{\text{sp}}^\parallel(T)} . \quad (4.4)$$

The spontaneous emission rates for a light polarization vector  $\mathbf{a}$  perpendicular and parallel to the WZ  $c$ -axis are denoted by  $R_{\text{sp}}^\perp$  and  $R_{\text{sp}}^\parallel$  respectively. This approach is similar to the approach used in Ref. [212] for non  $c$ -plane InGaN/GaN QWs.

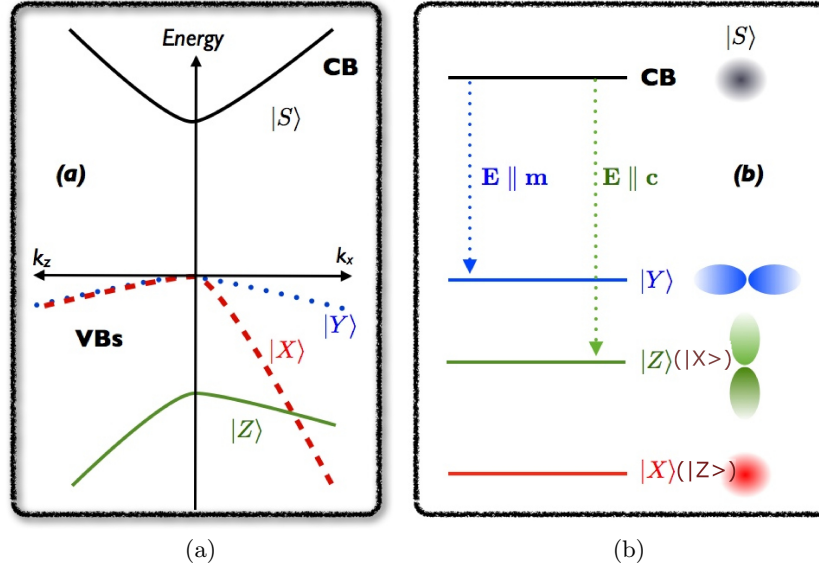


FIGURE 4.1: (a) Schematic illustration of the  $c$ -plane bulk band structure in the absence of the spin-orbit coupling. (b) Schematic illustration of the energy level ordering of an  $a$ -plane system with confinement along the  $a$ -axis. Selection rules for the electric field  $\mathbf{E}$  (light polarization vector  $\mathbf{a}$ ) parallel to the  $c$ - and  $m$ -axis are also indicated by the dashed arrows. The orbital character of different bands according to our convention is denoted in brackets.

As input for  $R_{\text{sp}}(T)$  the energy levels for electrons  $E_i^e$  and holes  $E_j^h$  and the momentum matrix element  $|\mathbf{a} \cdot \mathbf{p}_{i,j}|^2$  from the electron and hole states  $i$  and  $j$  are required. Consequently, insights into the electronic structure of nonpolar InGaN/GaN dots is of central importance. To this end, we have performed  $\mathbf{k} \cdot \mathbf{p}$ -based framework introduced in the previous chapter.

To calculate the DOLP  $\rho(T)$ , Eq. (4.4), information about the QD geometry is required. Based on the discussions presented in the last chapter, we have assumed as a model geometry a lens shaped dot with a base diameter of 30 nm and a height of 2.5 nm. It should be noted that previous calculations on *nonpolar* InGaN/GaN QDs have made similar assumptions for the dot geometry [161, 162]. All calculations were performed on a  $50 \times 50 \times 30 \text{ nm}^3$  supercell with periodic boundary conditions. In this study, we discuss the results on the basis that the  $z$ -axis of our coordinate system is parallel to the crystal  $a$ -axis.

## 4.2 Results and discussion

Equipped with the theoretical framework and geometry of the QD structures, we turn now to present the results of our analysis. In a first step, we examine the polarization properties of  $a$ -plane QDs under cryogenic conditions, meaning our calculations are carried out at a temperature  $T$  of  $T = 0 \text{ K}$ . Here, we are mainly interested in investigating the DOLP  $\rho$  as a function of In content and deformations in the QD shape. After that, we move to the calculations of the DOLP as a function of temperature  $T$  and explore ways to engineer QD properties with the aim to achieve highly polarized emission at thermoelectrically cooled temperatures.

### 4.2.1 Theoretical calculations of DOLP at cryogenic conditions

Before turning to the calculated  $\rho$  values, it is important to discuss and understand general band structure features of nonpolar WZ InGaN/GaN heterostructures, given that  $\rho$  depends on the orbital character of the involved electron and hole states  $i$  and  $j$  [cf. Eq. (4.2) and (4.4)]. Here, we start with a general discussion of a  $c$ -plane system using the standard convention that the  $c$ -direction is assumed to be parallel to the  $z$ -axis and the in-plane axes are the  $x$  ( $a$ )- and  $y$  ( $m$ )-axes. In this convention, as described in Sec. 2.1.1, Chapter 2,  $|X\rangle$ - and  $|Y\rangle$ -like states are energetically degenerate [90] at  $\mathbf{k} = \mathbf{0}$ , neglecting the weak SOC. Due to the positive crystal field splitting energy in InN and GaN, [62] the  $|Z\rangle$ -like state is shifted to lower energies. To understand how confinement effects affect the band structure of InGaN/GaN heterostructures, the effective masses of  $|X\rangle$ -,  $|Y\rangle$ - and  $|Z\rangle$ -like states near  $\mathbf{k} = \mathbf{0}$  are of central importance. Whilst the energy bands associated with  $|X\rangle$ - and  $|Z\rangle$ -like states have low effective masses along  $k_x$ - and  $k_z$ -directions, respectively, the  $|Y\rangle$ -like state has a light-hole mass along the  $k_y$ -direction [62, 213]. A schematic illustration of the situation is given in Fig. 4.1. Thus, for a system with a strong confinement along the  $c$ -axis, as for instance in  $c$ -plane InGaN/GaN QWs,  $|Z\rangle$ -like states are shifted to lower energies with respect to the valence band maximum. Therefore, the topmost valence band state in such a system is predominately  $|X\rangle$ - and  $|Y\rangle$ -like in character with little  $|Z\rangle$ -orbital character. In the case of  $c$ -plane QDs additional confinement effects are introduced by the lateral/in-plane confinement in the  $c$ -plane. Given the differences in the effective masses of  $|X\rangle$ - and  $|Y\rangle$ -like states, QD shape anisotropies will significantly affect band mixing effects and thus the orbital character of the QD hole states [172]. Consequently, the DOLP will be affected.

Turning now to a nonpolar system, the situation is different. Since the growth is along the  $a$ -axis, perpendicular to the  $c$ -axis, the symmetry between  $|X\rangle$ - and  $|Y\rangle$ -like states is broken given the strong confinement along the  $a$ -axis ( $x$ -axis). This results in the situation that the  $|X\rangle$ -like state is shifted to lower energies with respect to the  $|Y\rangle$ -like state. Consequently, the topmost valence state is entirely  $|Y\rangle$ -like in character, taking into account that the  $|Z\rangle$ -like state is already shifted to lower energies due to the positive crystal field splitting energy. A schematic illustration of the general valence band ordering in a system with confinement along the  $a$ -axis ( $x$ -axis) is given in Fig. 4.1. Please note that the above discussion is based on the  $c$ -plane convention for the coordinate system, meaning that the  $a$ -direction is assumed to be along  $x$ -axis.

However, in our  $\mathbf{k} \cdot \mathbf{p}$  framework, growth of the nanostructures is always assumed along the  $z$ -axis, meaning now that the  $a$ -direction is parallel to the  $z$ -axis of the rotated coordinate system. In this case, the  $c$ -axis is parallel to the  $x$ -axis and the  $m$ -axis is parallel to the  $y$ -axis. As one can see, in our convention,  $x$ - and  $z$ - axes are interchanged when compared to the usual  $c$ -plane convention. Therefore, a  $|X\rangle$ -like state in the conventional notation corresponds to a

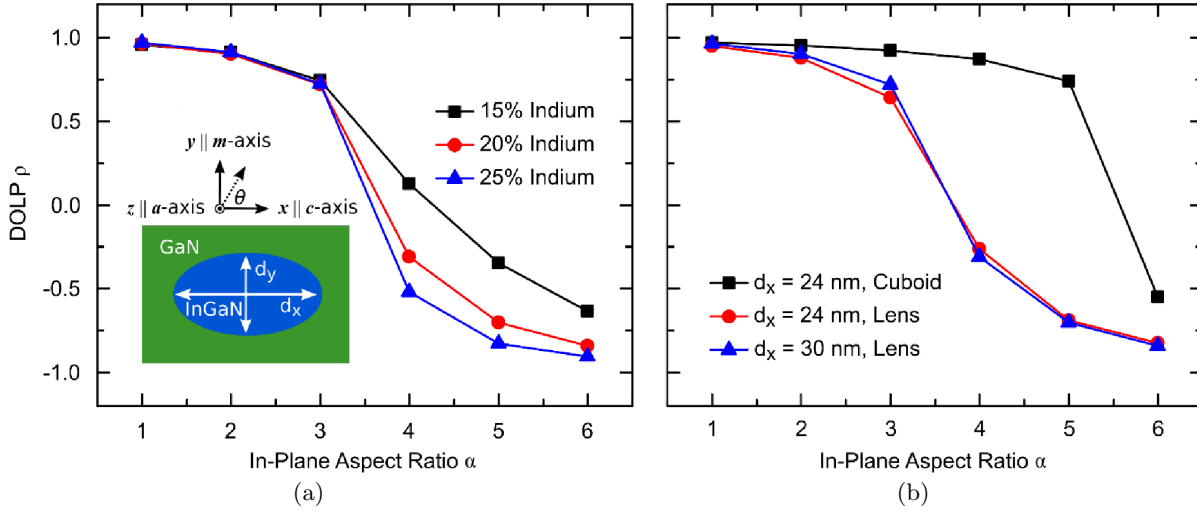


FIGURE 4.2: (a) DOLP  $\rho$  as a function of the in-plane aspect ratio  $\alpha$  and In content of a lens-shaped  $a$ -plane InGaN/GaN QD. The inset shows the coordinate system, the definition of  $\theta$  as the in-plane angle away from the crystal  $c$ -axis (same as that defined in the experimental setup), and the definitions of  $d_y$  and  $d_x$  as the in-plane dimensions of a QD used in the theoretical investigation.  $\alpha$  is defined as  $\alpha = d_x/d_y$ . (b)  $\rho$  as a function of  $\alpha$ , size, and geometry of a QD.

$|Z\rangle$ -like state in our notation and vice-versa. The orbital character of different bands according to the convention used in this work is denoted in brackets in Fig. 4.1. Overall, using the above discussion, we expect that the hole ground state in an  $a$ -plane InGaN/GaN QD with a circular symmetric base is predominately  $|Y\rangle$ -like in character. However, depending on the in-plane QD shape anisotropies, band mixing effects are expected to play an important role which are key for the DOLP calculations.

Equipped with a knowledge of the basic features of the band structure, we now turn to the calculation of DOLP in a nonpolar InGaN dot. In this section, we only analyze DOLP values at  $T = 0$  K. Here, our main aim is to explore the robustness of DOLP in these systems against shape deformations at cryogenic conditions. The outcome of our  $\mathbf{k}\cdot\mathbf{p}$  calculations for an  $a$ -plane InGaN QD with a circular base is predicted to have a  $\rho$  value of 0.96 (96%) indicating that the emitted light should be polarized perpendicular to the  $c$ -axis (along the  $m$ -axis). This result is in stark contrast with theoretical studies of  $c$ -plane InGaN QDs, where  $\rho$ , due to the  $c$ -plane symmetry, is 0 for dots with no in-plane anisotropies [201, 214].

However, it is important to note that self-assembled QDs are unlikely to be perfectly symmetrical given the difference in the underlying  $c$ - and  $a$ - lattice constants [62], and the stochastic self-assembly formation process. Results on both InGaAs QDs [172] and  $c$ -plane InGaN QDs [201, 214] reveal that dot shape anisotropy plays an important role and affects their properties quite significantly due to band mixing effects. Anisotropy affects the degree of quantum confinement, which causes energetic shifts in the  $|X\rangle$ -,  $|Y\rangle$ -, and  $|Z\rangle$ -like state and thus their contribution to the band mixing effects in the hole ground state. It is therefore important to study how significant this effect is in our QDs by modifying the dot geometry in the simulation.

Similar to Sec. 3.2, we define the in-plane aspect ratio  $\alpha$  as  $\alpha = d_x/d_y$ , where  $d_x$  and  $d_y$  are the in-plane dimensions of the dot base along  $c$  ( $x$ ) and  $m$  ( $y$ )-directions respectively. Please note we are working here in a rotated simulation frame. Therefore, for a circular base,  $d_x = d_y = 30$  nm, and  $\alpha = 1$ . A schematic illustration of the convention is given in the inset of Fig. 4.2.

A smaller dimension, and thus stronger confinement effects, along the  $x$ -direction will further increase the DOLP as it approaches unity. This is attributed to the lower effective mass of the  $|X\rangle$ -like states along this direction and results in an increase in the energetic separation of  $|Y\rangle$ - and  $|X\rangle$ -like states. Correspondingly, the more interesting situation is what happens if the dot geometry is modified along the  $y$ -direction. Such an anisotropy should affect states with a high  $|Y\rangle$ -like orbital contribution more strongly, again due to the fact that  $|Y\rangle$ -like ( $|X\rangle$ -like) states exhibit a low (high) effective mass along the  $y$ -direction [213]. Hence, calculations were performed at  $d_y = 30, 15, 7, 6$  and  $5$  nm, as the QD base becomes more elliptical. To account for the change in In content, the In content is varied between 15% and 25%. The results for  $\rho$  as a function of  $\alpha$  and In content are shown in Fig. 4.2. We see that  $\rho$  is almost constant for  $\alpha$  values between 1 and 2, and decreases only slightly for  $\alpha = 3$ , independent of In content. It is important to note that  $\alpha = 3$  already presents a significant “deformation” of the dot ( $d_x = 30$  nm,  $d_y = 10$  nm). Consequently, the calculations show that in  $a$ -plane InGa<sub>N</sub> QDs, the DOLP  $\rho$  is very insensitive against shape anisotropies and In composition changes. It should be noted that, in principle, Coulomb effects can mix contributions from excited (single-particle) states into the excitonic ground state [136]. However, our calculations reveal that the first few excited hole states are all almost entirely  $|Y\rangle$ -like in character. Thus, mixing of different hole states via Coulomb effects will not affect the orbital character discussed here. A detailed discussion of excited states and how this affects the DOLP at elevated temperatures is presented in the next section.

To strengthen the argument that the DOLP in nonpolar InGa<sub>N</sub>/Ga<sub>N</sub> QDs is extremely robust against shape anisotropies, we have also varied the geometry and size of the dot. Firstly, to study the impact of the QD size on the DOLP, we have kept the geometry to be lens-shaped but reduced the in-plane dimensions of the system. Here, for the symmetric dot,  $d_x = d_y = 24$  nm. To consider the same range of in-plane aspect ratios  $\alpha$ ,  $d_y$  has been varied between 24 and 4 nm. The results of this study are shown in Fig. 4.2 (red circles), revealing that the change in the QD in-plane dimensions affects the DOLP only very slightly.

To further extend this analysis, we have also investigated the influence of the QD geometry on the DOLP. To this end, we have drastically changed the QD geometry from a lens-shaped dot to a cuboid. The length and width of the cuboid is assumed to be of 24 nm with a height of 2.5 nm. Fig. 4.2 (b) shows the data (black squares) of the DOLP as a function of  $\alpha$  for the cuboidal dot. As one can infer from this study, in comparison with the lens shaped systems,

the reduction of the DOLP only happens at higher  $\alpha$  values ( $\alpha = 5$ ). Consequently, the DOLP in cuboid-shaped dots would even be more robust against shape anisotropies.

As such, our theoretical studies predict high experimental DOLP values, with very small variations caused by QD shape anisotropies, In content variations, size and geometry differences. A detailed comparison of our simulation results with the experimental findings is presented in later sections. Having discussed the robustness of DOLP values at cryogenic temperatures, we now turn to analyze the temperature dependence of the DOLP  $\rho$  in nonpolar InGaN QDs.

### 4.2.2 Theoretical study on the impact of temperature and QD geometry on DOLP

Here, we start our analysis with a symmetric dot ( $\alpha = 1$ ) and calculate DOLP as a function of temperature  $T$ . For these calculations, the In content is set to 20%. The corresponding data for  $\rho$  are given by the red circles in Fig. 4.3. For low temperatures [ $T \lesssim 20$  K] the DOLP value is extremely high [ $\rho(20) \approx 0.96$ ]. In line with the discussions presented in the last section, the hole ground state is found to be predominately  $|Y\rangle$ -like in character. Furthermore, given the low temperature of  $T = 20$  K, contributions from excited states are negligible. Consequently a high DOLP  $\rho$  is expected, consistent with the calculated value of 0.96. We observe here that  $\rho$  stays approximately constant up to 80 K. Over this temperature range mainly hole states with a large percentage of  $|Y\rangle$ -like orbital character are populated and thus,  $R_{\text{sp}}^{\perp} \gg R_{\text{sp}}^{\parallel}$ . Above 80 K we observe that contributions from states with a higher percentage of  $|X\rangle$ -like character become important. This results in the situation that  $R_{\text{sp}}^{\perp}$  decreases with increasing temperature  $T$  while at the same time  $R_{\text{sp}}^{\parallel}$  starts to increase. Consequently, based on Eq. (4.4),  $\rho$  starts to decrease with increasing temperature  $T$ . At 200 K  $\rho$  is reduced to approximately 0.82 and at 300 K this values drops to 0.71.

As already mentioned above, such a symmetric dot is unlikely. Since we are interested in how different anisotropies affect the DOLP values at high temperatures, the in-plane geometry of the QD has been varied. We first investigate temperature dependence of the DOLP for a lens-shaped dot characterized by  $\alpha = 2$  ( $d_x = 30$  nm,  $d_y = 15$  nm). Based on our previous discussions, in such a situation band mixing effects between  $|Y\rangle$ - and  $|X\rangle$ -like states are expected to be increased. This originates from the fact that states with a larger  $|Y\rangle$ -like orbital contribution should be much more strongly affected by the increased confinement effect along the  $y$ -axis when compared with predominately  $|X\rangle$ -like states. Consequently, in comparison to the symmetric QD ( $\alpha = 1$ ), one could expect that at low temperatures the DOLP  $\rho$  is reduced, accompanied by an earlier onset of the reduction in  $\rho$  with increasing temperature. This behaviour is indeed reflected in the calculated values for  $\rho(T)$  of this dot, which are given by the blue triangles in Fig. 4.3. In comparison to symmetric QDs (red circles), we find already

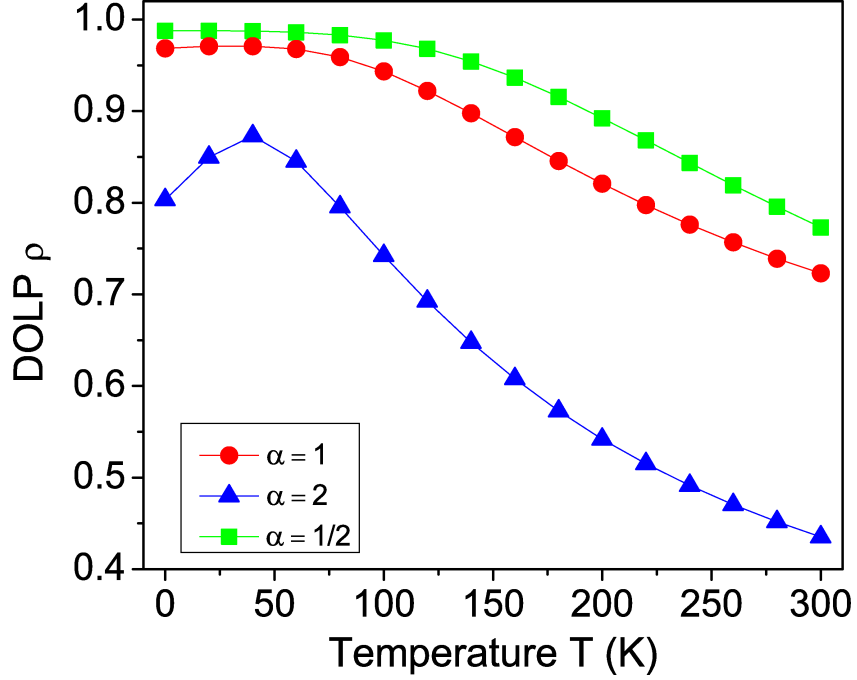


FIGURE 4.3: DOLP  $\rho$  as a function of the temperature  $T$  in a lens-shaped  $\text{In}_{0.2}\text{Ga}_{0.8}\text{N}/\text{GaN}$  dots for three different in-plane aspect ratios ( $\alpha$ ).

lower DOLP values at low temperatures ( $T \lesssim 20$  K). Additionally,  $\rho$  starts to decrease rapidly at much lower temperatures ( $T \gtrsim 40$  K). At 200 K,  $\rho$  drops to 0.54.

Making use of the insight gained into the band structure and how the QD geometry affects the temperature dependence of the DOLP, we can now provide a potential way forward to improve the temperature stability of  $\rho(T)$  further. Given the positive crystal field splitting energy and taking into account the light-hole mass of predominately  $|X\rangle$ -like states along the  $c$ -axis ( $x$ -axis), greater confinement along the  $c$ -axis should decrease band mixing effects between  $|Y\rangle$ - and  $|X\rangle$ -like states, which would be especially relevant for excited hole states. Consequently, by reducing the dimension of the QD along the  $c$ -axis,  $\rho$  should stay approximately constant over a wider temperature range when compared to cases of  $\alpha = 1$  and  $\alpha = 2$ . Also, the DOLP  $\rho$  should be larger at low temperatures in comparison with the symmetric dot, for instance. To verify this prediction, we have performed calculations for a QD having  $\alpha=1/2$  ( $d_y = 30$  nm and  $d_x = 15$  nm). In Fig. 4.3 the green squares show the corresponding DOLP  $\rho$  values as a function of the temperature  $T$ . As expected from our analysis above,  $\rho(T)$  for  $\alpha = 1/2$  is always higher than in the case of  $\alpha = 1$  (red square) and  $\alpha = 2$  (blue triangle). Furthermore, for  $\alpha = 1/2$ , up to 200 K the drop in  $\rho(T)$  is strongly reduced in comparison to  $\alpha = 2$  and still clearly reduced with respect to  $\alpha = 1$ . Moreover, for  $\alpha = 1/2$ ,  $\rho(T)$  stays approximately constant ( $\rho \approx 0.98$ ) up to 100 K, before it starts to slightly decrease over the temperature range of 100 K to 200 K. At  $T = 200$  K we find here a value of  $\rho(200) \approx 0.90$ . Even up to room temperature ( $T = 300$  K), strongly polarized emission is observed ( $\rho(300) \approx 0.77$ ).

Our theory thus provides a guideline to target asymmetric QD structures for achieving emitters with a further improved temperature stability of the DOLP  $\rho$ . For example, with QDs squeezed along the  $c$ -axis (elongation along  $m$ -axis), we would be able to achieve even higher polarization degrees at ambient conditions. Having discussed the robustness of DOLP against shape deformations in  $a$ -plane InGaN QDs from a theoretical perspective, in the next section, we compare our theoretical results with the experimental findings obtained by our collaborators through optical characterization of  $a$ -plane InGaN/GaN QDs.

### 4.3 Comparison with experiment

The  $a$ -plane InGaN QD samples were grown by our collaborators at University of Cambridge, UK in the group of Prof. R. A. Oliver using a modified droplet epitaxy method [14]. Subsequently, polarization resolved micro photoluminescence (PL) of the grown samples were carried out using a two-photon excitation method by our collaborators at University of Oxford, UK in the group of Prof. R. A. Taylor. The DOLP values were obtained using Eq. (4.1) where  $I_{\perp}$  and  $I_{\parallel}$  are the PL emission intensities perpendicular and parallel to  $c$ -axis respectively. More details on the growth and optical characterization of the samples can be found elsewhere [215]. We start this section by analysing experimental DOLP values at cryogenic temperatures and subsequently will move to the discussion of temperature sensitivity of the DOLP  $\rho$ .

#### 4.3.1 QD emission at cryogenic temperatures: Theory experiment comparison

In order to achieve statistical significance, the absolute DOLP values of 180 QDs were studied experimentally by our collaborators. The distribution of  $|\rho|$  for these QDs is shown in Fig. 4.4. All  $|\rho|$  data of QDs fall in the range between 0.60 to 1.00. The high mean  $|\rho|$  of 0.90 provides direct evidence that nonpolar  $a$ -plane InGaN QDs are strongly polarized photon emitters. The spread of the values in Fig. 4.4 is attributed to variations of QD size, shape, and In content. There are 23 QDs for which DOLP was found to be unity. As explained in the theoretical simulation, this could be caused by a compression of the QD geometry along the  $c$ -direction. Those with DOLP values lower than average could be attributed to a compression along the  $m$ -axis (cf. Fig. 4.2). Furthermore, the calculated standard deviation is only 0.08, which signifies very small fluctuations around the high average DOLP. As such, the robustness of DOLP against changes in size, shape anisotropy, and In content have been demonstrated both theoretically and experimentally. The data in Fig. 4.4 indicate that there are no discernible correlations between QD energy and DOLP, thus  $a$ -plane InGaN QDs emit highly polarized photons across all attainable wavelengths.

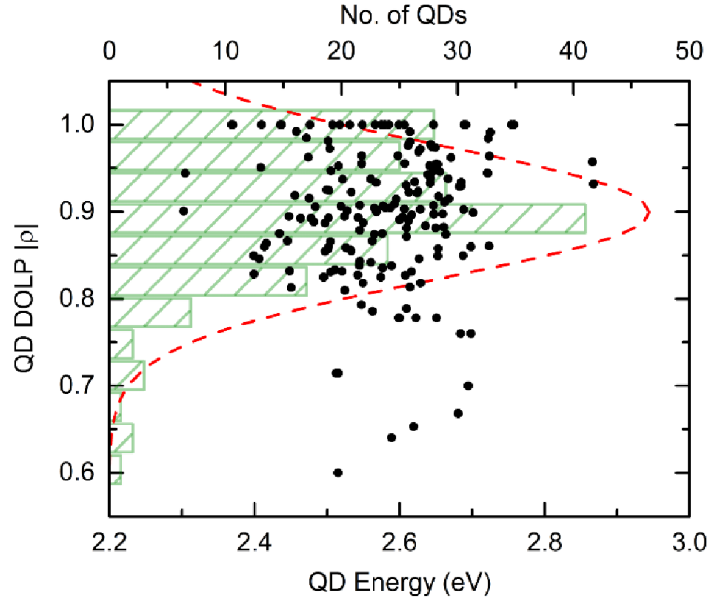


FIGURE 4.4: 180  $a$ -plane InGaN/GaN QD DOLP variation with emission energy. The statistical distributions have been fitted with Gaussian profiles. The means and standard deviations of the Gaussian distributions are  $0.90 \pm 0.08$

In the next step, the alignment of the polarization axis during the polarization measurement was also studied. It was found that 91% of the QDs exhibit polarization aligned along the  $m$ -axis, which agrees well with the simulation results. However, 9% of the studied QDs emit light polarized along the  $c$ -axis. In our theoretical framework, this would mean that the hole ground state is predominantly  $|X\rangle$ -like in orbital character. From Fig. 4.2, one can infer that  $\rho$  drops significantly for  $\alpha > 3$ , and more so with higher In content, as the confinement effects due to increased band offsets become stronger, making asymmetries in the QD geometry more prominent. Producing a predominant  $|X\rangle$ -like hole ground state would hence require an extreme deformation of the QD ( $d_x = 30$  nm,  $d_y = 6$  nm) and very high In content. It is also to note that in addition to strong shape anisotropies, alloy fluctuation effects might also contribute to the observed behavior [187]. However overall, our experimental and theoretical data show that  $a$ -plane InGaN/GaN QDs are able to achieve efficient linearly polarized photon emission with consistently high DOLP values and a deterministic polarization axis.

#### 4.3.2 Statistical study of DOLP as a function of temperature: Theory experiment comparison

In the next step, to assess temperature dependence of the polarization properties, temperature-dependent polarization-resolved  $\mu$ -PL experiments were carried out in Oxford. The temperature dependence of the DOLP for an arbitrary QD in 20 K steps up to 200 K is shown in Fig. 4.5 (a). By using polarization formula, Eq. (4.1), a polarization degree of 0.93 at 5 K was obtained in the experimental studies. As we can see from Fig. 4.5 (a), the measurements show that

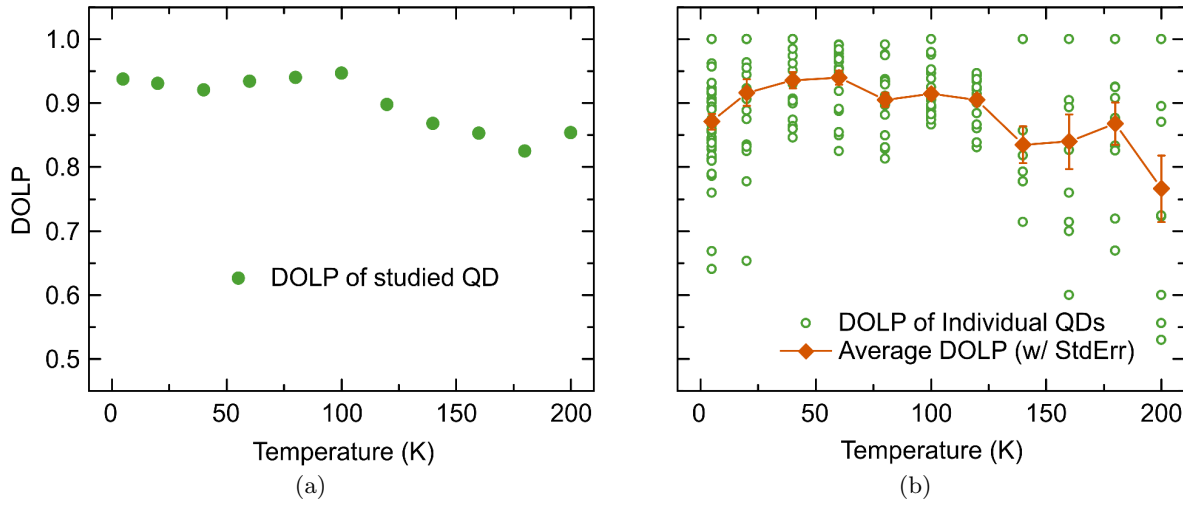


FIGURE 4.5: (a) DOLP of the studied QD at 5 K, and from 20 to 200 K at 20 K intervals. With a slight reduction at higher temperatures, the DOLP always remained at 0.80 and above. (b) Statistical study of the DOLP variation (open circles) with temperature. Also shown is the average DOLP (filled diamonds) with standard error at each temperature step, which stays above 0.75.

the polarization degree stays fairly constant up to 100 K. The DOLP then starts to decrease slowly at higher temperatures, reaching 0.85 at 200 K. This small decrease of 8%, and the consequent insensitivity to changes in temperature indicate that the studied  $a$ -plane InGa $N$  QD is indeed a reliable polarized photon emitter even at thermoelectrically cooled temperatures. This experimental  $\rho$  data for the studied QD is in good agreement with the DOLP values obtained for QDs having  $\alpha = 1$  and  $\alpha = 2$  in Sec. 4.2.2. In order to achieve statistical significance for this finding, the polarization properties of 200 individual QDs with no selection bias at different temperatures have been studied in the experiment. An average DOLP (filled diamonds) with standard error at each temperature was evaluated and is displayed with the DOLP data for individual QDs (open circles) in Fig. 4.5 (b). The average stays above 0.85 and remains relatively constant from 5 to 120 K, before small drops occur beyond this temperature range. In fact, around half of the measured QDs have a DOLP of 0.9 or higher for  $T \leq 100$  K. It is worth noting that several QDs had a DOLP of 1, and a few more very close to 1 at each temperature step was measured. Conversely, QDs with lower DOLP values were also found. This difference in DOLP values can be attributed partly to the previously described differences in shape anisotropies which might be present in these dots. Additionally, recent atomistic calculations [187] on  $m$ -plane InGa $N$ /Ga $N$  QDs have revealed that alloy fluctuations might cause band mixing effects and accordingly, a reduced DOLP. Therefore, different alloy microstructures can also contribute to the spread in DOLP values here. The larger spreads observed at higher temperatures are indicative of the presence of lower DOLP for some QDs in this temperature range. In addition to the shape anisotropies, this may be caused by the above discussed band mixing effects in the excited states. Nonetheless, all average DOLP data remain at or above 0.77, indicating statistically high DOLP up to 200 K, comparable even

to most low-temperature QD DOLP reports from the literature [198, 199, 216, 217]. In line with our theoretical findings, the direction of polarization of these QDs also coincides with the crystal  $m$ -axis (perpendicular to the  $c$ -axis) at all temperatures studied here.

## 4.4 Conclusion

In summary, our theoretical studies combining Fermi-Dirac Statistics and  $\mathbf{k} \cdot \mathbf{p}$  theory have demonstrated high DOLP values for  $a$ -plane InGaN QDs. These high DOLP values are relatively insensitive to both QD anisotropies and temperature changes, thanks to the reduced band mixing effect caused by the change in symmetry in  $a$ -plane structures compared to a  $c$ -plane case. Statistically significant experimental investigations by our collaborators demonstrate highly polarized emission with an average DOLP of  $> 0.9$  at  $T \leq 100\text{K}$  which agrees very well with our theoretical results. Additionally, the polarization axis has been theoretically and experimentally determined to be mostly along the crystallographic  $m$ -axis direction, with a small (9%) minority along the  $c$ -axis. The results presented in this work as a whole shows that efficient polarization control in on-chip temperatures can be achieved in solid-state QDs, a step forward for the development or related optoelectronic and quantum information applications. This work also leads to the fact that one can achieve linearly polarized single photon emission from these dots up to elevated temperatures [215] as demonstrated (not shown here) by our experimental collaborators.



## Chapter 5

# Impact of second-order piezoelectricity on built-in fields, electronic and optical properties of *c*- and non-*c*-plane heterostructures

In previous chapters, the piezoelectric polarization vector field in WZ InGaN/GaN QDs has been calculated by taking into account linear piezoelectric contributions only. For several years, a similar first-order approach has been used to describe piezoelectric fields in ZB heterostructures such as InAs/GaAs QDs [56, 137]. But, in recent years, several groups have reported that in addition to first-order piezoelectric contributions, second-order effects, quadratic in strain, play an important role for an accurate description of the piezoelectric vector fields and thus connected electronic and optical properties of these systems [57, 172]. These second-order piezoelectric effects have been widely neglected in WZ III-N materials. Only recently second-order piezoelectric coefficients for GaN, AlN and InN have been reported [218–220]. Based on these coefficients, electric fields in *c*-plane nitride-based QWs have been studied, showing that when including second-order piezoelectricity, in general, a better agreement between theory and experiment is achieved [59, 218, 220]. However, there exist no detailed analysis of how second-order piezoelectricity affects the built-in field in semipolar QWs and/or polar, semi- and nonpolar QDs. Especially, given that first-order piezoelectric effects are strongly reduced in semi- and nonpolar systems, it is still an open question how important second-order contributions are for the total built-in field. This question is significant not only from a fundamental physics perspective; it is also essential from an application point of view, given the interest in these semi- and nonpolar nitride-based heterostructures for optoelectronic devices.

Moreover, it is also important to understand how the change in built-in field due to second-order piezoelectricity affects the electronic and optical properties such as wave function overlaps and oscillator strength in III-N QDs. Especially, as we will show later, given the recent drive for  $\text{In}_x\text{Ga}_{1-x}\text{N}$  QD based light emitters with high In contents ( $x \approx 0.4$ ) for high-performance red-emitting laser diodes [21, 22], the question of how vital second-order piezoelectric effects are for an accurate description of red emitting systems.

In this chapter, we address these questions by means of the continuum-based framework discussed in Sec. 3.1. The present chapter is organized as follows. Sec. 5.1 gives a general overview of the theoretical framework used here. After that, we move to present the results of our studies in Sec. 5.2. In Sec. 5.2.1 we show how built-in fields in different systems are affected by second-order piezoelectricity. We start, in Sec. 5.2.1.1, with WZ III-N QWs before turning to QD structures in Sec. 5.2.1.2 where we focus on GaN/AlN and InGaN/GaN QD systems grown on different substrate orientations. In the next section, Sec. 5.2.2 we only focus on InGaN/GaN QDs and analyze how changes in the built-in field affect the electronic and optical properties of these dots. Finally, in Sec. 5.2.3, we investigate the electronic and optical properties of the red emitting *c*-plane InGaN/GaN QDs and discuss how second-order piezoelectric effects affect the emission wavelength and radiative lifetime of these dots when the In content in the dot is varied .

## 5.1 Theory

We start in Sec. 5.1.1 with a brief overview of the second-order piezoelectric polarization vector field in III-N systems. This is followed by a summary of the theoretical framework applied.

### 5.1.1 Polarization vector fields in WZ III-N semiconductor nanostructures

As described in the introduction, Sec. 1.2.2 (cf. Eq. (1.2)) the total piezoelectric polarization vector field in a WZ system can be expressed as a sum of first- and second-order contributions [57]. In Sec. 2.5, we have already discussed the widely used first-order contribution,  $P_{\text{pz},\mu}^{\text{FO}}$ . In this section, we focus our attention on the second-order piezoelectric contribution,  $P_{\text{pz},\mu}^{\text{SO}} = \frac{1}{2} \sum_{jk=1}^6 B_{\mu jk} \varepsilon_j \varepsilon_k$ , cf. Eq. (1.2). In general, it should be stressed that the second-order piezoelectric effect is not just a second-order term in a polynomial expansion of the piezoelectric response of a material. Pal *et al.* [218] pointed this already out for III-N materials. Additionally, Beya-Wakata *et al.* [221] and Caro *et al.* [222] highlighted in their work on ZB III-V materials that in certain materials second-order effects can dominate over first-order contributions, even for small strain. Fundamentally different factors contribute to first- and second-order piezoelectricity, for example, linear and nonlinear contributions to internal strain parameters and

the material electronic response [222]. Furthermore, similar to first-order piezoelectric coefficients, the symmetry of the underlying crystal structure of the material under consideration determines the number of non-vanishing and independent second-order piezoelectric coefficients  $B_{\mu jk}$ . [55]

Based on symmetry considerations, for instance given by Grimmer [55], one can show that for systems with a WZ crystal structure  $B_{\mu jk}$  has 17 non-vanishing components of which 8 are independent. Using this information and Eq. (1.2), for a  $c$ -plane system where the  $z$ -axis of the coordinate system is parallel to the WZ  $c$ -axis, different components of the second-order piezoelectric polarization vector field  $\mathbf{P}_{\text{pz}}^{\text{SO}}$  is given by:

$$\begin{aligned} P_{\text{pz},x}^{\text{SO}} &= 2B_{115}(\varepsilon_{xx}\varepsilon_{xz} + \varepsilon_{xy}\varepsilon_{yz}) + 2B_{135}\varepsilon_{zz}\varepsilon_{xz} - 2B_{125}(\varepsilon_{xy}\varepsilon_{yz} - \varepsilon_{yy}\varepsilon_{xz}); \\ P_{\text{pz},y}^{\text{SO}} &= 2B_{115}(\varepsilon_{yy}\varepsilon_{yz} + \varepsilon_{xy}\varepsilon_{xz}) + 2B_{135}\varepsilon_{zz}\varepsilon_{yz} + 2B_{125}(\varepsilon_{xx}\varepsilon_{yz} - \varepsilon_{xy}\varepsilon_{xz}); \\ P_{\text{pz},z}^{\text{SO}} &= \frac{B_{311}}{2}(\varepsilon_{xx}^2 + \varepsilon_{yy}^2 + 2\varepsilon_{xy}^2) + B_{312}(\varepsilon_{xx}\varepsilon_{yy} - \varepsilon_{xy}^2) + B_{313}(\varepsilon_{xx}\varepsilon_{zz} + \varepsilon_{yy}\varepsilon_{zz}) \\ &\quad + 2B_{344}(\varepsilon_{yz}^2 + \varepsilon_{xz}^2) + \frac{1}{2}B_{333}\varepsilon_{zz}^2. \end{aligned} \quad (5.1)$$

Please note, like Eq. (2.59), the Cartesian notation for the strain tensor  $\varepsilon_{ij}$  has been used here. In comparison to the first-order piezoelectric polarization vector field, cf. Eq. (2.59), the interplay of the different strain contributions is far more complicated. The  $x$ - and  $y$ -components no longer just depend on shear strain components  $\varepsilon_{ij}$  with  $i \neq j$ . Here, also products of shear strain parts and diagonal components  $\varepsilon_{ii}$  arise. Furthermore, the  $z$ -component is now not only dependent on diagonal parts of the strain tensor  $\varepsilon_{ii}$ , also shear strain components become important. Moreover, the increased number of second-order piezoelectric coefficients  $B_{\mu jk}$ , especially related to shear strains, presents also a significant difference compared to the first-order piezoelectric component. This means that one could expect in systems where shear strain contributions are significant, e.g. semipolar WZ QWs, second-order piezoelectricity is important for an accurate description of the connected electrostatic built-in fields in these systems. Using the expressions given in Eq. (1.3), Eq. (2.59) and Eq. (5.1), the total polarization vector field  $\mathbf{P}_{\text{Tot}}$  can be calculated as  $\mathbf{P}_{\text{Tot}} = \mathbf{P}_{\text{SP}} + \mathbf{P}_{\text{pz}}^{\text{FO}} + \mathbf{P}_{\text{pz}}^{\text{SO}}$ . Subsequently, the connected electrostatic built-in potential  $\phi_p$  in III-N heterostructures can be evaluated by solving Poisson's equation as described in detail in Sec. 2.5.

In order to study the effect of second-order piezoelectricity on the built-in potential of WZ III-N heterostructures, such as QWs and more challenging QDs, grown on different crystallographic planes one has to rotate the expressions for the polarization vector fields and strain tensors according to the methodology discussed in Sec. 2.2.1. In nitride-based QWs and for first-order piezoelectricity this is a widely used approach [65, 223–225]. However, all these works do not account for second-order piezoelectric effects. But, once the analytic expression for  $\mathbf{P}_{\text{pz}}^{\text{SO}}$  as a function of  $\theta$  is known, it can be easily implemented in existing symmetry adapted QW

codes. We provide this expression for  $\mathbf{P}_{\text{pz}}^{\text{SO}}$ , along with the one for  $\mathbf{P}_{\text{pz}}^{\text{FO}}$ , in Appendix C. When treating the QW as a one-dimensional system, only the  $z$ -component of the total polarization vector field is required for calculating the built-in potential. For QD systems, due to their three-dimensional confinement, the  $x$ -,  $y$ - and  $z$ -components are relevant. Thus the expressions provided here allow for the calculation of electrostatic built-in potentials of both QD and QW systems grown along arbitrary crystallographic directions characterized by the incline angle  $\theta$ .

So far we have introduced general aspects of the polarization vector fields and connected electrostatic potentials in WZ semiconductor heterostructures up to second-order piezoelectricity. In the next step, we briefly discuss the theoretical framework in which our calculations have been carried out.

### 5.1.2 Theoretical Framework and Material input parameters

Equipped with the analytic expressions for spontaneous, first- and second-order piezoelectric polarization vector fields as a function of  $\theta$ , cf. Appendix C, these terms have been implemented in the highly flexible plane-wave based software library S/Phi/nX [126, 163]. As described earlier in Sec. 3.1, S/Phi/nX in general allows for defining arbitrary elastic and piezoelectric tensors as well as  $\mathbf{k} \cdot \mathbf{p}$  Hamiltonians.

In the first step, we study the impact of second-order piezoelectric effects on the electrostatic built-in fields in nitride-based QW and QD structures grown along different crystallographic directions. In Sec. 2.5, we have already outlined how to calculate the electrostatic built-in potential  $\phi_p$  once the polarization vector field is known. However, as further input, the (position dependent) strain tensor  $\varepsilon_{ij}$  of the system under consideration is required. Here, we use a continuum-based approach detailed in Sec. 2.4.2 to calculate the strain tensor components. Having calculated the strain field and built-in potentials, in a second step, a 6+2 band  $\mathbf{k} \cdot \mathbf{p}$  Hamiltonian is employed to obtain the electronic structure of the here considered QD systems. This Hamiltonian is already described in Sec. 2.2.1.1. The strain effects are included via the Pikus-Bir Hamiltonian as described in Sec. 2.3.1. The built-in potential enters the Hamiltonian as a diagonal correction (cf. Sec. 2.5).

Finally, we account for excitonic corrections by using the  $\mathbf{k} \cdot \mathbf{p}$  wave functions as input for self-consistent Hartree calculations [172]. The details of Hartree calculations employed in this work can be found in Sec. 2.6. In addition to the QW dimensions and QD geometries, which will be discussed below, material parameters are required as input. In the following we focus our attention on systems based on InN, GaN, AlN and their respective alloys. Table B.2 of Appendix B, summarizes the here used material parameters for the binary materials. While there are several reports on first-order piezoelectric coefficients, only very few studies have been

performed to extract second-order piezoelectric coefficients  $B_{\mu jk}$  for WZ III-N systems [218–220]. In the following we use the parameter set by Prodhomme *et al.* [220] since it contains for the material systems InN, GaN and AlN values for all non-vanishing coefficients  $B_{\mu jk}$ . Thus it provides a consistent parameter set for our study here. Overall, our main focus is to gain insight into trends of how second-order piezoelectric effects affect the electrostatic built-in fields, and as a result electronic and optical properties of nitride-based nanostructures grown on different substrate orientations. Therefore, to describe alloys we assume a linear interpolation for all material parameters except the spontaneous polarization, where we apply the bowing parameters  $b_{\text{SP}}$  from Ref. [226]. Further, more detailed calculations, looking at impact and importance of different material parameter sets and the choice of bowing parameters, can be performed in a straightforward way once these quantities are known. However, this is beyond the scope of the present study where we are interested in general effects. Having established the theoretical framework, we now present the results of our analysis in the next section.

## 5.2 Results

Here, in a first step, in Sec. 5.2.1, we focus on how the built-in potential of III-N heterostructures grown along different crystallographic directions is affected by second-order piezoelectricity. In the next step, in Sec. 5.2.2, the impact of second-order piezoelectric effects on the electronic and optical properties of III-N InGaN/GaN QD systems is studied in detail. Finally, in Sec. 5.2.3, we analyze how second-order piezoelectricity affects the emission wavelength and radiative lifetime of *c*-plane InGaN/GaN QDs as a function of the In content.

### 5.2.1 Built-in potential in III-N heterostructures grown along different crystallographic directions

This section is organized as follows. In Sec. 5.2.1.1, we focus on QW structures and study polarization fields for different material combinations and growth directions. In Sec. 5.2.1.2, we turn our attention to the built-in potential in GaN/AlN and InGaN/GaN QD systems grown on different substrate orientations.

#### 5.2.1.1 Impact of second-order piezoelectricity on built-in fields in III-N QWs

An ideal QW structure can be treated as a one-dimensional system since quantum confinement is present along one direction only. We use this approximation here and start from *c*-plane structures where the *c*-axis is parallel to the *z*-axis of the coordinate system. In the following, the QW growth direction is always the *z'*-axis of the rotated coordinate system. In this

one-dimensional problem discontinuities in the polarization vector field  $\mathbf{P}$  occur only along the growth direction. Therefore, only the  $z$ -component of  $\mathbf{P}$  is relevant for a QW structure. The situation is more complex for a QD system where the three-dimensional confinement of the dot comes into play and the full polarization vector field needs to be considered. This question will be addressed in Sec. 5.2.1.2 and 5.2.1.2. Here, to gain insight into the interplay of second-order piezoelectricity and growth plane, we start with the most extreme cases by studying GaN/AlN, InN/AlN and InN/GaN systems. Figure 5.1 displays the  $z$ -component of the different contributions to the full *piezoelectric* response,  $P_{\text{pz},z'}^{\text{FO}} + P_{\text{pz},z'}^{\text{SO}}$ , as a function the incline angle  $\theta$  for GaN/AlN (Fig. 5.1 (a)), InN/AlN (Fig. 5.1 (b)) and InN/GaN (Fig. 5.1 (c)). To shed light onto the importance of the second-order piezoelectric contribution, results are shown for (i) “standard” first-order terms only,  $P_{\text{pz},z'}^{\text{FO}}$  (red circles), (ii) taking only second-order piezoelectric effects into account,  $P_{\text{pz},z'}^{\text{SO}}$  (black squares), and (iii) the sum of first- and second-order components  $P_{\text{pz},z'}^{\text{FO}} + P_{\text{pz},z'}^{\text{SO}}$  (blue triangles). The vertical dashed lines in Fig. 5.1 indicate some of the experimentally relevant growth planes for semi- and nonpolar nitride-based QWs [45, 224, 227–229]. Overall, for the three systems under consideration, the second-order contribution (black squares) is smaller than the first-order contribution (red circles). Furthermore, we find that for certain planes, for instance the  $(10\bar{1}3)$ -plane, second-order piezoelectricity has a negligible effect on the  $z$ -component of the total piezoelectric polarization vector field. This originates from the fact that the second-order contribution is changing sign around this angle ( $\theta \approx 30^\circ$ ). However, for  $c$ -plane systems and structures grown on planes described by  $\theta$  values in the range of  $55^\circ \leq \theta \leq 80^\circ$  and  $105^\circ \leq \theta \leq 120^\circ$ , the magnitude of the total piezoelectric polarization (blue triangles) is clearly increased by second-order piezoelectricity. More specifically, for the polar  $c$ -plane structures ( $\theta = 0^\circ$ ) of the three different systems studied here, the full piezoelectric polarization values increase by 11%-14% when taking second-order piezoelectric effects into account. It should be noted that this increase is consistent with the  $c$ -plane results presented in Ref. [218] where a different first- and second-order piezoelectric coefficient set has been used. However, the  $c$ -plane data presented in Ref. [220], applying a slightly different first-order parameter set  $e_{\mu j}$  but the same second-order parameter set  $B_{\mu j k}$ , indicated a decrease in  $P_{\text{pz},z'}^{\text{FO}} + P_{\text{pz},z'}^{\text{SO}}$  for InN/GaN systems when compared to  $P_{\text{pz},z'}^{\text{FO}}$  only. Based on a closer inspection of the results in Ref. [220] we relate the observed reduction in  $P_{\text{pz},z'}^{\text{FO}} + P_{\text{pz},z'}^{\text{SO}}$  to differences in the applied Poisson ratio/biaxial coefficient. In our case we assume for all the systems studied here a homogenous biaxial strain along the  $z'$ -axis. For a  $c$ -plane system this results in  $\varepsilon_{zz} = -\frac{2C_{13}}{C_{33}}\varepsilon_{xx}$ . As input we use the parameters given in Table B.2 of Appendix B.

Turning to the semipolar planes, where the magnitude of  $P_{\text{pz},z'}^{\text{FO}}$  is reduced compared to the  $c$ -plane system, the impact of the second-order piezoelectric effect is even larger. For example, at  $\theta = 75^\circ$ , the  $(20\bar{2}1)$ -plane, the magnitude of the overall piezoelectric response changes by 33%, 44% and 32% for GaN/AlN, InN/AlN and InN/GaN systems, respectively, when second-order piezoelectric effects are included.

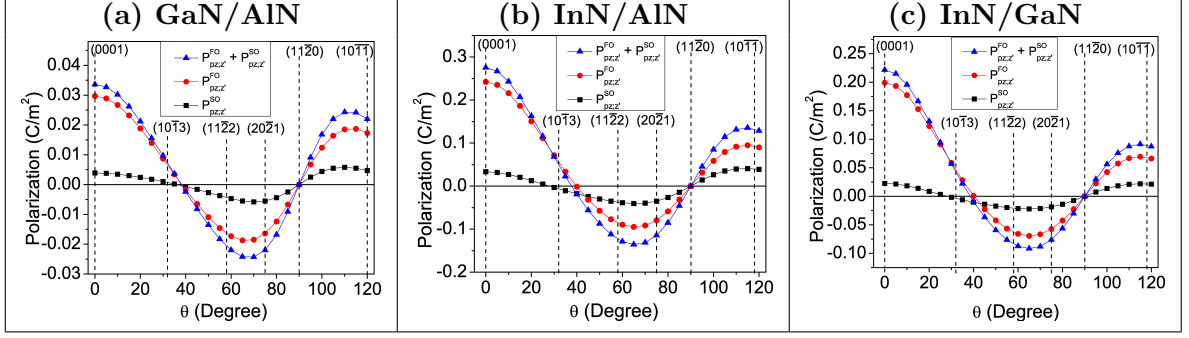


FIGURE 5.1:  $z$ -component of piezoelectric polarization vector fields in (a) GaN/AlN, (b) InN/AlN and (c) InN/GaN systems as a function of the incline angle  $\theta$  to the wurtzite  $c$ -axis. The contributions arising from first-order piezoelectricity are denoted by (red) circles. Contributions entirely stemming from second-order piezoelectricity are given by (black) squares. The total piezoelectric polarization, which includes first- and second-order piezoelectric polarization, is given by (blue) triangles. Dashed vertical lines indicate selected experimentally relevant growth planes.

Based on these general trends we discuss now how second-order piezoelectric effects affect the built-in electric field in nitride-based QWs grown on different substrate orientations. For this analysis we focus on two material systems, namely GaN/AlN and InGaN/GaN-based QWs. Such structures have been studied experimentally in the literature for different substrate orientations [14, 45, 175, 227, 228]. To be able to compare our theoretical results to experimental literature data, we calculate the built-in field inside a multi-QW (MQW) system via [218]

$$F_p(\theta) = - \frac{\left[ P_{sp,z'}^B(\theta) - P_{sp,z'}^W(\theta) \right] + \left[ P_{pz,z'}^B(\theta) - P_{pz,z'}^W(\theta) \right]}{\epsilon_r^W + \epsilon_r^B(t^W/t^B)}. \quad (5.2)$$

Here  $t^W$  ( $t^B$ ) is the QW (barrier) thickness and  $P_{sp,z'}^W(\theta)$  ( $P_{sp,z'}^B(\theta)$ ) is the angle dependent spontaneous polarization in the well (barrier). The angle dependent piezoelectric polarization in the well (barrier) is denoted by  $P_{pz,z'}^W(\theta)$  ( $P_{pz,z'}^B(\theta)$ ).

Equipped with Eq. (5.2) and the analytic expressions given in Appendix C, we can now compare calculated and measured built-in electric fields. The results are summarized in Table 5.1. It should be noted that only a few experimental reports on built-in fields in QW structures grown on semipolar planes are available in the literature [228]. To highlight the impact of the second-order piezoelectric polarization, calculations using Eq. (5.2) have been performed in the absence and in the presence of second-order contributions. In the absence of second-order piezoelectricity,  $P_{pz,z'}^W = P_{pz,z'}^{FO}$ , only first-order piezoelectric coefficients  $e_{\mu j}$  are relevant. In the presence of first- and second-order effects,  $P_{pz,z'}^W = P_{pz,z'}^{FO} + P_{pz,z'}^{SO}$ ,  $P_{pz,z'}^W$  is determined by the combined contributions of both  $e_{\mu j}$  and  $B_{\mu jk}$ . Overall, as expected from our discussion above, when including second-order effects in the calculations, the magnitude of the electric field is increased when compared to a standard first-order only calculation for both GaN/AlN and

TABLE 5.1: Built-in electric fields in GaN/AlN and InGaN/GaN multi-quantum well structures. The well (barrier) thickness is denoted by  $t_w$  ( $t_b$ ). The growth plane, and thus the incline angle to the  $c$ -axis, is given by  $\theta$ . Experimental data taken from the literature is denoted by  $F_{\text{exp}}$ . Our theoretical data including only first-order piezoelectricity and spontaneous polarization, is given by  $F_{\text{theo}}^{\text{FO+SP}}$ . The results of the full calculation, including second-order piezoelectric effects, is denoted by  $F_{\text{theo}}^{\text{FO+SO+SP}}$ .

Material	$t_w$ (nm)	$t_b$ (nm)	$\theta(^{\circ})$	$F_{\text{exp}}$ (kV/cm)	$F_{\text{theo}}^{\text{FO+SP}}$ (kV/cm)	$F_{\text{theo}}^{\text{FO+SO+SP}}$ (kV/cm)
GaN/AlN	2.6	100	0	1020 [230]	957	1004
GaN/AlN	2.5	6	0	800 [231]	710	744
GaN/AlN	2.3	1.9	0	504 [232]	465	488
GaN/AlN	1.4	1.9	0	607 [232]	586	614
In <sub>0.12</sub> Ga <sub>0.88</sub> N/GaN	3	6	0	1600 [229]	1530	1620
In <sub>0.12</sub> Ga <sub>0.88</sub> N/GaN	4	30	58	-575±150 [228]	-397	-444
In <sub>0.15</sub> Ga <sub>0.85</sub> N/GaN	4	30	118	840±150 [228]	587	666
In <sub>0.06</sub> Ga <sub>0.94</sub> N/GaN	3	3	0	610 [229]	593	610
In <sub>0.22</sub> Ga <sub>0.78</sub> N/GaN	3	8	0	3090 [229]	2940	3220
In <sub>0.09</sub> Ga <sub>0.91</sub> N/GaN	3	3	0	1000 [229]	880	920

InGaN/GaN systems, cf. Table 5.1. One can also conclude from Table 5.1 that the second-order piezoelectric contributions have a larger impact on the magnitude of the built-in field in semipolar structures and changes of 12%-14% in magnitude are observed. The experimental reports presented here are not direct measurements of the built-in fields, rather they are deduced from the variation of the PL emission energy with well-width [229, 230]. Additionally, the PL peak position could also be affected by alloy disorder effects in addition to the QCSE [114]. Nonetheless, in general, when comparing the calculated fields to the experimental data, we find that with first-order piezoelectricity only the theoretical values underestimate the magnitude of the electric field in the respective structures. When including second-order piezoelectricity, an improved agreement between theory and experiment is observed.

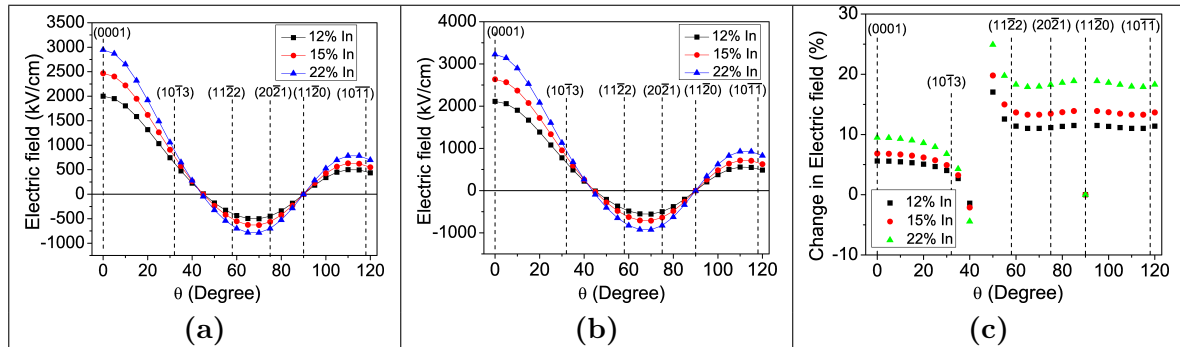


FIGURE 5.2: Built-in electric field in InGaN/GaN multi-QWs (MQWs) as a function of the incline angle  $\theta$  to the wurtzite  $c$ -axis. Results for MQW systems with 12% In (black square), 15% In (red circle) and 22% (blue triangle) are displayed. More details about the systems are given in Table 5.1 and in the text. (a) Only first-order piezoelectricity and spontaneous polarization components are taken into account. (b) First- and second-order piezoelectricity as well as spontaneous polarization are included in the calculations. (c) Relative changes in the electric field due to second-order piezoelectric effects.

To study the impact of the second-order piezoelectric effect on the electric field in more detail and how the growth plane contributes to this,  $F_p(\theta)$  (cf. Eq. 5.2) is shown as a function of the incline angle  $\theta$  for different  $\text{In}_x\text{Ga}_{1-x}\text{N}/\text{GaN}$  QW systems in Fig. 5.2. The electric field  $F_p(\theta)$ , Eq. (5.2), has been calculated for three different In contents  $x$ , namely 12%, 15% and 22%. For the 12% and 15% In system we use the experimental results in terms of well and barrier thickness given in Ref. [228] based on  $(11\bar{2}2)$ - and  $(10\bar{1}1)$ -oriented MQWs. Applying the experimental findings of Ref. [228], well and barrier thickness are chosen to be  $t^W = 4$  nm and  $t^B = 30$  nm, [228] respectively. For the 22% In MQW system the settings reported by Hangleiter *et al.* [229] for a  $(0001)$ -oriented system have been used ( $t^W = 3$  nm;  $t^B = 8$  nm) [229]. When varying the incline angle  $\theta$  in our calculations the barrier and QW thicknesses of the here considered structures have been kept constant to achieve a consistent comparison. Figure 5.2 (a) displays the calculated electric field in the absence of second-order contributions to the piezoelectric polarization in  $P_{\text{pz},z'}^W$ , cf. Eq. (5.2). Given the strain dependence of the piezoelectric polarization, the total electric field is largest in the sample with the highest In content (blue triangle). Independent of the In content, at  $\theta \approx 45^\circ$  and  $\theta = 90^\circ$  the electric field changes sign. When including second-order piezoelectric contributions in the calculations, cf. Fig. 5.2 (b), this behavior of zero electric field and sign change is approximately unaffected. However, the magnitude of the electric field, independent of the incline angle  $\theta$ , is always increased. To flesh out this effect even more clearly, Fig. 5.2 (c) depicts the electric field increase in percent obtained from the difference between the results displayed in Fig. 5.2 (a) (no second-order contributions) and (b) (with second-order effects). The data further confirms that especially for semipolar planes, where fields are significantly reduced compared to the  $c$ -plane structures, second-order effects can play an important role for an accurate description of the built-in fields in these structures. More specifically, for the  $(20\bar{2}1)$ -plane ( $\theta = 75^\circ$ ) the magnitude of the electric field increases by 11%, 13%, 18% for an In content of 12%, 15% and 22%, respectively, due to second-order piezoelectricity.

Having presented a detailed analysis of the impact of second-order piezoelectric effects on the electric built-in fields in nitride-based QWs grown along different crystallographic directions, we turn now to discuss nitride-based QDs. The results of this analysis are presented in the following section.

### 5.2.1.2 Impact of second-order piezoelectricity on built-in potential in wurtzite III-N QDs

In this section we focus our attention on the impact of the second-order piezoelectric effect on the electrostatic built-in potential in nitride-based QDs. Again, special attention is paid to the impact of the growth plane on the results. To focus entirely on changes arising from second-order piezoelectric effects and the growth plane, we keep the QD geometry fixed throughout

this study. A detailed analysis of the impact of the QD geometry is beyond the scope of the present analysis. Furthermore, given the three-dimensional QD geometry, the built-in potential and thus the electric field inside and around the nanostructure are position dependent. Thus, and in contrast to the QW systems discussed above, these quantities cannot be characterized by a single number. Therefore, instead of varying the incline angle  $\theta$  continuously, we focus on selected experimentally relevant growth planes. In addition to  $c$ -plane InGaN/GaN and GaN/AlN QD systems, QD growth on the  $(11\bar{2}2)$ -plane has also been reported in the literature [17, 45, 227]. This plane is schematically shown in Fig. 1.3. Also, as described in previous chapters, both InGaN/GaN and GaN/AlN QDs have been grown on the nonpolar  $a$ -plane [14, 174–176, 215, 233]. In the following, we have directed our attention towards these three planes. For these studies we have assumed a lens-shaped dot geometry, which has also been considered in other theoretical works [161, 162, 234]. A QD base diameter of 14 nm and a height of 3 nm has been used in all calculations. These values are in the range of experimentally reported dimensions for dots grown on different planes [174, 235]. Moreover, for the InGaN/GaN QD systems studied in this section, we consider an In content of 20%, inline with several experimental reports on  $c$ - and nonpolar systems [14, 175, 185].

Starting from this information, the calculated built-in potentials for GaN/AlN and  $\text{In}_{0.2}\text{Ga}_{0.8}\text{N}$ /GaN QDs grown on different substrate orientations are discussed in the following.

### Built-in potentials in GaN/AlN QDs

Figure 5.3 shows contour plots of the electrostatic built-in potential  $\phi_p$  in GaN/AlN QDs grown along different crystallographic directions. The first row displays the results for the  $c$ -plane case ( $\theta = 0^\circ$ ), the middle one for the semipolar  $(11\bar{2}2)$ -system ( $\theta = 58^\circ$ ), and the lowest row depicts data for the nonpolar structure ( $\theta = 90^\circ$ ). Here, a slice through the QD center in  $x' - z'$ -plane is chosen where the  $z'$ -axis is always parallel to the growth direction. The (blue) dashed lines indicate the QD geometry. In the left column, Fig. 5.3 (a), the results of the calculations in the absence of second-order piezoelectric contributions are depicted. Thus only “standard” first-order piezoelectric effects and the spontaneous polarization are taken into account. The middle column, Fig. 5.3 (b), shows the second-order piezoelectric contribution on its own. This means that calculations in the absence of spontaneous and first-order piezoelectric polarization have been performed. The results of the full calculation, including first- and second-order piezoelectricity as well as the spontaneous polarization, are displayed in Fig. 5.3 (c), right column. We start our analysis by looking at Fig. 5.3 (a), thus neglecting second-order piezoelectricity. In the case of the  $c$ -plane system, upper part of Fig. 5.3 (a), we observe the well-known, very strong potential drop across the nanostructure along the growth direction. This particularity of the potential profile has the effect of spatially separating electron and hole wave functions along the growth direction and results in strongly increased radiative lifetimes

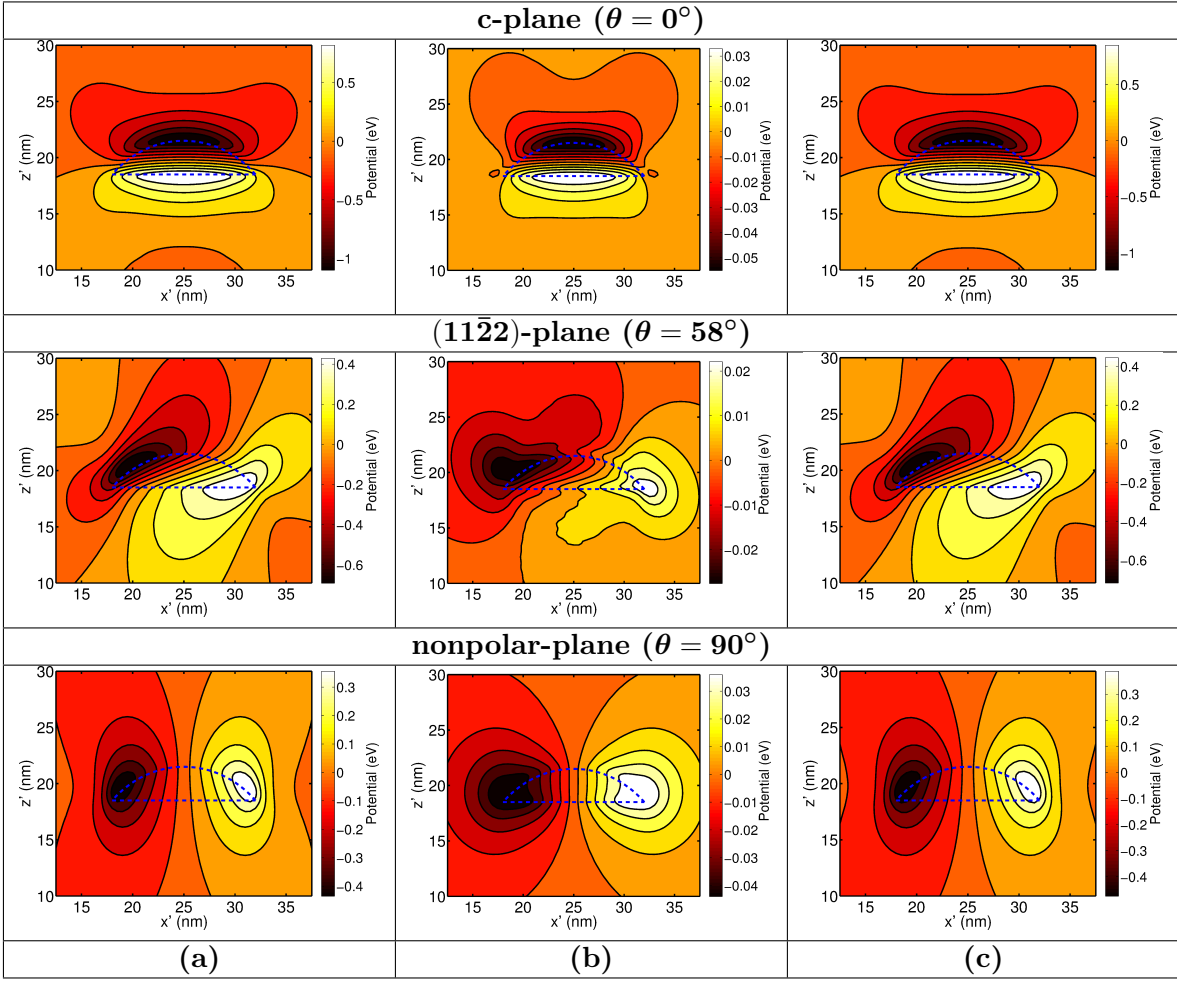


FIGURE 5.3: Contour plots of the electrostatic built-in potential of lens-shaped GaN/AlN QDs grown on  $c$ - (upper row),  $(11\bar{2}2)$ - (middle row) and nonpolar  $a$ -planes (lower row). The contour plots are shown for a slice through the center of the QD in the  $x' - z'$ -plane where the  $z'$ -axis is parallel to the different growth directions considered here. (a) Built-in potential stemming from first-order piezoelectricity and spontaneous polarization. (b) Built-in potential arising from second-order piezoelectricity only. (c) Total built-in potential, originating from spontaneous polarization, first- and second-order piezoelectricity.

when compared to situations without such a field [236]. Turning to the semipolar case, middle part of Fig. 5.3 (a), we find, as expected from our discussion above, a strongly reduced built-in potential. This stems from the fact that the  $c$ -axis describes now a non-vanishing angle with the growth direction. Thus, the potential drop does not occur along the growth direction but still along the direction of the  $c$ -axis. Finally, when turning to the nonpolar case, lower part of Fig. 5.3 (a), we find that the built-in potential is not zero as in the QW. This is attributed to the fact that the QD still exhibits facets oriented along the  $c$ -axis [154, 237]. Interestingly, for the dot geometry chosen here, the magnitude of the built-in potential in the nonpolar case is comparable to the magnitude of the built-in potential in the semipolar system. Thus, in terms of the built-in potential magnitude, our calculations do not indicate a significant improvement when moving from the  $(11\bar{2}2)$ -system to the nonpolar growth plane. However, it should be noted that this feature could be related to the particular QD geometry chosen here. When

considering different QD geometries, which could and probably will vary between the two growth planes, the situation might be different. We will come back to the question of the QD geometry further below.

We now turn to discuss second-order piezoelectric effects. To do so, we neglect spontaneous polarization and first-order piezoelectricity and focus on the second-order piezoelectric contribution only. The data of this investigation is shown in Fig. 5.3 (b). Before looking in detail into the results, please note the different potential scales between Fig. 5.3 (a) and (b). When comparing Fig. 5.3 (a) and (b), we clearly observe that for GaN/AlN QDs second-order piezoelectric effects, at least for the chosen dot geometry, are significantly smaller when compared to the combined spontaneous and first-order piezoelectric polarization response. The second-order piezoelectric contribution is at least a factor of order 10 smaller. This finding is independent of the growth plane. Thus our calculations indicate that for GaN/AlN dots, second-order piezoelectric effects are of secondary importance for the total built-in potential. This is confirmed by the fact that the total built-in potential displayed in Fig. 5.3 (c) is basically unchanged in comparison to Fig. 5.3 (a), where second-order piezoelectric effects are absent.

Even though our results signal that second-order piezoelectric effects are small in GaN/AlN QDs, it should be noted that independent of the growth plane, this contribution is of the same symmetry as the combined response of first-order piezoelectric and spontaneous polarization. Therefore, if the second-order piezoelectric response would be larger, an increase in the total built-in potential is expected when accounting for these effects. This is in contrast to the situation in InGaAs/GaAs QDs, where first- and second-order piezoelectric contributions are opposite in sign [57]. This effect might even lead to a complete cancelation of first- and second-order built-in potentials and consequently to a field free situation [57]. We find a similar situation for InGaN/GaN QDs grown on certain crystallographic planes, as we show in the following section. Also, we will discuss in more detail, the origin of the observation that the second-order piezoelectric effect for the here studied GaN/AlN dots is of secondary importance and how this compares to InGaN/GaN systems.

### Built-in potentials in InGaN/GaN QDs

Following the GaN/AlN QD analysis, Fig. 5.4 displays the electrostatic built-in potential for lens-shaped  $\text{In}_{0.2}\text{Ga}_{0.8}\text{N}/\text{GaN}$  QDs grown along the  $c$ - ( $\theta = 0^\circ$ , upper row), the  $[11\bar{2}2]$ - ( $\theta = 58^\circ$ , middle row) and the nonpolar  $a$ -axis ( $\theta = 90^\circ$ , lower row), respectively. The QD geometry is indicated by the (white) dashed lines. The contour plots are again shown for a slice through the center of the dot in the  $x'$ - $z'$ -plane, where the  $z'$ -axis is parallel to the respective growth axes. The left column, Fig. 5.4 (a), depicts the “standard” calculation accounting for first-order piezoelectricity and spontaneous polarization but not second-order piezoelectricity. The middle column, Fig. 5.4 (b), shows the second-order contribution only (no first-order piezoelectric and

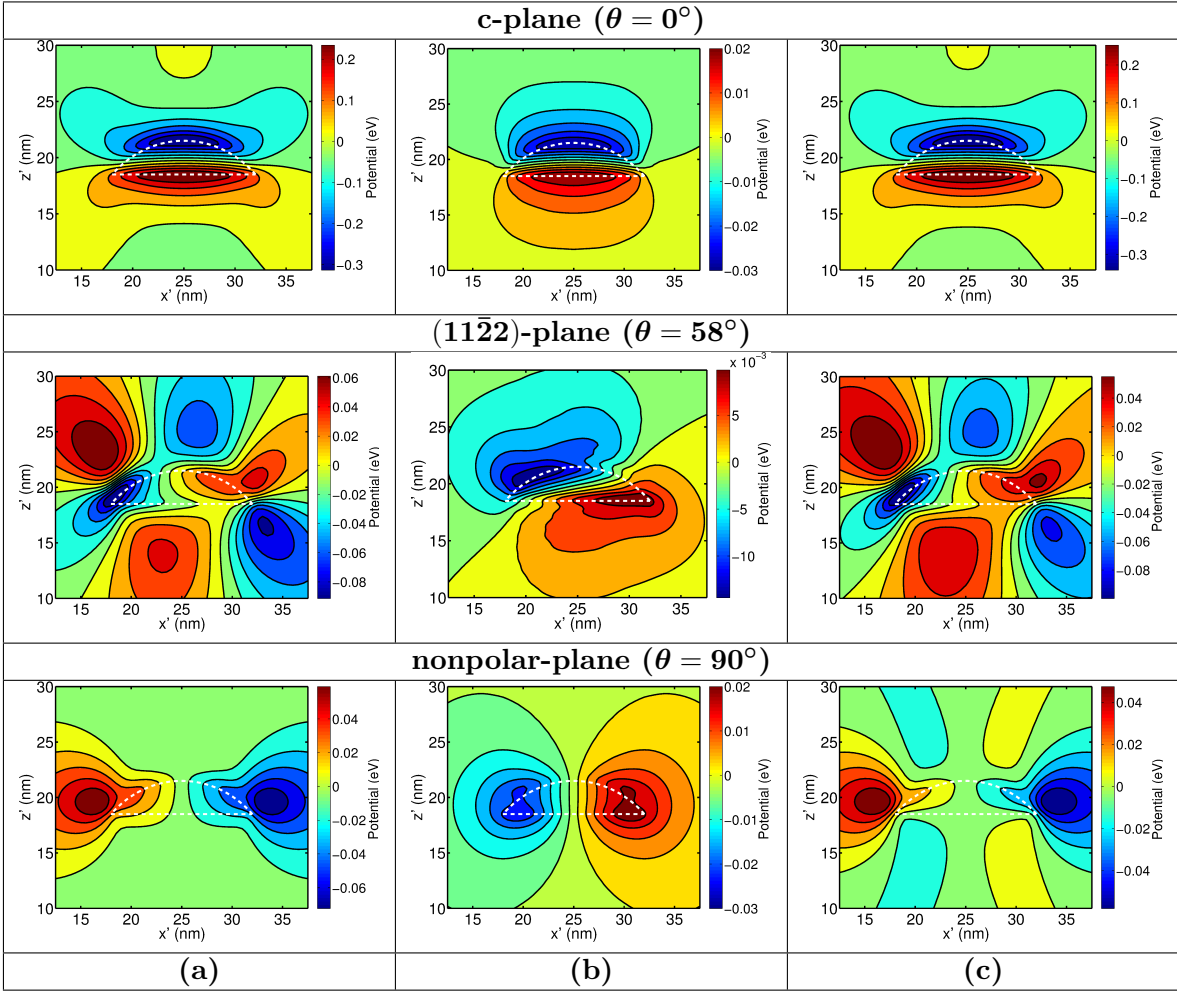


FIGURE 5.4: Contour plots of the electrostatic built-in potential of lens-shaped  $\text{In}_{0.2}\text{Ga}_{0.8}\text{N}/\text{GaN}$  QDs grown on  $c$ - (upper row),  $(11\bar{2}2)$ - (middle row) and nonpolar planes (lower row). The contour plots are shown for a slice through the center of the QD in the  $x' - z'$ -plane where the  $z'$ -axis is parallel to the different growth directions considered here. (a) Built-in potential stemming from first-order piezoelectricity and spontaneous polarization. (b) Built-in potential arising from second-order piezoelectricity only. (c) Total built-in potential, originating from spontaneous polarization, first- and second-order piezoelectricity.

no spontaneous polarization) for the respective systems. The results of the full calculation, accounting for first- and second-order piezoelectricity as well as spontaneous polarization, are displayed in the right column, Fig. 5.4 (c).

Similarly to the  $\text{GaN}/\text{AlN}$  QD data, when looking at Fig. 5.4 (a) first, the semi- ( $\theta = 58^\circ$ ) and nonpolar ( $\theta = 90^\circ$ ) systems exhibit a strongly reduced built-in potential compared to the  $c$ -plane structure ( $\theta = 0^\circ$ ). In the  $c$ -plane system, upper part of Fig. 5.4 (a), the potential drop occurs along the growth direction. In the semipolar case the built-in potential exhibits an extremely complicated profile. For the nonpolar structure we observe a potential drop along the  $x'$ -axis, which is parallel to the WZ  $c$ -axis. It should be noted that in the nonpolar system, even though the built-in potential is not zero, the maxima and minima are located *outside* the nanostructure. Thus inside the QD the built-in potential is almost zero, resulting in a strong

electron and hole wave function overlap in contrast to a  $c$ -plane system, as we will discuss in later sections. Furthermore, the potential profiles and magnitudes of the built-in potential are also different to the GaN/AlN dot systems studied in Fig. 5.3. We attribute this in part to the fact that the spontaneous polarization response for InGaN/GaN systems is much smaller when compared to GaN/AlN [124, 238]. While in GaN/AlN systems the spontaneous polarization contributes approximately 50% to the total built-in potential, in InGaN/GaN systems it is mainly dominated by the strain dependent piezoelectric contributions [124, 238]. We come back to this point further below.

We now turn to discuss second-order piezoelectric effects. Comparing the upper parts of Fig. 5.4 (a) and (b) for the  $c$ -plane  $\text{In}_{0.2}\text{Ga}_{0.8}\text{N}/\text{GaN}$  dot system first, we find that the second-order piezoelectric contribution is significantly smaller than the potential arising from the combination of first-order piezoelectricity and spontaneous polarization. Again, please note the different potential scales. Thus for the here considered  $c$ -plane system with 20% In the second-order contribution is of secondary importance. This is also confirmed by the result of the full calculation shown in Fig. 5.4 (c), top figure. However, it is important to stress here that with increasing In content in  $c$ -plane InGaN/GaN QDs the effects of second-order piezoelectricity might change. A detailed analysis of the built-in potential in  $c$ -plane InGaN/GaN QDs as a function of In content will be presented in Sec. 5.2.3.

Turning to the QD structure grown on the  $(11\bar{2}2)$ -plane, Fig. 5.4 (b), we find that the second-order piezoelectric effect is still noticeable smaller than the combined first-order piezoelectric and spontaneous polarization contribution, cf. Fig. 5.4 (a), middle row. For the here considered lens-shaped  $\text{In}_{0.2}\text{Ga}_{0.8}\text{N}/\text{GaN}$  QD system the second-order piezoelectric contribution is a factor of order 5 smaller. Again it should be noted that for larger In contents, similar to the  $c$ -plane system, stronger second-order contributions are expected. So further studies on these systems with different In contents shall be targeted in future work. Also, and this is in contrast to the GaN/AlN QD system, the built-in potential stemming from first-order piezoelectric and spontaneous polarization has a slightly different symmetry than the second-order piezoelectric contribution. This affects the overall built-in potential, cf. Fig. 5.4 (c) (middle row), both in and around the QD. Thus, our results here give already first indications that a more complicated interplay of first- and second-order piezoelectric effects in InGaN/GaN QDs grown on semipolar planes could be expected especially for higher In contents and for different QD geometries.

The effect of built-in potential profile changes due to second-order piezoelectricity is even more pronounced for the nonpolar case, cf. Fig. 5.4 (lower row). When comparing Fig. 5.4 (a) and (b) for the nonpolar system, we observe that the built-in potential arising from spontaneous and first-order piezoelectric polarization (Fig. 5.4 (a)) has a similar symmetry than the second-order piezoelectric contribution (Fig. 5.4 (b)). However, and in contrast to Fig. 5.4 (a) where the maxima and minima are located *outside* the nanostructure, the second-order piezoelectric

contribution has its maxima and minima near the interfaces *inside* the dot. Furthermore, and most importantly, we find that inside the dot the magnitude of the built-in potential due to second-order piezoelectricity is comparable to the magnitude of the built-in potential stemming from spontaneous polarization and first-order piezoelectricity; but these contributions are opposite in sign. Consequently, the magnitude of the resulting total built-in potential is reduced compared to a situation where only first-order piezoelectricity and spontaneous polarization are accounted for. The total built-in potential is shown in Fig. 5.4 (c). Thus, for the here considered nonpolar lens-shaped  $\text{In}_{0.2}\text{Ga}_{0.8}\text{N}/\text{GaN}$  QD not only the built-in potential magnitude is reduced, also the potential profile is modified both in and around the nanostructure.

In summary, we find here that for the considered semi- and nonpolar QD systems the second-order piezoelectric contribution is of secondary importance for  $\text{GaN}/\text{AlN}$ . This is in contrast to the  $\text{InGaN}/\text{GaN}$  system, even though the same QD geometry and approximately the same lattice mismatch has been chosen ( $\varepsilon_{xx}^{\text{In}_{0.2}\text{Ga}_{0.8}\text{N}/\text{GaN}} \approx 2.2\%$ ;  $\varepsilon_{xx}^{\text{GaN}/\text{AlN}} \approx 2.4\%$ ). The observed difference in the significance of the second-order piezoelectric effect originates mainly from the importance/unimportance of the spontaneous polarization in both systems as mentioned already above. Thus the considered  $\text{GaN}/\text{AlN}$  QDs are dominated by spontaneous polarization effects while in  $\text{InGaN}/\text{GaN}$  dots a complex interplay of first-, second-order and spontaneous polarization contributions is observed, particularly for semi- and nonpolar QDs. In the next section, we focus only on  $\text{InGaN}/\text{GaN}$  QDs and address the question how this change in the built-in field due to second-order piezoelectric effects will affect the electronic and optical properties along different crystallographic directions.

## 5.2.2 Electronic and optical properties of $\text{InGaN}/\text{GaN}$ QDs grown along different crystallographic directions

Equipped with the knowledge about the variation of the built-in potential with growth plane, we analyze here the behavior of the electronic and optical properties of the polar, semi- and nonpolar lens-shaped  $\text{In}_{0.2}\text{Ga}_{0.8}\text{N}/\text{GaN}$  QDs considered above with and without second-order effects. We start this section by considering only spontaneous and first-order piezoelectric polarization effects followed by a discussion on the impact of second-order piezoelectric effects.

### 5.2.2.1 Impact of first-order piezoelectricity and spontaneous polarization on electronic and optical properties

We start with data in the absence of excitonic effects, thus with the single-particle results. The electron (red) and hole (green) ground state charge densities for the three different QD systems are depicted in the upper row of Fig. 5.5 as isosurface plots. The light (dark) isosurfaces correspond to 5% (25 %) of the maximum charge density values. The data are shown for a

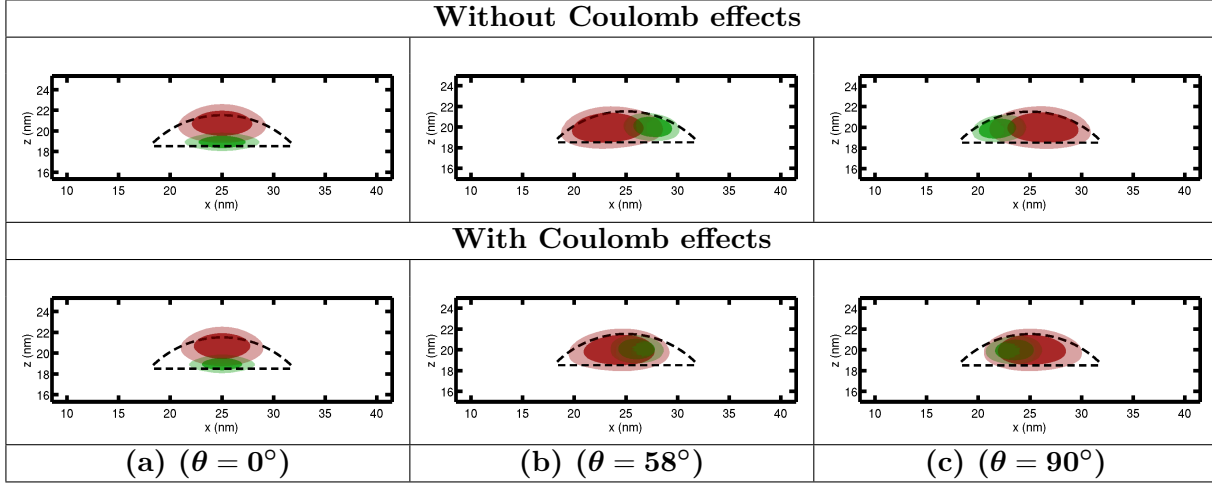


FIGURE 5.5: Isosurface plots of the electron (red) and hole (green) ground state charge densities at 5% (light surface) and 25% (dark surface) in the absence (first row) and presence (second row) of Coulomb effects. Here, only first-order piezoelectricity and spontaneous polarization is included in the calculations. The quantum dot geometry is indicated by the dashed lines. (a) polar ( $\theta = 0^\circ$ ); (b) semipolar ( $\theta = 58^\circ$ ); (c) nonpolar ( $\theta = 90^\circ$ ).

slice through the center of the QD in the  $x - z$ -plane, where  $z$  is always parallel to the growth direction. The QD geometry is indicated by dashed lines.

In a first step we turn to the  $c$ -plane (polar) system, Fig. 5.5 (a). Due to the strong electrostatic built-in field along the  $c$ -axis ( $z$ -axis), as discussed in Sec. 5.2.1.2, the well known spatial separation of the ground state electron and hole charge densities along this direction is observed. This result is consistent with the analysis presented in Sec. 3.3.1.

Focussing on the semipolar ( $11\bar{2}2$ )-system ( $\theta = 58^\circ$ ) in a second step, Fig. 5.5 (b), we also observe a spatial separation of the electron and hole ground state charge densities in this system. Two factors are now important when comparing the electronic properties of the  $c$ -plane and the semipolar dot. First, the built-in potential in the semipolar case is significantly reduced compared to the polar system (cf. Fig. 5.4 (b)). Second, while in the  $c$ -plane system the wave functions are *separated along the growth direction*, in the semipolar QD they are mainly *separated in the growth plane*. Thus, even though the built-in field is reduced in the semipolar case, the wave functions are separated over a larger distance (dot height  $h=3$  nm; dot diameter  $d=14$  nm). Therefore, it is not directly obvious if this system leads to an improvement in the wave function overlap and thus the oscillator strength in comparison to a  $c$ -plane dot of the same In content and the same geometry. Similar arguments hold for the nonpolar case. Here the built-in field is strongly reduced compared to the  $c$ -plane system (cf. Fig. 5.4), but ground state electron and hole wave functions are also separated in the growth plane (cf. Fig. 5.5 (c)). An interesting feature here is that the positions of electrons and holes are swapped in the nonpolar case in comparison to the semipolar QD (cf. Fig. 5.5 (b)). We attribute this effect to

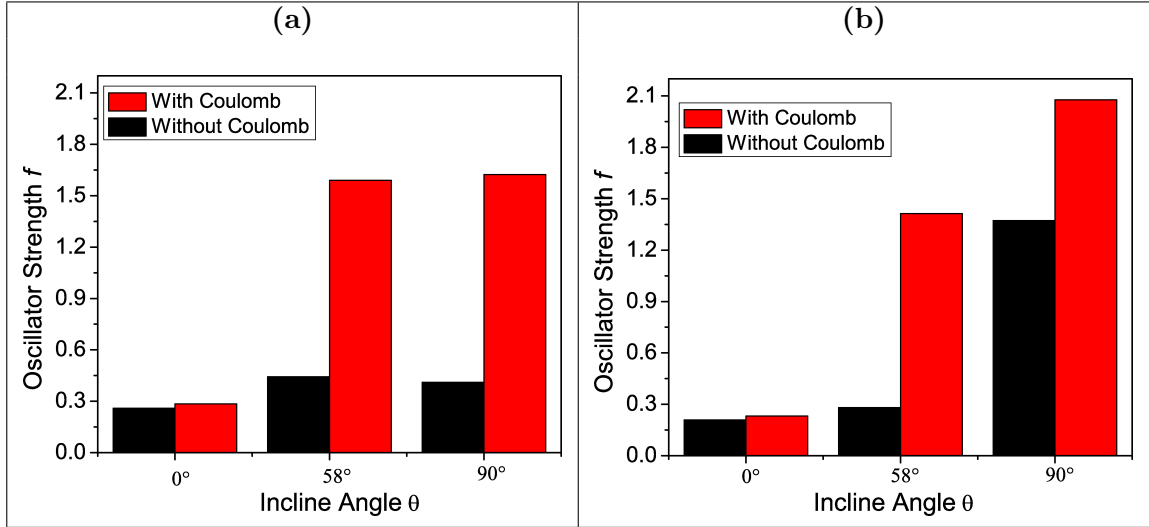


FIGURE 5.6: Oscillator strength  $f$  of the lens-shaped  $\text{In}_{0.20}\text{Ga}_{0.80}\text{N}/\text{GaN}$  QD for different growth planes in the presence (red) and absence (black) of Coulomb effects. (a) Results when including first-order piezoelectricity and spontaneous polarization; (b) Same as in (a) including second-order piezoelectricity.

differences in the built-in potential profile in and around the two systems (cf. Fig. 5.4 (b) and (c)).

To gain initial insight into the question if growth of semi- and nonpolar QD structures is beneficial in terms of the wave function overlap when compared to the same  $c$ -plane system, the oscillator strength  $f$  of the three different structures in the absence of Coulomb effects has been calculated, using Eq. (3.2). The results are shown by the black bars in Fig. 5.6 (a). As one can infer from this figure,  $f$  increases from  $f_{\text{polar}}^{\text{FO+SP}} = 0.258$  to  $f_{\text{semipolar}}^{\text{FO+SP}} = 0.442$  when moving from the  $c$ -plane system to the semipolar dot. In the nonpolar case, we find an oscillator strength of  $f_{\text{nonpolar}}^{\text{FO+SP}} = 0.410$ . We attribute the slightly lower value in  $f$  when comparing the nonpolar with the semipolar system to the above discussed effect that the built-in potential profiles between the semi- and the nonpolar structures are slightly different.

However, so far we have neglected the attractive Coulomb interaction between electron and hole in the calculations. Given that electrostatic built-in fields in the semi- and nonpolar dots are significantly reduced compared to the  $c$ -plane QD, the resulting spatial separation of electron and hole wave functions could be compensated by excitonic effects. The outcome of the self-consistent Hartree calculation in terms of the renormalized charge densities are shown in the lower row of Fig. 5.5, with (a) depicting the results for the polar dot ( $\theta = 0^\circ$ ), (b) the data for the semipolar structure ( $\theta = 58^\circ$ ) and (c) the results for the nonpolar QD ( $\theta = 90^\circ$ ). We infer from the comparison of upper (no Coulomb effect) and lower (with Coulomb effect) row of Fig. 5.5 that in the  $c$ -plane structure no significant change in the charge densities is observed due to excitonic effects. Thus, still a strong spatial separation along the growth direction is observed. The situation changes for the semi- and nonpolar system. Due to the presence of the attractive

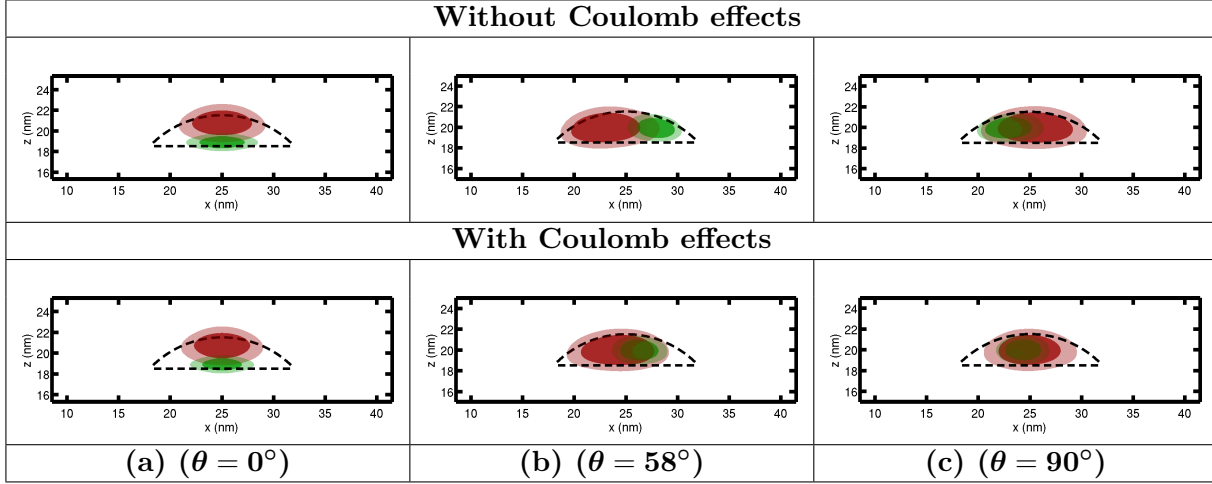


FIGURE 5.7: Isosurface plots of the electron (red) and hole (green) ground state charge densities at 5% (light surface) and 25% (dark surface) of the maximum charge density values. The data are shown in the absence (first row) and the presence (second row) of Coulomb effects. Here, spontaneous polarization as well as first- and second-order piezoelectricity are included in the calculations. The quantum dot geometry is indicated by the dashed lines. (a) polar ( $\theta = 0^\circ$ ); (b) semipolar ( $\theta = 58^\circ$ ); (c) nonpolar ( $\theta = 90^\circ$ ).

Coulomb interaction between electron and hole, charge densities are now strongly overlapping in space (cf. lower row of Fig. 5.5 (b) and (c)), when comparing this to the single-particle results (cf. upper row of Fig. 5.5 (b) and (c)). Thus, the Coulomb interaction compensates the spatial separation of electron and hole, here originating from spontaneous and first-order piezoelectric polarization induced built-in fields. This is also reflected in the calculated oscillator strength  $f$  as shown in Fig. 5.6 (a) (red bars). Focussing on the  $c$ -plane results first, the data confirms that the excitonic effect is of secondary importance for the oscillator strength/wave function overlap in the here studied system. In this case,  $f$  increases only from  $f_{\text{polar}}^{\text{FO+SP}} = 0.258$  (No Coulomb; black bars) to  $f_{\text{polar}}^{\text{FO+SP,C}} = 0.284$  (Coulomb; red bars). The situation is significantly different for the semi- and nonpolar QDs (cf. Fig. 5.6 (a)). In the semipolar case,  $f$  increases from  $f_{\text{semipolar}}^{\text{FO+SP}} = 0.442$  (No Coulomb; black bars) to  $f_{\text{semipolar}}^{\text{FO+SP,C}} = 1.590$  (Coulomb; red bars) due to the attractive Coulomb interaction between electron and hole. Turning to the nonpolar QD,  $f_{\text{nonpolar}}^{\text{FO+SP}} = 0.410$  (No Coulomb; black bars) increases to  $f_{\text{nonpolar}}^{\text{FO+SP,C}} = 1.623$  (Coulomb; red bars). The strong increase in the oscillator strength due to Coulomb effects in the semi- and nonpolar dot goes back to the above-discussed reduction in built-in field when moving away from  $c$ -plane growth. Thus we find here that Coulomb effects are essential for an accurate description of the optical properties of the here studied semi- and nonpolar dot systems. Also, this study reveals that in terms of the wave function overlap, there is almost no difference between the semi- and nonpolar system, at least when geometry and In content are kept the same. However, our analysis in Sec. 5.2.1.2 indicates already that in the nonpolar case first and second-order piezoelectric effects can cancel each other inside the dot, while in the semipolar case it is less clear cut. We address the impact of second-order piezoelectricity on the electronic and optical properties in the following section.

### 5.2.2.2 Impact of second-order piezoelectric effects on the electronic and optical properties

In this section, we discuss the electronic and optical properties of the above QDs when second-order piezoelectricity is included in the calculations. Again special attention is paid to the impact of excitonic effects on the wave function overlap thus the oscillator strength  $f$  and the radiative lifetime  $\tau$ .

We start our analysis here by looking at the electron (red) and hole (green) ground state charge densities, calculated when taking second-order piezoelectric effects into account but neglecting Coulomb effects. These calculations include now spontaneous polarization, first- and second-order piezoelectric fields. Isosurface plots of the ground state electron and hole charge densities are presented in the upper row of Fig. 5.7. Here, the  $c$ -plane ( $\theta = 0^\circ$ ) data is presented in Fig. 5.7 (a), (b) displays the results for the semipolar ( $\theta = 58^\circ$ ) dot while (c) shows the nonpolar ( $\theta = 90^\circ$ ) case. When comparing these results with the outcome of the calculations in the absence of second-order piezoelectric effects (cf. Fig. 5.5 (a)-(c), upper row), at a first glance no major differences are observed. To quantify the impact of the second-order piezoelectric effect in more detail, Fig. 5.6 (b) displays the oscillator strength  $f$  (black bars) for the polar ( $f_{\text{polar}}^{\text{Tot}}$ ), semi- ( $f_{\text{semipolar}}^{\text{Tot}}$ ) and the nonpolar ( $f_{\text{nonpolar}}^{\text{Tot}}$ ) QDs in the absence of Coulomb effects. Comparing the data of the polar and the semipolar system when including second-order piezoelectric effects, in terms of the oscillator strength the results are not vastly different ( $f_{\text{polar}}^{\text{Tot}} = 0.208$ ;  $f_{\text{semipolar}}^{\text{Tot}} = 0.281$ ). In fact, when analyzing these results with respect to the data in the absence of second-order piezoelectricity (black bars in Fig. 5.6 (a)), second-order piezoelectricity has a detrimental effect on  $f$  in the semipolar case and reduces  $f_{\text{semipolar}}$  from  $f_{\text{semipolar}}^{\text{FO+SP}} = 0.442$  to  $f_{\text{semipolar}}^{\text{Tot}} = 0.281$ . We attribute this to the increase in the built-in field due to second-order piezoelectric effects, as discussed in Sec. 5.2.1.2.

For the nonpolar case, a very strong increase in  $f$  is observed when second-order piezoelectricity is taken into account. Compared to the nonpolar case in the absence of the second-order piezoelectric contribution,  $f$  increases by a factor of 3.34, ( $f_{\text{nonpolar}}^{\text{FO+SP}} = 0.410$  vs.  $f_{\text{nonpolar}}^{\text{Tot}} = 1.372$ ). We trace this behavior back to the effect that first- and second-order piezoelectric contributions almost cancel each other inside the nonpolar dot (cf. Sec. 5.2.1.2).

In a second step, we now account for excitonic effects. The charge densities are plotted in the lower row of Fig. 5.7, with (a) depicting the  $c$ -plane ( $\theta = 0^\circ$ ), (b) the semi- ( $\theta = 58^\circ$ ) and (c) the nonpolar dot ( $\theta = 90^\circ$ ). For  $c$ -plane the Coulomb effect has again a negligible impact on the charge densities; this is also confirmed by the fact that the oscillator strength is unaffected by the Coulomb effect (black vs. red bars in Fig. 5.6 (b)). This behavior is expected given that, in terms of the wave function overlap, already the built-in field arising from spontaneous polarization and first-order piezoelectricity dominate over the excitonic effect.

Second-order piezoelectricity leads to a further increase of the built-in field in the  $c$ -plane QD. For the nonpolar case, keeping in mind that the second-order piezoelectric effect cancels basically spontaneous and first-order piezoelectric polarization contributions inside the dot, the Coulomb effect leads to a significant increase in the wave function overlap. Therefore, the corresponding  $f$  value increases significantly ( $f_{\text{nonpolar}}^{\text{Tot}} = 1.372$  vs.  $f_{\text{nonpolar}}^{\text{Tot,C}} = 2.077$ ; black vs. red bars in Fig. 5.6 (b)). Turning to the semipolar system, here the Coulomb effect strongly increases the wave function overlap, as one can infer from the charge density plots in Fig. 5.7 (b) and also the oscillator strengths shown in Fig. 5.6 (b) ( $f_{\text{semipolar}}^{\text{Tot}} = 0.281$  vs.  $f_{\text{semipolar}}^{\text{Tot,C}} = 1.413$ ; black vs. red bars in Fig. 5.6 (b)).

Overall, we find here that for the wave function overlap, excitonic effects are of secondary importance for the here studied  $c$ -plane  $\text{In}_{0.2}\text{Ga}_{0.8}\text{N}/\text{GaN}$  QD. The situation is very different for the equivalent semipolar system analyzed here. Here, Coulomb effects are essential to achieve an accurate description of the oscillator strength of the structure. We also find that second-order piezoelectric effects, at least for the here studied In content and dot geometry, are of secondary importance for wave function overlap of the semipolar system when Coulomb effects are included. The situation is more complicated in the nonpolar dot. When neglecting second-order piezoelectric effects and also Coulomb effects, the wave function overlap in the nonpolar dot is very similar to the semipolar system (Fig. 5.6 (a)). However, when including second-order piezoelectric effects, already in a single-particle picture, the wave function overlap and therefore the oscillator strength in the nonpolar case is significantly increased (black bars in Fig. 5.6 (a) and (b)). Coulomb effects further increase the oscillator strength (red bars in Fig. 5.6 (b)). Therefore, in the nonpolar case a calculation neglecting the Coulomb effects but including second-order piezoelectricity will give a reasonable approximation of a full calculation (including second-order piezoelectricity and excitonic effects), in contrast to the semipolar system.

Having calculated the oscillator strength  $f$ , we can use this information now to study the radiative lifetime  $\tau$  of the different systems. This allows us also to compare our theoretical data with literature experimental values. Here, we find that for the  $c$ -plane QD,  $\tau$  increases from  $\tau_{\text{polar}}^{\text{FO+SP,C}} = 4.60$  ns to  $\tau_{\text{polar}}^{\text{Tot,C}} = 5.79$  ns in the presence of second-order effects. This is traced back to the slight increase in  $f$  in the presence of second-order effects. For the here studied semipolar dot, we find that second-order piezoelectricity leads to an increase in  $\tau$  since second-order piezoelectric effects result in a slight reduction in  $f_{\text{semipolar}}^{\text{Tot,C}}$  when compared to  $f_{\text{semipolar}}^{\text{FO+SP,C}}$ . More specifically, the calculated  $\tau$  value increases from  $\tau_{\text{semipolar}}^{\text{FO+SP,C}} = 699$  ps (no second-order piezoelectric effect) to  $\tau_{\text{semipolar}}^{\text{Tot,C}} = 787$  ps (with second-order piezoelectricity). This corresponds to an increase of about 12%. For the nonpolar system the calculated  $\tau$  value decreases when including second-order piezoelectricity in the calculations. Here, we find

$\tau_{\text{nonpolar}}^{\text{FO+SP,C}} = 675$  ps (no second-order piezoelectric effect) and  $\tau_{\text{nonpolar}}^{\text{Tot,C}} = 525$  ps (with second-order piezoelectricity). This originates from the fact that due to second-order piezoelectricity  $f$  increases in the nonpolar system.

The calculated radiative lifetime  $\tau$  for the  $c$ -plane QD is consistent with the measured  $\tau$  values in the literature which are in the range of few nano seconds [184, 185]. Additionally, few experimental studies have also reported  $\tau$  values for semi- and nonpolar InGaN/GaN QDs [14, 67, 186, 199]. For instance, Gačević *et al.* [199] performed measurements on semipolar QDs grown along the  $[10\bar{1}1]$  ( $\theta \approx 62^\circ$ ) crystallographic direction which is similar to the semipolar  $(11\bar{2}2)$  ( $\theta \approx 58^\circ$ ) plane considered in this work. They found  $\tau$  values in the range of 600-900 ps. The semipolar QDs studied in Ref. [199] have also been characterized in terms of their In content in Ref. [239]. This analysis revealed that the semipolar InGaN/GaN dots exhibiting radiative lifetimes between 600-900 ps, have an In content of 10%. Our here calculated radiative lifetime for a semipolar dot with 20% In (including second-order piezoelectric effects) is  $\tau_{\text{semipolar}}^{\text{Tot,C}} = 787$  ps. Given that when reducing the In content the built-in field will be reduced, we expect that our calculated value will be reduced. Overall, the here obtained radiative lifetimes in the semipolar system are in good agreement with the literature values from Ref. [199].

Similarly, there are several reports on  $\tau$  values for nonpolar InGaN/GaN systems [14, 67, 199]. All of these works quote radiative lifetimes in the range of 400-600 ps in nonpolar InGaN/GaN QDs. Again, these numbers are consistent with the value calculated in this work (525 ps). Another study [186] on nonpolar InGaN/GaN QDs revealed even shorter lifetimes in the range of 250-300 ps. However, it is important to note that these values will strongly depend on the dot geometry and the In content in the dot. A detailed theory experiment comparison is beyond the scope of this work, since it will require a detailed study of the interplay between In content, dot geometry and second-order piezoelectricity. Nevertheless, the here presented initial results show already that the calculated values for  $\tau$  are in good agreement with reported experimental values on semi- and nonpolar InGaN/GaN dots.

Finally, from the analysis of the built-in field presented in Sec. 5.2.1.2, it is expected that with increasing In content, the second-order piezoelectric effect is likely to become even more important in InGaN/GaN QDs. These high In content structures are important since with increasing the In content, emission can in principle be moved into the red spectral regime. Recently, Frost and co-workers [21] were able to grow high-efficiency red emitting lasers using  $c$ -plane  $\text{In}_{0.4}\text{Ga}_{0.6}\text{N}/\text{GaN}$  QDs. Therefore, it is also important to investigate how second-order piezoelectric effects affect the optical properties of  $c$ -plane InGaN/GaN QDs as a function of the In content. In the course of this discussion, we will mainly focus on the emission wavelength  $\lambda$  and the radiative lifetime  $\tau$  which are two important optical properties while targeting red emission from  $c$ -plane InGaN/GaN QDs. This is the topic of the next section.

### 5.2.3 Impact of second-order piezoelectricity on emission wavelength and radiative lifetime as a function of In content

Figure 5.8 shows the emission wavelength  $\lambda$  of the here considered  $c$ -plane  $\text{In}_x\text{Ga}_{1-x}\text{N}/\text{GaN}$  QD for In contents varying between 10% and 50%. The black squares ( $\lambda^{\text{FO+SP}}$ ) denote the results in the absence of second-order piezoelectric contributions [only first-order (FO) piezoelectricity and spontaneous (SP) polarization], while the red circles ( $\lambda^{\text{Tot}}$ ) show the data when including also second-order piezoelectric effects. Again, it should be noted that for emitters operating in the red wavelength regime, In contents of 40% have been reported in the literature [21], so that the here studied In content range is relevant to recent experimental studies. From Fig. 5.8 one can infer that for lower In contents (up to 20%), the second-order piezoelectric contribution has little effect on  $\lambda$ . In fact in this case the difference in the emission wavelength  $\Delta\lambda = \lambda^{\text{Tot}} - \lambda^{\text{FO+SP}}$ , obtained from a calculation with spontaneous and first-order piezoelectric polarization only,  $\lambda^{\text{FO+SP}}$ , and a calculation including second-order piezoelectric effects,  $\lambda^{\text{Tot}}$ , is less than 10 nm. To show this effect more clearly, the inset in Fig. 5.8 depicts  $\Delta\lambda$  as a function of the In content  $x$ . Between 30% and 40% In, second-order piezoelectric effects lead to a noticeable difference, resulting in  $\Delta\lambda$  values of approximately 20 nm to 50 nm, respectively. At 50% In we observe a wavelength shift of  $\Delta\lambda = 120$  nm. Overall, the wavelength shift is almost equally distributed between electron and hole ground state energy shifts. We attribute this to the combined effect of differences in electron and hole effective masses and the asymmetry in the magnitude of the built-in potential between the upper and lower QD interface. Moreover, the change in the confinement potential due to second-order piezoelectricity might also affect the Coulomb interaction between the carriers and can lead to further contributions to the wavelength shift discussed here in the single-particle picture. Overall, our calculations reveal two things. First, when targeting QD-based emitters operating in the red spectral regime ( $\approx 650$  nm), second-order piezoelectric effects can play a significant role. Furthermore, the second-order piezoelectric contribution shifts the emission to longer wavelength. Thus, when designing emitters operating in this long wavelength regime, the required In content predicted from a model including second-order effects would be lower as expected from a “standard model”, which accounts for first-order piezoelectric effects and spontaneous polarization only.

Even though our analysis indicates that lower In contents are sufficient to reach emission at longer wavelength, the increase in the built-in potential responsible for this effect will have a detrimental effect on the wave function overlap and consequently on the radiative lifetime  $\tau$ . To study the impact of second-order piezoelectricity on the radiative lifetime  $\tau$ , Fig. 5.9 depicts  $\tau$  in the absence ( $\tau^{\text{FO+SP}}$ , black squares) and in the presence ( $\tau^{\text{Tot}}$ , red circles) of second-order piezoelectric contributions. The inset of Fig. 5.9 depicts the difference in the radiative lifetime  $\Delta\tau = \tau^{\text{Tot}} - \tau^{\text{FO+SP}}$ , obtained from calculations including ( $\tau^{\text{Tot}}$ ) and neglecting ( $\tau^{\text{FO+SP}}$ ) second-order piezoelectric contributions. Similar to the wavelength shift discussed above, in

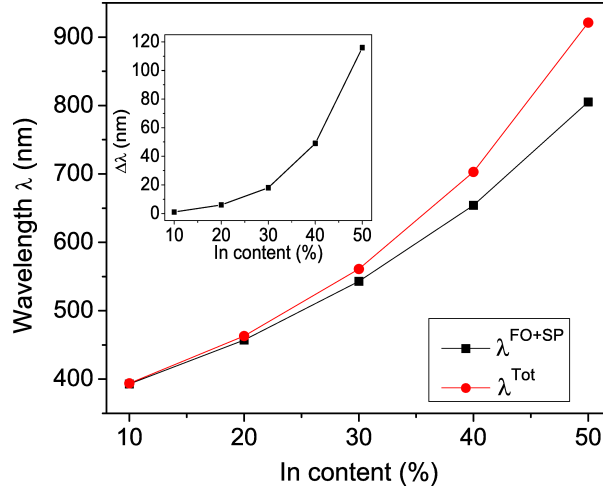


FIGURE 5.8: Emission wavelength  $\lambda$  as a function of In content  $x$ . Results in absence of second-order piezoelectricity, taking only spontaneous (SP) and first-order (FO) piezoelectric polarization into account, are given by the black squares ( $\lambda^{\text{FO+SP}}$ ). The red circles denote data when including second-order piezoelectricity ( $\lambda^{\text{Tot}}$ ). The inset shows  $\Delta\lambda = \lambda^{\text{Tot}} - \lambda^{\text{FO+SP}}$ .

the In content range of 10% to 20% the influence of second-order piezoelectricity is of secondary importance ( $\Delta\tau \leq 2$  ns). Again, as pointed out earlier, the calculated radiative lifetimes in the 10% to 20% In regime are in the range of 3 ns to 10 ns, which is in good agreement with reported experimental data on these systems [184, 185]. However, for higher In contents we clearly observe a significant contribution from second-order piezoelectricity. At 30% the  $\tau$  value is a factor of order 1.5 larger ( $\tau^{\text{FO+SP}} = 12$  ns;  $\tau^{\text{Tot}} = 19$  ns) when including second-order piezoelectric effects in the calculations. At 40% and 50% In, the value of  $\Delta\tau$  becomes 23 ns and 62 ns, respectively. But, it should be noted that the here calculated radiative lifetimes for a  $c$ -plane  $\text{In}_{0.4}\text{Ga}_{0.6}\text{N}$  QD, even without second-order effects, are much larger than the experimental values ( $\tau^{\text{exp}} = 3$  ns) reported in the literature for InGaN dots with 40% In [21]. Further studies, both theoretically and experimentally, are required to shed more light onto the physics of  $\text{In}_x\text{Ga}_{1-x}\text{N}$  QDs operating in the long wavelengths regime (green to red). However, overall our calculations reveal that with increasing In content the second-order piezoelectric effect becomes important in InGaN/GaN QDs for an accurate description of electronic and optical properties.

Finally, it is to remind the reader that calculations presented in this chapter have been performed using continuum-based electronic structure theory. Therefore, our results do not take into account atomistic effects such as alloy fluctuations, which can also affect the emission spectra of these dots [240]. Nevertheless, since we are mainly interested in the trend of emission wavelength and radiative lifetime in the presence of second order piezoelectricity, our approach is sufficient for this purpose. More details on the effects of carrier localization on the electronic and optical properties of these dots will be presented in the next chapter.

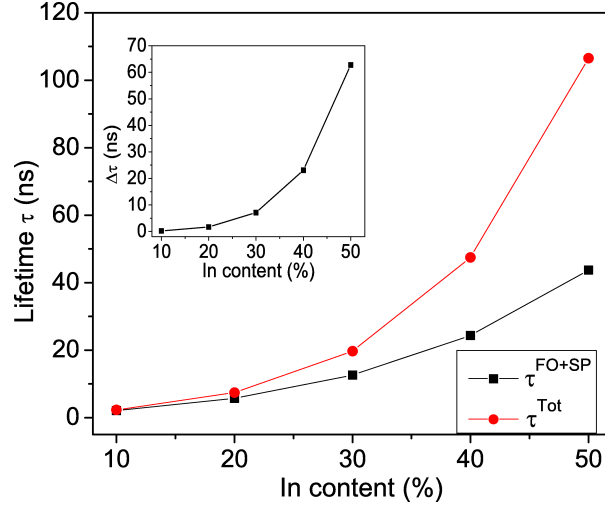


FIGURE 5.9: Radiative lifetime  $\tau$  as a function of In content  $x$ . Results in absence of second-order piezoelectricity, including spontaneous (SP) and first-order (FO) piezoelectric polarization only, are given by the black squares ( $\tau^{\text{FO+SP}}$ ). The red circles denote the data when including second-order piezoelectricity ( $\tau^{\text{Tot}}$ ). The inset shows  $\Delta\tau = \tau^{\text{Tot}} - \tau^{\text{FO+SP}}$ .

### 5.3 Conclusion

In summary, we have presented a detailed analysis of second-order piezoelectric effects in WZ nitride-based heterostructures grown along different crystallographic directions. To accomplish this task, we have derived analytic expressions for the full second-order piezoelectric polarization vector field as a function of the incline angle  $\theta$  to the WZ  $c$ -axis. Even though our approach is applied to WZ III-N systems, it can also be applied to other WZ semiconductor systems such as ZnO once second-order piezoelectric coefficients are known.

Our calculations on III-N QW systems revealed that especially for semipolar growth planes with a high incline angle value ( $55^\circ \leq \theta \leq 85^\circ$  and  $105^\circ \leq \theta \leq 120^\circ$ ), second-order piezoelectric effects noticeably affect the built-in potential and thus the resulting electric field. More specifically, in an  $\text{In}_{0.22}\text{Ga}_{0.78}\text{N}/\text{GaN}$  MQW system, grown along the  $[11\bar{2}2]$ -direction, the electric field is increased by approximately 20% due to second-order piezoelectricity. Overall, we find that when including second-order piezoelectric effects in the theoretical framework, electric fields calculated for realistic MQW systems show a much better agreement with experimentally reported values. This further emphasizes the importance of second-order piezoelectric contributions for an accurate description of electrostatic built-in fields in nitride-based QWs.

In the next step, we studied the electrostatic built-in potentials in lens-shaped GaN/AlN and  $\text{In}_{0.2}\text{Ga}_{0.8}\text{N}/\text{GaN}$  QDs grown on different substrate orientations, namely the  $c$ -, the  $(11\bar{2}2)$ - and the nonpolar  $a$ -plane. Our calculations reveal that, at least for the here chosen QD geometry, second-order piezoelectric contributions have a very small effect on the overall built-in potential in GaN/AlN systems. For the InGaN/GaN dot systems studied here the situation is different. While for a  $c$ -plane InGaN/GaN QD with 20% In the second-order contribution is of secondary

importance, the situation is changed for the systems with high In content or semi- and nonpolar systems. For example, in the nonpolar case, where the built-in potential is significantly reduced compared to the same *c*-plane structures, first- and second-order piezoelectric contributions are comparable in magnitude inside the dot. Moreover, the first- and second-order contributions are similar in symmetry but opposite in sign so that cancelation effects occur. This results also in changes in the built-in potential profile in and around the nanostructure. We relate the observed difference in the importance of second-order piezoelectricity in GaN/AlN and InGaN/GaN dot systems to the magnitude of the spontaneous polarization induced built-in potential.

Building on the calculated built-in fields, we then studied the electronic and optical properties of InGaN/GaN QD systems in the absence and presence of second-order piezoelectric effects. Special attention was paid to the impact of Coulomb interactions (excitonic effects). Our calculations reveal that second-order piezoelectric effects are of secondary importance for the oscillator strength of the polar and semipolar system. However, for the nonpolar case, due to the above mentioned cancelation effects in the built-in potential inside the dot, second-order effects significantly affect the wave function overlap and therefore the oscillator strength. Here, we find that in the presence of second-order piezoelectricity, but neglecting Coulomb effects, the oscillator strength strongly increases in the nonpolar case compared to a “standard” calculation including only first-order piezoelectricity and spontaneous polarization. When including excitonic effects in the theoretical framework, the oscillator strength is basically unchanged in the *c*-plane dot, indicating that the electronic and optical properties of this system are dominated by the strong electrostatic built-in fields. The situation is vastly different for the semi- and nonpolar system. Here, due to the reduced built-in fields compared to the *c*-plane system, Coulomb effects become essential for an accurate description of the wave function overlap and the oscillator strength. We find that the oscillator strength is significantly increased when Coulomb effects are taken into account for these systems. However, when neglecting second-order piezoelectric effects, the oscillator strength of the semipolar system is almost identical to that of the nonpolar system. This picture changes noticeably when including second-order piezoelectricity. The nonpolar QD now exhibits a much larger oscillator strength compared to the semipolar system. Thus, our calculations indicate that when growing non-*c*-plane InGaN QDs, the nonpolar system should exhibit a shorter radiative lifetime compared to the here studied (11 $\bar{2}2$ ) semipolar dot system. This is also confirmed by the experimental studies [199].

Finally, we closed this chapter by analyzing the effects of second-order piezoelectricity on the emission wavelength and radiative lifetime in *c*-plane InGaN/GaN QDs as a function of In content. When looking at emission wavelength shifts or radiative lifetime values, at In contents around 10% to 20%, these quantities are almost unaffected by second-order piezoelectricity. But, when exceeding 30% In, both quantities are impacted significantly by second-order contributions. The second-order piezoelectric effect induced built-in field increase leads to the

situation that the emission is shifted to longer wavelength in comparison to a calculation based on spontaneous and first-order piezoelectric polarization effects only. This means that when accounting for second-order effects, lower In contents can be considered to reach for instance emission in the red spectral region. On the other hand, the increase in the built-in potential due to second-order piezoelectric contributions results in a strong increase in the radiative lifetime for long wavelength, high In content emitters when compared to results from a “standard” first-order study. Overall, our results reveal that when targeting  $\text{In}_x\text{Ga}_{1-x}\text{N}$  QD-based emitters operating in the yellow to red spectral regime, second-order piezoelectricity cannot be neglected and should be taken into account for designing and understanding the electronic and optical properties of these systems.

## Chapter 6

# Atomistic analysis of electronic and optical properties of wurtzite QDs

In chapters 3, 4 and 5, the electronic and optical properties of III-N nanostructures have been modeled by employing continuum-based multi-band  $\mathbf{k} \cdot \mathbf{p}$  approaches. Calculated radiative lifetime  $\tau$  and DOLP  $\rho$  values based on 6+2 band  $\mathbf{k} \cdot \mathbf{p}$  calculations have been found to be in good agreement with experimentally observed  $\tau$  and  $\rho$  values, as discussed in Chapter 3 and 4 respectively. Despite the success of these continuum-based calculations in describing the electronic and optical properties of QDs, they are not suitable to provide a complete atomistic description of the underlying crystal structure. For instance, as pointed out earlier by Bester *et al* [56], the investigation of ideal (e.g. lens) shaped ZB QDs through continuum  $\mathbf{k} \cdot \mathbf{p}$  models can not capture the correct  $C_{2v}$  symmetry as atomistic models correctly predict. Furthermore, continuum-based models described in previous chapters inherently overlook microscopic effects such as alloy fluctuations. However, several reports have highlighted that incorporation of alloy fluctuations is necessary for an accurate modeling of III-N systems [240, 241]. For instance, Auf der Maur *et al.* [240] have reported that the origin of the green gap in *c*-plane nitride light emitting diodes may be attributed to a decrease in the radiative recombination coefficient with increasing In content due to (random) In fluctuations present in an alloy of InGa<sub>1-x</sub>N. Even though modified continuum-based approaches [241, 242] are applied to mimic the impact of alloy fluctuations on the optoelectronic properties of WZ nanostructures, it has been shown for instance by Schulz, *et al* [119] that the conclusion drawn from these works (e.g. localization properties of electrons and holes) do not necessarily match the results from atomistic-based models. Additionally, these models do not account for strain and built-in potential fluctuations on a microscopic level which has been shown to be important for III-N alloys [243].

In this chapter, we investigate electronic and optical properties of InGa<sub>1-x</sub>N/GaN QDs grown along the *c*-axis of an WZ crystal structure in the framework of an atomistic nearest neighbor

$sp^3$  TB model [244] which has been described in detail in Sec. 2.2.1.2. We start this chapter by performing virtual crystal approximation (VCA) based calculations in Sec. 6.2. The purpose of these calculations is two fold. First, we want to use VCA based calculations as a benchmark to test the  $C_{3v}$  symmetry of the system. For instance, as discussed in Chapter 2, without SOC one should expect doubly degenerate  $p$ -like states in the energy spectrum of the carrier wave functions for a QD having  $C_{3v}$  symmetry. Secondly, the VCA based calculations present a good reference for analyzing the impact of alloy fluctuations on the electronic and optical properties of  $c$ -plane InGaN QDs. In the next step, Sec. 6.3 deals with the investigation of single-particle properties by including random alloy fluctuations in the analysis. Here, we take as an example a series of  $\text{In}_{0.20}\text{Ga}_{0.80}\text{N}/\text{GaN}$  QDs and study the impact of alloy fluctuations on the electronic eigenstates and energies. Finally, we move to many particle properties in Sec. 6.4 and treat Coulomb effects in the CI scheme based on the calculated electron and hole TB single-particle wave functions. Here, we discuss the FSS values for these systems given their importance to achieve entangled photon emission as discussed in Sec. 2.6.4. Before going to the results, we motivate the assumed QD geometry in the following.

## 6.1 Dot geometry

In this study, we consider a truncated-cone shaped  $\text{In}_{0.20}\text{Ga}_{0.80}\text{N}$  QD embedded inside a GaN matrix. The QD geometry is schematically shown in Fig. 6.1. Recent structural investigations of InGaN QDs [47] using transmission electron microscopy (TEM) revealed that  $c$ -plane InGaN QDs are approximately truncated-cone shaped. Additionally, in the same study the average radii of the QDs is found out to be  $\approx 10\text{-}20$  nm with heights varying between 3-5 nm [47]. Therefore, in accordance with these recent results we have assumed a truncated-cone shaped QD with a base diameter of ( $D_1 = 13$  nm) and a height  $h$  of 3 nm. Previous theoretical studies on  $c$ -plane InGaN QDs have also assumed similar geometries [245, 246]. The symmetry of the combined system of underlying WZ lattice and our assumed QD geometry is  $C_{3v}$ . A cubic supercell having dimension of  $\approx (29.33 \text{ nm} \times 25.40 \text{ nm} \times 18.66 \text{ nm})$  (1218816 atoms) with periodic boundary conditions is used in our calculations. The system is large enough such that the electronic structure properties of interest are not affected. For instance, the cubic symmetry of the supercell does not allow for degeneracy in the  $p$ -like states in the energy spectrum where a truncated-cone shaped WZ QD having  $C_{3v}$  symmetry should ideally have doubly degenerate  $p$ -like states when SOC is neglected. Therefore, a large enough supercell is chosen such that the doubly degenerate  $p$ -like states do not split in the absence of SOC in our simulation cell as we will highlight below.

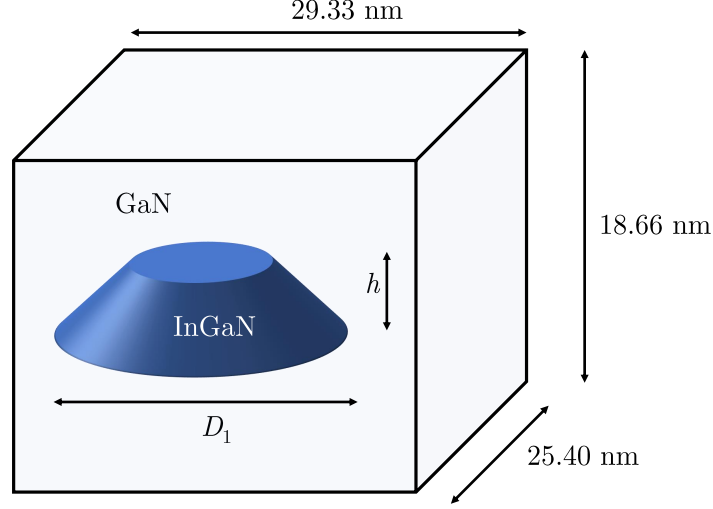


FIGURE 6.1: Schematic illustration of a truncated-cone shaped InGaN QD buried in a GaN matrix. The diameter and the height of the QD is denoted by  $D_1$  and  $h$  respectively.

## 6.2 Single-particle states and energies by VCA

In this section, we present the calculated single-particle states and energies of bound electron and hole states in the VCA approach. In VCA calculations, instead of several randomly chosen atomic distributions of an alloy, a TB representation of a virtual binary material mimicking the alloy is used. For several semiconductors this is a useful approximation in terms of e.g. band gap energies [247]. In our case, the TB parameters for the virtual crystal  $\text{In}_{0.20}\text{Ga}_{0.80}\text{N}$  are obtained by a concentration weighted average of the parent binaries InN and GaN.

Here, strain and built-in potential effects are calculated using the surface integral method described in Sec. 2.4.1. Using Eqs. (2.52), (2.60) and (2.61), strain and built-in potential values are evaluated at each atomic site and subsequently added as on-site corrections to the TB Hamiltonian as described in Sec. 2.3.2 and Sec. 2.5. To test the spatial symmetries of the system, we first switch off the SOC. As stated earlier, by treating the alloy as a VCA, our QD system should possess a  $C_{3v}$  symmetry. Thus, it can ideally act as a reference point for random alloy calculations presented in later sections. Therefore, while doing these calculations the symmetry of the system should not be altered due to numerical artefacts arising from the use of a continuum method (surface integral) on an atomistic grid. This is also essential in the sense that in the later parts of this work, we are interested in the FSS values which are usually of the order of  $\mu\text{eV}$  in III-V systems [29]. To achieve this, we carried out a symmetrization procedure over the region of the dot material. We performed strain and built-in field calculations for one batch of the supercell and subsequently assigned these values to grid points situated at  $120^\circ$  and  $240^\circ$  to construct e.g. a symmetric potential that fulfils a  $C_{3v}$  symmetry. It should be noted that without this symmetrization process, the  $p$ -state splitting of the electrons is already  $\leq 10 \mu\text{eV}$ . For most studies, e.g. band gap values or polarization anisotropies this is sufficient.

However, for FSS values which are in the range of  $\mu\text{eV}$  this is not acceptable. Therefore, through this, we ensured that the symmetry of the QD system is not destroyed by numerical artefacts and results which will be obtained due to random alloy fluctuations in Sec. 6.3 stem entirely from random alloy effects. Finally, to incorporate SOC in our calculations, spin-orbit terms are added to the TB Hamiltonian through the spin-orbit operator,  $\hat{H}_{\text{so}}$  as outlined in Sec. 2.2.1.2. The matrix elements of  $\hat{H}_{\text{so}}$  is calculated using Eq. 2.41. A detailed discussion on the procedure to include SOC in the TB model is already given in Sec. 2.2.1.2. The TB parameters for InN and GaN with and without SOC are tabulated in Table B.3 of Appendix B.

Having outlined the QD geometry and ingredients of the calculation framework employed in the VCA based calculations, we now move to the discussion of single-particle results. Here, the influence of strain and electrostatic built-in field on single-particle states and energies are addressed in Sec. 6.2.1. After that, the influence of SOC on the single-particle properties are highlighted in Sec. 6.2.2.

### 6.2.1 Effect of strain and built-in field

In order to assess the impact of strain and built-in potential separately, we have performed our calculations in three steps. In a first step, we neglect both strain ( $\varepsilon_{ij}=0$ ) and built-in potential ( $V_p=0$ ). In the next step, we introduce only the built-in potential ( $\varepsilon_{ij}=0$  and  $V_p \neq 0$ ) in the TB model. In the final step, both strain and built-in potential contributions ( $\varepsilon_{ij} \neq 0$  and  $V_p \neq 0$ ) are taken into account. It is to note that since these calculations neglect SOC, the symmetry of the eigenstates can be represented by single group IRRs of  $C_{3v}$  point group, which allow doubly degenerate states in the energy spectrum.

#### Case a: $\varepsilon_{ij}=0$ and $V_p=0$

Figure 6.2 shows the top-view of the isosurfaces of modulus squared wave functions  $|\phi(\mathbf{r})|^2$  for first three single-particle electron (left) and hole (right) states in red and green, respectively. Here, the light and dark isosurfaces correspond to 10% and 50% of the maximum probability density, respectively. The corresponding single-particle energies  $E_i$  are also listed. The dotted lines indicate the upper and lower base of the truncated-cone shaped QD. The atomic orbital contributions to the TB wave functions for each state are also presented.

For our analysis, we denote now the electron (hole) ground, the first and second excited state as  $e_0$  ( $h_0$ ),  $e_1$  ( $h_1$ ) and  $e_2$  ( $h_2$ ), respectively. By examining the nodal structure of the wave functions, the depicted electron states can be classified as  $s$ - and  $p$ -like states. The charge density of electron ground state  $e_0$  reveals an atomic  $s$ -like state whereas the excited electron states  $e_1$  and  $e_2$  can be classified as  $p$ -like states. This type of classification is not possible for the hole states due to mixing of different orbitals. The hole ground state is a torus-like state.

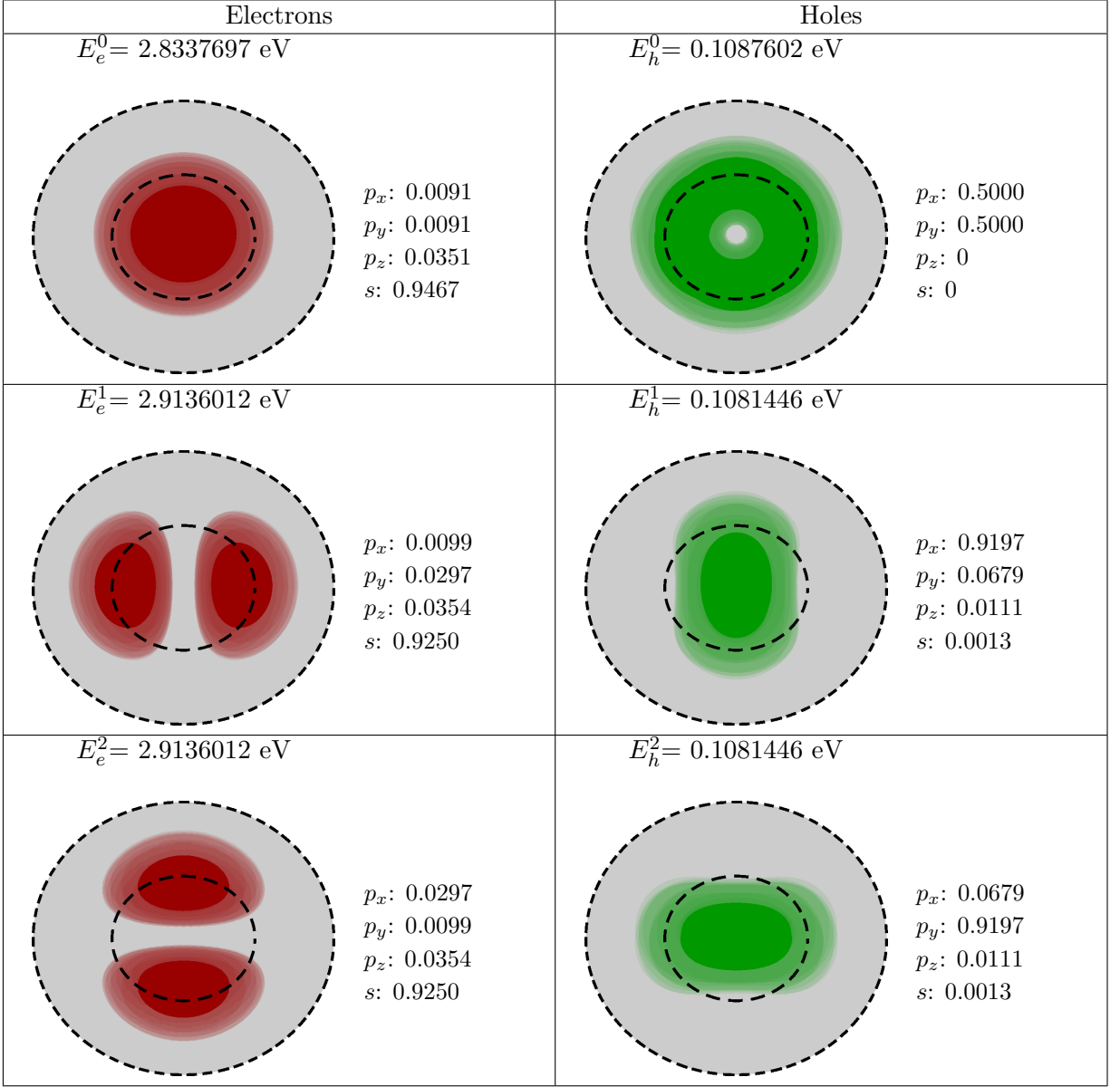


FIGURE 6.2: Single-particle electron (left) and hole (right) states for a  $\text{In}_{0.20}\text{Ga}_{0.80}\text{N}$  QD in the absence of strain, built-in potential and SOC. Here, the picture shows the top view of the 10% (light) and 50% (dark) isosurfaces of the probability density distribution  $|\phi|^2$ . The first, second and third row represents the ground state, the first and second excited state in that order for both electrons (left) and holes (right). The energies and orbital characters of the single-particle states are also listed.

Looking at the single-particle energies, we find degenerate states for both electrons and holes. This is consistent with the discussions presented in Sec 2.6.4 where we have stressed that due to the underlying  $C_{3v}$  symmetry, we can have two-dimensional IRR in the single group of  $C_{3v}$  and therefore, degeneracies are allowed unlike in a  $C_{2v}$  symmetric system [148]. From the energy level structure of the states, we find that the level spacing in holes are much smaller than for the electrons. This can be explained in terms of larger effective mass of holes [76].

Additionally, using group theory we can now classify different single-particle states also according to their transformation properties [136]. It can be shown that [136] both non-degenerate single-particle electron and hole states are invariant under a rotation by  $\frac{2\pi}{3}$  and the energetically degenerate states transform under the action of the elements of  $C_{3v}$  like  $x$  and  $y$ . Therefore, the ground electron and hole states are denoted as  $s$ -states while the excited states are denoted as  $p$ -states.

Looking at the orbital contributions, we observe that all of the electron states are dominated by  $s$ -orbital ( $\geq 94\%$ ) contributions. This is consistent with the discussion presented in Sec. 2.1.1. On the other hand, for the hole ground state,  $p_x$ - and  $p_y$ -orbitals contribute equally. As seen from Fig. 6.2, we conclude that mainly  $p_x$ - and  $p_y$ -orbitals contribute to the formation of QD hole states. Absence of  $p_z$  contribution is traced back to the previously discussed shift of valence band edges due to the confinement effects in Sec. 4.2.1.

#### Case b: $\varepsilon_{ij}=0$ and $V_p \neq 0$

Now, we include built-in field in the analysis. In the presence of the built-in field, the level ordering of the electron states is unchanged. However the ordering of the holes states is changed in a way that the hole ground state is formed by the two-fold degenerate states while the first excited state is the non-degenerate state. Here, as expected from the discussions presented in previous chapters, with the inclusion of the built-in field, a spatial separation of electron and hole probability densities along the  $c$ -direction is observed. Correspondingly, the electron states are squeezed into the top-interface of the QD and the hole states are pushed to the bottom. This is clearly visible from the side-view plot of the isosurfaces of the ground state charge densities of electrons and holes (cf. Fig. 6.3).

Furthermore, we observe that when the built-in field is introduced in the system ( $\varepsilon_{ij}=0$  and  $V_p \neq 0$ ), a strong modification (not shown here) in the energies of the electron and hole ground states is obtained as compared to a field free case. For instance, the electron ground state energy is shifted to lower energies by about 81 meV and the hole ground state is shifted to higher energies by about 134 meV. This is in accordance with the redshift observed in nitride systems due to QCSE as discussed in Sec. 1.2.2.

#### Case c: $\varepsilon_{ij} \neq 0$ and $V_p \neq 0$

Finally, strain effects are included in the model. The isosurfaces of the charge density for electrons (left) and holes (right) including strain and built-in potential are shown in Fig. 6.4. For each state, single-particle energies and orbital contributions are given. Due to in-plane isotropy of the WZ structure, strain in the  $x-y$  plane containing  $a$  and  $m$  direction is isotropic. Therefore, the strain present in the structure shifts  $p_x$ - and  $p_y$ -like states in the same way. As a result, the orbital contributions to the hole states in general remain unchanged and degeneracies of the states remain intact when strain and built-in field contributions are included. The strains

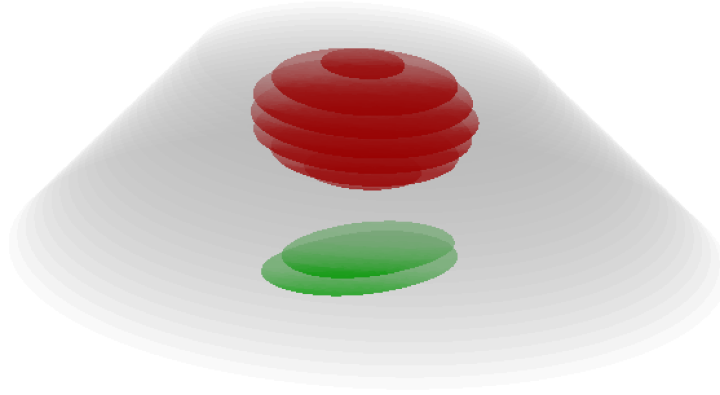


FIGURE 6.3: The figure shows 50% isosurfaces of the ground state charge density distribution for electrons (red) and holes (green) in side-view in the presence of the built-in potential. The QD is shown in grey.

only introduce energetic shifts in the system. Also, the level ordering remains same as the previous case (Case b). Again, symmetry is not affected in the presence of strain.

Overall, through the above discussions, we have shown that all expected symmetries are present in the studied truncated-cone shaped QD system and this is reflected in the degeneracies present in the energy spectrum of the single-particle states. So far, we have neglected the influence of SOC in the analysis. In the next section, we investigate the effect of SOC contributions on the single-particle states and energies.

### 6.2.2 Influence of spin-orbit coupling

To focus on the impact of SOC, both strain and built-in potential effects are included here given that we have already shown that these effects do not affect the symmetry of the system. The first three single-particle states and energies with SOC are illustrated in Fig. 6.5. Again, the electron and hole states are plotted in red and green, respectively. Similar to previous cases, here light and dark isosurfaces correspond to 10% and 50% of the maximum probability density, respectively. The orbital contributions to the TB single-particle wave functions for each state are also presented. Here, each state is two-fold degenerate due to time reversal symmetry [111].

While looking at the nodal structure of the electron charge densities, we observe that the electron ground state is *s*-like since it has no nodes. On the other hand, the first two excited electron states can be classified as the  $p_+$  and  $p_-$  states which can be formed by any linear combinations of  $p_x$  and  $p_y$  states. Such a classification is not possible for the holes due to mixing of different orbitals. In the previous section, we observed that the presence of built in field switches the level ordering of single-particle states. When comparing with the Case c (SOC=0,  $\varepsilon_{ij} \neq 0$  and  $V_p \neq 0$ ), we find that SOC does not alter the single-particle level structure (cf. Fig. 6.5).

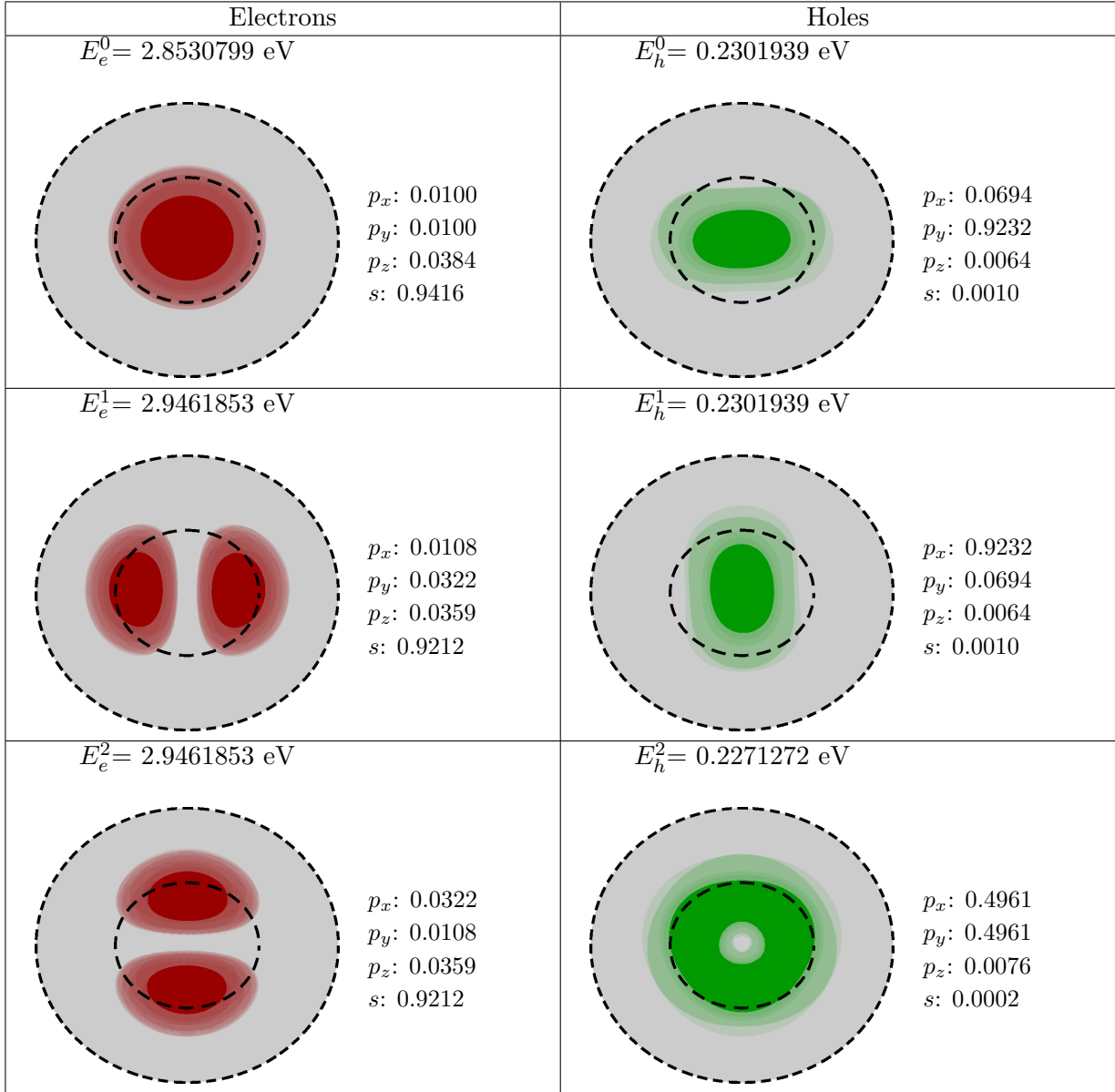


FIGURE 6.4: Single-particle electron (left) and hole (right) states for a  $\text{In}_{0.20}\text{Ga}_{0.80}\text{N}$  QD in presence of strain and built-in potential. Here, the picture shows the top view of the 10% (light) and 50% (dark) isosurfaces of the probability density distribution  $|\phi|^2$ . The first, second and third row represents the ground state, the first and second excited state in that order for both electrons (left) and holes (right). The energies and orbital characters of the single-particle states are also listed.

We now analyze the effect of SOC on the electron and hole single-particle energies. As seen from Fig. 6.5, in the presence of SOC, we find that the degeneracy of the  $p$  states are lifted for both electrons and holes. This is traced back to the discussions presented in Sec. 2.6.4, where we have shown that in the presence of SOC, one has to deal with double group IRRs of the  $C_{3v}$  which contains only 2-D IRRs even if the degeneracies due to time reversal symmetry are included [76]. This explains the splitting of  $p$  states in the presence of SOC. The splittings in our case is found out to be  $10.6 \mu\text{eV}$  ( $E_e^2 - E_e^1$ ) and  $2.6 \text{ meV}$  ( $E_h^0 - E_h^1$ ) for electrons and holes respectively.

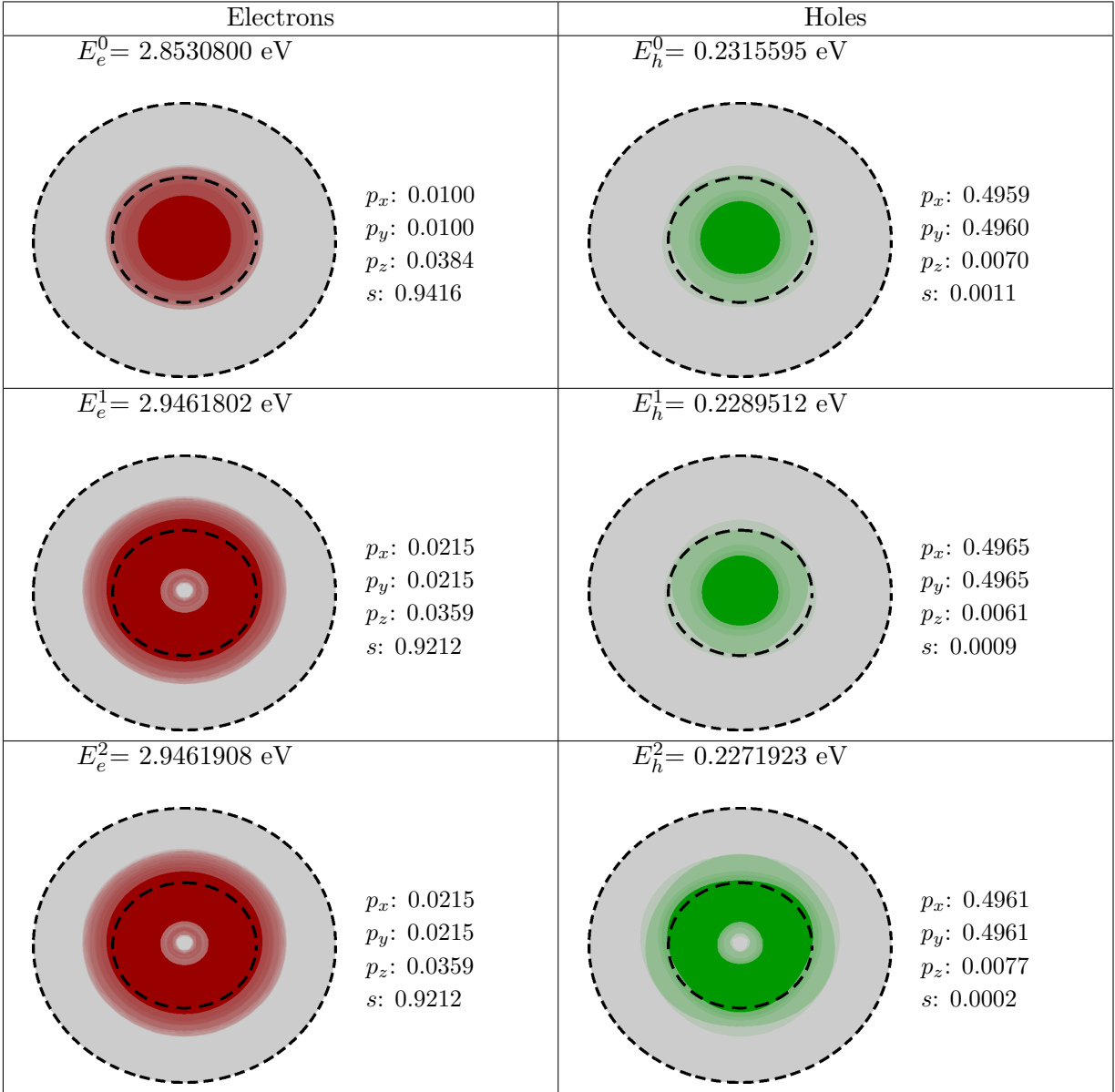


FIGURE 6.5: Single-particle electron (left) and hole (right) states for a  $\text{In}_{0.20}\text{Ga}_{0.80}\text{N}$  QD in presence of strain, built-in potential and SOC. Here, the picture shows the top view of the 10% (light) and 50% (dark) isosurfaces of the probability density distribution  $|\phi|^2$ . The first, second and third row represents the ground state, the first and second excited state in that order for both electrons (left) and holes (right). The energies and orbital characters of the single-particle states are also listed.

In summary, we have established the general electronic structure of *c*-plane InGaN QDs and how different contributions such as strain, built-in potential and SOC effects affect this through VCA-type calculations. In the next section, we turn to study the impact of random alloy fluctuations on the electronic properties of InGaN QDs. The VCA-type calculations presented above acts as an ideal starting point to understand how much the idealized  $C_{3v}$  symmetry is affected in the presence of random alloy fluctuations.

### 6.3 Impact of Random alloy fluctuations on electronic properties

In this step, we treat the InGaN alloy on a microscopic level and randomly replace Ga atoms by In atoms inside the QD region to get  $\text{In}_{0.20}\text{Ga}_{0.80}\text{N}$ . This allows us to study the impact of alloy microstructures on the results. Here, we use the  $sp^3$  TB model introduced in Sec. 2.2.2.2 to describe the alloy fluctuations. The relaxed atomic positions are determined by the VFF model described in Sec. 2.4.3. For the local built-in potential contributions, we use the local polarization theory (cf. Sec. 2.5) and for the clamp-ion contributions, we utilize the surface integral method discussed in Sec. 2.5.

With this framework, we have calculated the single-particle properties of the first three electron and hole states to be able to compare our results with the previously presented VCA-case. The above calculations are performed for five random configurations to study the impact of different alloy microstructures on the results. As an example, we have chosen an arbitrary configuration (Config-4) here and plotted the top-view of the charge densities isosurfaces in Fig. 6.6. Following the previous chapter, the electron and hole charge densities are plotted in red and green, respectively. The light and dark isosurfaces correspond to 10% and 50% of the respective maximum values. Several interesting features are visible from these plots. The nodal structure of the electron charge densities still represents to a first approximation  $s$ - and  $p$ -like character; however they are deformed due to the random distributions of In and Ga atoms. We find that this classification according to the nodal structure for the hole states is not possible indicating already that the random alloy fluctuations have a significant impact on the electronic structure. Furthermore, we find here that while the electron charge densities are affected by the local fluctuations, they are still localized in the region as we have seen in the VCA-type calculations. However, in contrast to the VCA-case, the hole states do not necessarily localize directly under the electron wave functions and we can also find situations where they localize near the interface. As compared to the electron states, hole states are localized in a smaller region. This can be attributed to the high effective mass of holes as pointed out earlier [76]. Overall, our results indicate that although random alloy fluctuations perturb the electron wave functions, they have a more dramatic effect on the hole wave functions. The strong hole localization obtained in this work is also consistent with what has been observed in InGaN/GaN QW systems [119]. In the next step, we plot the isosurfaces of the ground state electron (red) and hole (green) charge densities for the same configuration as shown in Fig. 6.7 in the side-view ( $\perp$  to  $c$ -axis). We observe here that similar to the previous case, the strong electrostatic built-in field along the  $c$ -axis leads to a spatial separation of electron and hole wave functions along this direction. The strong localization of hole wave functions described above is also visible from the side-view of the charge densities. Overall, we see that as compared to the VCA-case, significant changes in the electronic structure especially for the holes occur

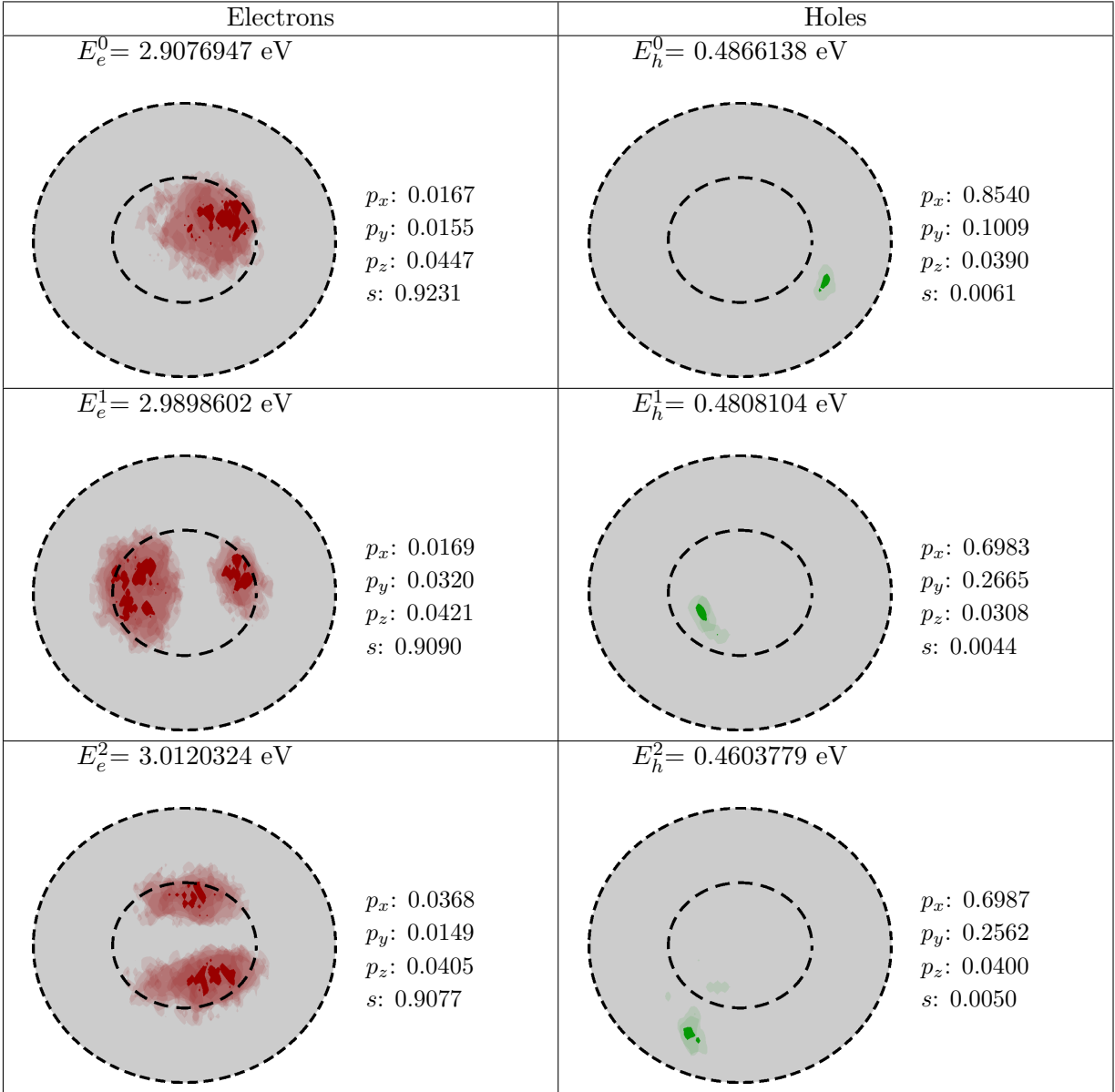


FIGURE 6.6: Single-particle electron (left) and hole (right) states for a  $\text{In}_{0.20}\text{Ga}_{0.80}\text{N}$  QD in the presence of random alloy fluctuations for an arbitrarily chosen configuration (Config-4). Here, the picture shows the top view of the 10% (light) and 50% (dark) isosurfaces of the probability density distribution  $|\phi|^2$ . The first, second and third row represents the ground state, the first and second excited state in that order for both electrons (left) and holes (right). The energies and orbital characters of the single-particle states are also listed.

when we take into account random alloy fluctuations. As we will show later, this is important for instance while calculating Coulomb matrix elements and optical properties.

Having discussed the impact of alloy fluctuations on electron and hole wave functions, we analyze now how different single-particle energies are affected by the alloy disorder. In Fig. 6.6, we also provide the energy eigenvalues connected to these wave functions. If the two excited electron states are considered as  $p$ -like, we find here a very large  $p$ -state splitting ( $\approx 22$  meV) for the electrons. It is to remind the reader that in the VCA-type calculation, the value of this

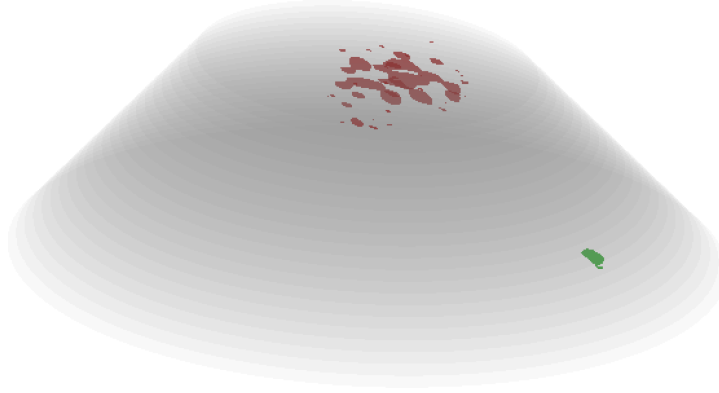


FIGURE 6.7: The picture shows 50% isosurfaces of the ground state charge density distribution for electrons (red) and holes (green) in side-view for Config-4. The QD is shown in grey.

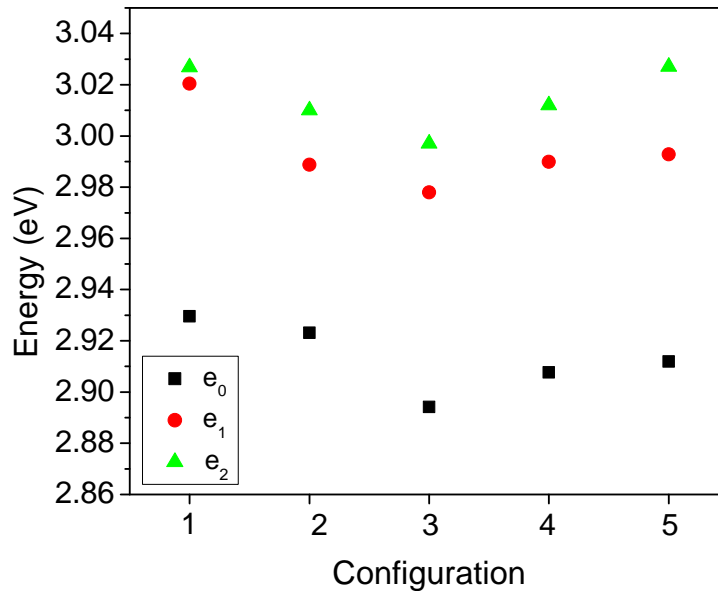


FIGURE 6.8: Electron energies for different configurations.  $e_0$ ,  $e_1$  and  $e_2$  denote the ground state, the first and second excited states for electrons.

splitting is  $10.6 \mu\text{eV}$ . Turning to the hole states, while we can no longer classify the hole states as  $p$ -like, the first two hole states are split by  $\approx 6 \text{ meV}$ . Again, the value of this splitting is  $2.6 \text{ meV}$  in the VCA-case. This means that splittings introduced due to random alloy fluctuations are higher when compared to a VCA-case. This conclusion is not just a particularity of the configuration. We find consistently that the electron  $p$ -state splittings vary between  $\approx 6 - 34 \text{ meV}$  depending on the microscopic configuration. Similarly, splittings between the first two hole states is also significantly dependant on the configuration number and correspondingly vary between  $\approx 1 - 15 \text{ meV}$ . This finding is summarized in Fig. 6.8 and Fig. 6.9 which illustrates respectively, the electron and hole energies of the first three bound states for five different configurations. Finally, we plot the ground state transition energies ( $E_e^0 - E_h^0$ ) for five different configurations in Fig. 6.10. We observe from Fig. 6.10 that the variation of transition energies between the lowest (Config-4) and the highest (Config-1) energy value is  $\approx 27 \text{ meV}$ . Overall,

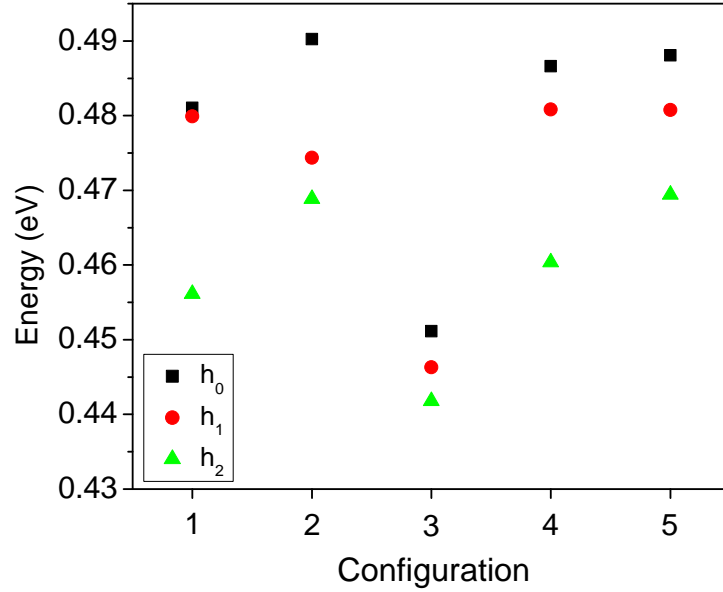


FIGURE 6.9: Hole energies for different configurations.  $h_0$ ,  $h_1$  and  $h_2$  denote the ground state, the first and second excited states for holes.

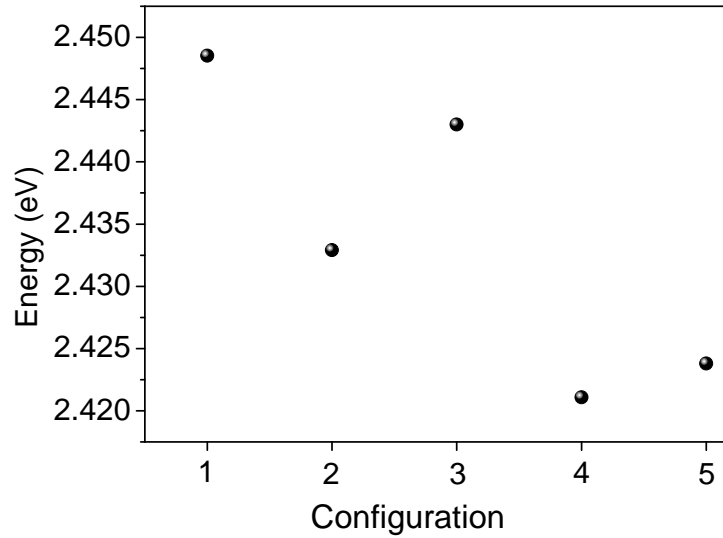


FIGURE 6.10: Ground state transition energies for five different configurations

from the above analysis we find that local fluctuations in the alloy significantly affect the symmetry and single-particle energies of polar InGa<sub>N</sub>/Ga<sub>N</sub> QDs.

Now turning to the orbital character of different states, we observe that similar to the VCA-case described in the last section, the electron ground state wave function mainly consists of  $s$  orbital contribution with much weaker contributions from  $p_x$ ,  $p_y$  and  $p_z$ . However, this situation is completely different for the hole case. In the VCA-case, with SOC, we observed that the ground and first excited hole states have a dominant  $p_x$  and  $p_y$  character respectively where as the second excited state has 50%  $p_x$  and  $p_y$  character. However, here we observe strong variations in the  $p_x$  and  $p_y$  orbital contributions for different hole states. Since local alloy fluctuations

break the symmetry of the  $c$ -plane, it is expected that  $p_x$  and  $p_y$  orbital starts to mix and contributes differently to the hole states.

Overall, it is to note that the conclusions drawn above is not a particularity of the configuration and qualitatively similar results are obtained from all of the configurations. Quantitatively, the single-particle energies and accordingly, orbital contributions to different states vary between configurations. This can be related to the differences in impact of local alloy fluctuations for different configurations. Furthermore, we found that alloy fluctuations alter the symmetry of the system and as a result, the splitting between  $p$ -like states is increased. Now the question is which point group can reflect the spatial symmetry of these systems? One could probably think that in the presence of alloy effects, we are dealing with a  $C_1$  symmetry [71] in which rotations by  $360^\circ$  should bring the system back in its original position. This point group basically contains a single group IRR  $A$  and a double group IRR  $A_{1/2}$  [71]. Both of these IRRs are 1-D; this might explain the non degeneracies of the different states in the presence of alloy fluctuations.

In summary, we have discussed the single-particle states and energies. We find very strong changes in the electronic structure when we take alloy fluctuations into account. That now asks immediately the question what excitonic structure is expected for a case where random alloy fluctuations have been included and how does this change in symmetry affect the FSS ? This FSS as discussed before is of central importance if we want to achieve entangled photon emission. So, it is not immediately obvious how these changes in symmetry will affect the FSS values. Therefore, initially one might think since  $C_{3v}$  symmetry is spoiled, we probably have a system that is not ideally suited for entangled photon emission. However, as we will show in the next section, we get a very surprising result that these systems might be suited for entangled photon emission.

Having discussed the single-particle states and energies in the presence of alloy fluctuations, we now move to investigate the optical properties of these QDs. As pointed out earlier, we are mainly interested in the fine structure behaviour of excitons which has applications in quantum entanglement. We have stressed in our discussions of theoretical framework (Chapter 2) that for an accurate modeling of these properties, we need to account many-body effects in the calculations. Accordingly, we will now focus on the excitonic structures of QDs in the next section using previously described CI framework.

## 6.4 Fine structure splitting

As discussed in detail in Sec. 2.6.4, quantum information applications require generation of entangled photons and zero bright-bright FSS is essential to achieve this [12]. Therefore, in

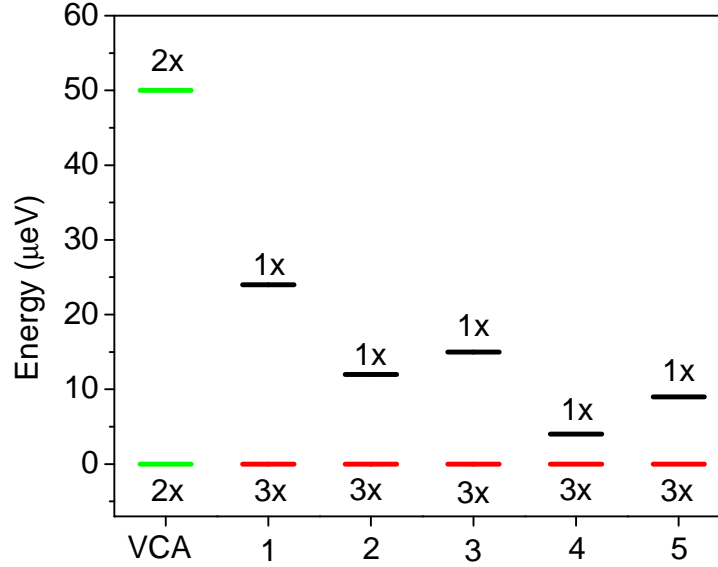


FIGURE 6.11: Fine structure splitting values for VCA-case and five different configurations

this discussion, our main aim is to study fine structure of the exciton ground state for WZ QDs with a  $C_{3v}$  symmetry and the influence of alloy fluctuations on the results. We include many-body effects in the calculations by using the CI scheme described in Sec. 2.6.2. In this method, the many-body Hamiltonian is constructed in the basis of anti-symmetrized products of bound single-particle electron and hole states. As a consequence, this method requires evaluation of Coulomb matrix elements describing the attractive electron-hole interaction and the electron-hole exchange interaction. These elements are calculated using the expressions given in Eq. 2.90 employing TB wave functions. Here, we analyze the difference between the results from the VCA and five different random alloy configurations.

Before looking at the results, we recap the exciton ground state properties using symmetry arguments and predict the degeneracies from a group-theoretical point of view. For this analysis, we follow the discussion introduced in Sec. 2.6.4. Thus, we start with classifying the single-particle states and exciton states according to symmetry. In a first step, we focus on the reference VCA structure in the presence of strain, built-in potential and SOC. As described earlier, in the presence of SOC, the eigenstates of each of the single-particle states can be represented by the IRR of the  $C_{3v}$  double group. In Sec. 6.2.2 we have shown that the hole ground state has  $p_x$ - and  $p_y$ -like character and correspondingly transforms according to a two-dimensional  $E_{3/2}$  representation. On the other hand, the electron ground state has dominant  $s$ -like character and transforms as the two-dimensional IRR  $E_{1/2}$ . Accordingly, as described in Sec. 2.6.4, one should expect Type-I ground state exciton-formed by an electron in the ground state ( $E_{1/2}$ ) and a hole in the ground state ( $E_{3/2}$ ). Correspondingly, the symmetry of this exciton state is labelled as  $E_{1/2} \otimes E_{3/2} = E \oplus E$ . Since  $E$  is a 2-D IRR of the  $C_{3v}$  group, we expect two two-fold degenerate states which are split by the electron-hole exchange interaction. Additionally, in the absence of SOC, the exchange interaction splits the exciton ground state into a singlet and

triplet states. On the other hand, since symmetry of the single-particle states are destroyed by random alloy fluctuations, let us now discuss what is expected in the exciton spectra if we assign the InGaN QDs with random alloy fluctuations to be of  $C_1$  symmetry. In the presence of SOC, one should expect that these excitons transform according to  $A_{1/2} \otimes A_{1/2} = A$  symmetry since  $C_1$  group has only one element ( $A_{1/2}$ ) in its double group IRR. Since  $A$  is a 1-D IRR, one expects four non-degenerate states in the ground state exciton spectra. Similarly, in the absence of SOC, one expects the excitons to have  $A \otimes A = A$  symmetry, since the single group IRR of  $C_1$  group also contains only one element  $A$ . This is a 1-D IRR and when spin is included in the description, we expect that the exciton ground state will split into a singlet and triplet states in the presence of exchange interaction.

Equipped with this group theoretical analysis, we now move to the FSS calculations of our reference VCA structure which represents an ideal  $C_{3v}$  symmetry. Subsequently, we include random alloy effects in the analysis. To compare the ground state exciton energies between VCA and the different microscopic configurations, we proceed in the following way. We always plot higher lying exciton states with respect to the ground state energy where the ground state energy is taken as a zero of the energy for the VCA and the respective configurations. In other words, we plot ( $\Delta E^X = E^X - E_{\text{GS}}^X$ ) for the random configurations and the VCA-case which is shown in Fig. 6.11. For our purpose here, gaining insight into the FSS and how it is impacted by random alloy fluctuations, this analysis is sufficient.

For the VCA-case, we have included six energetically lowest single-particle electron and hole states in the CI basis. This is due to the fact that the energy separation to higher lying states beyond these states is expected to contribute less to the correlation effects as compared to lower lying states. As expected from the group theoretical analysis presented above, our calculation yields (cf. Fig. 6.11) two doubly degenerate exciton states which are split by around 50  $\mu\text{eV}$  for the VCA. This is a calculation including electron-hole direct Coulomb and exchange interaction. In the absence of Coulomb effects, we obtain a four-fold degenerate exciton state and the inclusion of only direct Coulomb interaction did not split the degeneracy. Therefore, we obtain the expected result that the exchange interaction is responsible for the FSS of the excitonic states. Even though we have not performed any calculations on the optical activity of the exciton states, according to group theoretical arguments, both of these states should be bright and polarized in the  $(x, y)$  plane. Furthermore, following the discussion presented in Sec. 2.6.4, one can argue that in spite of the presence of a bright-bright splitting of 50  $\mu\text{eV}$ , one is left with zero bright-bright splitting from each pair of degenerate bright states. In this ideal picture,  $c$ -plane WZ QDs should be ideally suited for entangled photon emission. It is also to note that the excitonic structure obtained for WZ QDs in this study is completely different from the excitonic structure of (001) ZB QDs. As discussed in our theoretical framework section (cf. Sec. 2.6.4) for ideal ZB QDs, all of the four excitonic states are non-degenerate due to the

underlying  $C_{2v}$  symmetry. Therefore, there is no possibility of zero bright-bright splitting and as a result, entanglement is prohibited.

In the next step, we turn to the case where we have included random alloy fluctuations in the model. Here, FSS calculations have been performed for five different configurations. In the discussions presented in Sec. 6.3, we pointed out that hole states are strongly affected in the presence of alloy fluctuations and the energy level splitting of hole states is smaller as compared to electrons. Additionally, it was noted that the energetic difference between hole states also vary between configurations. Therefore, it is not immediately clear how different configurations will be affected by randomness in the alloy. If energetic difference between the hole states are small, one could expect that more hole states will have to be taken into account in the CI expansion to obtain accurate results for FSS values. Keeping this in mind, we include more hole states (first ten hole states) in our CI framework. For the electrons we include the six energetically lowest single-particle states. It is to note that in order to predict the absolute values of energies in the excitonic structure, it might be necessary to include more electron and hole states in the analysis. However, since we are mainly interested in how different alloy microstructures affect the symmetry and degeneracies of the excitonic states, the above assumptions are sufficient for this purpose. Looking at Fig. 6.11, we find that in the presence of random alloy fluctuations, a single non-degenerate state and an approximate triply degenerate state is obtained for all of the configurations. Additionally, we find that the splitting between the singlet and triplet states vary among the configurations. This reflects the dependence of excitonic energies on specific microscopic random alloy configuration. This result is in contrast to our group theoretical prediction presented above, where we had expected four non-degenerate states to be present in exciton ground state. However, it is quite interesting to observe that the excitonic structure for this case is similar to the case described in Sec. 2.6.4 without SOC where spin is a good quantum number. Therefore, and in contrast to the VCA-case, SOC is negligible here and we get back the situation without SOC. This might stems from the fact that hole states are strongly localized due to alloy fluctuations and the SOC is much smaller in InN and GaN as compared to InAs and GaAs systems. Keeping this in mind, it is important to examine what excitonic structure is expected in the absence of SOC if we assign the InGaN QDs with random alloy fluctuations to be of  $C_1$  symmetry. As described earlier, group theoretical analysis in this case gives the observed singlet-triplet splitting in the presence of electron-hole exchange interaction. Therefore, all of these discussions point towards the fact that negligible values of SOC might be the origin of singlet-triplet splitting observed in case of InGaN QDs having random alloy fluctuations.

To validate this argument, we calculated single-particle energies for one of the configurations in the absence of SOC. We find almost same single-particle energies and electronic structures with and without SOC at least for the ten lowest lying hole states. This points to the fact that SOC is negligible in the presence of alloy fluctuations where we can decouple orbital and spin

Configuration number	Config-1	Config-2	Config-3	Config-4	Config-5
$V_{1111}^{eh,ex}$ ( $\mu\text{eV}$ )	4	0.1	0.5	1.9	0.2

TABLE 6.1: Typical value of electron-hole exchange Coulomb matrix elements for five different configurations as calculated from the TB wave functions.

parts to get back the situation of singlet-triplet excitonic structure. Furthermore, similar to the last case, without many-body effects, we obtain a four-fold degenerate state and the attractive Coulomb interaction introduces only energetic shifts, but preserves the four-fold degeneracy of the exciton ground state. Therefore, one can conclude that the electron-hole exchange interaction is responsible for this splitting. However, the magnitude of this splitting tends to be small. We have listed as an example, electron-hole exchange matrix elements  $V_{1111}^{eh,ex}$  for different configurations in Table 6.1. It can be seen that the values of exchange matrix elements are only within a few  $\mu\text{eV}$  which is smaller by a factor of around 100-1000 compared to typical InAs/GaAs dots [29]. For instance, one such reports on InAs/GaAs QDs find electron-hole exchange matrix elements to be around 250-330  $\mu\text{eV}$  [29]. The small values of here calculated FSS can be attributed to the presence of strong-built in field along the  $c$ -axis, which separates the carriers. Since these exchange matrix elements are responsible for the splitting between the excitonic states, the magnitude of splitting are also small and are on the order of few  $\mu\text{eV}$ . Additionally, as pointed out earlier, the spin-orbit splitting values of As based systems is much higher than the considered III-N systems. Therefore, the magnitude of splittings between the different excitonic states is also much higher.

## 6.5 Conclusion

In summary, we have investigated the electronic and optical properties of truncated-cone shaped (0001)-oriented InGaN/GaN QDs of realistic size using an  $sp^3$  nearest neighbor atomistic TB model including local strain and piezoelectric potential effects. We started our discussion with an ideal VCA structure. From this analysis, we find that electro-static built-in field leads to a reordering of the hole states and SOC lifts certain degeneracies in the energy spectrum of single-particle states. This result is traced back to the group theoretical analysis of  $C_{3v}$  point group which reveals that no four-fold degenerate state can exist since there is no 4-D IRR in the  $C_{3v}$  double group. However, from our calculations we obtain only small splittings, i.e. in the order of few  $\mu\text{eV}$  for electron states and a few meV for the hole states. In the next step, the impact of random alloy fluctuations on the electronic and optical properties of (0001) QD is studied. We find that random alloy fluctuations lead to a very strong hole wave function localization effects inside the dot. Our calculations also show that random alloy fluctuations lead to a symmetry reduction of the electron and hole states. This was visible from the asymmetry of the obtained charge densities.

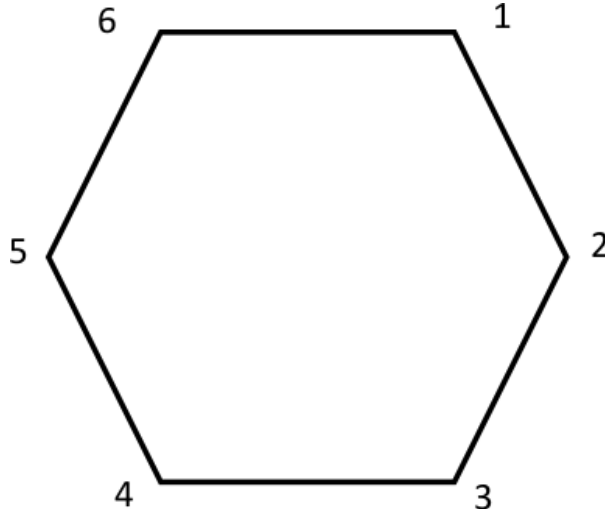
Turning to the many-body properties, we find that the excitonic structure of these systems are vastly different from conventional (001)-oriented InAs/GaAs systems where entanglement is prohibited due to the underlying  $C_{2v}$  symmetry. In VCA-type calculations, we find that these dots could be ideal for entangled photon emission due to the presence of zero bright-bright splitting in the excitonic structure. When random alloy fluctuations are included in the analysis, due to combined effects of strong hole localization and small SOC we find a very different excitonic structure as compared to the VCA-case. Here, independent of configurations studied, we find a singlet-triplet structure in the first four exciton states. Since spin is now a good quantum number, due to spin selection rules, the triplet state is expected to contain two bright states which are energetically degenerate. Therefore, these systems might be attractive for entangled photon emission. However, further studies are now required to analyze the optical spectra of these systems which is beyond the scope of this thesis.



## Appendix A

# Classes and Irreducible representations of $C_{6v}$ point group

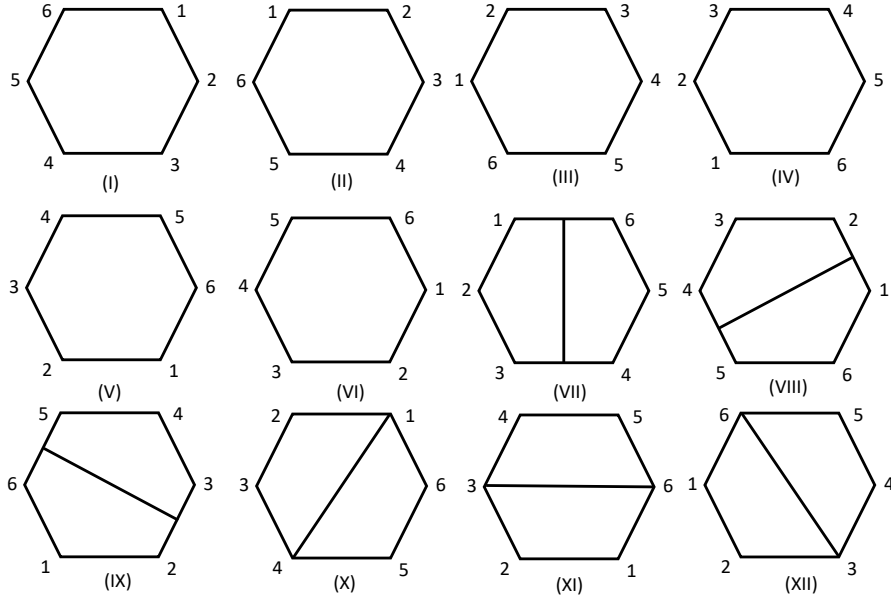
In this appendix, the classes corresponding to a  $C_{6v}$  point group is discussed in detail. For this problem, I have followed the lecture notes on “Group theory” by Prof. Dimitri Vvedensky at Imperial College London, UK [248] and simply used the symmetry operation of a regular hexagon. Let us assume a regular hexagon as follows:



We will use the following notation to denote how different symmetry operations transform the vertices of a hexagon.

$$\begin{pmatrix} 1 & 2 & 3 & 4 & 5 & 6 \\ v_1 & v_2 & v_3 & v_4 & v_5 & v_6 \end{pmatrix} \quad (\text{A.1})$$

Here, the first row corresponds to the order of the vertices before any transformation and  $v_i$  in the second row denotes the number of the  $i$ th vertex after a transformation has been applied. Correspondingly, the symmetry operation of a hexagon will be,



$$\begin{aligned}
 (I) E &= \begin{pmatrix} 1 & 2 & 3 & 4 & 5 & 6 \\ 1 & 2 & 3 & 4 & 5 & 6 \end{pmatrix} \\
 (II) C_6 &= \begin{pmatrix} 1 & 2 & 3 & 4 & 5 & 6 \\ 2 & 3 & 4 & 5 & 6 & 1 \end{pmatrix} \\
 (III) C_6^2 = C_3 &= \begin{pmatrix} 1 & 2 & 3 & 4 & 5 & 6 \\ 3 & 4 & 5 & 6 & 1 & 2 \end{pmatrix} \\
 (IV) C_6^3 = C_2 &= \begin{pmatrix} 1 & 2 & 3 & 4 & 5 & 6 \\ 4 & 5 & 6 & 1 & 2 & 3 \end{pmatrix} \\
 (V) C_6^4 = C_3^2 &= \begin{pmatrix} 1 & 2 & 3 & 4 & 5 & 6 \\ 5 & 6 & 1 & 2 & 3 & 4 \end{pmatrix} \\
 (VI) C_6^5 &= \begin{pmatrix} 1 & 2 & 3 & 4 & 5 & 6 \\ 6 & 1 & 2 & 3 & 4 & 5 \end{pmatrix} \\
 (VII) \sigma_{v,1} &= \begin{pmatrix} 1 & 2 & 3 & 4 & 5 & 6 \\ 6 & 5 & 4 & 3 & 2 & 1 \end{pmatrix} \\
 (VIII) \sigma_{v,2} &= \begin{pmatrix} 1 & 2 & 3 & 4 & 5 & 6 \\ 2 & 1 & 6 & 5 & 4 & 3 \end{pmatrix} \\
 (IX) \sigma_{v,3} &= \begin{pmatrix} 1 & 2 & 3 & 4 & 5 & 6 \\ 4 & 3 & 2 & 1 & 6 & 5 \end{pmatrix} \\
 (X) \sigma_{d,1} &= \begin{pmatrix} 1 & 2 & 3 & 4 & 5 & 6 \\ 1 & 6 & 5 & 4 & 3 & 2 \end{pmatrix} \\
 (XI) \sigma_{d,2} &= \begin{pmatrix} 1 & 2 & 3 & 4 & 5 & 6 \\ 3 & 2 & 1 & 6 & 5 & 4 \end{pmatrix} \\
 (XII) \sigma_{d,3} &= \begin{pmatrix} 1 & 2 & 3 & 4 & 5 & 6 \\ 5 & 4 & 3 & 2 & 1 & 6 \end{pmatrix}
 \end{aligned} \tag{A.2}$$

As summarized above, the symmetry operations of a hexagon consists of the identity (E), rotations by angles of  $\frac{n\pi}{3}$  ( $C_6, C_3, C_2, C_3^2, C_6^5$ ), three mirror planes ( $\sigma_{v,1}, \sigma_{v,2}, \sigma_{v,3}$ ) passing through opposite faces of the hexagon and three mirror planes ( $\sigma_{d,1}, \sigma_{d,2}, \sigma_{d,3}$ ) passing through opposite vertices of the hexagon.

Now, we will divide the symmetry elements into different *classes* according to following postulates.

- All the elements of a class correspond to the same type of operation, and is related by symmetry operations. For instance, identity, rotation and mirror planes are three different operations.
- All the elements of a *class* has the same *order*. The order of an element  $a$  is the smallest integer such that  $a^n = E$  (the identity). Here, rotations  $C_2$  has order 2,  $C_3$  and  $C_3^2$  have order 3,  $C_6$  and  $C_6^5$  have order 6. On the other hand,  $\sigma_{v,i}$  and  $\sigma_{d,i}$  have order 2.
- Two elements  $i$  and  $j$  of a group are in the same class, only if there is another element  $k$  in the group such that  $j = k^{-1}ik$ . Correspondingly,  $\sigma_{v,i}$  and  $\sigma_{d,i}$  belong to different classes as there is no group element which transforms  $\sigma_{v,i}$  to  $\sigma_{d,i}$ .

Using the above postulates, we obtain six different classes of  $C_{6v}$  group as

$$\begin{aligned}
 E &\equiv \{E\}, \\
 2C_6 &\equiv \{C_6, C_6^5\}, \\
 2C_3 &\equiv \{C_3, C_3^2\}, \\
 C_2 &\equiv \{C_2\}, \\
 3\sigma_v &\equiv \{\sigma_{v,1}, \sigma_{v,2}, \sigma_{v,3}\}, \\
 3\sigma_d &\equiv \{\sigma_{d,1}, \sigma_{d,2}, \sigma_{d,3}\}.
 \end{aligned} \tag{A.3}$$

#### *Derivation of IRRs in a coordinate basis*

The symmetry operations presented above can be represented by  $3 \times 3$  matrices that transforms a set of old  $x, y$ , and  $z$  coordinates into new  $x', y'$  and  $z'$  coordinates. For instance, a rotation around  $z$  axis can be written as,

$$\begin{pmatrix} x' \\ y' \\ z' \end{pmatrix} = \begin{pmatrix} \cos \theta & -\sin \theta & 0 \\ \sin \theta & \cos \theta & 0 \\ 0 & 0 & 1 \end{pmatrix} \begin{pmatrix} x \\ y \\ z \end{pmatrix}. \tag{A.4}$$

Now, in this basis, the symmetry operations of a  $C_{6v}$  point group can be written as,

$$\begin{aligned} E &= \begin{pmatrix} 1 & 0 & 0 \\ 0 & 1 & 0 \\ 0 & 0 & 1 \end{pmatrix} & C_6 &= \begin{pmatrix} 1/2 & -\sqrt{3}/2 & 0 \\ \sqrt{3}/2 & 1/2 & 0 \\ 0 & 0 & 1 \end{pmatrix} \\ C_2 &= \begin{pmatrix} -1 & 0 & 0 \\ 0 & -1 & 0 \\ 0 & 0 & 1 \end{pmatrix} & C_3 &= \begin{pmatrix} -1/2 & -\sqrt{3}/2 & 0 \\ \sqrt{3}/2 & -1/2 & 0 \\ 0 & 0 & 1 \end{pmatrix} \\ \sigma_d &= \begin{pmatrix} -1 & 0 & 0 \\ 0 & 1 & 0 \\ 0 & 0 & 1 \end{pmatrix} & \sigma_v &= \begin{pmatrix} 1 & 0 & 0 \\ 0 & -1 & 0 \\ 0 & 0 & 1 \end{pmatrix} \end{aligned} \quad (A.5)$$

The set of these matrices form the matrix representation of  $C_{6v}$  point group. Now, the trace of the matrix (character) gives the short hand version of the matrices  $\Gamma_{\text{general}}$  as

$C_{6v}$	$E$	$2C_6$	$2C_3$	$C_2$	$3\sigma_d$	$3\sigma_v$
$\Gamma_{\text{general}}$	3	2	0	-1	1	1

(A.6)

$\Gamma_{\text{general}}$  is a reducible representation since it can be simplified further by “Block Diagonalization”. In the illustrated case of  $C_{6v}$ , since  $x$  and  $y$  are not independent, Block diagonalization gives  $2 \times 2$  ( $x, y$ ) and  $1 \times 1$  ( $z$ ) matrices. Accordingly, the matrices in Bloch form can be written as,

$$\begin{aligned} E &= \begin{pmatrix} \begin{bmatrix} 1 & 0 \\ 0 & 1 \end{bmatrix} & 0 \\ 0 & 0 & \begin{bmatrix} 1 \end{bmatrix} \end{pmatrix} & C_6 &= \begin{pmatrix} \begin{bmatrix} 1/2 & -\sqrt{3}/2 \\ 1/2 & 1 \end{bmatrix} & 0 \\ 0 & 0 & \begin{bmatrix} 1 \end{bmatrix} \end{pmatrix} \\ C_2 &= \begin{pmatrix} \begin{bmatrix} -1 & 0 \\ 0 & -1 \end{bmatrix} & 0 \\ 0 & 0 & \begin{bmatrix} 1 \end{bmatrix} \end{pmatrix} & C_3 &= \begin{pmatrix} \begin{bmatrix} -1/2 & -\sqrt{3}/2 \\ \sqrt{3}/2 & -1/2 \end{bmatrix} & 0 \\ 0 & 0 & \begin{bmatrix} 1 \end{bmatrix} \end{pmatrix} \\ \sigma_d &= \begin{pmatrix} \begin{bmatrix} -1 & 0 \\ 0 & 1 \end{bmatrix} & 0 \\ 0 & 0 & \begin{bmatrix} 1 \end{bmatrix} \end{pmatrix} & \sigma_v &= \begin{pmatrix} \begin{bmatrix} 1 & 0 \\ 0 & -1 \end{bmatrix} & 0 \\ 0 & 0 & \begin{bmatrix} 1 \end{bmatrix} \end{pmatrix} \end{aligned} \quad (A.7)$$

Subsequently, we can find the traces of  $2 \times 2$  and  $1 \times 1$  matrices and obtain the symmetry transformations for the the irreducible representations as:

$C_{6v}$	$E$	$2C_6$	$2C_3$	$C_2$	$3\sigma_d$	$3\sigma_v$	$Coordinates(basis)$	(A.8)
$E_1$	2	1	-1	-2	0	0	$(x, y)$	
$A_1$	1	1	1	1	1	1	$z$	



## Appendix B

# Material parameter sets used for k·p and tight-binding calculations

Parameter	AlN
$a_{\text{lat}}(\text{\AA})$ [62]	3.112
$c_{\text{lat}}(\text{\AA})$ [62]	4.982
$C_{11}$ (GPa) [249]	410.2
$C_{12}$ (GPa) [249]	142.4
$C_{13}$ (GPa) [249]	110.1
$C_{33}$ (GPa) [249]	385.0
$C_{44}$ (GPa) [249]	122.9
$e_{15}$ (C/m <sup>2</sup> ) [61]	-0.39
$e_{31}$ (C/m <sup>2</sup> ) [61]	-0.63
$e_{33}$ (C/m <sup>2</sup> ) [61]	1.46
$B_{115}$ (C/m <sup>2</sup> ) [220]	4.4
$B_{125}$ (C/m <sup>2</sup> ) [220]	2.4
$B_{135}$ (C/m <sup>2</sup> ) [220]	-0.1
$B_{311}$ (C/m <sup>2</sup> ) [220]	3.0
$B_{312}$ (C/m <sup>2</sup> ) [220]	3.0
$B_{313}$ (C/m <sup>2</sup> ) [220]	3.8
$B_{333}$ (C/m <sup>2</sup> ) [220]	-26.0
$B_{344}$ (C/m <sup>2</sup> ) [220]	3.2
$P_{\text{sp}}$ (C/m <sup>2</sup> ) [61]	-0.091
$\epsilon_r$ [160]	8.5
$b_{\text{sp}}$ (C/m <sup>2</sup> ) [226]	-0.0191 (AlGaIn)

TABLE B.1: Material parameters for AlN used in this study. It is to note that for this material system, we are only interested in the calculation of polarization properties. No electronic structure calculations have been performed.  $a_{\text{lat}}$  and  $c_{\text{lat}}$  denotes lattice constants along in-plane and out-of plane directions respectively. Elastic constants are denoted by  $C_{ij}$ , first-order piezoelectric coefficients by  $e_{\mu j}$  and second-order ones by  $B_{\mu j k}$ . The spontaneous polarization is given by  $P_{\text{sp}}$  and related bowing parameters for InGaIn and AlGaIn are denoted as  $b_{\text{sp}}$ . The dielectric constant is given by  $\epsilon_r$ .

Parameter	GaN	InN
$a_{\text{lat}}(\text{\AA})$ [62]	3.189	3.545
$c_{\text{lat}}(\text{\AA})$ [62]	5.185	5.703
$C_{11}$ (GPa) [249]	368.6	233.8
$C_{12}$ (GPa) [249]	131.6	110.0
$C_{13}$ (GPa) [249]	95.7	91.6
$C_{33}$ (GPa) [249]	406.2	238.3
$C_{44}$ (GPa) [249]	101.7	55.4
$e_{15}(C/m^2)$ [61]	-0.32	-0.42
$e_{31}(C/m^2)$ [61]	-0.44	-0.58
$e_{33}(C/m^2)$ [61]	0.74	1.07
$B_{115}$ (C/m <sup>2</sup> ) [220]	3.8	4.5
$B_{125}$ (C/m <sup>2</sup> ) [220]	2.3	2.8
$B_{135}$ (C/m <sup>2</sup> ) [220]	2.7	1.6
$B_{311}$ (C/m <sup>2</sup> ) [220]	6.2	4.8
$B_{312}$ (C/m <sup>2</sup> ) [220]	3.3	3.7
$B_{313}$ (C/m <sup>2</sup> ) [220]	0.4	0.5
$B_{333}$ (C/m <sup>2</sup> ) [220]	-21.4	-18.6
$B_{344}$ (C/m <sup>2</sup> ) [220]	0.4	0.5
$P_{\text{sp}}(C/m^2)$ [61]	-0.040	-0.049
$\epsilon_r$ [164]	9.6	15.3
$E_g$ (eV) [31]	3.51	0.69
$\Delta_{\text{CF}}$ (eV) [250]	0.019	0.024
$\Delta_{\text{SO}}$ (eV) [62]	0.017	0.005
$m_e(m_0)$ [36]	0.209	0.068
$A_1(\hbar^2/2m_0)$ [36]	-5.947	-15.803
$A_2(\hbar^2/2m_0)$ [36]	-0.528	-0.497
$A_3(\hbar^2/2m_0)$ [36]	5.414	15.251
$A_4(\hbar^2/2m_0)$ [36]	-2.512	-7.151
$A_5(\hbar^2/2m_0)$ [36]	-2.510	-7.060
$A_6(\hbar^2/2m_0)$ [36]	-3.202	-10.078
$a_c$ (eV) [62]	-4.08	-7.2
$a_c - D_1$ (eV) [250]	-5.81	-3.64
$a_c - D_2$ (eV) [250]	-8.92	-4.58
$D_3$ (eV) [250]	5.45	2.68
$D_4$ (eV) [250]	-2.97	-1.78
$D_5$ (eV) [250]	-2.87	-2.07
$D_6$ (eV) [250]	-3.95	-3.02
$E_{P\parallel}$ (eV) [36, 171]	18.7	8.742
$E_{P\perp}$ (eV) [36, 171]	17.7	8.809
$\Delta E_{\text{VB}}^{\text{InN/GaN}}$ (eV) [166]	0.62	
	InGaN	
$b_{\text{sp}}$ (C/m <sup>2</sup> ) [226]	-0.037	

TABLE B.2: Material parameters used in this study for GaN and InN for  $\mathbf{k}\cdot\mathbf{p}$  calculations.  $a_{\text{lat}}$  and  $c_{\text{lat}}$  denotes lattice constants along in-plane and out-of plane directions respectively. Elastic constants are denoted by  $C_{ij}$ , first-order piezoelectric coefficients by  $e_{\mu j}$  and second-order ones by  $B_{\mu jk}$ . The spontaneous polarization is given by  $P_{\text{sp}}$  and the related bowing parameter for InGaN is denoted as  $b_{\text{sp}}$ . The dielectric constant is given by  $\epsilon_r$ .  $E_g$  denotes the band gap,  $\Delta_{\text{so}}$  the spin-orbit coupling,  $\Delta_{\text{cf}}$  the crystal-field splitting,  $m_e$  the effective electron mass and  $A_i$  are Luttinger-like hole effective masses.  $a_c$  and  $D_i$  denote conduction and valence band deformation potentials respectively. Interband matrix element for the momentum operator parallel and perpendicular to the  $c$ -axis is given by  $E_{P\parallel}$  and  $E_{P\perp}$ .  $\Delta E_{\text{VB}}$  is the valence band offset.

	$\Delta_{\text{so}} = 0$		$\Delta_{\text{so}} \neq 0$	
	InN [eV]	GaN [eV]	InN [eV]	GaN [eV]
E(s,a)	-11.9173	-10.6158	-11.9173	-10.6158
E(p,a)	0.4886	0.8183	0.4867	0.8127
E(p <sub>z</sub> ,a)	0.4558	0.7926	0.4572	0.7849
E(s,c)	0.4837	0.9122	0.4837	0.9122
E(p,c)	6.5322	6.6788	6.5322	6.6788
V(s,s)	-1.6124	-5.9749	-1.6124	-5.9749
V(x,x)	1.7863	2.3381	1.7863	2.3381
V(x,y)	4.8338	5.4697	4.8338	5.4697
V(sa,pc)	1.8919	4.0909	1.8919	4.0909
V(pa,sc)	6.1355	8.6655	6.1355	8.6655
$\lambda_a$	0	0	0.0017	0.0052
$\lambda_c$	0	0	0.0017	0.0052

TABLE B.3: Tight-binding parameters (in eV) for the nearest neighbors of wurtzite InN and GaN. Ref. [102] notation is used.



## Appendix C

# Expressions for first- and second-order piezoelectric, spontaneous polarization vector fields as a function of $\theta$

In this appendix, we summarize the analytic expressions for first- and second-order piezoelectric polarization vector fields derived from the approach presented in Sec. 2.2.1. Please note that the expression for the first-order piezoelectric polarization vector can also be found in Ref. [160] which are similar to the expressions given in Ref. [225]. The equations for the rotated elastic tensor are explicitly given in Ref. [160] and are not repeated here.

### First-order piezoelectric and spontaneous polarization vector field as a function of the incline angle $\theta$

Using the transformation rules described in Sec. 2.2.1, The  $x$ -,  $y$ - and  $z$ -components of the first-order piezoelectric polarization vector field, as a function of  $\theta$ , are given by:

$$P_{\text{pz},x'}^{\text{FO}} = \varepsilon_{x'x'} \left[ e_{33} \sin^3 \theta + \left( \frac{e_{31} - 2e_{15}}{2} \right) \sin(2\theta) \cos \theta \right] \quad (\text{C.1})$$

$$+ \varepsilon_{z'z'} \left[ e_{31} \sin^3 \theta + \left( \frac{e_{31} + 2e_{15}}{2} \right) \sin(2\theta) \cos \theta \right] \\ + \varepsilon_{y'y'} [e_{31} \sin \theta] + \varepsilon_{x'z'} [2e_{15} \cos(2\theta) \cos \theta - e_{33} \sin(2\theta) \sin \theta] ,$$

$$P_{\text{pz},y'}^{\text{FO}} = 2e_{15} [\varepsilon_{y'z'} \cos \theta - \varepsilon_{x'y'} \sin \theta] , \quad (\text{C.2})$$

$$P_{\text{pz},z'}^{\text{FO}} = \varepsilon_{x'x'} \left[ e_{31} \cos^3 \theta + \left( \frac{e_{33} - 2e_{15}}{2} \right) \sin(2\theta) \sin \theta \right] \quad (\text{C.3})$$

$$+ \varepsilon_{z'z'} \left[ e_{33} \cos^3 \theta + \left( \frac{e_{31} + 2e_{15}}{2} \right) \sin(2\theta) \sin \theta \right] \\ + \varepsilon_{y'y'} [e_{31} \cos \theta] + \varepsilon_{x'z'} [(e_{31} - e_{33}) \sin(2\theta) \cos \theta + 2e_{15} \cos(2\theta) \sin \theta] .$$

The required strain tensor components in the rotated frame are denoted by  $\varepsilon_{i'j'}$ . For QW systems analytic expressions for  $\varepsilon_{i'j'}$  can be derived and are for instance given in Ref. [225].

For the spontaneous polarization  $\mathbf{P}_{\text{SP}}$  we find: [160]

$$\mathbf{P}_{\text{SP}} = \begin{pmatrix} -P_{\text{sp}} \sin \theta \\ 0 \\ P_{\text{sp}} \cos \theta \end{pmatrix} . \quad (\text{C.4})$$

### Second-order piezoelectric polarization vector field as a function of the incline angle $\theta$

Using the transformation rules described in Sec. 2.2.1, the  $x$ -,  $y$ - and  $z$ -components of the second-order piezoelectric polarization vector field as a function of incline angle  $\theta$  read:

$$P_{\text{pz},x'}^{\text{SO}} = 2B_{115} \cos \theta [A - BC] - 2B_{135} \cos \theta (FC) - 2B_{125} \cos \theta [A + \varepsilon_{y'y'} C] \quad (\text{C.5})$$

$$- \frac{B_{311}}{2} \sin \theta [B^2 + 2D^2 + \varepsilon_{y'y'}^2] + B_{312} \sin \theta [D^2 - \varepsilon_{y'y'} B] \\ - B_{313} \sin \theta [BF + \varepsilon_{y'y'} F] - 2B_{344} \sin \theta [E^2 + C^2] - \frac{1}{2} \sin \theta B_{333} F^2$$

$$P_{\text{pz},y'}^{\text{SO}} = 2B_{115} [\varepsilon_{y'y'} E - DC] + 2B_{135} EF + 2B_{125} [DC + EB] \quad (\text{C.6})$$

$$P_{\text{pz},z'}^{\text{SO}} = 2B_{115} \sin \theta [A - BC] - 2B_{135} \sin \theta (FC) - 2B_{125} \sin \theta [A + \varepsilon_{y'y'} C] \quad (\text{C.7})$$

$$+ \frac{B_{311}}{2} \cos \theta [B^2 + 2D^2 + \varepsilon_{y'y'}^2] - B_{312} \cos \theta [D^2 - \varepsilon_{y'y'} B] \\ + B_{313} \cos \theta [BF + \varepsilon_{y'y'} F] + 2B_{344} \cos \theta [E^2 + C^2] + \frac{1}{2} \cos \theta B_{333} F^2 ,$$

where the coefficients  $A, \dots, F$  are given by

$$\begin{aligned}
 A &= [\varepsilon_{x'y'} \cos \theta + \varepsilon_{y'z'} \sin \theta] [\varepsilon_{y'z'} \cos \theta - \varepsilon_{x'y'} \sin \theta] , \\
 B &= \varepsilon_{x'x'} \cos^2 \theta + \varepsilon_{z'z'} \sin^2 \theta + \varepsilon_{x'z'} \sin(2\theta) , \\
 C &= \left[ \frac{\varepsilon_{x'x'} - \varepsilon_{z'z'}}{2} \right] \sin(2\theta) - \varepsilon_{x'z'} \cos(2\theta) , \\
 D &= \varepsilon_{x'y'} \cos \theta + \varepsilon_{y'z'} \sin \theta , \\
 E &= \varepsilon_{y'z'} \cos \theta - \varepsilon_{x'y'} \sin \theta , \\
 F &= \varepsilon_{x'x'} \sin^2 \theta + \varepsilon_{z'z'} \cos^2 \theta - \varepsilon_{x'z'} \sin(2\theta) .
 \end{aligned}$$



# Bibliography

- [1] <https://www.businesswire.com/news/home/20180730005527/en/Global-Market-Quantum-Dots-2030-27.5-Billion>.
- [2] <https://www.nanosysinc.com/news/2018/10/15/ihs-markit-quantum-dot-tv-outpaces-oled-tv-growth-in-2019>.
- [3] T. Frecker, D. Bailey, X. Arzeta-Ferrer, J. McBride, and S. J. Rosenthal, “Review-quantum dots and their application in lighting, displays, and biology,” *ECS J. Solid State Sci. Technol.* **5**, R3019 (2016).
- [4] M. K. Choi, J. Yang, T. Hyeon, and D.-H. Kim, “Flexible quantum dot light-emitting diodes for next-generation displays,” *npj Flexible Electronics* **2**, 10 (2018).
- [5] X. Gao, Y. Cui, R. M. Levenson, L. W. K. Chung, and N. S., “In vivo cancer targeting and imaging with semiconductor quantum dots,” *Nat. Biotechnol.* **22**, 969 (2004).
- [6] T. Alizadeh and M. Shokri, “A new humidity sensor based upon graphene quantum dots prepared via carbonization of citric acid,” *Sens. Actuators B:Chem.* **222**, 728 (2016).
- [7] M. Gschrey, A. Thoma, P. Schnauber, M. Seifried, R. Schmidt, B. Wohlfeil, L. Krüger, J. H. Schulze, T. Heindel, S. Burger, et al., “Highly indistinguishable photons from deterministic quantum-dot microlenses utilizing three-dimensional in situ electron-beam lithography,” *Nat. Commun.* **6**, 7662 (2015).
- [8] B. Z. Ristic, M. M. Milenkovic, I. R. Dakic, B. M. Todorovic-Markovic, M. S. Milosavljevic, M. D. Budimir, V. G. Paunovic, M. D. Dramicanin, Z. M. Markovic, and V. S. Trajkovic, “Photodynamic antibacterial effect of graphene quantum dots,” *Biomaterials* **35**, 4428 (2014).
- [9] O. E. Semonin, J. M. Luther, and M. C. Beard, “Quantum dots for next-generation photovoltaics,” *Materials Today* **15**, 508 (2012).
- [10] B. Mohanty, M. Ghorbani-Asl, S. Kretschmer, A. Ghosh, P. Guha, S. K. Panda, B. Jena, A. V. Krashennnikov, and B. K. Jena, “MoS<sub>2</sub> Quantum Dots as Efficient Catalyst Materials for the Oxygen Evolution Reaction,” *ACS Catalysis* **8**, 1683 (2018).

- [11] X. Ding, Y. He, Z.-C. Duan, N. Gregersen, M.-C. Chen, S. Unsleber, S. Maier, C. Schneider, M. Kamp, S. Höfling, et al., “On-demand single photons with high extraction efficiency and near-unity indistinguishability from a resonantly driven quantum dot in a micropillar,” *Phys. Rev. Lett.* **116**, 020401 (2016).
- [12] R. Hafenbrak, S. M. Ulrich, P. Michler, L. Wang, A. Rastelli, and O. G. Schmidt, “Triggered polarization-entangled photon pairs from a single quantum dot up to 30 K,” *New J. Phys.* **9**, 315 (2007).
- [13] X. Yang, M. Arita, S. Kako, and Y. Arakawa, “Formation of m-plane ingan/gan quantum dots using strain engineering of algan/aln interlayers,” *Applied Physics Letters* **99**, 061914 (2011).
- [14] T. Zhu, F. Oehler, B. P. L. Reid, R. M. Emery, R. A. Taylor, M. J. Kappers, and R. A. Oliver, “Non-polar (11-20) InGaN quantum dots with short exciton lifetimes grown by metal-organic vapor phase epitaxy,” *Appl. Phys. Lett.* **102**, 251905 (2013).
- [15] T. Wang, T. J. Puchler, T. Zhu, J. C. Jarman, R. A. Oliver, and R. A. Taylor, “High-temperature performance of non-polar (11-20) InGaN quantum dots grown by a quasi-two-temperature method,” *Phys. Status Solidi (b)* **254**, 1600724 (2017).
- [16] G. Bester, X. Wu, D. Vanderbilt, and A. Zunger, “Importance of second-order piezoelectric effects in zinc-blende semiconductors,” *Phys. Rev. Lett.* **96**, 187602 (2006).
- [17] J. Brault, D. Rosales, B. Damilano, M. Leroux, A. Courville, M. Korytov, S. Chenot, P. Vennéguès, B. Vinter, P. D. Mierry, et al., “Polar and semipolar GaN/Al<sub>0.5</sub>Ga<sub>0.5</sub>N nanostructures for UV light emitters,” *Semicond. Sci. Technol.* **29**, 084001 (2014).
- [18] Y.-R. Wu, Y.-Y. Lin, H.-H. Huang, and J. Singh, “Electronic and optical properties of InGaN quantum dot based light emitters for solid state lighting,” *J. Appl. Phys.* **105**, 013117 (2009).
- [19] G. Weng, Y. Mei, J. Liu, W. Hofmann, L. Ying, J. Zhang, Y. Bu, Z. Li, H. Yang, and B. Zhang, “Low threshold continuous-wave lasing of yellow-green InGaN-QD vertical-cavity surface-emitting lasers,” *Opt. Express* **24**, 15546 (2016).
- [20] Y. Mei, G.-E. Weng, B.-P. Zhang, J.-P. Liu, W. Hofmann, L.-Y. Ying, J.-Y. Zhang, Z.-C. Li, H. Yang, and H.-C. Kuo, “Quantum dot vertical-cavity surface-emitting lasers covering the ‘green gap’,” *Light Sci. Appl.* **6**, e16199 (2017).
- [21] T. Frost, A. Hazari, A. Aiello, M. Z. Baten, L. Yan, J. Mirecki-Millunchick, and P. Bhattacharya, “High performance red-emitting multiple layer InGaN/GaN quantum dot lasers,” *Jpn. J. Appl. Phys.* **55**, 032101 (2016).

- [22] G.-L. Su, T. Frost, P. Bhattacharya, and J. M. Dallesasse, “Physical model for high indium content InGaN/GaN self-assembled quantum dot ridge-waveguide lasers emitting at red wavelengths ( $\lambda \approx 630$  nm),” *Opt. Express* **23**, 12850 (2015).
- [23] M. J. Holmes, K. Choi, S. Kako, M. Arita, and Y. Arakawa, “Room-temperature triggered single photon emission from a III-nitride site-controlled nanowire quantum dot,” *Nano Lett.* **14**, 982 (2014).
- [24] M. J. Holmes, S. Kako, K. Choi, M. Arita, and Y. Arakawa, “Single photons from a hot solid-state emitter at 350 K,” *ACS Photonics* **3**, 543 (2016).
- [25] C.-H. Teng, L. Zhang, T. A. Hill, B. Demory, H. Deng, and P.-C. Ku, “Elliptical quantum dots as on-demand single photons sources with deterministic polarization states,” *Appl. Phys. Lett.* **107**, 191105 (2015).
- [26] R. Singh and G. Bester, “Nanowire quantum dots as an ideal source of entangled photon pairs,” *Phys. Rev. Lett.* **103**, 063601 (2009).
- [27] Y.-M. He, Y. He, Y.-J. Wei, D. Wu, M. Atatüre, C. Schneider, S. Höfling, M. Kamp, C.-Y. Lu, and J.-W. Pan, “On-demand semiconductor single-photon source with near-unity indistinguishability,” *Nat. Nanotechnol.* **8**, 213 (2013).
- [28] N. Somaschi, V. Giesz, L. De Santis, J. C. Loredó, M. P. Almeida, G. Hornecker, S. L. Portalupi, T. Grange, C. Antón, J. Demory, et al., “Near-optimal single-photon sources in the solid state,” *Nat. Photonics* **10**, 340 (2016), article.
- [29] E. Goldmann, Ph.D. thesis, University of Bremen (2014).
- [30] P. Bhattacharya, “Properties of lattice-matched and strained indium gallium arsenide” (INSPEC, London, 1993).
- [31] J. Wu, “When group-III nitrides go infrared: New properties and perspectives,” *J. Appl. Phys.* **106**, 011101 (2009).
- [32] P. J. Parbrook and T. Wang, “Light emitting and laser diodes in the ultraviolet,” *IEEE J. Sel. Top. Quantum Electron.* **17**, 1402 (2011).
- [33] J. Y. Tsao, S. Chowdhury, M. A. Hollis, D. Jena, N. M. Johnson, K. A. Jones, R. J. Kaplar, S. Rajan, C. G. Van de Walle, E. Bellotti, et al., “Ultrawide-bandgap semiconductors: Research opportunities and challenges,” *Adv. Electron. Mater.* **4**, 1600501 (2018).
- [34] E. T. Yu, “II-V Nitride Semiconductors: Applications and Devices” (CRC Press, 2002).
- [35] B. Gil, ed., “III-Nitride Semiconductors and their Modern Devices” (Oxford University Press, 2014).

- [36] P. Rinke, M. Winkelnkemper, A. Qteish, D. Bimberg, J. Neugebauer, and M. Scheffler, “Consistent set of band parameters for the group-III nitrides AlN, GaN, and InN,” *Phys. Rev. B* **77**, 075202 (2008).
- [37] J. Speck and S. Rosner, “The role of threading dislocations in the physical properties of GaN and its alloys,” *Physica B: Condens. Matter* **273–274**, 24 (1999).
- [38] F. Bernardini, V. Fiorentini, and D. Vanderbilt, “Spontaneous polarization and piezoelectric constants of III-V nitrides,” *Phys. Rev. B* **56**, R10024 (1997).
- [39] O. Ambacher, J. Majewski, C. Miskys, A. Link, M. Hermann, M. Eickhoff, M. Stutzmann, F. Bernardini, V. Fiorentini, V. Tilak, et al., “Pyroelectric properties of Al(In)Ga<sub>N</sub>/Ga<sub>N</sub> hetero- and quantum well structures,” *J. Phys. Condens. Matter* **14**, 3399 (2002).
- [40] C. B. Murray, D. J. Norris, and M. G. Bawendi, “Synthesis and characterization of nearly monodisperse CdE (E = sulfur, selenium, tellurium) semiconductor nanocrystallites,” *J. Am. Chem. Soc.* **115**, 8706 (1993).
- [41] H. Jiang and J. Singh, “Self-assembled semiconductor structures: electronic and optoelectronic properties,” *IEEE J. Quant. Electron.* **34**, 1188 (1998).
- [42] M. Korkusinski, W. Sheng, and P. Hawrylak, “Designing quantum systems in self-assembled quantum dots,” *Phys. Status Solidi (b)* **238**, 246 (2003).
- [43] P. Michler, “Single Semiconductor Quantum Dots” (Springer, Berlin, 2009).
- [44] R. A. Oliver, G. A. D. Briggs, M. J. Kappers, C. J. Humphreys, S. Yasin, J. H. Rice, J. D. Smith, and R. A. Taylor, “InGa<sub>N</sub> quantum dots grown by metalorganic vapor phase epitaxy employing a post-growth nitrogen anneal,” *Appl. Phys. Lett.* **83**, 755 (2003).
- [45] A. Das, P. Sinha, Y. Kotsar, P. Kandaswamy, G. Dimitrakopoulos, T. Kehagias, P. Komninou, G. Nataf, P. D. Mierry, and E. Monroy, “Growth and characterization of polar (0001) and semipolar (11-22) InGa<sub>N</sub>/Ga<sub>N</sub> quantum dots,” *J. Cryst. Growth* **323**, 161 (2011).
- [46] G. P. Dimitrakopoulos, E. Kalesaki, J. Kioseoglou, T. Kehagias, A. Lotsari, L. Lahourcade, E. Monroy, I. Häusler, H. Kirmse, W. Neumann, et al., “Morphology and strain of self-assembled semipolar Ga<sub>N</sub> quantum dots in (11 $\bar{2}$ 2) AlN,” *J. Appl. Phys.* **108**, 104304 (2010).
- [47] J. M. Woodward, A. Y. Nikiforov, K. F. Ludwig, and T. D. Moustakas, “Analysis of InGa<sub>N</sub> nanodots grown by droplet heteroepitaxy using grazing incidence small-angle X-ray scattering and electron microscopy,” *J. Appl. Phys.* **122**, 065305 (2017).
- [48] M. Henini, “Molecular Beam Epitaxy” (Elsevier, 2012).

- [49] N. Koguchi, K. Ishige, and S. Takahashi, “New selective molecular-beam epitaxial growth method for direct formation of GaAs quantum dots,” *J. Vac. Sci. Technol. B: Microelectron. Nanometer Struct. Process. Meas. Phenom.* **11**, 787 (1993).
- [50] T. Hanada, “Oxide and nitride semiconductors” (Springer, Berlin, 2009).
- [51] H. Masui, J. Sonoda, N. Pfaff, I. Koslow, S. Nakamura, and S. P. DenBaars, “Quantum-confined stark effect on photoluminescence and electroluminescence characteristics of InGaN-based light-emitting diodes,” *J. Phys. D: Applied Physics* **41**, 165105 (2008).
- [52] M. A. Caro Bayo, Ph.D. thesis, University College Cork, Cork (2013).
- [53] P. Yu and M. Cardona, “Fundamentals of Semiconductors: Physics and Materials Properties” (Springer International Publishing, 2010).
- [54] G. Kozlowski, B. Corbett, and S. Schulz, “Color stability, wave function overlap and leakage currents in InGaN-based LED structures: the role of the substrate orientation,” *Semicond. Sci. Technol.* **30**, 055014 (2015).
- [55] H. Grimmer, “The piezoelectric effect of second order in stress or strain: its form for crystals and quasicrystals of any symmetry,” *Acta Crystallogr. Sect. A* **63**, 441 (2007).
- [56] G. Bester and A. Zunger, “Cylindrically shaped zinc-blende semiconductor quantum dots do not have cylindrical symmetry: Atomistic symmetry, atomic relaxation, and piezoelectric effects,” *Phys. Rev. B* **71**, 045318 (2005).
- [57] G. Bester, A. Zunger, X. Wu, and D. Vanderbilt, “Effects of linear and nonlinear piezoelectricity on the electronic properties of InAs/GaAs quantum dots,” *Phys. Rev. B* **74**, 081305 (2006).
- [58] A. D. Andreev and E. P. O’Reilly, “Theory of the electronic structure of GaN/AlN hexagonal quantum dots,” *Phys. Rev. B* **62**, 15851 (2000).
- [59] M. A. Migliorato, J. Pal, R. Garg, G. Tse, H. Y. Al-Zahrani, U. Monteverde, S. Tomić, C.-K. Li, Y.-R. Wu, B. G. Crutchley, et al., “A review of non linear piezoelectricity in semiconductors,” *AIP Conf. Proc.* **1590**, 32 (2014).
- [60] A. Schliwa, G. Hönig, and D. Bimberg, “Electronic Properties of III-V Quantum Dots” (Springer International Publishing, Cham, 2014), pp. 57–85.
- [61] M. A. Caro, S. Schulz, and E. P. O’Reilly, “Theory of local electric polarization and its relation to internal strain: Impact on polarization potential and electronic properties of group-III nitrides,” *Phys. Rev. B* **88**, 214103 (2013).
- [62] I. Vurgaftman and J. R. Meyer, “Band parameters for nitrogen-containing semiconductors,” *J. Appl. Phys.* **94**, 3675 (2003).

- [63] S. Amoly, Ph.D. thesis, Linköping University, Sweden (2013).
- [64] H. A. Haus and J. R. Melcher, “Electromagnetic Fields and Energy” (Prentice-Hall, NJ, 1989).
- [65] H. Masui, S. Nakamura, S. P. DenBaars, and U. K. Mishra, “Nonpolar and semipolar III-nitride light-emitting diodes: Achievements and challenges,” *IEEE Trans. Electron Devices* **57**, 88 (2010).
- [66] G. Zhao, L. Wang, S. Yang, H. Li, H. Wei, D. Han, and Z. Wang, “Anisotropic structural and optical properties of semi-polar (11 $\bar{2}2$ ) GaN grown on m-plane sapphire using double AlN buffer layers,” *Sc. Rep.* **6**, 20787 (2016).
- [67] J. T. Griffiths, T. Zhu, F. Oehler, R. M. Emery, W. Y. Fu, B. P. L. Reid, R. A. Taylor, M. J. Kappers, C. J. Humphreys, and R. A. Oliver, “Growth of non-polar (11 $\bar{2}0$ ) InGaN quantum dots by metal organic vapour phase epitaxy using a two temperature method,” *APL Mater.* **2**, 126101 (2014).
- [68] M. S. Dresselhaus, G. Dresselhaus, and A. Jorio, “Group Theory: Application to the Physics of Condensed Matter” (Springer International Publishing, 2008).
- [69] J. F. Cornwell, “Group Theory and electronic energy bands in solids” (North- Holland Publishing Company, Amsterdam, 1969).
- [70] R. C. Powell, “Symmetry, Group Theory, and the Physical Properties of Crystals” (Springer International Publishing, 2010).
- [71] S. L. Altmann and H. P., “Point-Group Theory Tables” (Clarendon Press, 1994).
- [72] D. D. Stancill and A. Prabhakar, “Spin Waves-Theory and Applications” (Springer, 2009).
- [73] B. Thaller, “The Dirac equation” (Springer-Verlag, 1992).
- [74] M. Forsberg, Ph.D. thesis, Linköping University, Sweden (2016).
- [75] T. Uenoyama and M. Suzuki, “Valence subband structures of wurtzite GaN/AlGaIn quantum wells,” *Appl. Phys. Lett.* **67**, 2527 (1995).
- [76] S. Schulz, Ph.D. thesis, University of Bremen (2007).
- [77] M. Gmitra and J. Fabian, “First-principles studies of orbital and spin-orbit properties of GaAs, GaSb, InAs, and InSb zinc-blende and wurtzite semiconductors,” *Phys. Rev. B* **94**, 165202 (2016).
- [78] G. Kresse and J. Furthmüller, “Efficient iterative schemes for ab initio total-energy calculations using a plane-wave basis set,” *Phys. Rev. B* **54**, 11169 (1996).

- [79] J. P. Perdew and A. Zunger, “Self-interaction correction to density-functional approximations for many-electron systems,” *Phys. Rev. B* **23**, 5048 (1981).
- [80] X. Marie and N. Balkan, eds., “Semiconductor Modeling Techniques” (Springer, 2012).
- [81] D. J. Chadi and M. L. Cohen, “Tight-binding calculations of the valence bands of diamond and zincblende crystals,” *Phys. Status Solidi B* **68**, 405 (1975).
- [82] W. A. Harrison, “Bond-orbital model and the properties of tetrahedrally coordinated solids,” *Phys. Rev. B* **8**, 4487 (1973).
- [83] S. T. Bromley and M. A. Zwijnenburg, “Computational Modeling of Inorganic Nanomaterials” (CRC Press, 2016).
- [84] E. O. Kane, “The  $\mathbf{k}\cdot\mathbf{p}$  method,” *Phys. Rev.* **1**, 75 (1967).
- [85] E. O. Kane, “Band structure of indium antimonide,” *J. Phys. Chem. Solids* **1**, 249 (1957).
- [86] J. C. Phillips, “Energy-band interpolation scheme based on a pseudopotential,” *Phys. Rev.* **112**, 685 (1958).
- [87] M. L. Cohen and T. K. Bergstresser, “Band structures and pseudopotential form factors for fourteen semiconductors of the diamond and zinc-blende structures,” *Phys. Rev.* **141**, 789 (1966).
- [88] O. Stier, M. Grundmann, and D. Bimberg, “Electronic and optical properties of strained quantum dots modeled by 8-band  $\mathbf{k}\cdot\mathbf{p}$  theory,” *Phys. Rev. B* **59**, 5688 (1999).
- [89] A. D. Carlo, “Microscopic theory of nanostructured semiconductor devices: beyond the envelope-function approximation,” *Semicond. Sci. Technol.* **18**, R1 (2002).
- [90] S. L. Chuang and C. S. Chang, “ $\mathbf{k} \cdot \mathbf{p}$  method for strained wurtzite semiconductors,” *Phys. Rev. B* **54**, 2491 (1996).
- [91] S. L. Chuang, “Physics of photonic devices” (Wiley, New Jersey, 2nd edition, 2009).
- [92] I. Ivashev, Ph.D. thesis, Wilfrid Laurier University, Waterloo, ON (2016).
- [93] P. Löwdin, “A note on the quantum-mechanical perturbation theory,” *J. Chem. Phys* **19**, 1396 (1951).
- [94] J. Appel, “Effect of Spin-Orbit Coupling and Other Relativistic Corrections on Donor States in Ge and Si,” *Phys. Rev.* **133**, A280 (1964).
- [95] L. C. L. Y. Voon and M. Willatzen, eds., “The  $\mathbf{k}\cdot\mathbf{p}$  Method” (Springer, 2009).

- [96] M. Winkelnkemper, A. Schliwa, and D. Bimberg, “Interrelation of structural and electronic properties in  $\text{In}_x\text{Ga}_{1-x}\text{N}/\text{GaN}$  quantum dots using an eight-band  $\mathbf{k} \cdot \mathbf{p}$  model,” *Phys. Rev. B* **74**, 155322 (2006).
- [97] O. Marquardt, E. P. O’Reilly, and S. Schulz, “Electronic properties of site-controlled (111)-oriented zinc-blende  $\text{InGaAs}/\text{GaAs}$  quantum dots calculated using a symmetry-adapted  $\mathbf{k} \cdot \mathbf{p}$  Hamiltonian,” *J. Phys. Condens. Matter* **26**, 035303 (2013).
- [98] J.-H. Kang, M. Galicka, P. Kacman, and H. Shtrikman, “Wurtzite/zinc-blende k-shape inas nanowires with embedded two-dimensional wurtzite plates,” *Nano Lett.* **17**, 531 (2017).
- [99] C. Stampfl and C. G. Van de Walle, “Energetics and electronic structure of stacking faults in  $\text{AlN}$ ,  $\text{GaN}$ , and  $\text{InN}$ ,” *Phys. Rev. B* **57**, R15052 (1998).
- [100] S. Schulz, M. A. Caro, E. P. O’Reilly, and O. Marquardt, “Symmetry-adapted calculations of strain and polarization fields in (111)-oriented zinc-blende quantum dots,” *Phys. Rev. B* **84**, 125312 (2011).
- [101] M. Grundmann, “The Physics of Semiconductors”, Graduate Texts in Physics (Springer, Berlin, 2010).
- [102] A. Kobayashi, O. F. Sankey, S. M. Volz, and J. D. Dow, “Semiempirical tight-binding band structures of wurtzite semiconductors:  $\text{AlN}$ ,  $\text{CdS}$ ,  $\text{CdSe}$ ,  $\text{ZnS}$ , and  $\text{ZnO}$ ,” *Phys. Rev. B* **28**, 935 (1983).
- [103] A. Pecchia and A. D. Carlo, “Atomistic theory of transport in organic and inorganic nanostructures,” *Rep. Prog. Phys.* **67**, 1497 (2004).
- [104] J. C. Slater and G. F. Koster, “Simplified LCAO Method for the Periodic Potential Problem,” *Phys. Rev.* **94**, 1498 (1954).
- [105] G. Seifert, “Tight binding Density functional Theory: An Approximate Kohn-Sham DFT Scheme,” *J. Phys. Chem. A* **111**, 5609 (2007).
- [106] A. Pecchia, G. Penazzi, L. Salvucci, and A. D. Carlo, “Non-equilibrium Greens functions in density functional tight binding: method and applications,” *New J. Phys.* **10**, 065022 (2008).
- [107] S. Schulz and G. Czycholl, “Tight-binding model for semiconductor nanostructures,” *Phys. Rev. B* **72**, 165317 (2005).
- [108] P. Vogl, H. P. Hjalmarson, and J. D. Dow, “A semi-empirical tight-binding theory of the electronic structure of semiconductors,” *J. Phys. Chem. Solids* **44**, 365 (1983).

- [109] D. J. Chadi, “Spin-orbit splitting in crystalline and compositionally disordered semiconductors,” *Phys. Rev. B* **16**, 790 (1977).
- [110] T. B. Boykin, “More complete treatment of spin-orbit effects in tight-binding models,” *Phys. Rev. B* **57**, 1620 (1998).
- [111] S. Schulz, S. Schumacher, and G. Czycholl, “Spin-orbit coupling and crystal-field splitting in the electronic and optical properties of nitride quantum dots with a wurtzite crystal structure,” *Euro Phys. J. B* **64**, 51 (2008).
- [112] C. Galeriu, Ph.D. thesis, Worcester Polytechnic Institute (2005).
- [113] O. Steir, Ph.D. thesis, TU Berlin (2005).
- [114] D. S. P. Tanner, M. A. Caro, E. P. O’Reilly, and S. Schulz, “Random alloy fluctuations and structural inhomogeneities in c-plane  $\text{In}_x\text{Ga}_{1-x}\text{N}$  quantum wells: theory of ground and excited electron and hole states,” *RSC Adv.* **6**, 64513 (2016).
- [115] G. L. Bir and G. E. Pikus, “Symmetry and Strain-induced Effects in Semiconductors” (Wiley, New York, 1974).
- [116] Y. M. Niquet, D. Rideau, C. Tavernier, H. Jaouen, and X. Blase, “Onsite matrix elements of the tight-binding hamiltonian of a strained crystal: Application to silicon, germanium, and their alloys,” *Phys. Rev. B* **79**, 245201 (2009).
- [117] W. A. Harrison, ed., “Electronic Structure and the Properties of Solids” (Freeman, San Francisco, 1980).
- [118] T. B. Boykin, G. Klimeck, R. C. Bowen, and F. Oyafuso, “Diagonal parameter shifts due to nearest-neighbor displacements in empirical tight-binding theory,” *Phys. Rev. B* **66**, 125207 (2002).
- [119] S. Schulz, M. A. Caro, C. Coughlan, and E. P. O’Reilly, “Atomistic analysis of the impact of alloy and well-width fluctuations on the electronic and optical properties of  $\text{InGaN}/\text{GaN}$  quantum wells,” *Phys. Rev. B* **91**, 035439 (2015).
- [120] Q. Yan, P. Rinke, M. Scheffler, and C. G. Van de Walle, “Strain effects in group-III nitrides: Deformation potentials for  $\text{AlN}$ ,  $\text{GaN}$ , and  $\text{InN}$ ,” *Appl. Phys. Lett.* **95**, 121111 (2009).
- [121] L. D. Landau and E. M. Lifshitz, “Theory of Elasticity” (Oxford: Pergamon, 1986).
- [122] C. Pryor, J. Kim, L. W. Wang, A. J. Williamson, and A. Zunger, “Comparison of two methods for describing the strain profiles in quantum dots,” *J. Appl. Phys.* **83**, 2548 (1998).

- [123] S. Ahmed, N. Kharche, R. Rahman, M. Usman, S. Lee, H. Ryu, H. Bae, S. Clark, B. Haley, M. Naumov, et al., “Multimillion Atom Simulations with Nemo3D” (Springer New York, New York, NY, 2009), pp. 5745–5783.
- [124] D. P. Williams, A. D. Andreev, E. P. O’Reilly, and D. A. Faux, “Derivation of built-in polarization potentials in nitride-based semiconductor quantum dots,” *Phys. Rev. B* **72**, 235318 (2005).
- [125] M. Povolotskyi, M. Auf der Maur, and A. Di Carlo, “Strain effects in freestanding three-dimensional nitride nanostructures,” *Phys. Status Solidi (c)* **2**, 3891 (2005).
- [126] O. Marquardt, S. Boeck, C. Freysoldt, T. Hickel, and J. Neugebauer, “Plane-wave implementation of the real-space formalism and continuum elasticity theory,” *Comput. Phys. Commun.* **181**, 765 (2010).
- [127] M. J. P. Musgrave and J. A. Pople, “A general valence force field for diamond,” *Proceedings of the Royal Society of London. Series A. Mathematical and Physical Sciences* **268**, 474 (1962).
- [128] P. N. Keating, “Effect of invariance requirements on the elastic strain energy of crystals with application to the diamond structure,” *Phys. Rev.* **145**, 637 (1966).
- [129] R. M. Martin, “Elastic Properties of ZnS Structure Semiconductors,” *Phys. Rev. B* **1**, 4005 (1970).
- [130] D. S. P. Tanner, Ph.D. thesis, University College Cork, Cork (2017).
- [131] D. Camacho and Y. Niquet, “Application of keating’s valence force field model to non-ideal wurtzite materials,” *Physica E: Low-dimensional Systems and Nanostructures* **42**, 1361 (2010).
- [132] S. Plimpton, “Fast parallel algorithms for short-range molecular dynamics,” *J. Comput. Phys.* **117**, 1 (1995).
- [133] J. F. Nye, “Physical Properties of Crystals: Their Representation by Tensors and Matrices” (Oxford University Press, New York, 1985).
- [134] D. P. Williams, S. Schulz, A. D. Andreev, and E. P. O’Reilly, “Theory of GaN Quantum Dots for Optical Applications,” *IEEE J. Quant. Electron.* **15**, 1092 (2009).
- [135] N. Baer, P. Gartner, and F. Jahnke, “Coulomb effects in semiconductor quantum dots,” *Eur. Phys. J. B* **42**, 231 (2004).
- [136] N. Baer, S. Schulz, P. Gartner, S. Schumacher, G. Czycholl, and F. Jahnke, “Influence of symmetry and coulomb correlation effects on the optical properties of nitride quantum dots,” *Phys. Rev. B* **76**, 075310 (2007).

- [137] O. Stier, M. Grundmann, and D. Bimberg, “Electronic and optical properties of strained quantum dots modeled by 8-band  $\mathbf{k}\cdot\mathbf{p}$  theory,” *Phys. Rev. B* **59**, 5688 (1999).
- [138] A. Barenco and M. A. Dupertuis, “Quantum many-body states of excitons in a small quantum dot,” *Phys. Rev. B* **52**, 2766 (1995).
- [139] T. Jennewein, C. Simon, G. Weihs, H. Weinfurter, and A. Zeilinger, “Quantum cryptography with entangled photons,” *Phys. Rev. Lett.* **84**, 4729 (2000).
- [140] S. Tomić and N. Vukmirović, “Excitonic and biexcitonic properties of single GaN quantum dots modeled by 8-band  $\mathbf{k}\cdot\mathbf{p}$  theory and configuration-interaction method,” *Phys. Rev. B* **79**, 245330 (2009).
- [141] D. Williams, A. Andreev, and E. P. O’Reilly, “Self-consistent calculations of exciton, biexciton and charged exciton energies in InGaN/GaN quantum dots,” *Superlattices Microstruct.* **36**, 791 (2004).
- [142] M. Wimmer, S. V. Nair, and J. Shumway, “Biexciton recombination rates in self-assembled quantum dots,” *Phys. Rev. B* **73**, 165305 (2006).
- [143] G. Czycholl, “Theoretical solid state physics” (Vieweg, Braunschweig/Wiesbaden, 2000).
- [144] G. Bester, S. Nair, and A. Zunger, “Pseudopotential calculation of the excitonic fine structure of million-atom self-assembled  $\text{In}_{1-x}\text{Ga}_x\text{As}/\text{GaAs}$  quantum dots,” *Phys. Rev. B* **67**, 161306 (2003).
- [145] J. D. Plumhof, R. Trotta, A. Rastelli, and O. G. Schmidt, “Experimental methods of post-growth tuning of the excitonic fine structure splitting in semiconductor quantum dots,” *Nanoscale Res. Lett.* **7**, 336 (2012).
- [146] S. Tomić and N. Vukmirović, “Symmetries in Multiband Hamiltonians for Semiconductor Quantum Dots: Advanced Mathematical Models and Numerical Techniques” (Springer International Publishing, Cham, 2014), pp. 87–126.
- [147] G. Burns, “Introduction to Group Theory with Applications” (Elsevier, 1977).
- [148] M. A. Dupertuis, K. F. Karlsson, D. Y. Oberli, E. Pelucchi, A. Rudra, P. O. Holtz, and E. Kapon, “Symmetries and the polarized optical spectra of exciton complexes in quantum dots,” *Phys. Rev. Lett.* **107**, 127403 (2011).
- [149] G. Juska, V. Dimastrodonato, L. O. Mereni, A. Gocalinska, and E. Pelucchi, “Towards quantum-dot arrays of entangled photon emitters,” *Nature Photonics* **7**, 527 (2013).
- [150] S. Deshpande, T. Frost, A. Hazari, and P. Bhattacharya, “Electrically pumped single-photon emission at room temperature from a single InGaN/GaN quantum dot,” *Appl. Phys. Lett.* **105**, 141109 (2014).

- [151] A. D. Andreev and E. P. O'Reilly, "Optical transitions and radiative lifetime in GaN/AlN self-organized quantum dots," *Appl. Phys. Lett.* **79**, 521 (2001).
- [152] N. Baer, S. Schulz, S. Schumacher, P. Gartner, G. Czycholl, and F. Jahnke, "Optical properties of self-organized wurtzite InN/GaN quantum dots: A combined atomistic tight-binding and full configuration interaction calculation," *Appl. Phys. Lett.* **87**, 231114 (2005).
- [153] E. Monroy, E. Muñoz, F. J. Sánchez, F. Calle, E. Calleja, B. Beaumont, P. Gibart, J. A. Muñoz, and F. Cussó, "High-performance GaN p-n junction photodetectors for solar ultraviolet applications," *Semicond. Sci. Technol.* **13**, 1042 (1998).
- [154] S. Schulz, A. Berube, and E. P. O'Reilly, "Polarization fields in nitride-based quantum dots grown on nonpolar substrates," *Phys. Rev. B* **79**, 081401 (2009).
- [155] H. Matsui and H. Tabata, "In-plane light polarization in nonpolar m-plane  $\text{Cd}_x\text{Zn}_{1-x}\text{O}/\text{ZnO}$  quantum wells," *Appl. Phys. Lett.* **98**, 261902 (2011).
- [156] H. Matsui and H. Tabata, in "Luminescence", edited by J. Thirumalai (IntechOpen, Rijeka, 2016), chap. 4.
- [157] J. E. Avron, G. Bisker, D. Gershoni, N. H. Lindner, E. A. Meirom, and R. J. Warburton, "Entanglement on demand through time reordering," *Phys. Rev. Lett.* **100**, 120501 (2008).
- [158] F. Ding, R. Singh, J. D. Plumhof, T. Zander, V. Krapek, Y. H. Chen, M. Benyoucef, V. Zwiller, K. Dorr, G. Bester, et al., "Tuning the exciton binding energies in single self-assembled InGaAs/GaAs quantum dots by piezoelectric-induced biaxial stress," *Phys. Rev. Lett.* **104**, 067405 (2010).
- [159] K. B. Hong and M. K. Kuo, "Effect of piezoelectric constants in electronic structures of InGaN quantum dots," *Semicond. Sci. Technol.* **28**, 105006 (2013).
- [160] S. Schulz and O. Marquardt, "Electronic structure of polar and semipolar  $(11\bar{2}2)$ -oriented nitride dot-in-a-well systems," *Phys. Rev. Applied* **3**, 064020 (2015).
- [161] K. Schuh, S. Barthel, O. Marquardt, T. Hickel, J. Neugebauer, G. Czycholl, and F. Jahnke, "Strong dipole coupling in nonpolar nitride quantum dots due to coulomb effects," *Appl. Phys. Lett.* **100**, 092103 (2012).
- [162] S. Barthel, K. Schuh, O. Marquardt, T. Hickel, J. Neugebauer, F. Jahnke, and G. Czycholl, "Interplay between coulomb interaction and quantum-confined stark-effect in polar and nonpolar wurtzite InN/GaN quantum dots," *Eur. Phys. J. B* **86**, 449 (2013).
- [163] S. Boeck, C. Freysoldt, A. Dick, L. Ismer, and J. Neugebauer, "The object-oriented DFT program library S/PHI/nX," *Comput. Phys. Commun.* **182**, 543 (2011).

- [164] M. A. Caro, S. Schulz, S. B. Healy, and E. P. O' Reilly, "Built-in field control in alloyed c-plane III-N quantum dots and wells," *J. Appl. Phys.* **109**, 084110 (2011).
- [165] U. M. E. Christmas, A. D. Andreev, and D. A. Faux, "Calculation of electric field and optical transitions in InGaN/GaN quantum wells," *J. Appl. Phys.* **98**, 073522 (2005).
- [166] P. G. Moses, M. Miao, Q. Yan, and C. G. Van de Walle, "Hybrid functional investigations of band gaps and band alignments for AlN, GaN, InN, and InGaN," *J. Chem. Phys.* **134**, 084703 (2011).
- [167] H.-H. Huang and Y.-R. Wu, "Light emission polarization properties of semipolar InGaN/-GaN quantum well," *J. Appl. Phys.* **107**, 053112 (2010).
- [168] V. A. Fonoberov and A. A. Balandin, "Excitonic properties of strained wurtzite and zinc-blende GaN/Al<sub>x</sub>Ga<sub>1-x</sub>N quantum dots," *J. Appl. Phys.* **94**, 7178 (2003).
- [169] N. Antoine-Vincent, F. Natali, M. Mihailovic, A. Vasson, J. Leymarie, P. Disseix, D. Byrne, F. Semond, and J. Massies, "Determination of the refractive indices of AlN, GaN, and Al<sub>x</sub>Ga<sub>1-x</sub>N grown on (111)Si substrates," *J. Appl. Phys.* **93**, 5222 (2003).
- [170] M. Winkelnkemper, M. Dworzak, T. P. Bartel, A. Strittmatter, A. Hoffmann, and D. Bimberg, "Origin of the broad lifetime distribution of localized excitons in InGaN/GaN quantum dots," *Phys. Status Solidi (b)* **245**, 2766 (2008).
- [171] S. Shokhovets, G. Gobsch, and O. Ambacher, "Momentum matrix element and conduction band nonparabolicity in wurtzite GaN," *Appl. Phys. Lett.* **86**, 161908 (2005).
- [172] A. Schliwa, M. Winkelnkemper, and D. Bimberg, "Impact of size, shape, and composition on piezoelectric effects and electronic properties of In(Ga)As/GaAs quantum dots," *Phys. Rev. B* **76**, 205324 (2007).
- [173] F. Ferdos, S. Wang, Y. Wei, A. Larsson, M. Sadeghi, and Q. Zhao, "Influence of a thin GaAs cap layer on structural and optical properties of InAs quantum dots," *Appl. Phys. Lett.* **81**, 1195 (2002).
- [174] S. Founta, C. Bougerol, H. Mariette, B. Daudin, and P. Vennéguès, "Anisotropic morphology of nonpolar a-plane GaN quantum dots and quantum wells," *J. Appl. Phys.* **102**, 074304 (2007).
- [175] T. Zhu, J. T. Griffiths, W. Y. Fu, A. Howkins, I. W. Boyd, M. J. Kappers, and R. A. Oliver, "Growth of non-polar InGaN quantum dots with an underlying AlN/-GaN distributed bragg reflector by metal-organic vapour phase epitaxy," *Superlattices Microstruct.* **88**, 480 (2015).

- [176] S. Founta, F. Rol, E. Bellet-Amalric, J. Bleuse, B. Daudin, B. Gayral, H. Mariette, and C. Moisson, “Optical properties of GaN quantum dots grown on nonpolar (11-20) SiC by molecular-beam epitaxy,” *Appl. Phys. Lett.* **86**, 171901 (2005).
- [177] B. P. L. Reid, T. Zhu, C. C. S. Chan, C. Kocher, F. Oehler, R. Emery, M. J. Kappers, R. A. Oliver, and R. A. Taylor, “High temperature stability in non-polar (11 $\bar{2}$ 0) InGa $\bar{\text{N}}$  quantum dots: Exciton and biexciton dynamics,” *Phys. Status Solidi (c)* **11**, 702 (2014).
- [178] S. C. Davies, D. J. Mowbray, F. Ranalli, and T. Wang, “Influence of the GaN barrier thickness on the optical properties of InGa $\bar{\text{N}}$ /Ga $\bar{\text{N}}$  multilayer quantum dot heterostructures,” *Appl. Phys. Lett.* **96**, 251904 (2010).
- [179] S. Schulz, M. A. Caro, and E. P. O’Reilly, “Prediction of strong ground state electron and hole wave function spatial overlap in nonpolar Ga $\bar{\text{N}}$ /Al $\bar{\text{N}}$  quantum dots,” *Appl. Phys. Lett.* **101**, 113107 (2012).
- [180] M. Funato and Y. Kawakami, “Excitonic properties of polar, semipolar, and nonpolar InGa $\bar{\text{N}}$ /Ga $\bar{\text{N}}$  strained quantum wells with potential fluctuations,” *J. Appl. Phys.* **103**, 093501 (2008).
- [181] S. Schulz and E. P. O’Reilly, “Excitonic binding energies in non-polar Ga $\bar{\text{N}}$  quantum wells,” *Phys. Status Solidi (c)* **7**, 1900 (2010).
- [182] S. Wei, Y. Jia, and C. Xia, “Excitonic optical absorption in wurtzite InGa $\bar{\text{N}}$ /Ga $\bar{\text{N}}$  quantum wells,” *Superlattices Microstruct.* **51**, 9 (2012).
- [183] D. Simeonov, A. Dussaigne, R. Butté, and N. Grandjean, “Complex behavior of biexcitons in Ga $\bar{\text{N}}$  quantum dots due to a giant built-in polarization field,” *Phys. Rev. B* **77**, 075306 (2008).
- [184] J. W. Robinson, J. H. Rice, A. Jarjour, J. D. Smith, R. A. Taylor, R. A. Oliver, G. A. D. Briggs, M. J. Kappers, C. J. Humphreys, and Y. Arakawa, “Time-resolved dynamics in single InGa $\bar{\text{N}}$  quantum dots,” *Appl. Phys. Lett.* **83**, 2674 (2003).
- [185] A. F. Jarjour, R. A. Oliver, A. Tahraoui, M. J. Kappers, C. J. Humphreys, and R. A. Taylor, “Control of the oscillator strength of the exciton in a single InGa $\bar{\text{N}}$ -Ga $\bar{\text{N}}$  quantum dot,” *Phys. Rev. Lett.* **99**, 197403 (2007).
- [186] S. Kanta Patra, T. Wang, T. J. Puchtler, T. Zhu, R. A. Oliver, R. A. Taylor, and S. Schulz, “Theoretical and experimental analysis of radiative recombination lifetimes in nonpolar InGa $\bar{\text{N}}$ /Ga $\bar{\text{N}}$  quantum dots,” *Phys. Status Solidi (b)* **254** (2017).
- [187] S. Schulz, D. P. Tanner, E. P. O’Reilly, M. A. Caro, T. L. Martin, P. A. J. Bagot, M. P. Moody, F. Tang, J. T. Griffiths, F. Oehler, et al., “Structural, electronic, and

- optical properties of  $m$ -plane InGaN/GaN quantum wells: Insights from experiment and atomistic theory,” *Phys. Rev. B* **92**, 235419 (2015).
- [188] H. Kawamoto, “The History of Liquid-Crystal Displays,” *Proc. IEEE* **90** (2002).
- [189] D. Loss and D. P. DiVincenzo, “Quantum computation with quantum dots,” *Phys. Rev. A* **57**, 120 (1998).
- [190] C. H. Bennett and G. Brassard, “Quantum cryptography: Public key distribution and coin tossing,” *Proc. IEEE Inter. Conf. Computers, Systems Signal Process.* pp. 175 – 179 (1984).
- [191] C. Kurtsiefer, P. Zarda, M. Halder, H. Weinfurter, P. M. Gorman, P. R. Tapster, and J. G. Rarity, “Quantum cryptography: A step towards global key distribution,” *Nature* **419** (2002).
- [192] C.-Z. Peng, T. Yang, X.-H. Bao, J. Zhang, X.-M. Jin, F.-Y. Feng, B. Yang, J. Yang, J. Yin, Q. Zhang, et al., “Experimental free-space distribution of entangled photon pairs over 13 km: Towards satellite-based global quantum communication,” *Phys. Rev. Lett.* **94**, 150501 (2005).
- [193] H. J. Kimble, M. Dagenais, and L. Mandel, “Photon antibunching in resonance fluorescence,” *Phys. Rev. Lett.* **39**, 691 (1977).
- [194] B. Lounis and W. E. Moerner, “Single photons on demand from a single molecule at room temperature,” *Nature* **407**, 491 (2000).
- [195] T. T. Tran, K. Bray, M. J. Ford, M. Toth, and I. Aharonovich, “Quantum emission from hexagonal boron nitride monolayers,” *Nat. Nanotechnol.* **11**, 37 (2016).
- [196] M. Kianinia, B. Regan, S. A. Tawfik, T. T. Tran, M. J. Ford, I. Aharonovich, and M. Toth, “Robust solid-state quantum system operating at 800 K,” *ACS Photonics* **4**, 768 (2017).
- [197] B. Monemar, “Fundamental energy gap of GaN from photoluminescence excitation spectra,” *Phys. Rev. B* **10**, 676 (1974).
- [198] S.-H. Gong, J.-H. Kim, Y.-H. Ko, C. Rodriguez, J. Shin, Y.-H. Lee, L. S. Dang, X. Zhang, and Y.-H. Cho, “Self-aligned deterministic coupling of single quantum emitter to nanofocused plasmonic modes,” *Proc. Natl. Acad. Sci.* **112**, 5280 (2015).
- [199] Ž. Gačević, M. Holmes, E. Chernysheva, M. Müller, A. Torres-Pardo, P. Veit, F. Bertram, J. Christen, J. M. González Calbet, Y. Arakawa, et al., “Emission of linearly polarized single photons from quantum dots contained in nonpolar, semipolar, and polar sections of pencil-like InGaN/GaN nanowires,” *ACS Photonics* **4**, 657 (2017).

- [200] M. J. Holmes, S. Kako, K. Choi, M. Arita, and Y. Arakawa, “Proc. SPIE” (2016), vol. 9748, chap. Linearly polarized single photons from small site-controlled GaN nanowire quantum dots, p. 97481E.
- [201] T. Jemsson, H. Machhadani, P.-O. Holtz, and K. F. Karlsson, “Polarized single photon emission and photon bunching from an InGaN quantum dot on a GaN micropillar,” *Nanotechnology* **26**, 65702 (2015).
- [202] S. Kremling, C. Tessarek, H. Dartsch, S. Figge, S. Höfling, L. Worschech, C. Kruse, D. Hommel, and A. Forchel, “Single photon emission from InGaN/GaN quantum dots up to 50 K,” *Appl. Phys. Lett.* **100**, 061115 (2012).
- [203] J.-H. Kim, Y.-H. Ko, S.-H. Gong, S.-M. Ko, and Y.-H. Cho, “Ultrafast single photon emitting quantum photonic structures based on a nano-obelisk,” *Sci. Rep.* **3**, 2150 (2013).
- [204] L. Zhang, C.-H. Teng, P.-C. Ku, and H. Deng, “Site-controlled InGaN/GaN single-photon-emitting diode,” *Appl. Phys. Lett.* **108**, 153102 (2016).
- [205] S. Deshpande, J. Heo, A. Das, and P. Bhattacharya, “Electrically driven polarized single-photon emission from an InGaN quantum dot in a GaN nanowire,” *Nat. Commun.* **4**, 1675 (2013).
- [206] S. Deshpande, A. Das, and P. Bhattacharya, “Blue single photon emission up to 200 K from an InGaN quantum dot in AlGaIn nanowire,” *Appl. Phys. Lett.* **102**, 161114 (2013).
- [207] T. J. Puchler, T. Wang, C. X. Ren, F. Tang, R. A. Oliver, R. A. Taylor, and T. Zhu, “Ultrafast, polarized, single-photon emission from m-plane InGaIn quantum dots on GaIn nanowires,” *Nano Lett.* **16**, 7779 (2016).
- [208] A. Lundskog, C.-W. Hsu, K. Fredrik Karlsson, S. Amloy, D. Nilsson, U. Forsberg, P. Olof Holtz, and E. Janzén, “Direct generation of linearly polarized photon emission with designated orientations from site-controlled InGaIn quantum dots,” *Light Sci. Appl.* **3**, e139 (2014).
- [209] A. Al-Qasimi, O. Korotkova, D. James, and E. Wolf, “Definitions of the degree of polarization of a light beam,” *Opt. Lett.* **32**, 1015 (2007).
- [210] E. Wolf, “Coherence properties of partially polarized electromagnetic radiation,” *Il Nuovo Cimento* (1955-1965) **13**, 1165 (1959).
- [211] B. P. Reid, T. Zhu, T. J. Puchler, L. J. Fletcher, C. C. Chan, R. A. Oliver, and R. A. Taylor, “Origins of spectral diffusion in the micro-photoluminescence of single InGaIn quantum dots,” *Jpn. J. Appl. Phys.* **52**, 08JE01 (2013).

- [212] C. Mounir, U. T. Schwarz, I. L. Koslow, M. Kneissl, T. Wernicke, T. Schimpke, and M. Strassburg, “Impact of inhomogeneous broadening on optical polarization of high-inclination semipolar and nonpolar  $\text{In}_x\text{Ga}_{1-x}\text{N}/\text{GaN}$  quantum wells,” *Phys. Rev. B* **93**, 235314 (2016).
- [213] S. Schulz, T. J. Badcock, M. A. Moram, P. Dawson, M. J. Kappers, C. J. Humphreys, and E. P. O’Reilly, “Electronic and optical properties of nonpolar  $a$ -plane GaN quantum wells,” *Phys. Rev. B* **82**, 125318 (2010).
- [214] R. Bardoux, T. Guillet, B. Gil, P. Lefebvre, T. Bretagnon, T. Taliercio, S. Rousset, and F. Semond, “Polarized emission from GaN/AlN quantum dots: Single-dot spectroscopy and symmetry-based theory,” *Phys. Rev. B* **77**, 235315 (2008).
- [215] T. Wang, T. J. Puchtler, S. K. Patra, T. Zhu, M. Ali, T. J. Badcock, T. Ding, R. A. Oliver, S. Schulz, and R. A. Taylor, “Direct generation of linearly polarized single photons with a deterministic axis in quantum dots,” *Nanophotonics* **6**, 1175 (2017).
- [216] P. Mrowiński, K. Tarnowski, J. Olszewski, A. Somers, M. Kamp, J. P. Reithmaier, W. Urbanczyk, J. Misiewicz, P. Machnikowski, and G. Sek, “Tailoring the photoluminescence polarization anisotropy of a single InAs quantum dash by a post-growth modification of its dielectric environment,” *J. Appl. Phys.* **120**, 074303 (2016).
- [217] I. Favero, G. Cassabois, A. Jankovic, R. Ferreira, D. Darson, C. Voisin, C. Delalande, P. Roussignol, A. Badolato, P. M. Petroff, et al., “Giant optical anisotropy in a single InAs quantum dot in a very dilute quantum-dot ensemble,” *Appl. Phys. Lett.* **86**, 041904 (2005).
- [218] J. Pal, G. Tse, V. Haxha, M. A. Migliorato, and S. Tomić, “Second-order piezoelectricity in wurtzite III-N semiconductors,” *Phys. Rev. B* **84**, 085211 (2011).
- [219] L. Pedesseau, C. Katan, and J. Even, “On the entanglement of electrostriction and nonlinear piezoelectricity in non-centrosymmetric materials,” *Appl. Phys. Lett.* **100**, 031903 (2012).
- [220] P.-Y. Prodhomme, A. Beya-Wakata, and G. Bester, “Nonlinear piezoelectricity in wurtzite semiconductors,” *Phys. Rev. B* **88**, 121304 (2013).
- [221] A. Beya-Wakata, P.-Y. Prodhomme, and G. Bester, “First- and second-order piezoelectricity in III-V semiconductors,” *Phys. Rev. B* **84**, 195207 (2011).
- [222] M. A. Caro, S. Schulz, and E. P. O’Reilly, “Origin of nonlinear piezoelectricity in III-V semiconductors: Internal strain and bond ionicity from hybrid-functional density functional theory,” *Phys. Rev. B* **91**, 075203 (2015).

- [223] M. Funato, M. Ueda, D. Inoue, Y. Kawakami, Y. Narukawa, and T. Mukai, “Experimental and theoretical considerations of polarization field direction in semipolar InGaN/GaN quantum wells,” *Appl. Phys. Express* **3**, 071001 (2010).
- [224] D. F. Feezell, J. S. Speck, S. P. DenBaars, and S. Nakamura, “Semipolar (20 $\bar{2}$ 1) InGaN/-GaN light-emitting diodes for high-efficiency solid-state lighting,” *J. Disp. Technol.* **9**, 190 (2013).
- [225] A. E. Romanov, T. J. Baker, S. Nakamura, J. S. Speck, and E. U. Group, “Strain-induced polarization in wurtzite III-nitride semipolar layers,” *J. Appl. Phys.* **100**, 023522 (2006).
- [226] H. Morkoç, “Electronic Band Structure and Polarization Effects” (Wiley-VCH Verlag GmbH & Co. KGaA, 2009), pp. 131–321.
- [227] A. Das, G. P. Dimitrakopoulos, Y. Kotsar, A. Lotsari, T. Kehagias, P. Komninou, and E. Monroy, “Improved luminescence and thermal stability of semipolar (11-22) InGaN quantum dots,” *Appl. Phys. Lett.* **98**, 201911 (2011).
- [228] H. Shen, G. A. Garrett, M. Wraback, H. Zhong, A. Tyagi, S. P. DenBaars, S. Nakamura, and J. S. Speck, “Polarization field crossover in semi-polar InGaN/GaN single quantum wells,” *Phys. Status Solidi (c)* **7**, 2378 (2010).
- [229] A. Hangleiter, F. Hitzel, S. Lahmann, and U. Rossow, “Composition dependence of polarization fields in GaInN/GaN quantum wells,” *Appl. Phys. Lett.* **83**, 1169 (2003).
- [230] C. Adelmann, E. Sarigiannidou, D. Jalabert, Y. Hori, J.-L. Rouvière, B. Daudin, S. Fanget, C. Bru-Chevallier, T. Shibata, and M. Tanaka, “Growth and optical properties of GaN/AlN quantum wells,” *Appl. Phys. Lett.* **82**, 4154 (2003).
- [231] A. Helman, M. Tchernycheva, A. Lusson, E. Warde, F. H. Julien, K. Moumanis, G. Fishman, E. Monroy, B. Daudin, D. L. S. Dang, et al., “Intersubband spectroscopy of doped and undoped GaN/AlN quantum wells grown by molecular-beam epitaxy,” *Appl. Phys. Lett.* **83**, 5196 (2003).
- [232] C. Buchheim, R. Goldhahn, A. T. Winzer, G. Gobsch, U. Rossow, D. Fuhrmann, A. Hangleiter, F. Furtmayr, and M. Eickhoff, “Stark shift of interband transitions in AlN/GaN superlattices,” *Appl. Phys. Lett.* **90**, 241906 (2007).
- [233] X. Yang, M. Arita, S. Kako, and Y. Arakawa, “Formation of m-plane InGaN/GaN quantum dots using strain engineering of AlGaIn/AlN interlayers,” *Appl. Phys. Lett.* **99**, 061914 (2011).
- [234] S. Schulz and E. P. O’Reilly, “Theory of reduced built-in polarization field in nitride-based quantum dots,” *Phys. Rev. B* **82**, 033411 (2010).

- [235] M. Sénès, K. L. Smith, T. M. Smeeton, S. E. Hooper, and J. Heffernan, “Strong carrier confinement in  $\text{In}_x\text{Ga}_{1-x}\text{N}$  quantum dots grown by molecular beam epitaxy,” *Phys. Rev. B* **75**, 045314 (2007).
- [236] J. Simon, N. T. Pelekanos, C. Adelmann, E. Martinez-Guerrero, R. André, B. Daudin, L. S. Dang, and H. Mariette, “Direct comparison of recombination dynamics in cubic and hexagonal GaN/AlN quantum dots,” *Phys. Rev. B* **68**, 035312 (2003).
- [237] S. K. Patra and S. Schulz, “Non-polar  $\text{In}_x\text{Ga}_{1-x}\text{N}/\text{GaN}$  quantum dots: impact of dot size and shape anisotropies on excitonic and biexcitonic properties,” *J. Phys. D: Appl. Phys.* **50**, 025108 (2017).
- [238] C. X. Ren, “Polarisation fields in III-nitrides: effects and control,” *Mater. Sci. Technol.* **32**, 418 (2016).
- [239] Ž. Gačević, N. Vukmirović, N. García-Lepetit, A. Torres-Pardo, M. Müller, S. Metzner, S. Albert, A. Bengoechea-Encabo, F. Bertram, P. Veit, et al., “Influence of composition, strain, and electric field anisotropy on different emission colors and recombination dynamics from InGaN nanodisks in pencil-like GaN nanowires,” *Phys. Rev. B* **93**, 125436 (2016).
- [240] M. Auf der Maur, A. Pecchia, G. Penazzi, W. Rodrigues, and A. Di Carlo, “Efficiency drop in green InGaN/GaN light emitting diodes: The role of random alloy fluctuations,” *Phys. Rev. Lett.* **116**, 027401 (2016).
- [241] D. Watson-Parris, M. J. Godfrey, and P. Dawson, “Carrier localization mechanisms in  $\text{In}_x\text{Ga}_{1-x}\text{N}/\text{GaN}$  quantum wells,” *Phys. Rev. B* **83**, 115321 (2011).
- [242] T.-J. Yang, R. Shivaraman, J. S. Speck, and Y.-R. Wu, “The influence of random indium alloy fluctuations in indium gallium nitride quantum wells on the device behavior,” *J. Appl. Physics* **116**, 113104 (2014).
- [243] S. Schulz, M. A. Caro, L.-T. Tan, P. J. Parbrook, R. W. Martin, and E. P. O’Reilly, “Composition-Dependent Band Gap and Band-Edge Bowing in AlInN: A Combined Theoretical and Experimental Study,” *Appl. Phys. Express* **6**, 121001 (2013).
- [244] S. Schulz, S. Schumacher, and G. Czycholl, “Tight-binding model for semiconductor quantum dots with a wurtzite crystal structure: From one-particle properties to coulomb correlations and optical spectra,” *Phys. Rev. B* **73**, 245327 (2006).
- [245] W. Tsai, K. Hong, and M. Kuo, “Effects of composition distribution on electronic structures of self-assembled InGaN/GaN quantum dots,” *Phys. Status Solidi (b)* **247**, 1764 (2010).

- [246] K. B. Hong and M. K. Kuo, “Fully coupled and semi-coupled piezoelectric models on the optical properties of InGaN quantum dots,” *Semicond. Sci. Tech.* **25**, 065005 (2010).
- [247] M. O. Nestoklon, R. Benchamekh, and P. Voisin, “Virtual crystal description of III–v semiconductor alloys in the tight binding approach,” *J. Phys. Condens. Matter* **28**, 305801 (2016).
- [248] D. Vvedensky, “Lecture notes on Group Theory” (Imperial College London, UK, 2001).
- [249] M. A. Caro, S. Schulz, and E. P. O’Reilly, “Hybrid functional study of the elastic and structural properties of wurtzite and zinc-blende group-III nitrides,” *Phys. Rev. B* **86**, 014117 (2012).
- [250] Q. Yan, P. Rinke, M. Winkelkemper, A. Qteish, D. Bimberg, M. Scheffler, and C. G. V. de Walle, “Band parameters and strain effects in ZnO and group-III nitrides,” *Semicond. Sci. Technol.* **26**, 014037 (2011).